

Geotechnical modelling of a deep tunnel excavation in the Boom Clay formation

Michail Miliaritsas

Master of Science Thesis

Geotechnical modelling of a deep tunnel excavation in the Boom Clay formation

MASTER OF SCIENCE THESIS

For the degree of Master of Science in Geo-Engineering at Delft
University of Technology

Michail Milioritsas

21st October 2014

Photo cover image:

Fully plastic zone (red points) and shear hardening zone (green points) around a tunnel excavation, numerically simulated with the PLAXIS 2D 2011 finite element code. The material (Boom Clay) response has been modelled with the Hardening Soil model.



Published through the Delft University of Technology Institutional Repository, based on Open Access.

Copyright © M. Milioritsas, 2014

All rights reserved. Reproduction or translation of any part of this work in any form by print, photocopy or any other means, without the prior permission of either the author, members of the graduation committee or Delft University of Technology is prohibited.

DELFT UNIVERSITY OF TECHNOLOGY
DEPARTMENT OF
CIVIL ENGINEERING AND GEOSCIENCES

The undersigned hereby certify that they have read and recommend to the Faculty of Civil Engineering and Geosciences for acceptance a thesis entitled

GEOTECHNICAL MODELLING OF A DEEP TUNNEL EXCAVATION IN THE BOOM CLAY FORMATION

by

MICHAIL MILIORITSAS

in partial fulfillment of the requirements for the degree of

MASTER OF SCIENCE GEO-ENGINEERING

Dated: 21st October 2014

Supervisors:

Prof. Dr. Michael A. Hicks

Prof. Dr. Cristina Jommi

Dr. Philip J. Vardon

MSc. dipl.-ing. Patrick Arnold

Reader:

Prof. Dr. Athanasios (Tom) Scarpas

Abstract

In this study a deep tunnel excavation in the Boom Clay (BC) formation, in the context of constructing a repository for the deep geological disposal of radioactive waste in the Netherlands, is investigated by means of numerical modelling.

First the selection of a constitutive soil model, that captures adequately the known aspects of the mechanical behaviour of natural BC, is addressed. To this purpose, three conventional, drained, strain-controlled triaxial compression tests and one high pressure oedometer test, performed on intact BC samples originating from Essen (Belgium) which were extracted from the literature, were numerically simulated utilising the lab test facility of the *PLAXIS 2D 2011* software. The Linear Elastic Perfectly Plastic-Mohr Coulomb model, the Modified Cam-Clay model, the Soft Soil-Creep model and the Hardening Soil (HS) model were calibrated on the basis of the test results. Based on the comparison of the numerical results with the test data, it was concluded that the HS model performed best, that is, especially in terms of reproducing the evolution of stiffness and mobilised shear strength under triaxial compression, which are deemed to be the most predominant processes affecting the behaviour of the BC host rock due to a tunnel excavation.

Subsequently, the level of influence of the geotechnical properties of BC, used as input parameters for the HS model, on the radial extent of the fully Plastic Zone (PZ) and of the Hydro-Mechanical (HM) disturbance, caused by an undrained tunnel excavation, is investigated. The level of influence of the soil properties on the magnitude of the hoop forces (N) in the tunnel liner and on the magnitude of the generated pore water pressures (u) around the excavation is examined as well. This was achieved by numerically simulating an undrained tunnel excavation in the BC host rock, in two-dimensional plane strain conditions, with the *PLAXIS 2D 2011* finite element program. A mechanical sensitivity analysis was performed by varying, individually, selected HS model input parameters to upper and lower bound values. It was found that the thickness of the PZ was mainly influenced by the magnitude of the elastoplastic shear stiffness of the material. The radial extent of the HM disturbance was mostly affected by the elastic shear stiffness of the soil. Finally, the magnitude of N in the liner and the magnitude of u in the vicinity of the excavation were found to be primarily influenced by the value of the effective friction angle (φ') of the BC material.

Acknowledgements

I would like to express my gratitude to Michael Hicks, Cristina Jommi, Phil Vardon and Tom Scarpas for their expert guidance and supervision during my graduation project. I would also like to thank my daily supervisor, Patrick Arnold, for his continuous support, expert advice and constructive comments on my work.

Last but not least, I am very grateful to my parents and brother for their constant encouragement and support throughout my studies.

Delft, University of Technology
21st October 2014

Michail Miliaritsas

Contents

Acknowledgements	iii
Glossary	xxiii
1 Introduction	1
1-1 Radioactive waste disposal in Boom Clay	1
1-2 Life-time phases of a radioactive waste repository	2
1-3 Problem Definition	3
1-4 Research questions and research approach	3
2 Characterisation of Boom Clay	5
2-1 Introduction	5
2-2 Geological setting	5
2-2-1 Geography	5
2-2-2 Stratigraphy	6
2-2-3 Mineralogy	7
2-3 Physical properties	8
2-4 Hydro-mechanical properties and constitutive response	9
2-4-1 Friction angle and cohesion	9
2-4-2 Stiffness, mobilised shear strength and volumetric response	10
2-4-3 Swelling potential in triaxial stress conditions	14
2-4-4 Comparison of the response of BC in triaxial stress conditions at the Essen and Mol sites	15
2-4-5 Response in oedometer stress conditions	17
2-4-6 Initial and induced anisotropy	21
2-4-7 Hydraulic conductivity	26
2-4-8 Ranges of geotechnical BC property values	28
2-5 Summary	29
3 Validation of soil models for Boom Clay	31

3-1	Introduction	31
3-2	Brief description of the evaluated soil models	32
3-3	Evaluation of soil models with the lab test facility of <i>PLAXIS</i>	33
3-3-1	Set up of the laboratory tests simulations	33
3-3-2	Comments on the numerical simulations and the produced results	35
3-3-3	Evaluation of the response of the LEPP-MC model	35
3-3-4	Evaluation of the response of the MCC model	39
3-3-5	Evaluation of the response of the SS-C model	39
3-3-6	Evaluation of the response of the HS model	41
3-3-7	Selection of the model that captures the BC response the best	44
3-4	The Hardening Soil model	46
3-4-1	General description	46
3-4-2	Yield function for shear hardening	46
3-4-3	Calculation of the axial strains	48
3-4-4	Evolution of plastic volumetric strains due to shear hardening	49
3-4-5	Cap yield surface	50
3-4-6	Specifics of the HS model	52
3-4-7	HS model input parameters	54
3-4-8	On the internal algorithm and the internal parameters of the HS model	55
3-5	Investigating the influence of the HS model input parameters	58
3-5-1	Changes in the values of the HS model input parameters	59
3-5-2	Effects of the model input parameters on the results of the simulation of the <i>Ess75Tr01</i> test	60
3-5-3	Effects of the model input parameters on the results of the simulation of the <i>Ess75Tr02</i> test	65
3-5-4	Effects of the model input parameters on the results of the simulation of the <i>Ess75Tr03</i> test	69
3-5-5	On the response of the cap of the HS model	72
3-6	Limitations of the laboratory tests and the numerical tool	73
3-7	Summary	75
4	Modelling a deep tunnel excavation in the Boom Clay formation	77
4-1	Introduction	77
4-2	Set up of the numerical simulations	78
4-2-1	Set up of the geotechnical model	78
4-2-2	Calculation phases	81
4-2-3	Set up of the mechanical sensitivity analysis	82
4-3	Discussion on the numerical results	83
4-3-1	Effective stress paths in the vicinity of the tunnel	84
4-3-2	Influence of the varied model input parameters on the numerical results	88
4-4	Level of influence of the varied model input parameters	108
4-5	Summary	110
5	Conclusions and recommendations	113
5-1	Conclusions	113
5-1-1	On the performance of the HS model in simulating the laboratory tests .	113

5-1-2 On the findings of the numerical simulations of the undrained tunnel ex-	
cavation	114
5-1-3 On the limitations of the research	114
5-2 Recommendations for further research	115
A Numerical results of the mechanical sensitivity analysis	117

List of Figures

1-1	Phases of a radioactive waste repository in the Netherlands (Verhoef et al., 2011)	2
2-1	The Boom Clay formation in Belgium, with its depth and thickness (Arnold et al., 2014)	6
2-2	The Boom Clay formation in the Netherlands, with indication of its depth (CORA, 2001a)	6
2-3	Scanning Electron Microscopy (SEM) images of a BC sample, before (a) and after (b) undrained shearing in a triaxial apparatus (Yu et al., 2012)	7
2-4	Failure envelopes for the BC material, originating from Essen and Mol, in the mean effective stress (p') versus deviator stress (q) plane (Deng et al., 2011b)	9
2-5	Deviator stress (q) versus axial strain (ε_a), for undrained triaxial tests performed on BC samples (CU1, CU2 and CU3) originating from Mol (Digitised from Yu et al., 2012)	10
2-6	Results of the triaxial tests on BC of the <i>Ess75</i> core. p'_0 is the isotropic consolidation stress before the initiation of shearing, p' is the mean effective stress, q is the deviator stress, ε_a is the axial strain and ε_v is the volumetric strain (After Deng et al., 2011b)	13
2-7	Applied pressure versus elapsed time diagram for the phase of isotropic consolidation on a BC specimen originating from Mol (Bésuelle et al., 2013)	14
2-8	Effect of the magnitude of the isotropic consolidation pressure on the rate of swelling of the BC material. The measurements are taken after the relationship between the swelling rate and the time of consolidation has become linear (Bésuelle et al., 2013)	15
2-9	Triaxial tests results for different values of OCR and for varying duration of swelling before shearing, for BC samples from Mol, in terms of deviator stress (q) versus axial strain (ε_a) (a) and volumetric strain (ε_v) versus ε_a (b) diagrams. (Bésuelle et al., 2013)	16

2-10 Deviator stress (q) versus axial strain (ε_a) (a) and volumetric strain (ε_v) versus ε_a (b) diagrams for a sample from Essen (Ess75Tr02, OCR = 2.2) and a sample from Mol (BC20, OCR = 2.17) (Digitised from Deng et al., 2011b and Bésuelle et al., 2013 , respectively).	16
2-11 Void ratio (e) versus logarithm of vertical effective stress ($\log\sigma'_v$) plot for the oedometer test on the BC from core <i>Ess75</i> (After Deng et al., 2011b).	18
2-12 Logarithm of vertical effective stress ($\log\sigma'_v$) versus elapsed time (a) and displacement – elapsed time (b) plots for the oedometer test on the BC from core <i>Ess75</i> (Deng et al., 2011b).	18
2-13 Void ratio (e) versus logarithm of vertical effective stress ($\log\sigma'_v$) plot for a high pressure oedometer test performed on an Ypresian clay sample. The threshold stresses (σ_{si}) are obtained from the intersection of the extended linear parts of the unloading and reloading branches of the diagram (Cui et al., 2013).	19
2-14 Void ratio (e) versus logarithm of vertical effective stress ($\log\sigma'_v$) plot for the qualitative representation of the mechanical and physico-chemical processes that take place in an unloading-reloading path, in an Ypresian clay. Their effects on the soil micro-structure are also depicted. (M) denotes mechanically dominated process and (P-C) represents physico-chemically dominated process. σ_s^{reload} and σ_s^{unload} are the threshold stresses in an unloading-reloading loop (After Cui et al., 2013).	20
2-15 Estimation of the compressibility parameters and the yield stresses from a void ratio (e) versus logarithm of vertical effective stress ($\log\sigma'_v$) graph, for test <i>Ess75Oedo1</i> (Deng et al., 2011b).	21
2-16 Yield curves of the BC at its initial state and after isotropic consolidation of the samples at 9MPa. The former is normalised with respect to the maximum mean effective stress, determined by the intersection of the K_0 -line with the initial yield surface and the latter with respect to the maximum applied mean effective stress during the tests ($p' = p'_{c0} = 9$ MPa). q is the deviator stress and K_0 is the coefficient of earth pressures at rest (Sultan et al., 2010).	22
2-17 X-Ray Computed Tomography (XRCT) scans of a cross section at the mid-height of a BC sample cored parallel to the bedding (indicated by the back dashed lines), before (a) and after (b) unloading in the hollow cylinder apparatus (Labrouse et al., 2013).	23
2-18 Identification of the eye-shaped Excavation Damaged Zone (EDZ), based on the radial displacements (solid black curves) measured parallel and perpendicular to the bedding (Labrouse et al., 2013).	24
2-19 Development of the magnitude of the effective cohesion (c'), according to the angle between the major principal stress and the direction normal to the bedding (α_{σ_1}) (François et al., 2013).	25
2-20 Logarithm of permeability ($\log k$) versus void ratio (e) diagram for a BC sample from Essen, derived from 3 different techniques (Deng et al., 2011a).	26
2-21 Void ratio (e) versus logarithm of permeability ($\log k$) diagram from an isotropic compression test on BC material from Mol (Bésuelle et al., 2013).	26
2-22 Variation of the logarithm of the vertical permeability (k_V , in m/s) in the BC formation, according to depth and location (see Figure 2-1). The reference depth is the level of the HADES URF. <i>Tr.zone</i> refers to the <i>Boeretang</i> member (Jeannée et al., 2013).	27

3-1	Example of input in the lab test facility of <i>PLAXIS</i> for the set up of the simulation of the triaxial test <i>Ess75Tr01</i> performed by Deng et al. (2011b).	33
3-2	Input in the lab test facility of <i>PLAXIS</i> for the set up of the simulation of the oedometer test <i>Ess75Oedo1</i> performed by Deng et al. (2011b).	34
3-3	Deviator stress (q) versus axial strain (ε_a) for the numerical simulations of the <i>Ess75Tr01</i> test with four soil models. The triaxial data (blue curve) have been digitised from Deng et al. (2011b).	36
3-4	Volumetric strains (ε_v) versus axial strain (ε_a) for the numerical simulations of the <i>Ess75Tr01</i> test with four soil models. The triaxial data (blue curve) have been digitised from Deng et al. (2011b).	36
3-5	Deviator stress (q) versus axial strain (ε_a) for the numerical simulations of the <i>Ess75Tr02</i> test with four soil models. The triaxial data (blue curve) has been digitised from Deng et al. (2011b).	37
3-6	Volumetric strains (ε_v) versus axial strain (ε_a) for the numerical simulations of the <i>Ess75Tr02</i> test with four soil models. The triaxial data (blue curve) have been digitised from Deng et al. (2011b).	37
3-7	Deviator stress (q) versus axial strain (ε_a) for the numerical simulations of the <i>Ess75Tr03</i> test with four soil models. The triaxial data (blue curve) have been digitised from Deng et al. (2011b).	38
3-8	Volumetric strains (ε_v) versus axial strain (ε_a) for the numerical simulations of the <i>Ess75Tr03</i> test with four soil models. The triaxial data (blue curve) have been digitised from Deng et al. (2011b).	38
3-9	Void ratio (e) versus vertical effective stress (σ'_v) for the numerical simulation of the <i>Ess75Oedo1</i> test with the MCC model. The oedometer test results (blue curve) have been digitised from Deng et al. (2011b).	40
3-10	Displacement versus elapsed time for the numerical simulation of the <i>Ess75Oedo1</i> test with the MCC model. The oedometer test results (blue curve) have been digitised from Deng et al. (2011b). It is noted that, although the MCC model does not account for the time dependent response of the material, this figure is utilised for the comparison of the actual displacements with the ones that are numerically predicted.	40
3-11	Void ratio (e) versus vertical effective stress (σ'_v) for the numerical simulation of the <i>Ess75Oedo1</i> test with the SS-C model. The oedometer test results (blue curve) have been digitised from Deng et al. (2011b).	42
3-12	Displacement versus elapsed time for the numerical simulation of the <i>Ess75Oedo1</i> test with the SS-C model. The oedometer test results (blue curve) have been digitised from Deng et al. (2011b).	42
3-13	Void ratio (e) versus vertical effective stress (σ'_v) for the numerical simulation of the <i>Ess75Oedo1</i> test with the HS model. The oedometer test results (blue curve) have been digitised from Deng et al. (2011b).	43
3-14	Displacement versus elapsed time for the numerical simulation of the <i>Ess75Oedo1</i> test with the HS model. The oedometer test results (blue curve) have been digitised from Deng et al. (2011b). It is noted that, although the HS model does not account for the time dependent response of the material, this figure is utilised for comparing the actual displacements with the ones that are numerically predicted.	43

3-15 Hyperbolic stress-strain relationship in a deviator stress (q) versus axial strain ($\varepsilon_a = \varepsilon_1$ for triaxial compression) plot for a standard drained triaxial test. E_i is the initial secant modulus, E_{50} is the stress-dependent secant modulus, E_{ur} is the stress-dependent unloading-reloading modulus, q_a is the asymptotic value of the shear strength and q_f is the ultimate deviator stress (Plaxis, 2011a).	47
3-16 Deviator stress, $ \sigma_1 - \sigma_3 $, versus axial strain ($\varepsilon_1 = \varepsilon_a$ for triaxial compression) diagrams resulting from 2 drained triaxial tests at different confining pressures (σ_3), for determining the stress dependency of stiffness (m). E_{50} is the secant modulus (Brinkgreve, 2011).	48
3-17 Shear hardening loci in a deviator stress, $ \sigma_1 - \sigma_3 $, versus mean effective stress plot for cohesionless soil, for stress dependency of stiffness $m = 0.5$ and for different values of the shear hardening parameter (γ^p). The locus moves upwards with increasing γ^p (Plaxis, 2011a).	49
3-18 Cap and shear hardening loci in the deviator stress of the HS model (\tilde{q}) versus mean stress (p) graph, with indication of the stiffness zones and the related moduli. α is the cap parameter of the HS model, p_c is the isotropic pre-consolidation stress, c is the cohesion, φ is the friction angle, E_{50} is the stress-dependent secant modulus, E_{oed} is the stress-dependent oedometer modulus and E_{ur} is the stress-dependent un-/reloading modulus (After Plaxis, 2011a and Karstunen, 2013).	51
3-19 Determination of the reference oedometer modulus (E_{oed}^{ref}) from the resulting major principal (vertical) effective stress (σ'_1) versus major principal (vertical) strain (ε_1) plot of an oedometer test at a reference pressure (p^{ref}) (After Plaxis, 2011a). . .	52
3-20 Yield contour of the HS model in the principal stress space. The soil cohesion is zero and the shear hardening locus coincides with the MC failure surface. σ_1 , σ_2 and σ_3 are the major, intermediate and minor principal stresses, respectively (Benz, 2006).	52
3-21 Illustration of the in-situ stress state for calculating the Over-Consolidation ratio (OCR) (a) and the Pre-Overburden Pressure (POP) (b). σ'_{v0} is the initial vertical effective stress and σ'_c is the vertical pre-consolidation stress (After Plaxis, 2013).	53
3-22 Determination of the initial horizontal effective stresses (σ'_{h0}) in a finite element mesh for the HS model. σ'_{v0} is the initial vertical effective stress, σ'_c is the vertical pre-consolidation stress, K_0^{NC} is the coefficient of earth pressures in NC conditions, ν_{ur} is the unloading-reloading Poisson's ratio and POP is the Pre-Overburden Pressure (After Brinkgreve, 2011).	54
3-23 Deviator stress (q) versus axial strain (ε_a) resulting from varying some of the input parameters of the HS model, for the numerical simulation of the Ess75Tr01 test. E_{50}^{ref} is the reference secant modulus and m is a measure of the stress dependency of stiffness. The triaxial data (blue curve) have been digitised from Deng et al. (2011b).	61
3-24 Volumetric strain (ε_v) versus axial strain (ε_a) resulting from varying some of the input parameters of the HS model, for the simulation of the Ess75Tr01 test. E_{50}^{ref} is the reference secant modulus, E_{oed}^{ref} is the reference oedometer modulus, E_{ur}^{ref} is the reference unloading-reloading modulus, ν_{ur} is the unloading-reloading Poisson's ratio and m is a measure of the stress dependency of stiffness. The triaxial data (blue curve) have been digitised from Deng et al. (2011b).	62

3-25 Deviator stress (q) versus axial strain (ε_a) resulting from varying some of the input parameters of the HS model, for the simulation of the <i>Ess75Tr02</i> test. E_{50}^{ref} is the reference secant modulus and E_{oed}^{ref} is the reference oedometer modulus. The triaxial data (blue curve) have been digitised from Deng et al. (2011b)	65
3-26 Volumetric strain (ε_v) versus axial strain (ε_a) resulting from varying some of the input parameters of the HS model, for the simulation of the <i>Ess75Tr02</i> test. E_{50}^{ref} is the reference secant modulus, E_{oed}^{ref} is the reference oedometer modulus, E_{ur}^{ref} is the reference unloading-reloading modulus, ν_{ur} is the unloading-reloading Poisson's ratio and m is a measure of the stress dependency of stiffness. The triaxial data (blue curve) have been digitised from Deng et al. (2011b)	66
3-27 Representation, on the deviator stress (q) versus mean effective stress (p') plane, of the initial caps of the HS model resulting from changing some of the model input parameters. The grey line concerns the stress path of the <i>Ess75Tr02</i> test. E_{50}^{ref} is the reference secant modulus, E_{oed}^{ref} is the reference oedometer modulus, E_{ur}^{ref} is the reference unloading-reloading modulus, ν_{ur} is the unloading-reloading Poisson's ratio, m is a measure of the stress dependency of stiffness and α is an internal model parameter which determines the steepness of the caps. MC denotes Mohr Coulomb. The resulting cap for $E_{50}^{ref} = 6\text{MPa}$ is not visible since it coincides with that of $m = 0.55$	67
3-28 Deviator stress (q) versus axial strain (ε_a) resulting from varying some of the input parameters of the HS model, for the numerical simulation of the <i>Ess75Tr03</i> test. E_{50}^{ref} is the reference secant modulus and m is a measure of the stress dependency of stiffness. The triaxial data (blue curve) have been digitised from Deng et al. (2011b)	69
3-29 Volumetric strain (ε_v) versus axial strain (ε_a) resulting from varying some of the input parameters of the HS model, for the simulation of the <i>Ess75Tr03</i> test. E_{50}^{ref} is the reference secant modulus, E_{ur}^{ref} is the reference unloading-reloading modulus, ν_{ur} is the unloading-reloading Poisson's ratio and m is a measure of the stress dependency of stiffness. The triaxial data (blue curve) have been digitised from Deng et al. (2011b)	70
3-30 Representation, on the deviator stress (q) versus mean effective stress (p') plane, of the initial caps of the HS model resulting from changing some of the model input parameters. The grey line concerns the stress path of the <i>Ess75Tr03</i> test. E_{50}^{ref} is the reference secant modulus, E_{oed}^{ref} is the reference oedometer modulus, E_{ur}^{ref} is the reference unloading-reloading modulus, ν_{ur} is the unloading-reloading Poisson's ratio, m is a measure of the stress dependency of stiffness and α is an internal model parameter which determines the steepness of the caps. MC denotes Mohr Coulomb. The resulting cap for $E_{50}^{ref} = 6\text{MPa}$ is not visible since it coincides with that of $m = 0.55$	71
3-31 Void ratio (e) versus vertical effective stress (σ'_v) for the numerical simulation of the <i>Ess75Oedo1</i> test with the <i>Initial data</i> of the HS model, for $\nu_{ur} = 0.25$. The oedometer test results (blue curve) have been digitised from Deng et al. (2011b)	74

4-1	Relevant part of the geotechnical domain used for the analyses (a) and finite element discretisation of the relevant part of the geotechnical domain (b). The term "relevant" refers to the extent of the domain beyond which its boundaries are deemed not to affect significantly the results of the numerical analyses.	79
4-2	Effective Stress Path, (ESP) in the deviator stress (q) versus mean effective stress (p') plot, of a stress point next to the tunnel sidewall (SW) for the analysis with the <i>mean data</i> and for zero dilatancy angle. The red line indicates the position of the Mohr-Coulomb (MC) criterion for Triaxial Compression (TC). Point A signifies the end of the second calculation phase. Point B indicates the end of the calculation phase where the tunnel is introduced. Point C marks the peak deviator stress. The black arrow shows the position (point D) where the ESP meets the MC criterion. Point E marks the stress state at the completion of the calculation. K_0^{NC} is the coefficient of earth pressures for normal consolidation. The K_0^{NC} -line concerns triaxial compression. r is the tunnel radius.	84
4-3	Evolution of the excess pore water pressures (u_{excess}) of a point next to the tunnel sidewall (SW), in the course of the last calculation phase (tunnel contraction), for the simulation with the <i>mean data</i> and for zero dilatancy angle. The quantity $\Sigma MStage$ denotes the percentage of the completion of the calculation phase. r is the tunnel radius.	85
4-4	Schematic representation of the pressures acting on a soil segment situated at the walls of a circular cavity before (a) and after (b) undrained unloading.	86
4-5	Effective Stress Paths (ESP), in a deviator stress (q) versus mean effective stress (p') plot, of three stress points located at different horizontal distances (x) from the sidewall of the tunnel, for the simulation with the <i>mean data</i> and for zero dilatancy angle. The dashed blue line indicates the position where the ESP meets the MC criterion. The dashed-dotted lines indicate the end of the calculation phase where the tunnel is introduced. r is the tunnel radius.	87
4-6	Effective Stress Paths (ESP), in a deviator stress (q) versus mean effective stress (p') plot, of three stress points located close to the sidewall (SW), the crown (CR) and the invert (INV) of the tunnel, for the simulation with the <i>mean data</i> and for zero dilatancy angle. The dashed lines indicate the position of the ESP at the end of the analyses. r is the tunnel radius.	87
4-7	Illustration of part of the finite element mesh with the fully plastified (with red colour) stress points and the stress points of which the effective stress paths lie on the shear hardening locus of the HS model (with green colour), at the end of the analysis with the <i>mean data</i> and with zero dilatancy angle. The thickness of the fully Plastic Zone (PZ), the shear Hardening Zone (HZ) and the Disturbed Zone is indicated.	88
4-8	Deviator stress (q) versus deviatoric strains (γ_s) plot for a stress point 4cm away from the tunnel sidewall (SW), for different values of the reference secant modulus (E_{50}^{ref}) and for zero dilatancy angle. The dashed lines indicate the amount of strains at which the stress path meets the Mohr-Coulomb criterion. r is the tunnel radius.	90
4-9	Total radial stresses (σ_r) and total tangential stresses (σ_t), along a radial line, for different values of the reference secant modulus (E_{50}^{ref}) and for zero dilatancy angle. r is the tunnel radius.	91

4-10 Effective radial stresses (σ'_r) and effective tangential stresses (σ'_t), along a radial line, for different values of the reference secant modulus (E_{50}^{ref}) and for zero dilatancy angle. r is the tunnel radius.	91
4-11 Pore water pressures, along a radial line, for different values of the reference secant modulus (E_{50}^{ref}) and for zero dilatancy angle. r is the tunnel radius.	92
4-12 Effective Stress Paths (ESP), in a deviator stress (q) versus mean effective stress (p') plot, of a point 4cm away from the tunnel sidewall (SW), for different values of the reference secant modulus (E_{50}^{ref}) and for zero dilatancy angle. The dashed lines indicate the end of each ESP (with the corresponding colour) at the completion of the calculation. The dashed-dotted lines indicate the position at which the ESP meet the Mohr-Coulomb criterion. These lines coincide for the case of the analysis with $E_{50}^{ref} = 97\text{MPa}$. r is the tunnel radius.	92
4-13 Deviator stress (q) versus deviatoric strains (γ_s) plot for a stress point next to the tunnel sidewall (SW), for different values of the reference secant modulus (E_{50}^{ref}) and for dilatancy angle equal to 1° . The dashed lines indicate the amount of strains at which the stress path meets the Mohr-Coulomb criterion. r is the tunnel radius.	94
4-14 Effective Stress Paths (ESP), in a deviator stress (q) versus mean effective stress (p') plot, of a point 4cm away from the tunnel sidewall (SW), for a value of the reference secant modulus $E_{50}^{ref} = 145\text{MPa}$ and for values of the dilatancy angle $\psi = 0^\circ$ and 1° . The dashed lines indicate the position at which the ESP meet the Mohr-Coulomb criterion. r is the tunnel radius.	94
4-15 Deviator stress (q) versus deviatoric strains (γ_s) plot for a stress point next to the tunnel sidewall (SW), for different values of the reference unloading-reloading modulus (E_{ur}^{ref}) and for zero dilatancy angle. The dashed lines indicate the amount of strains at which the stress path meets the Mohr-Coulomb criterion. r is the tunnel radius. The amount of γ_s at which the material fully plastifies differs between this case and the respective case with $\psi = 1^\circ$ (Figure A-11), as the results of the former have been obtained for an increased accuracy of the analysis.	96
4-16 Total radial stresses (σ_r) and total tangential stresses (σ_t), along a radial line, for different values of the reference unloading-reloading modulus (E_{ur}^{ref}) and for zero dilatancy angle. r is the tunnel radius.	97
4-17 Pore water pressures, along a radial line, for different values of the reference unloading-reloading modulus (E_{ur}^{ref}) and for zero dilatancy angle. r is the tunnel radius	97
4-18 Effective radial stresses (σ'_r) and effective tangential stresses (σ'_t), along a radial line, for different values of the reference unloading-reloading modulus (E_{ur}^{ref}) and for zero dilatancy angle. r is the tunnel radius.	98
4-19 Effective Stress Paths (ESP), in a deviator stress (q) versus mean effective stress (p') plot, of a point next to the tunnel sidewall (SW), for different values of the reference unloading-reloading modulus (E_{ur}^{ref}) and for zero dilatancy angle. The dashed lines indicate the intersection of each ESP (with the corresponding colour) with the Mohr-Coulomb criterion. r is the tunnel radius.	98

4-20 Deviator stress (q) versus deviatoric strains (γ_s) plot for a stress point next to the tunnel sidewall (SW), for different values of the rate of stress dependency of stiffness (m) and for zero dilatancy angle. The dashed lines indicate the amount of strains at which the stress path meets the Mohr-Coulomb criterion. r is the tunnel radius.	100
4-21 Effective radial stresses (σ'_r) and effective tangential stresses (σ'_t), along a radial line, for different values of the rate of stress dependency of stiffness (m) and for zero dilatancy angle. r is the tunnel radius.	100
4-22 Pore water pressures, along a radial line, for different values of the rate of stress dependency of stiffness (m) and for zero dilatancy angle. r is the tunnel radius.	101
4-23 Total radial stresses (σ_r) and total tangential stresses (σ_t), along a radial line, for different values of the rate of stress dependency of stiffness (m) and for zero dilatancy angle. r is the tunnel radius.	101
4-24 Effective Stress Paths (ESP), in a deviator stress (q) versus mean effective stress (p') plot, of a point next to the tunnel sidewall (SW), for different values of the rate of stress dependency of stiffness (m) and for zero dilatancy angle. The dashed lines indicate the end of each ESP (with the corresponding colour) at the completion of the calculation. r is the tunnel radius.	102
4-25 Deviator stress (q) versus deviatoric strains (γ_s) plot for a stress point next to the tunnel sidewall (SW), for different values of the effective friction angle (φ') and for zero dilatancy angle. The dashed lines indicate the amount of strains at which the stress path meets the Mohr-Coulomb criterion. r is the tunnel radius.	103
4-26 Effective Stress Paths (ESP), in a deviator stress (q) versus mean effective stress (p') plot, of a point next to the tunnel sidewall (SW), for different values of the effective friction angle (φ') and for zero dilatancy angle. The dashed lines indicate the intersection of each ESP (with the corresponding colour) with the Mohr-Coulomb criterion. r is the tunnel radius.	104
4-27 Deviator stress (q) versus deviatoric strains (γ_s) plot for a stress point next to the tunnel sidewall (SW), for different values of the effective cohesion (c') and for zero dilatancy angle. The dashed lines indicate the amount of strains at which the stress path meets the Mohr-Coulomb criterion. r is the tunnel radius.	105
4-28 Effective radial stresses (σ'_r) and effective tangential stresses (σ'_t), along a radial line, for different values of the effective cohesion (c') and for zero dilatancy angle. r is the tunnel radius.	106
4-29 Total radial stresses (σ_r) and total tangential stresses (σ_t), along a radial line, for different values of the effective cohesion (c') and for zero dilatancy angle. r is the tunnel radius.	106
4-30 Effective Stress Paths (ESP), in a deviator stress (q) versus mean effective stress (p') plot, of a point next to the tunnel sidewall (SW), for different values of the effective cohesion (c') and for zero dilatancy angle. The dashed lines indicate the intersection of each ESP (with the corresponding colour) with the Mohr-Coulomb criterion. r is the tunnel radius.	107
4-31 Pore water pressures, along a radial line, for different values of the effective cohesion (c') and for zero dilatancy angle. r is the tunnel radius.	107

A-1 Effective radial stresses (σ'_r) and effective tangential stresses (σ'_t), along a radial line, for different values of the effective friction angle (φ') and for zero dilatancy angle. r is the tunnel radius.	117
A-2 Total radial stresses (σ_r) and total tangential stresses (σ_t), along a radial line, for different values of the effective friction angle (φ') and for zero dilatancy angle. r is the tunnel radius.	118
A-3 Pore water pressures, along a radial line, for different values of the effective friction angle (φ') and for zero dilatancy angle. r is the tunnel radius.	118
A-4 Effective radial stresses (σ'_r) and effective tangential stresses (σ'_t), along a radial line, for different values of the reference secant modulus (E_{50}^{ref}) and for dilatancy angle equal to 1° . r is the tunnel radius.	119
A-5 Total radial stresses (σ_r) and total tangential stresses (σ_t), along a radial line, for different values of the reference secant modulus (E_{50}^{ref}) and for dilatancy angle equal to 1° . r is the tunnel radius.	119
A-6 Effective Stress Paths (ESP), in a deviator stress (q) versus mean effective stress (p') plot, of a point next to the tunnel sidewall (SW), for different values of the reference secant modulus (E_{50}^{ref}) and for dilatancy angle equal to 1° . The dashed lines indicate the position of each ESP (with the corresponding colour) at the completion of the calculation. r is the tunnel radius.	120
A-7 Pore water pressures, along a radial line, for different values of the reference secant modulus (E_{50}^{ref}) and for dilatancy angle equal to 1° . r is the tunnel radius.	120
A-8 Effective radial stresses (σ'_r) and effective tangential stresses (σ'_t), along a radial line, for different values of the reference unloading-reloading modulus (E_{ur}^{ref}) and for dilatancy angle equal to 1° . r is the tunnel radius.	121
A-9 Total radial stresses (σ_r) and total tangential stresses (σ_t), along a radial line, for different values of the reference unloading-reloading modulus (E_{ur}^{ref}) and for dilatancy angle equal to 1° . r is the tunnel radius.	121
A-10 Effective Stress Paths (ESP), in a deviator stress (q) versus mean effective stress (p') plot, of a point next to the tunnel sidewall (SW), for different values of the reference unloading-reloading modulus (E_{ur}^{ref}) and for dilatancy angle equal to 1° . The dashed lines indicate the intersection of each ESP with the Mohr-Coulomb criterion. r is the tunnel radius.	122
A-11 Deviator stress (q) versus deviatoric strains (γ_s) plot for a stress point next to the tunnel sidewall (SW), for different values of the reference unloading-reloading modulus (E_{ur}^{ref}) and for dilatancy angle equal to 1° . The dashed lines indicate the amount of strains at which the stress path meets the Mohr-Coulomb criterion. r is the tunnel radius. The amount of γ_s at which the material fully plastifies differs between this case and the respective case with $\psi = 0^\circ$ (Figure 4-15), as the results of the latter have been obtained for an increased accuracy of the analysis.	122
A-12 Pore water pressures, along a radial line, for different values of the reference unloading - reloading modulus (E_{ur}^{ref}) and for dilatancy angle equal to 1° . r is the tunnel radius.	123
A-13 Effective radial stresses (σ'_r) and effective tangential stresses (σ'_t), along a radial line, for different values of the rate of stress dependency of stiffness (m) and for dilatancy angle equal to 1° . r is the tunnel radius.	123

A-14 Total radial stresses (σ_r) and total tangential stresses (σ_t), along a radial line, for different values of the rate of stress dependency of stiffness (m) and for dilatancy angle equal to 1° . r is the tunnel radius.	124
A-15 Effective Stress Paths (ESP), in a deviator stress (q) versus mean effective stress (p') plot, of a point next to the tunnel sidewall (SW), for different values of the rate of stress dependency of stiffness (m) and for dilatancy angle equal to 1° . The dashed lines indicate the intersection of each ESP with the Mohr-Coulomb criterion. r is the tunnel radius.	124
A-16 Deviator stress (q) versus deviatoric strains (γ_s) plot for a stress point next to the tunnel sidewall (SW), for different values of the rate of stress dependency of stiffness (m) and for dilatancy angle equal to 1° . The dashed lines indicate the amount of strains at which the stress path meets the Mohr-Coulomb criterion. r is the tunnel radius.	125
A-17 Pore water pressures, along a radial line, for different values of the rate of stress dependency of stiffness (m) and for dilatancy angle equal to 1° . r is the tunnel radius.	125
A-18 Effective radial stresses (σ'_r) and effective tangential stresses (σ'_t), along a radial line, for different values of the effective friction angle (φ') and for dilatancy angle equal to 1° . r is the tunnel radius.	126
A-19 Total radial stresses (σ_r) and total tangential stresses (σ_t), along a radial line, for different values of the effective friction angle (φ') and for dilatancy angle equal to 1° . r is the tunnel radius.	126
A-20 Effective Stress Paths (ESP), in a deviator stress (q) versus mean effective stress (p') plot, of a point next to the tunnel sidewall (SW), for different values of the effective friction angle (φ') and for dilatancy angle equal to 1° . The dashed lines indicate the intersection of each ESP (with the corresponding colour) with the Mohr-Coulomb criterion. r is the tunnel radius.	127
A-21 Deviator stress (q) versus deviatoric strains (γ_s) plot for a stress point next to the tunnel sidewall (SW), for different values of the effective friction angle (φ') and for dilatancy angle equal to 1° . The dashed lines indicate the amount of strains at which the stress path meets the Mohr-Coulomb criterion. r is the tunnel radius.	127
A-22 Pore water pressures, along a radial line, for different values of the effective friction angle (φ') and for dilatancy angle equal to 1° . r is the tunnel radius.	128
A-23 Effective radial stresses (σ'_r) and effective tangential stresses (σ'_t), along a radial line, for different values of the effective cohesion (c') and for dilatancy angle equal to 1° . r is the tunnel radius.	128
A-24 Total radial stresses (σ_r) and total tangential stresses (σ_t), along a radial line, for different values of the effective cohesion (c') and for dilatancy angle equal to 1° . r is the tunnel radius.	129
A-25 Effective Stress Paths (ESP), in a deviator stress (q) versus mean effective stress (p') plot, of a point next to the tunnel sidewall (SW), for different values of the effective cohesion (c') and for dilatancy angle equal to 1° . The dashed lines indicate the intersection of each ESP (with the corresponding colour) with the Mohr-Coulomb (MC) criterion. r is the tunnel radius. The stress paths for $c = 0.25\text{MPa}$ and $c = 0.40\text{MPa}$ reach the MC criterion at the same value of p'	129

A-26 Deviator stress (q) versus deviatoric strains (γ_s) plot for a stress point next to the tunnel sidewall (SW), for different values of the effective cohesion (c') and for dilatancy angle equal to 1° . The dashed lines indicate the amount of strains at which the stress path meets the Mohr-Coulomb criterion. r is the tunnel radius.	130
A-27 Pore water pressures, along a radial line, for different values of the effective cohesion (c') and for a dilatancy angle equal to 1° . r is the tunnel radius.	130

List of Tables

2-1	Composition of the main minerals of Boom Clay (Arnold et al., 2014)	8
2-2	Summary of some of the physical properties of the Boom Clay for depth of 0m to 560m (Arnold et al., 2014)	8
2-3	Physical properties of core <i>Ess75</i> (Deng et al., 2011b)	11
2-4	Mineralogical composition of the clay fraction (< 2 μ m) of core <i>Ess75</i> (Deng et al., 2011b)	12
2-5	Specifications of the triaxial tests performed by Deng et al., 2011b on the samples from the <i>Ess75</i> core.	12
2-6	Ranges of values of the geotechnical properties of the BC material, for depth of 200m to 560m (After Arnold et al., 2014)	28
3-1	Set up of the drained triaxial tests performed by Deng et al. (2011b) for the simulations with the lab test facility of <i>PLAXIS</i>	34
3-2	Values of the input parameters of the assessed soil models that gave the best fit with the test data.	45
3-3	Input parameters for the HS model (Plaxis, 2011a).	55
3-4	Summary of the <i>internal</i> parameters of the HS model with their (possible) dependency and influence, as inferred from the literature.	56
3-5	Values of the input parameters of the HS model obtained by the best fit of the results of some triaxial and oedometer tests performed by Deng et al. (2011b).	58
3-6	Effect of changing the value of the reference secant modulus (E_{50}^{ref}) on the values of the internal parameters of the HS model. The value in red colour concerns the <i>initial data</i>	61
3-7	Effect of changing the value of the reference oedometer modulus (E_{oed}^{ref}) on the values of the internal parameters of the HS model. The value in red colour concerns the <i>initial data</i>	62
3-8	Effect of changing the value of the reference un-/reloading modulus (E_{ur}^{ref}) on the values of the internal parameters of the HS model. The value in red colour concerns the <i>initial data</i>	63

3-9	Effect of changing the value of the un-/reloading Poisson's ratio (ν_{ur}) on the values of the internal parameters of the HS model. The value in red colour concerns the <i>initial data</i>	64
3-10	Effect of changing the value of the rate of stress dependency of stiffness (m) on the values of the internal parameters of the HS model. The value in red colour concerns the <i>initial data</i>	65
4-1	Characteristics of the tunnel and the tunnel liner used for the simulations of the mechanical sensitivity analysis (After Bernier et al., 2007b).	80
4-2	Values of the input parameters of the HS model for the mechanical sensitivity analysis.	83
4-3	Effect of changing the reference secant modulus (E_{50}^{ref}) on the thickness of the Plastic Zone (PZ), the Hardening Zone (HZ) and the Disturbed Zone (DZ), the hoop forces in the tunnel liner (N) and the pore water pressures (u) of a stress point next to the tunnel sidewall, at the end of the simulations.	89
4-4	Effect of changing the reference un-/reloading modulus (E_{ur}^{ref}) on the thickness of the Plastic Zone (PZ), the Hardening Zone (HZ) and the Disturbed Zone (DZ), the hoop forces in the tunnel liner (N) and the pore water pressures (u) of a stress point next to the tunnel sidewall, at the end of the simulations.	95
4-5	Effect of changing the level of stress dependency of stiffness (m) on the thickness of the Plastic Zone (PZ), the Hardening Zone (HZ) and the Disturbed Zone (DZ), the hoop forces in the tunnel liner (N) and the pore water pressures (u) of a stress point next to the tunnel sidewall, at the end of the simulations.	99
4-6	Effect of changing the effective friction angle (φ') on the thickness of the Plastic Zone (PZ), the Hardening Zone (HZ) and the Disturbed Zone (DZ), the hoop forces in the tunnel liner (N) and the pore water pressures (u) of a stress point next to the tunnel sidewall, at the end of the simulations.	102
4-7	Effect of changing the effective cohesion (c') on the thickness of the Plastic Zone (PZ), the Hardening Zone (HZ) and the Disturbed Zone (DZ), the hoop forces in the tunnel liner (N) and the pore water pressures (u) of a stress point next to the tunnel sidewall, at the end of the simulations.	105
4-8	Percentage change in the thickness of the Plastic Zone (PZ), the Hardening Zone (HZ) and the Disturbed Zone (DZ), the magnitude of the hoop forces in the tunnel liner (N) and the pore water pressures (u) of a stress point next to the tunnel sidewall, induced by the percentage changes in the values (from lower to upper bound, from lower bound to mean and from mean to upper bound) of the HS model input parameters. The results are obtained by utilising the data of Tables 4-3 to 4-7.	109

Glossary

This list contains definitions of acronyms and symbols used in this report, including the units and the page on which they are first met. The units are: length [L], mass [M], time [T] and degrees [°].

Symbol	Definition	Units	Page
Acronyms			
BC	Boom Clay		1
COVRA	Centrale Organisatie Voor Radioactief Afval		1
DZ	Disturbed Zone		88
EDZ	Excavation Damaged Zone		3
EdZ	Excavation disturbed Zone		3
ESP	Effective Stress Path		84
HADES URF	HADES Underground Research Facility		1
HS	Hardening Soil		31
HZ	Shear Hardening Zone		88
LEPP-MC	Linear Elastic Perfectly Plastic-Mohr Coulomb		31
LOC	Lightly Over-Consolidated		7
MC	Mohr-Coulomb		32
MCC	Modified Cam-Clay		31
NC	Normally Consolidated		12
OC	Over-Consolidated		13
OCR	Over-Consolidation Ratio		4
OPERA	OnderzoeksProgramma Eindberging Radioactief Afval		1
PZ	Fully Plastic Zone		88
SCK•CEN	Belgian Nuclear Research Centre		1
SEM	Scanning Electron Microscopy		10
SS-C	Soft Soil-Creep		31
XRCT	X-Ray Computed Tomography		23
Greek letters			
α	Cap parameter of the HS model	[$-$]	50
β	Cap parameter of the HS model	[$-$]	51

Symbol	Definition	Units	Page
$\dot{\gamma}_s^p$	Rate of plastic deviatoric strain	[T ⁻¹]	49
γ^p	Strain hardening parameter of the HS model	[\cdot]	46
γ_s^e	Elastic deviatoric strain	[\cdot]	84
γ_{sat}	Saturated unit weight	[ML ⁻² T ⁻²]	78
γ_w	Water unit weigh	[ML ⁻² T ⁻²]	78
$\dot{\varepsilon}^{pc}$	Rate of plastic cap strain	[T ⁻¹]	51
$\dot{\varepsilon}_a$	Rate of axial strain	[T ⁻¹]	11
$\dot{\varepsilon}_v^p$	Rate of plastic volumetric strain	[T ⁻¹]	49
ε_1	Major principal strain	[\cdot]	49
ε_1^e	Elastic major principal strain	[\cdot]	49
ε_1^p	Plastic major principal strain	[\cdot]	48
ε_2^e	Elastic intermediate principal strain	[\cdot]	49
ε_3^e	Elastic minor principal strain	[\cdot]	49
ε_a	Axial strain	[\cdot]	10
ε_a^p	Plastic axial strain	[\cdot]	48
ε_r	Radial strain	[\cdot]	63
ε_v	Volumetric strain	[\cdot]	11
ε_v^e	Elastic volumetric strain	[\cdot]	63
ε_v^{pc}	Plastic volumetric cap strain	[\cdot]	51
κ	Swelling index of the MCC model	[\cdot]	39
κ^*	Modified swelling index	[\cdot]	41
λ	Compression index of the MCC model	[\cdot]	39
λ	Plastic multiplier	[\cdot]	51
λ^*	Modified compression index	[\cdot]	41
μ^*	Modified creep index	[\cdot]	41
M	K_0^{NC} -related parameter of the SS-C model	[\cdot]	41
M	Slope of the critical state line	[\cdot]	39
ν'	Drained Poisson's ratio	[\cdot]	28
ν_i	Interface Poisson's ratio	[\cdot]	80
ν_{ur}	Unloading-reloading Poisson's ratio	[\cdot]	39
ρ	Bulk density	[ML ⁻³]	8
ρ_d	Dry density	[ML ⁻³]	8
σ'_1	Major principal effective stress	[ML ⁻¹ T ⁻²]	50
σ'_2	Intermediate principal effective stress	[ML ⁻¹ T ⁻²]	50
σ'_3	Minor principal effective stress	[ML ⁻¹ T ⁻²]	12
σ'_c	Vertical pre-consolidation stress	[ML ⁻¹ T ⁻²]	21
σ'_r	Effective radial stress	[ML ⁻¹ T ⁻²]	90
σ'_t	Effective tangential (hoop) stress	[ML ⁻¹ T ⁻²]	93
σ'_v	Vertical effective stress	[ML ⁻¹ T ⁻²]	17
σ'_y	Vertical yield stress	[ML ⁻¹ T ⁻²]	21
σ'_{h0}	Initial horizontal effective stress	[ML ⁻¹ T ⁻²]	53
σ'_{v0}	Initial vertical effective stress	[ML ⁻¹ T ⁻²]	11
σ_1	Major principal stress	[ML ⁻¹ T ⁻²]	48
σ_2	Intermediate principal stress	[ML ⁻¹ T ⁻²]	48
σ_3	Minor principal stress	[ML ⁻¹ T ⁻²]	48
σ_N	Normal stress	[ML ⁻¹ T ⁻²]	80
σ_r	Total radial stress	[ML ⁻¹ T ⁻²]	90
σ_t	Total tangential (hoop) stress	[ML ⁻¹ T ⁻²]	90
τ	Shear stress	[ML ⁻¹ T ⁻²]	80
φ'	Effective friction angle	[$^\circ$]	10

Symbol	Definition	Units	Page
φ_f	Friction angle at failure	[°]	50
φ_m	Mobilised friction angle	[°]	50
φ_{cv}	Constant volume friction angle	[°]	50
ψ	Dilatancy angle	[°]	13
ψ_f	Dilatancy angle at failure	[°]	50
ψ_m	Mobilised dilatancy angle	[°]	48

Latin letters

A	Cross sectional area	[L ²]	78
c'	Effective cohesion	[ML ⁻¹ T ⁻²]	10
C_c	Compression index	[‐]	20
C_s	Swelling index	[‐]	20
c_u	Undrained cohesion	[ML ⁻¹ T ⁻²]	28
CC	Carbonate Content	[‐]	11
d	Thickness of the tunnel liner	[L]	78
e	Void ratio	[‐]	17
E'	Drained Young's modulus	[ML ⁻¹ T ⁻²]	28
E_0	Initial Young's modulus	[ML ⁻¹ T ⁻²]	13
e_0	Initial void ratio	[‐]	11
E_i^{ref}	Initial secant stiffness	[ML ⁻¹ T ⁻²]	57
E_u	Undrained Young's modulus	[ML ⁻¹ T ⁻²]	28
E_{50}	Stress-dependent secant modulus	[ML ⁻¹ T ⁻²]	46
E_{50}^{ref}	Reference secant modulus	[ML ⁻¹ T ⁻²]	47
E_i	Stress-dependent initial secant modulus	[ML ⁻¹ T ⁻²]	46
$E_{oed,i}$	Interface oedometer modulus	[ML ⁻¹ T ⁻²]	80
E_{oed}	Stress-dependent oedometer modulus	[ML ⁻¹ T ⁻²]	51
E_{oed}^{ref}	Reference Oedometer modulus	[ML ⁻¹ T ⁻²]	51
E_{ur}	Stress-dependent unloading-reloading modulus	[ML ⁻¹ T ⁻²]	46
E_{ur}^{ref}	Reference unloading-reloading modulus	[ML ⁻¹ T ⁻²]	47
f	Yield function	[‐]	46
G	Shear modulus	[ML ⁻¹ T ⁻²]	84
g	Plastic potential	[‐]	48
G_i	Interface shear modulus	[ML ⁻¹ T ⁻²]	80
G_s	Specific gravity	[‐]	8
G_{50}^{ref}	Reference shear modulus in primary loading	[ML ⁻¹ T ⁻²]	57
G_{ur}	Unloading-reloading shear modulus	[ML ⁻¹ T ⁻²]	89
H	Hardening modulus of the HS model	[ML ⁻¹ T ⁻²]	56
I	Moment of inertia	[L ⁴]	78
I_P	Plasticity Index	[‐]	8
k	Hydraulic conductivity	[LT ⁻¹]	26
K'	Drained bulk modulus	[ML ⁻¹ T ⁻²]	84
K_0	Coefficient of earth pressures at rest	[‐]	11
K_0^{NC}	K_0 -value for normal consolidation	[‐]	41
K_c	Compression modulus of the HS model	[ML ⁻¹ T ⁻²]	56
k_H	Horizontal hydraulic conductivity	[LT ⁻¹]	26
K_s	Swelling modulus of the HS model	[ML ⁻¹ T ⁻²]	56
k_V	Vertical hydraulic conductivity	[LT ⁻¹]	26
m	Rate of stress dependency of stiffness	[‐]	47

Symbol	Definition	Units	Page
MB	Methylene Blue	[\cdot]	11
N	Hoop forces in the tunnel liner	[MLT^{-2}]	88
n	Porosity	[\cdot]	8
p'	Mean effective stress	[$ML^{-1}T^{-2}$]	10
p^{ref}	Reference stress for stiffness	[$ML^{-1}T^{-2}$]	47
p_c	Isotropic pre-consolidation pressure	[$ML^{-1}T^{-2}$]	14
p_c^{eq}	Equivalent pre-consolidation pressure	[$ML^{-1}T^{-2}$]	59
POP	Pre-Overburden Pressure	[$ML^{-1}T^{-2}$]	54
\tilde{q}	Deviatoric stress measure of the HS model	[$ML^{-1}T^{-2}$]	50
q	Deviator stress	[$ML^{-1}T^{-2}$]	10
q_a	Assymptotic value of the shear strength	[$ML^{-1}T^{-2}$]	46
q_f	Ultimate deviator stress	[$ML^{-1}T^{-2}$]	46
q_p	Peak deviator stress	[$ML^{-1}T^{-2}$]	35
r_{ext}	External tunnel radius	[L]	78
R_f	Failure ratio	[\cdot]	46
R_{inter}	Interface reduction factor	[\cdot]	80
r_{over}	Over-excavated radius	[L]	82
S_r	Degree of saturation	[\cdot]	11
t_i	Interface virtual thickness	[L]	80
u	Pore water pressures	[$ML^{-1}T^{-2}$]	86
u_0	Initial pore water pressures	[$ML^{-1}T^{-2}$]	86
u_{excess}	Excess pore water pressures	[$ML^{-1}T^{-2}$]	86
w	Water content	[\cdot]	8
w_L	Liquid Limit	[\cdot]	8
w_P	Plastic Limit	[\cdot]	8

Chapter 1

Introduction

1-1 Radioactive waste disposal in Boom Clay

Among various radioactive waste management schemes to date, deep geologic disposal is thought to be the most promising in terms of feasibility, safety and economy. Several countries such as the United States of America, Canada, France, Germany, Norway, Finland, Sweden and Belgium have been funding research programmes to investigate the dominant processes linked to this technique in different geologic formations ([Arnold et al., 2014](#)).

One of the candidate geologic formations for radioactive waste disposal is a tertiary clay formation named Boom Clay (BC), which is present in the subsurface of north-east Belgium and almost the whole of the Netherlands (see later Section 2-2). Research on BC was inaugurated in 1974 by the Belgian Nuclear Research Center (SCK•CEN), at the HADES Underground Research Facility (HADES URF) in the city of Mol. Since, a series of deep tunnel excavations in conjunction with in-situ measurements and laboratory tests have been, and are, being conducted for gaining an insight into the response of the host rock-repository-radioactive waste system ([Bernier et al., 2007a](#)).

Similarly, the Netherlands have been examining the feasibility of deep geological disposal through the Central Organisation For Radioactive Waste (COVRA), founded in 1982 (<http://www.covra.nl>). Whereas the suitability of salt as host rock has been confirmed in previous studies ([CORA, 2001b](#)), more investigation was needed in the case of BC. Hence, in 2009, the Research Programme for the Geological Disposal of Radioactive Waste (OPERA) for the 2011-2016 time frame was launched. The aim of OPERA is to re-evaluate and update existing safety and feasibility studies regarding the construction of an underground radioactive waste repository in the BC formation. Scientific knowledge can be gained and complemented through the findings of other research programmes such as the ones being conducted at the HADES URF, Belgium.

1-2 Life-time phases of a radioactive waste repository

According to [Birkholzer et al. \(2012\)](#), four stages can be distinguished during the life-time of a radioactive waste repository:

1. the *construction stage*, during which the underground excavation is carried out and the structural elements of the tunnel are installed,
2. the *open tunnel stage*, which lasts until the waste is emplaced and the repository is backfilled and sealed,
3. the *exploitation stage*, which is related to the post-closure ambient disturbance caused by the heat emitted by the waste, and
4. the *long-term post-closure stage*, during which radionuclides potentially start to migrate through the barriers.

An outline of the phases and the major decision points during the life-time of a radioactive waste repository in the Netherlands is shown in Figure 1-1.

The research performed as part of this MSc project focuses on the *construction stage*. The main process that occurs during this phase is the mechanical and the hydraulic perturbation of the host rock around the tunnel, which is induced by the excavation procedure and the subsequent redistribution of stresses in the soil.

After a limited number of excavation steps have been realised and the tunnel segments have been installed, an ideal short-term equilibrium between the soil and the liner takes place. The soil may be considered fully saturated and its response may be deemed to be undrained. Subsequently, consolidation, i.e. dissipation of the excavation-induced excess pore water pressures in the host rock commences, leading to a long-term equilibrium of the soil-tunnel liner system ([Tsang et al., 2005](#)). During this period, the material is partially saturated due to its exposure to the atmospheric pressure at the soil-liner interface. The process of consolidation continues also during the *open tunnel stage*. This research project will address only the initial (ideally fully saturated and undrained) state of the material.

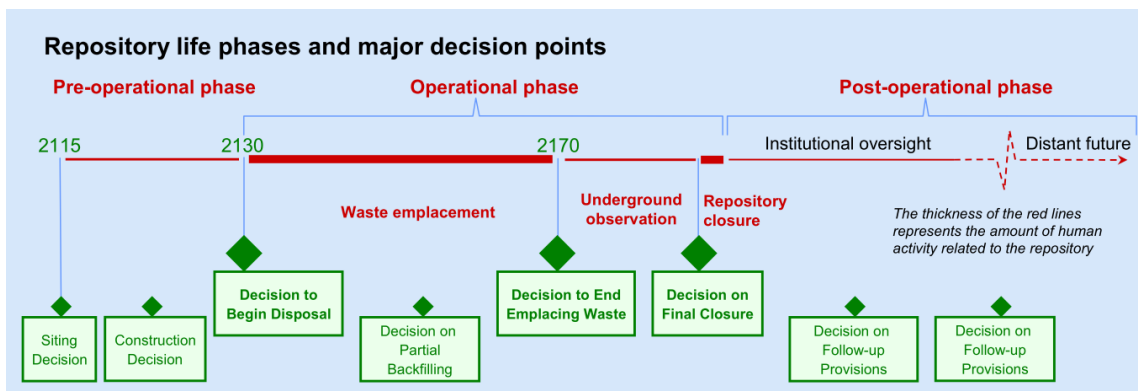


Figure 1-1: Phases of a radioactive waste repository in the Netherlands ([Verhoef et al., 2011](#)).

1-3 Problem Definition

A tunnel construction induces hydro-mechanical perturbations around the periphery of the excavation. Two zones affected from the excavation may be distinguished: the Excavation Damaged Zone (EDZ) and the Excavation disturbed Zone (EdZ). In the case of the BC formation, the former refers to alterations that may have negative impact on the safety and the performance of the repository, e.g. a significant increase in permeability. The EdZ refers to a zone where the perturbations induce substantial changes in the stress and the pore water pressures fields in the host rock however, the safety of the repository is not jeopardised. It is expected to be of larger extent than that of the EDZ ([Tsang et al., 2005](#)). The current research focuses on the disturbances occurring in these zones. An intersection of the disturbed zones, induced by the excavation of adjacent tunnels, may put in danger the stability of the repository. In addition, the function of the BC formation as a barrier against radionuclide migration may be weakened.

The extent of these perturbations will be decisive for the design of a radioactive waste repository such as the design diameter of the galleries, the excavation method, the stiffness and the thickness of the liner. It will also affect the dimensions and the layout of the facility, in terms of allowable spacing between individual galleries and between the waste disposal drifts connected to them. The implications of the aforementioned on the feasibility of the project, in terms of stability, safety and cost are apparent.

Apart from conducting in-situ measurements during a tunnel excavation and aside from performing laboratory tests on BC samples, the use of material models and geotechnical programs is indispensable for examining and predicting the soil-repository system response, which will be critical for the design of the radioactive waste facility.

For numerically simulating a tunnel excavation in the BC formation, the available soil models need to be evaluated regarding their ability to capture the response of the BC material sufficiently. Also, with increase of sophistication in the models commonly the number of required parameters increases, some of which may have little or no physical meaning. Thus, some parameters may be difficult and costly to be determined in the laboratory or in-situ. In addition, the amount of information on the BC is limited as there is scarcity of data at a depth of 500m, where the repository is planned to be constructed in the Netherlands (Figure 2-2). Therefore, identifying the material properties that influence the results of the numerical analyses the most is essential, for reasons of lowering the level of complexity of further testing procedures and design analyses.

1-4 Research questions and research approach

In this section, an attempt to address the problems described in Section 1-3 is described. These issues can be summarised and posed as questions, as follows:

- Which of the available soil models captures the known aspects of the mechanical behaviour of natural Boom Clay, relevant to tunnelling conditions, the best?
- How do the Boom Clay property values, used as model input parameters, influence the results of the numerical simulation of an undrained tunnel

excavation?

- Which Boom Clay property values, used as model input parameters, influence the numerical results the most, in terms of extent of the hydro-mechanical disturbance and tunnel liner forces?

The first step for answering the research questions is to perform a literature review on existing data for BC. First the geography, the geological setting, the mineralogy and the physical properties of BC are investigated. Subsequently, the mechanical response of the BC material is examined, in terms of mobilised shear strength, evolution of the stiffness, volumetric response, swelling potential and anisotropy. Information on the hydraulic conductivity of BC is also obtained. Finally, ranges of geotechnical BC property values, which are obtained from the literature review, are summarised.

The first research question is addressed by numerically simulating three conventional, drained, strain-controlled compression triaxial tests at different values of the Over-Consolidation Ratio (OCR), and of one high pressure oedometer test, performed by [Deng et al. \(2011b\)](#) on intact BC samples originating from the Essen site, in the north of Belgium (see Figure 2-1). The lab test facility of the finite element program *PLAXIS 2D 2011* ([Plaxis, 2011b](#)) is utilised for this purpose. The Linear Elastic Perfectly Plastic-Mohr Coulomb (LEPP-MC) model, the Modified Cam-Clay (MCC) model, the Soft Soil-Creep (SS-C) model and the Hardening Soil (HS) model are calibrated and subsequently assessed against the test data. The model that is considered to perform the best is selected and studied in more depth for gaining a better insight into its response. This is achieved by describing in detail the model formulation and by investigating the influence of selected model input parameters on the numerical results of the triaxial test simulations.

For addressing the second research question an undrained tunnel excavation is simulated in two-dimensional plane strain conditions with the *PLAXIS 2D 2011* finite element program. A mechanical sensitivity analysis is performed, during which the values of specific input parameters of the selected constitutive model are changed individually. Each parameter is given a lower bound value, an upper bound value, and a mean value, which are derived from the literature review on the BC material. The effect of the model input parameters on the numerical results is examined. The latter concern the resulting stress paths and the evolution of the shear stiffness of the soil close to the excavation as well as the profiles of the generated stresses and the pore water pressures in the proximity of the tunnel. The performance of the numerical results is assessed with respect to the radial extent of the hydro-mechanical disturbance around the excavation and the hoop forces in the tunnel liner.

Regarding the third research question, the most influential BC property value is considered to be the one which, when varied, causes a larger change in the value of a numerical result than the changes induced by all other varied BC property values.

The findings of the current study are complemented with conclusions and recommendations for further research.

Chapter 2

Characterisation of Boom Clay

2-1 Introduction

The suitability of the Boom Clay (BC) formation for the disposal of radioactive waste is attributed to its low hydraulic conductivity, its capability of retaining, adsorbing and lowering the solubility of radionuclides and to its self-sealing and self-healing capacity ([Horseman et al., 1987; Bastiaens et al., 2007](#)).

However, the present research is focused on examining the *geomechanical and geotechnical* aspects relevant to the construction of an underground nuclear waste facility, namely the hydro-mechanical behaviour of the soil, manifested during the excavation of the repository. Thus, only the geotechnical features of the BC material are discussed.

The scope of this section is to provide selective reference literature and information on the characteristics of the BC, so that the reader will be able to have a critical view of the discussion on evaluating the ability of the used soil models to capture the real response of the material and of the modelling approach used for simulating the tunnel excavation.

A brief description of the geological setting and the physical properties of the BC is given in Sections 2-2 and 2-3. The hydro-mechanical characteristics of the BC and the response of the material, as observed and measured in laboratory tests, are presented in detail in Section 2-4. The chapter is concluded with a summary in Section 2-5.

2-2 Geological setting

2-2-1 Geography

The BC formation is a marine deposit of the Tertiary Rupelian age of the Oligocene epoch, which spans the subsurface of north-east Belgium (Figure 2-1) and almost the whole of the Netherlands (Figure 2-2). A minor part of it outcrops along a zone at its south-west end (Belgium), then enters the subsurface with a dip of 1-2% to the north-east until the North Sea basin ([Dehandschutter et al., 2005](#)).

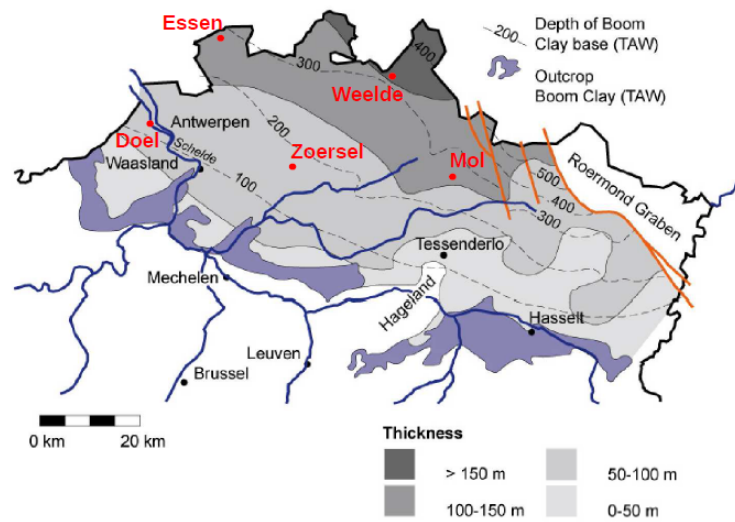


Figure 2-1: The Boom Clay formation in Belgium, with its depth and thickness ([Arnold et al., 2014](#)).

2-2-2 Stratigraphy

BC is generally characterised as a stiff, plastic, lightly over-consolidated (LOC) clay. The over-consolidation may not be attributed to the erosion of the strata overlying the BC formation, i.e. the removal of overburden. Instead, it may be ascribed to secondary compression and

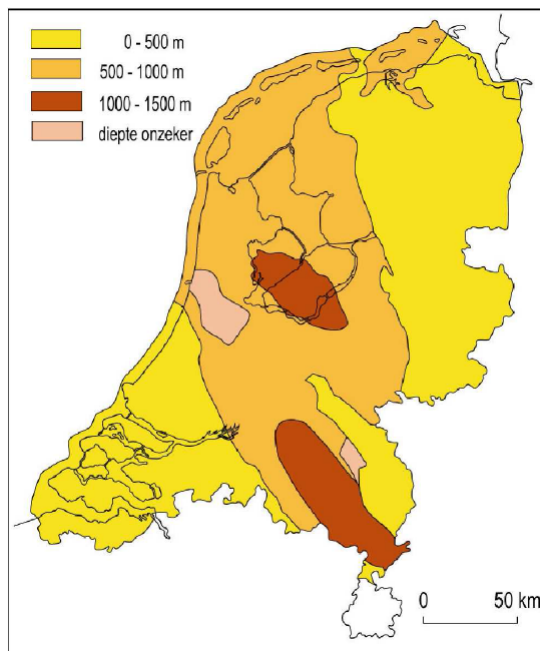


Figure 2-2: The Boom Clay formation in the Netherlands, with indication of its depth ([CORA, 2001a](#)).

diagenetic processes (Horseman et al., 1987). BC is also characterised by sedimentation-induced sub-horizontal bedding (Dehandschutter et al., 2004).

The BC formation is divided into four stratigraphic units, the first being the closest to the ground surface (Yu et al., 2013):

- the *Boeretang Member* (or the *Transition Zone*), which is silty, and has a thickness of approximately 25.1m,
- the *Putte Member*, about 46m thick, characterised by high organic content,
- the *Terhagen Member*, some 15.6m thick, with the lowest amount of coarse-grained material, and
- the deepest, the *Belsele-Waas Member*, which is silt-rich and has a thickness of about 15.9m.

It should be mentioned that the estimated thickness of the stratigraphic units refers to the Mol site (see Figure 2-1).

2-2-3 Mineralogy

The mineralogical composition of BC is shown in Table 2-1. The BC material consists mainly of the clay minerals Kaolinite, Smectite and Illite, and the non-clay minerals Quartz, K-feldspar, Na-plagioclase and Carbonates. A larger amount of clay minerals is present in clayey units (members), whereas more non-clay minerals are found in silty layers (Yu et al., 2013). The clay particles can be characterised flaky with large pores. They are arranged in face-to-face or face-to-edge configurations, forming bending structures (Figure 2-3a, Yu et al. 2012).

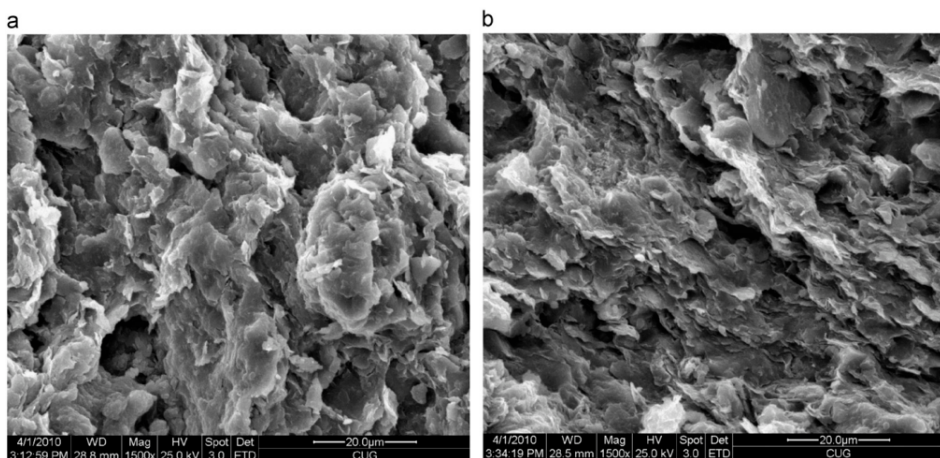


Figure 2-3: Scanning Electron Microscopy (SEM) images of a BC sample, before (a) and after (b) undrained shearing in a triaxial apparatus (Yu et al., 2012).

Table 2-1: Composition of the main minerals of Boom Clay ([Arnold et al., 2014](#)).

Definition	Range [%]	Source
Clay minerals	23 – 71	1,2,6,7,8,9
Kaolinite	1 – 36	1,2,5,7,9,11
Smectite	7 – 56	1,2,4,5,11
Illite-Muscovite	1 – 37	1,2,5,9,11
Vermiculite-Chlorite	1 – 4	7,9
Non-clay minerals	34 – 77	7,9
Quartz	20 – 66	1,3,5,7,9,11
K-feldspar	0 – 11	3,7,9,11
Na-plagioclase	0 – 6.3	7,9,11
Carbonates	0.24 – 5	7,10
Pyrite	0 – 9.6	3,5,7,9,11
Siderite	0 – 20.9	3,11

Sources: ¹[Decleer et al. \(1983\)](#), ²[Barnichon et al. \(2000\)](#), ³[De Craen et al. \(2000\)](#), ⁴[Wildenborg et al. \(2000\)](#), ⁵[De Craen \(2005\)](#), ⁶[Gens et al. \(2007\)](#), ⁷[Li et al. \(2007\)](#), ⁸[Bock et al. \(2010\)](#), ⁹[Zeelmaekers et al. \(2010\)](#), ¹⁰[Deng et al. \(2011b\)](#), ¹¹[Honty and De Craen \(2012\)](#)

2-3 Physical properties

The physical properties of the BC, for depth of 0m to 560m, are listed in Table 2-2.

Table 2-2: Summary of some of the physical properties of the Boom Clay for depth of 0m to 560m ([Arnold et al., 2014](#)).

Definition	Symbol	Unit	Range	Source
Bulk density	ρ	[kg/m ³]	1900 – 2100	7,8,10,11,16,19,23
Dry density	ρ_d	[kg/m ³]	1540 – 1780	1,4,5,8,9,10,14,22,23
Specific gravity	G_s	[–]	2.640 – 2.710	16,20,21
Porosity	n	[–]	0.204 – 0.460	1,4,5,7,8,9,10,11,12,13,14,15,17,19,22,24,25,26
Water content	w	[–]	0.095 – 0.400	7,8,9,10,11,12,14,15,16,19,20,22,23,25
Liquit limit	w_L	[–]	0.541 – 1.051	9,14,15,16,20,21
Plastic limit	w_P	[–]	0.210 – 0.330	2,3,6,9,15,16,18,20,21,25
Plasticity index	I_P	[–]	0.312 – 0.727	2,3,6,9,14,15,16,18,20,25

Sources: ¹[Baldi et al. \(1987\)](#), ²[Horseman et al. \(1987\)](#), ³[Baldi et al. \(1988\)](#), ⁴[Baldi et al. \(1991a\)](#), ⁵[Baldi et al. \(1991b\)](#), ⁶[Sultan \(1997\)](#), ⁷[Rijkers et al. \(1998\)](#), ⁸[Barnichon et al. \(2000\)](#), ⁹[Wildenborg et al. \(2000\)](#), ¹⁰[De Bruyn and Labat \(2002\)](#), ¹¹[Mertens et al. \(2004\)](#), ¹²[Bastiaens et al. \(2006\)](#), ¹³[Bernier et al. \(2007a\)](#), ¹⁴[Gens et al. \(2007\)](#), ¹⁵[Li et al. \(2007\)](#), ¹⁶[Piriyakul and Haegeman \(2007\)](#), ¹⁷[Desbois et al. \(2009\)](#), ¹⁸[Fran ois et al. \(2009\)](#), ¹⁹[Bock et al. \(2010\)](#), ²⁰[Deng et al. \(2011b\)](#), ²¹[Lima \(2011\)](#), ²²[Gens \(2012\)](#), ²³[Yu et al. \(2012\)](#), ²⁴[Aertsens et al. \(2013\)](#), ²⁵[B suelle et al. \(2013\)](#) ²⁶[Yu et al. \(2013\)](#),

2-4 Hydro-mechanical properties and constitutive response

The BC material exhibits a specific hydro-mechanical behaviour, which is of particular importance for the design, excavation, operation and long-term performance of an underground radioactive waste facility. The constitutive behaviour and the hydro-mechanical properties of the BC are discussed in this section, based on results of triaxial tests, an oedometer test and tests in the hollow cylinder apparatus, reported in the literature.

2-4-1 Friction angle and cohesion

The BC exhibits different values of effective friction angle (φ') and effective cohesion (c'), depending on the magnitude of confinement it undergoes when subjected to shearing in triaxial compression. At low and intermediate confining (with respect to the in-situ) stresses, φ' is larger, accompanied with almost zero c' . Conversely, at high confining stresses (comparable with the in-situ) φ' reduces and c' increases.

This behaviour can be illustrated by the curved failure envelopes, resulting from triaxial tests performed on BC samples, in the deviator stress (q) versus mean effective stress (p') plot in Figure 2-4. The failure envelopes of the intact material become less inclined beyond a level of mean effective stress, which implies a decrease in φ' and an increase in the intercept on the q – axis (hence an increase in c'). This behaviour may be explained by the orientation of the fine particles of the BC in the direction of shear. [Bishop et al. \(1965\)](#), who performed triaxial tests on natural stiff London Clay samples, suggested (based on the work of [Skempton, 1964](#)) that at low confining stresses, the transition from peak to strain softening in a q versus axial strains (ε_a) diagram is ascribed to the fact that the clay particles assume an orientation parallel to the direction of shearing with increasing strains. It was also proposed that at

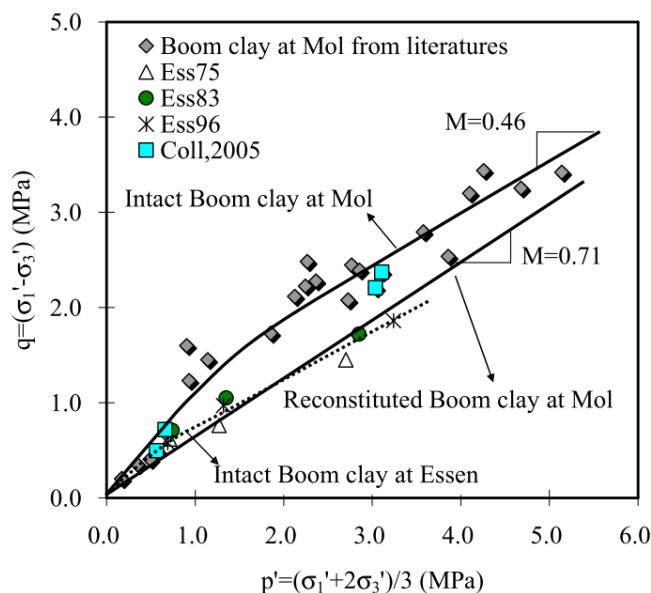


Figure 2-4: Failure envelopes for the BC material, originating from Essen and Mol, in the mean effective stress (p') versus deviator stress (q) plane ([Deng et al., 2011b](#)).

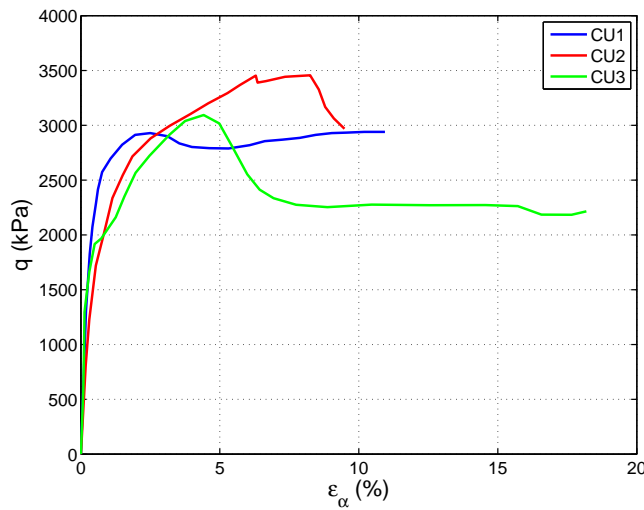


Figure 2-5: Deviator stress (q) versus axial strain (ϵ_a), for undrained triaxial tests performed on BC samples (CU1, CU2 and CU3) originating from Mol (Digitised from [Yu et al., 2012](#)).

large confining stresses, this change has already occurred at the moment the maximum shear strength is reached. Strain softening does not take place, since the friction angle has already reached its constant volume value. It should be noted that such phenomenon is not observed for the reconstituted BC material (Figure 2-4), owing to the fact that the micro-structure of the natural soil is lost. Also, based on this plot, it can be deduced that ϕ' may decrease and c' may increase with depth (increase in confining stress).

The change in orientation of the clay particles can be demonstrated by investigating the micro-structure of the BC before and after shearing. Figure 2-3 showed Scanning Electron Microscopy (SEM) images of a BC sample from the HADES URF, subjected to a consolidated-undrained triaxial test, performed by [Yu et al. \(2012\)](#). The part of the sample, from which the images are taken, is not specified. Before the test, the clay particles are arranged in face-to-face or face-to-edge configurations, without specific orientation (Figure 2-3a). After shearing however, the particles become oriented and assume a denser, face-to-face configuration (Figure 2-3b). It should be mentioned that in all performed tests, the samples exhibit peak and strain softening in $\epsilon_a - q$ plots (Figure 2-5). Therefore, the suggestion of [Bishop et al. \(1965\)](#) cannot be justified by utilising the SEM images of Figure 2-3.

[Deng et al. \(2011b\)](#) proposed that the larger shear strength of the intact BC from Mol, compared to the reconstituted material of the same origin and to the soil from Essen, may be attributed to the higher carbonate content of the first. It was also suggested that the cementation induced by the carbonates, leads to increase in the shear strength of the material. However, the cemented bonds are destroyed when the soil is reconstituted.

2-4-2 Stiffness, mobilised shear strength and volumetric response

In this section the results of three conventional consolidated-drained, strain-controlled triaxial tests, performed by [Deng et al. \(2011b\)](#) on a BC core from the Essen site in Belgium (Figure 2-1), are examined. The results of these tests are used to assess the evolution of the soil

stiffness and mobilised shear strength, as well as its volumetric response under triaxial stress conditions.

2-4-2-1 Material description

The BC material was obtained from a (presumably) vertical borehole, at depth between 218.91m and 219.91m, where the *Putte* member (Section 2-2-2) is present. The core, which is referred to as *Ess75*, was stored in a plastic sealed tube and then transferred for laboratory testing. Its physical properties and mineralogical composition of the clay fraction, which comprises 44 % of the total weight, are shown in Tables 2-3 and 2-4, respectively.

2-4-2-2 Sample preparation and triaxial tests specifications

The cylindrical soil specimens used for triaxial testing were trimmed with a wire saw to a height of 76mm and a diameter of 38mm. The samples were installed in the triaxial apparatus with the use of dry porous stones. Then a confining pressure, equal to the in-situ vertical effective stress of $\sigma'_{v0} = 2.2\text{MPa}$, was imposed and kept constant during saturation, in order for the sample not to lose its structure due to swelling. The soil specimen was isotropically consolidated, as the in-situ value of the coefficient of earth pressures at rest (K_0) was assumed to be equal to 1. The sample was saturated with synthetic water of the same composition as the in-situ water. Finally, equal steps of confining and back-pressure were applied, in order for the mean effective stress to remain constant and equal to σ'_{v0} , until a back-pressure of 1MPa was reached.

Consolidated-drained, strain-controlled triaxial tests were performed on three samples from core *Ess75*. The axial strain rate ($\dot{\varepsilon}_a$) during shearing was kept constant, equal to $1.31 \times 10^{-5}/\text{min}$. The test specifications are summarised in Table 2-5. In the first test (*Ess75Tr01*) the soil specimen was immediately sheared, thus with an OCR equal to 1, until an axial strain of $\varepsilon_a \approx 17.04\%$. In the second test (*Ess75Tr02*) the sample was isotropically unloaded to $p' = 1\text{MPa}$ (OCR = 2.2) and then sheared up to $\varepsilon_a \approx 18.87\%$. For the third test (*Ess75Tr03*) the specimen was isotropically unloaded to $p' = 0.5\text{MPa}$ (OCR = 4.4) and shearing followed until $\varepsilon_a \approx 18.48\%$. The test results are shown in $\varepsilon_a - q$, volumetric strain (ε_v) versus ε_a , $p' - q$ and $p' - \varepsilon_v$ diagrams in Figure 2-6. It should be mentioned that, although the BC material is

Table 2-3: Physical properties of core *Ess75* ([Deng et al., 2011b](#)).

Definition	Symbol	Value
Specific Gravity	G_s	2.65
Liquid Limit	w_L	78%
Plastic Limit	w_P	33%
Plasticity Index	I_P	45%
Water content	w	29.7%
Initial void ratio	e_0	0.785
Degree of Saturation	Sr	100%
Methylene Blue	MB	6.47
Carbonate Content	CC	0.91%

Table 2-4: Mineralogical composition of the clay fraction ($< 2\mu m$) of core *Ess75* (Deng et al., 2011b).

Mineral	Content (%)
Chlorite	5
Caolinite	35
Illite	20
Smectite	10
Illite/Smectite	30

characterised as LOC (Section 2-2-2), the soil from Essen was found to behave as NC by Deng et al. (2011b), after inspecting the results of isotropic compression tests in $e-\log p'$ plots.

2-4-2-3 Discussion on the results of the *Ess75* triaxial tests

Some general comments can be made on the behaviour of the BC material of the *Ess75* core, based on the $q - \varepsilon_a$ and $\varepsilon_a - \varepsilon_v$ plots of Figure 2-6.

- The soil behaviour is non-linear throughout the tests.
- The material response, in terms of mobilised shear strength, stiffness evolution and volume change, is highly dependent on the level of the confining stress and the amount of over-consolidation.
- The soil stiffness decreases with increasing ε_a . This decrease is less significant for $\varepsilon_a \leq 0.8\%$.

In the case of test *Ess75Tr01*, the soil exhibits the stiffest response and the shear strength is mobilised the most (Figure 2-6b). This can be explained by the high level of confinement ($\sigma'_3 = 2.2\text{MPa}$) and the low value of OCR (=1) during the execution of the test. In addition, the response of the soil is more ductile due to the Normally Consolidated (NC) conditions, which leads to the development of the largest ε_v (Figure 2-6d). It can be concluded that the evolution of the stiffness and the mobilised shear strength of the material is stress dependent.

It seems that the specimen has not reached the critical (or constant volume) state, as it continues to contract (Figure 2-6d). In addition, the deviator stress has not reached a plateau in Figure 2-6b, probably due to the large confining stress. More shearing (larger strains) is needed for the material to fail.

Table 2-5: Specifications of the triaxial tests performed by Deng et al., 2011b on the samples from the *Ess75* core.

Test	<i>Ess75Tr01</i>	<i>Ess75Tr02</i>	<i>Ess75Tr03</i>
Isotropic consolidation stress [MPa]	2.2	2.2	2.2
Pressure after isotropic unloading [MPa]	2.2	1.0	0.5
Over-Consolidation Ratio [-]	1.0	2.2	4.4

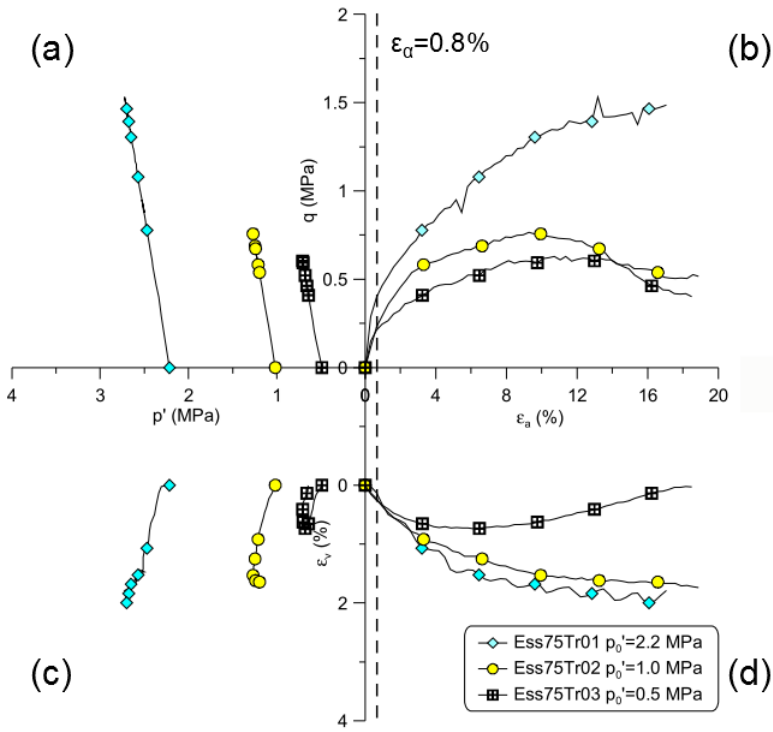


Figure 2-6: Results of the triaxial tests on BC of the *Ess75* core. p'_0 is the isotropic consolidation stress before the initiation of shearing, p' is the mean effective stress, q is the deviator stress, ε_a is the axial strain and ε_v is the volumetric strain (After Deng et al., 2011b).

In test *Ess75Tr02* the soil sample exhibits a less stiff behaviour and lower mobilised shear strength than in the NC case. Moreover, peak and strain softening is observed in Figure 2-6b, which promote the development of plastic deformations along the shear bands of the specimen. The softer response and the lower level of mobilised shear strength are attributed to the smaller confining stress ($\sigma'_3 = 1.0\text{ MPa}$) and the higher value of OCR ($=2.2$). The exhibited peak and strain softening is ascribed to the more brittle soil in Over-Consolidated (OC) conditions. The more ductile material response can be further justified by the smaller amount of volumetric strains, compared to the results of test *Ess75Tr01* (Figure 2-6d). Similarly to the NC case, neither the contraction of the specimen has ceased nor the deviator stress has reached a plateau, which, again, may be ascribed to the high level of confinement.

In test *Ess75Tr03* the material behaviour is the least stiff and the mobilised shear strength is the lowest. Peak and strain softening is observed in Figure 2-6b. The same explanations given and observations made for test *Ess75Tr02* apply in this case as well. Moreover, the soil response is dilatant, with a dilatancy angle $\psi = 2^\circ$. This is due to the OC conditions during the test and due to the $\text{OCR} = 4.4$ being larger than that of test *Ess75Tr02* ($\text{OCR} = 2.2$). The dilatancy angle is determined by the inclination of the linear part of the $\varepsilon_a - \varepsilon_v$ curve (Figure 2-6d) after increase in ε_v occurs, according to $\delta\varepsilon_v/\delta\varepsilon_a = 2\sin\psi/(1-\sin\psi)$.

The values of the initial Young's moduli (E_0) for tests *Ess75Tr01*, *Ess75Tr02* and *Ess75Tr03* were found to be by Deng et al. (2011b) equal to 103.8MPa, 50.0MPa and 30.8MPa, respectively. A $\varphi' = 12.4^\circ$ and a $c' = 0.11\text{ MPa}$ were also determined. The friction angle was back-calculated from the inclination, M , of the second branch of the failure envelope of the

material (slope of the dotted line in Figure 2-4 from about $p' = 1.0\text{ MPa}$ to $p' = 3.6\text{ MPa}$), according to:

$$\varphi' = \arcsin \left(\frac{3M}{6 + M} \right) \quad (2-1)$$

The effective cohesion was determined from the value of the intercept on the q -axis (c^*), which resulted from extending the linear part of second branch of the failure envelope, as follows:

$$c' = \frac{c^* \times (3 - \sin \varphi')}{6 \cos \varphi'} \quad (2-2)$$

2-4-3 Swelling potential in triaxial stress conditions

The BC material exhibits a high tendency to increase in volume (swelling potential) when unloaded, which affects the stiffness and ductility of the tested samples. Its propensity to swell is attributed to the presence of swelling clay minerals such as smectite and illite (Yu et al., 2012).

Bésuelle et al. (2013) performed a series of drained triaxial tests on BC material cored from the HADES URF in Mol, at depth of 223m ($\sigma'_v \approx 2.3\text{ MPa}$). The specimens were isotropically consolidated at different confining stresses, for reasons of investigating the effect of the level of confinement on the swelling rate. In addition, the duration of the isotropic consolidation before shearing was varied in order to examine the influence of the duration of swelling on the ductility of the soil. The process of isotropic consolidation for one of the tested specimens (sample BC07) is shown in Figure 2-7.

The effect of the magnitude of the isotropic consolidation pressure on the rate of swelling of the material is illustrated in Figure 2-8. Bésuelle et al. (2013) observed that an increase in the isotropic effective pressure leads to a decrease in the swelling rate. The latter becomes zero when the soil is NC, i.e. at a pressure of 5MPa, which was estimated to be the isotropic pre-consolidation pressure (p_c).

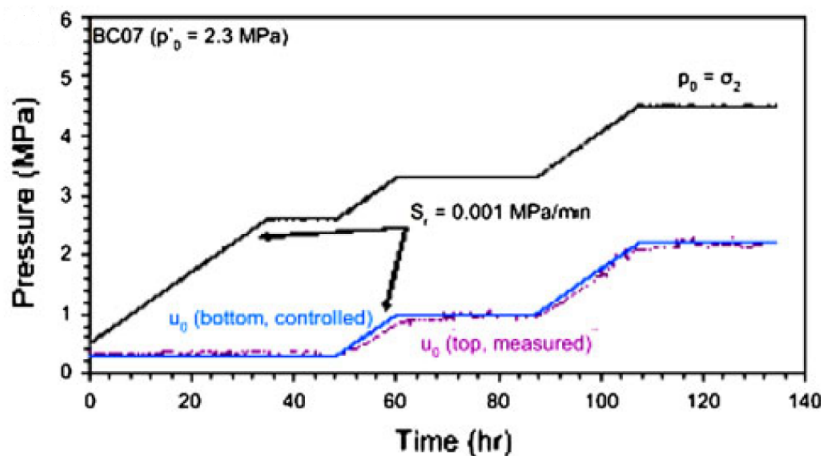


Figure 2-7: Applied pressure versus elapsed time diagram for the phase of isotropic consolidation on a BC specimen originating from Mol (Bésuelle et al., 2013).

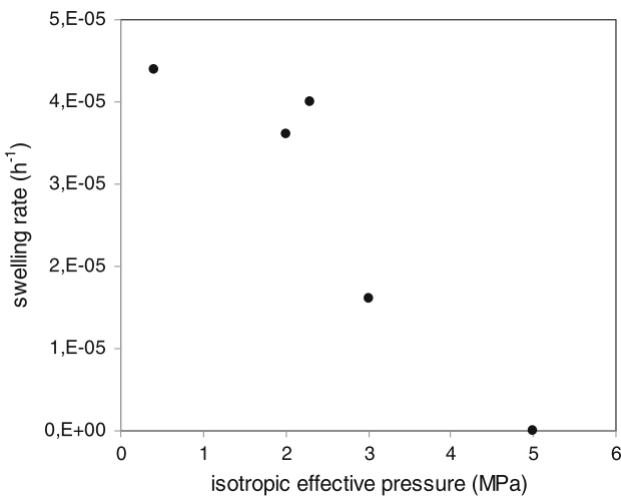


Figure 2-8: Effect of the magnitude of the isotropic consolidation pressure on the rate of swelling of the BC material. The measurements are taken after the relationship between the swelling rate and the time of consolidation has become linear (Bésuelle et al., 2013).

The influence of the duration of isotropic consolidation, and thus the duration of swelling, before shearing on the BC material is depicted in Figure 2-9. Samples BC08, 11 and 19 have an OCR = 12.5, whereas specimens BC07, 12 and 20 are have an OCR = 2.17 (Bésuelle et al., 2013). The axial strain rate during shearing was kept constant to $1 \times 10^{-7}/\text{s}$ for specimens BC07 and 20 and it was increased to $\dot{\varepsilon}_a = 1 \times 10^{-5}/\text{s}$ for sample BC12. However, the value of $\dot{\varepsilon}_a$ is not mentioned for the samples with OCR = 12.5. It is noted that comparison of the results is meaningful only among the samples with the same value of OCR.

Bésuelle et al. (2013) observed that an increase in the swelling duration (termed "tiso") leads to softer and more ductile response of the material, since the initial soil stiffness decreases and the peak shear strength is exhibited at larger axial strains (Figure 2-9a). In addition, they highlighted the fact that the volumetric strains increase and the dilatancy is weaker, a fact that also demonstrates the more ductile behaviour of the specimens (Figure 2-9b). It was concluded that an increase in the duration of swelling causes the soil to behave as if it were less over-consolidated. Furthermore, it was suggested that the results for sample BC12 may not be used for comparison as the high level of $\dot{\varepsilon}_a$ could have caused undrained conditions.

2-4-4 Comparison of the response of BC in triaxial stress conditions at the Essen and Mol sites

A comparison of results of triaxial tests performed on BC samples from different sites may prove useful to evaluate the transferability of knowledge on the soil (Deng et al., 2011b). In this section the results from the triaxial tests presented in Sections 2-4-2 (Essen site) and 2-4-3 (Mol site) are compared.

From Figures 2-6 and 2-9 it can be deduced that the non-linearity and the dependency of the soil behaviour on the level of confinement as well as on the value of OCR is observable at both sites. On the other hand, the specimen from Mol has a larger shear strength. For the samples

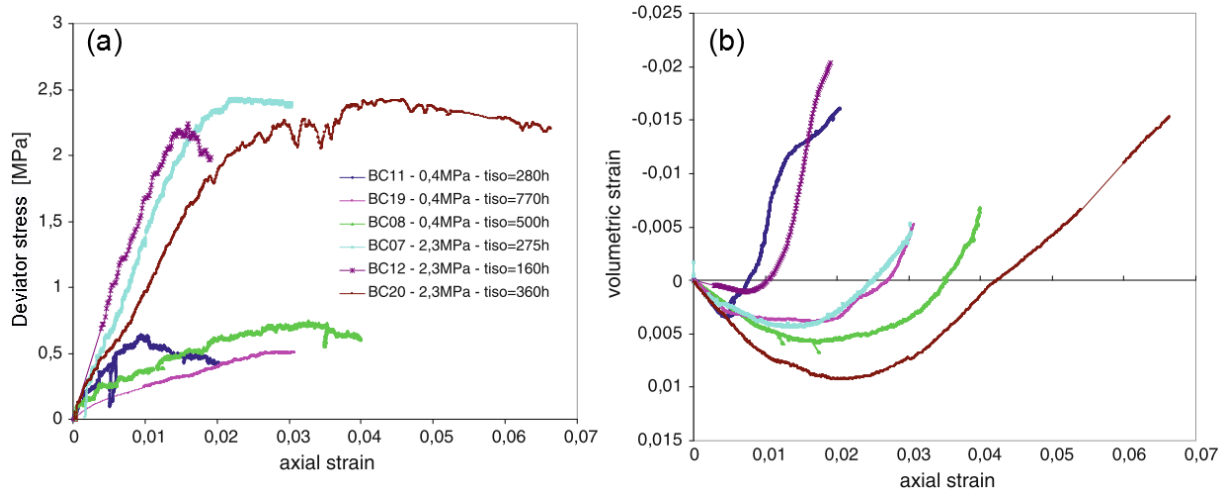


Figure 2-9: Triaxial tests results for different values of OCR and for varying duration of swelling before shearing, for BC samples from Mol, in terms of deviator stress (q) versus axial strain (ε_a) (a) and volumetric strain (ε_v) versus ε_a (b) diagrams. (Bésuelle et al., 2013).

from Mol with $\text{OCR} = 2.17$ (specimens BC07, 12 and 20 in Figure 2-9a), the peak deviator stress is about 2.4MPa at a confining stress $\sigma'_3 = 2.3\text{MPa}$, whereas its value is approximately 0.75MPa at $\sigma'_3 = 1.0\text{MPa}$ ($\text{OCR} = 2.2$) for the specimen from Essen (Figure 2-6b, *Ess75Tr02*). This difference is attributed to the higher level of confinement for the former, which is also responsible for its stiffer response. It should be mentioned that the axial strain rate is larger for the triaxial tests conducted on the material from Essen ($\dot{\varepsilon}_a = 1.31 \times 10^{-5}/\text{min}$, compared to $\dot{\varepsilon}_a = 6 \times 10^{-6}/\text{min}$ for the samples from Mol). Therefore, the stiffer response of the BC from Mol cannot be attributed to the rate of shearing.

The BC from Mol seems to be less ductile. In Figure 2-10 the digitised $q - \varepsilon_a$ and $\varepsilon_a - \varepsilon_v$ plots of specimens BC20 from Mol and *Ess75Tr02* from Essen ($\text{OCR} = 2.17$ and 2.2, respectively)

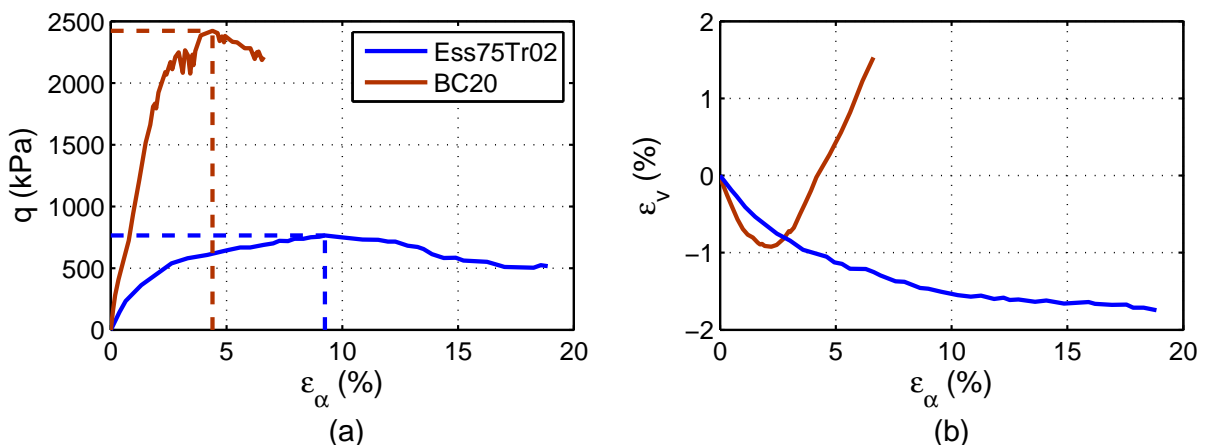


Figure 2-10: Deviator stress (q) versus axial strain (ε_a) (a) and volumetric strain (ε_v) versus ε_a (b) diagrams for a sample from Essen (Ess75Tr02, $\text{OCR} = 2.2$) and a sample from Mol (BC20, $\text{OCR} = 2.17$) (Digitised from Deng et al., 2011b and Bésuelle et al., 2013, respectively).

are depicted. The more ductile response of the latter is demonstrated by the absence of dilatancy (Figure 2-10b), despite the lower level of confining stress ($\sigma'_3 = 1.0\text{MPa}$ for the *Ess75* specimen and $\sigma'_3 = 2.3\text{MPa}$ for the BC20 sample).

The specimens BC08, 11 and 19 from Mol (Figure 2-9) react stiffer and exhibit larger shear strength, even though the confining stress is lower ($\sigma'_3 = 0.4\text{MPa}$) than the one of specimen *Ess75Tr03* ($\sigma'_3 = 0.5\text{MPa}$, Figure 2-6b). This may be ascribed to the higher carbonate content of the soil from the Mol site (Section 2-4-1). Also, the specimens from Mol are more dilatant (Figure 2-9b). It should be noted that the duration of isotropic consolidation for the soil samples from Essen, which would allow for a better comparison of the triaxial tests results in terms of swelling duration, was not provided from [Deng et al. \(2011b\)](#).

Moreover, whereas the isotropic pre-consolidation pressure of the BC from Essen was found to be equal to the in-situ stress, this was not the case for the soil from Mol ($p_c = 2.17 \times p'_0$).

2-4-5 Response in oedometer stress conditions

In this section the mechanical behaviour of BC in one-dimensional compression is examined. To this purpose, the results of one high pressure oedometer test, performed by [Deng et al. \(2011b\)](#) on the same BC core from Essen which was used for investigating the soil response in triaxial stress conditions (Section 2-4-2), are discussed. The presented results are considered representative of the BC response in oedometer conditions.

The test is described in detail here as it will serve as a basis for the simulation in the lab test facility of *PLAXIS*, in order to evaluate the ability of various soil models to capture the behaviour of the material.

2-4-5-1 Sample preparation and oedometer test specifications

The BC sample was prepared by wire saw trimming cut to a height of 20mm and a diameter of 50mm. Then, it was installed in the oedometer apparatus with the use of dry porous stones. Before saturation with synthetic water, the soil was subjected to a vertical effective stress equal to the in-situ value ($\sigma'_{v0} = 2.4\text{MPa}$), in order to prevent the sample from swelling-induced destructuration. The performed oedometer test is referred to as *Ess75Oedo1*.

The oedometer test results are shown, in terms of void ratio (e) versus vertical effective stress (σ'_v) diagram in Figure 2-11, and in terms of σ'_v – elapsed time and vertical displacement – elapsed time diagrams in Figure 2-12. The dashed line connecting the two white circular points in Figure 2-11 represents the loading of the sample under the in-situ stress before saturation. After this initial phase, the soil was stepwise unloaded to a vertical effective stress of 0.125MPa (path A–B). Then, it was reloaded to 16MPa (path B–C), unloaded to 0.125MPa (path C–D), reloaded to 32MPa (path D–E) and unloaded to 0.125MPa (path E–F). Each loading step lasted until the rate of displacement was considered low enough, i.e. equal to 0.01mm/h, which corresponded to $1.4 \times 10^{-7}/\text{s}$ for the considered test.

2-4-5-2 Discussion on the results of the oedometer test

Behaviour on unloading-reloading loops

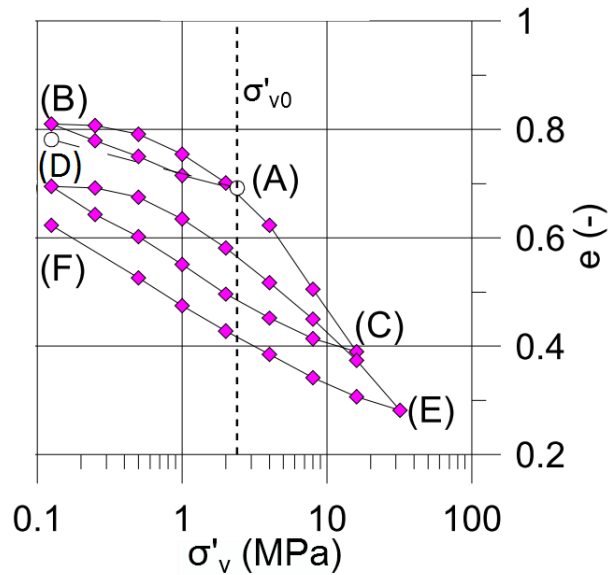


Figure 2-11: Void ratio (e) versus logarithm of vertical effective stress ($\log \sigma'_v$) plot for the oedometer test on the BC from core *Ess75* (After [Deng et al., 2011b](#)).

One of the most distinctive features of the behaviour of the BC material in oedometer stress conditions is the significant hysteresis it exhibits in unloading-reloading loops (Figure 2-11). The "bilinear" shape of the $\sigma'_v - e$ graph is also noticeable. The inclination of the diagram is initially smooth and becomes steeper with increasing (in the case of reloading) and decreasing (in the case of unloading) vertical load.

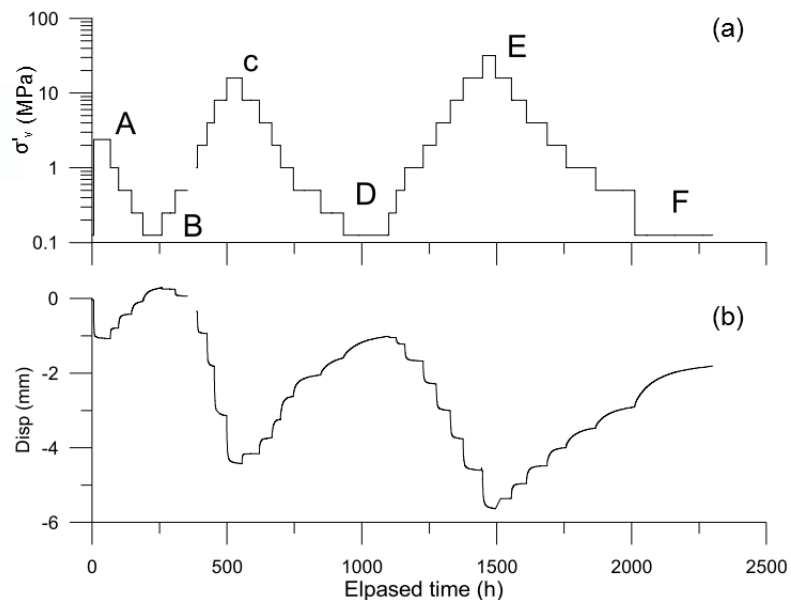


Figure 2-12: Logarithm of vertical effective stress ($\log \sigma'_v$) versus elapsed time (a) and displacement – elapsed time (b) plots for the oedometer test on the BC from core *Ess75* ([Deng et al., 2011b](#)).

Cui et al. (2013) performed high pressure oedometer tests on Ypresian clay samples. The results of one test on a specimen cored from a depth of about 330m are plotted in terms of a $\sigma'_v - e$ graph in Figure 2-13. The clay fraction of the tested specimen accounted for 54% of the total weight. In addition, the material comprised a significant fraction of the swelling clay mineral smectite and of the smectite/illite mixture (32% and 12%, respectively). Also, the plasticity index was found to be $I_P = 42\%$. The aforementioned values are similar to the ones of the BC material from Essen (see Section 2-4-2, Tables 2-3 and 2-4). Moreover, Ypresian clay is characterised as a stiff, natural clay, as is BC. Thus, the response of the Ypresian clay sample may be expected to be similar to that of the BC from the *Ess75* core. Subsequently, the behaviour of the latter might be explained by the findings of Cui et al. (2013).

According to Cui et al. (2013), the "bi-linear" shape of the unloading-reloading loops in the $\sigma'_v - e$ graph of Figure 2-13 may be attributed to the interplay between the mechanical and physico-chemical processes that occur in the micro-structure of the material. An illustrative representation of the interaction of the two processes, as well as their effect on the material micro-structure in unloading-reloading paths, is shown in Figure 2-14. Cui et al. (2013) suggested that the soil particles orientate parallel to each other during loading and they assume a face-to-face contact configuration. It was proposed that the latter invigorates the swelling potential, which leads to soil destructure, exhibited by a face-to-edge arrangement of the inter-particle contacts during unloading. Based on this line of reasoning, they suggested an explanation for the response of the Ypresian clay in one dimensional unloading-reloading, which follows below.

The points of transition in slope during unloading and reloading in Figure 2-13 correspond to stresses, which are referred to as threshold stresses (σ_{s1} to σ_{s5}). During unloading and for $\sigma'_v > \sigma_s^{unload}$ ($= \sigma_{s1-s3}$ in Figure 2-13, see also Figure 2-14) the slope is gentle, since the

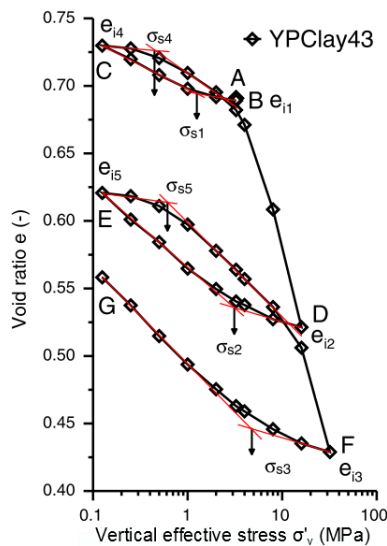


Figure 2-13: Void ratio (e) versus logarithm of vertical effective stress ($\log\sigma'_v$) plot for a high pressure oedometer test performed on an Ypresian clay sample. The threshold stresses (σ_{si}) are obtained from the intersection of the extended linear parts of the unloading and reloading branches of the diagram (Cui et al., 2013).

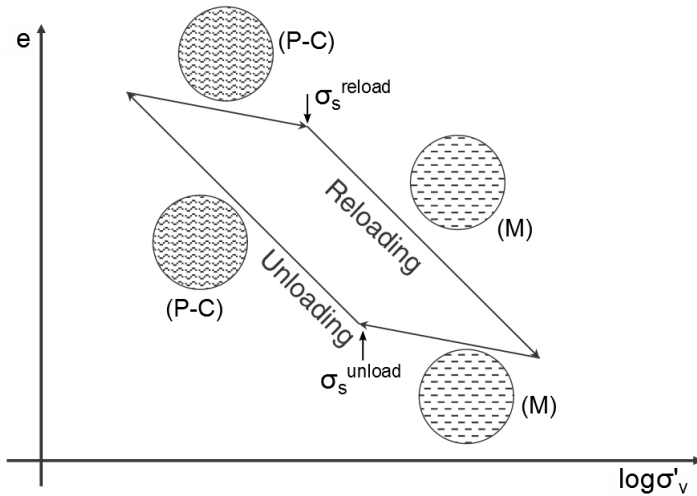


Figure 2-14: Void ratio (e) versus logarithm of vertical effective stress ($\log \sigma'_v$) plot for the qualitative representation of the mechanical and physico-chemical processes that take place in an unloading-reloading path, in an Ypresian clay. Their effects on the soil micro-structure are also depicted. (M) denotes mechanically dominated process and (P-C) represents physico-chemically dominated process. σ_s^{reload} and σ_s^{unload} are the threshold stresses in an unloading-reloading loop (After Cui et al., 2013).

influence of the vertical load (mechanical effect) is more significant than the swelling pressure exerted by the adsorbed water in the clay particles (physico-chemical effect). Conversely, the effect of the swelling pressure becomes predominant for $\sigma'_v < \sigma_s^{unload}$ and the inclination of the $\sigma'_v - e$ plot increases substantially. Similarly, in the case of reloading, for $\sigma'_v < \sigma_s^{reload}$ ($= \sigma_{s4-s5}$ in Figure 2-13, see also Figure 2-14) the mechanical effect is counter-balanced by the physico-chemical (induced by the preceding unloading path), leading to a small change in the void ratio, whereas the latter decreases abruptly when σ'_v surpasses its threshold value.

Compression and swelling indices

The compression index (C_c) was estimated by Deng et al. (2011b) to be equal to 0.378, by computing the inclination of the linear part of the reloading path B–C (Figure 2-15). The compression index is smaller for path D–E than for path B–C (Figure 2-11). Thus, the compressibility of the material decreases, i.e. the soil reacts stiffer in the second reloading path.

The swelling indices (C_s) were estimated by Deng et al. (2011b), by calculating the slope of the linear branch of the unloading paths (Figure 2-15). Three values were determined for paths A–B, C–D and E–F (Figure 2-11): 0.105, 0.165 and 0.158, respectively. The second and the third are almost equal and larger than the one corresponding to the first unloading path. This may be attributed to the larger swelling pressure, induced by the higher vertical loads applied during the reloading paths B–C and D–E (Figure 2-11), as explained in the previous section.

The ratio of the two indices (C_c/C_s) usually takes values from 5 to 10 (Brinkgreve, 2011). For the largest and the smallest value of C_s , it becomes $C_c/C_{sA-B} = 0.378/0.105 = 3.60$ and $C_c/C_{sC-D} = 0.378/0.165 = 2.29$, respectively, for the tested sample. This is much lower than

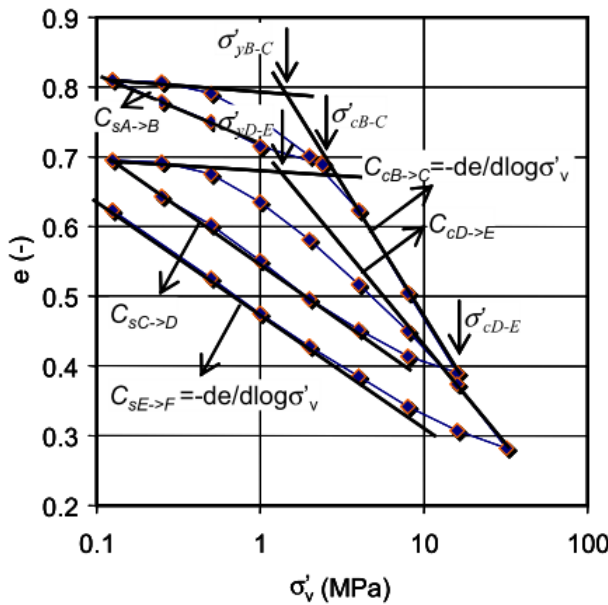


Figure 2-15: Estimation of the compressibility parameters and the yield stresses from a void ratio (e) versus logarithm of vertical effective stress ($\log \sigma'_v$) graph, for test *Ess75Oedo1* (Deng et al., 2011b).

the common range, owing to the large value of C_s , which is indicative of the strong swelling potential of the BC material.

Yield and pre-consolidation stresses

The value of the vertical yield stress (σ'_y) for the two loading paths B–C and D–E was estimated to be 1.4MPa by Deng et al. (2011b) (Figure 2-15). This was much lower than the corresponding vertical pre-consolidation stresses ($\sigma'_c = 2.4\text{MPa}$ and 16MPa for paths B–C and D–E, respectively), as well as lower than the in-situ stress of $\sigma'_{v0} = 2.2\text{MPa}$. Note that σ'_c refers to the maximum applied stress for every unloading-reloading path (σ'_v at point A for the first and σ'_v at point C for the second loop, see Figure 2-11). Based on these findings Deng et al. (2011b) deduced that:

- σ'_y is lower than the in-situ stress (σ'_{v0}), probably due to swelling-induced destructuration of the tested sample,
- the fact that $\sigma'_y \neq \sigma'_c$ implies that these two quantities have a different meaning in the case of the tested material and
- the OCR should be calculated based on σ'_c , rather than on σ'_y , in the case of the BC from Essen.

2-4-6 Initial and induced anisotropy

The BC material has been found to exhibit initial and stress-induced anisotropy. The former refers to the inherent anisotropy of the soil, which results from geological processes, such as deposition as well as from the plastic strain history it has undergone. The second concerns

its anisotropic behaviour owing only to the stress history. In order to discuss these aspects of the BC response, the results of triaxial and hollow cylinder tests are presented.

2-4-6-1 Anisotropic behaviour of BC in triaxial stress conditions

Sultan et al. (2010) investigated the yield and plastic behaviour of BC and proposed a constitutive model to account for the anisotropic BC response. Two series of triaxial tests on samples originating from the HADES URF (Mol) were performed.

The first series comprised tests where the specimens were isotropically consolidated at different confining pressures smaller than the estimated pre-consolidation stress, so as to prevent yielding before shearing. The purpose of these tests was to generate the initial yield curve of the material in $p' - q$ plane (Figure 2-16). The curve, which is normalised with respect to the pre-consolidation stress, is oriented along the K_0 -line of the material. Based on the previous research of other scholars, Sultan et al. (2010) concluded that this demonstrates the anisotropy of the BC material in its natural state.

However, Sultan et al. (2010) mentioned that the isotropic pre-consolidation stress of the soil ($p_c = 0.38\text{MPa}$) was found to be much lower than the in-situ stress ($\sigma'_{vo} \approx 2.4\text{MPa}$). This fact was ascribed to the swelling and thus to the loss of memory of the loading history of the specimen, during the isotropic consolidation test performed for obtaining p'_c . Assuming that all tested samples experienced swelling, the yield curve of Figure 2-16 might not represent the undisturbed state of the tested soil. Nevertheless, Sultan et al. (2010) suggested that the fabric anisotropy did not seem to be influenced by swelling substantially.

The second series included triaxial tests, for which the soil samples were first isotropically consolidated to a pressure of 9MPa, then isotropically unloaded to different p' (therefore vari-

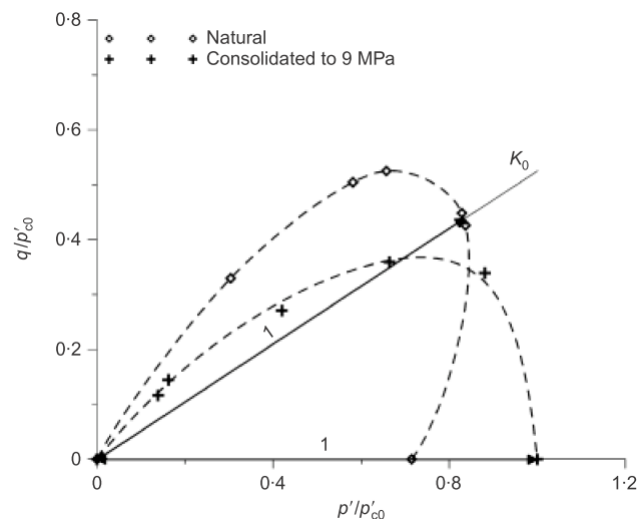


Figure 2-16: Yield curves of the BC at its initial state and after isotropic consolidation of the samples at 9MPa. The former is normalised with respect to the maximum mean effective stress, determined by the intersection of the K_0 -line with the initial yield surface and the latter with respect to the maximum applied mean effective stress during the tests ($p' = p'_{c0} = 9\text{MPa}$). q is the deviator stress and K_0 is the coefficient of earth pressures at rest (Sultan et al., 2010).

ous values of OCR) and finally sheared. The resulting yield curve (dashed curve with crosses in Figure 2-16), which is normalised with respect to the maximum applied pressure during the tests (9MPa), is inclined towards the hydrostatic axis. [Sultan et al. \(2010\)](#) concluded that this implies that the anisotropy of the material has vanished. It was also suggested that the initial inclination of the yield curve decreases, and therefore anisotropy is erased, with increasing level of confining stress.

2-4-6-2 Anisotropic behaviour of BC in a tunnel excavation reproduced in the hollow cylinder apparatus

[Labrouse et al. \(2013\)](#) reproduced a tunnel excavation in the hollow cylinder apparatus with BC samples originating from the HADES URF in order to investigate the Excavation Damaged Zone (EDZ).

The hollow cylinder apparatus allows for imposing separately different stresses, water pressures and drainage conditions at the central hole and the outer periphery of a hollow cylindrical specimen. Thus, the simulation of initial undrained conditions as well as of the consolidation stage of an excavation is possible ([Labrouse et al., 2013](#)).

Soil specimens, cored parallel and perpendicular to the bedding of the formation (see Section 2-2-2), were initially subjected to the in-situ stress state, then underwent undrained unloading, followed by a stage of pore water pressure equalisation (consolidation).

Figure 2-17 shows X-Ray Computed Tomography (XRCT) scans of the cross section at the mid-height of a sample, which was cored parallel to the bedding, before and after unloading. ([Labrouse et al., 2013](#)) observed that the inner and outer peripheries of the specimen converge in an anisotropic manner. For the former, the displacements parallel to the bedding direction (indicated by the black dashed lines in Figure 2-17b) are larger than the ones perpendicular to it. For the latter, the displacements are larger perpendicular to the bedding.

Moreover, [Labrouse et al. \(2013\)](#) identified an eye-shaped pattern for the EDZ, after measuring the radial displacements parallel and perpendicular to the bedding (Figure 2-18). The

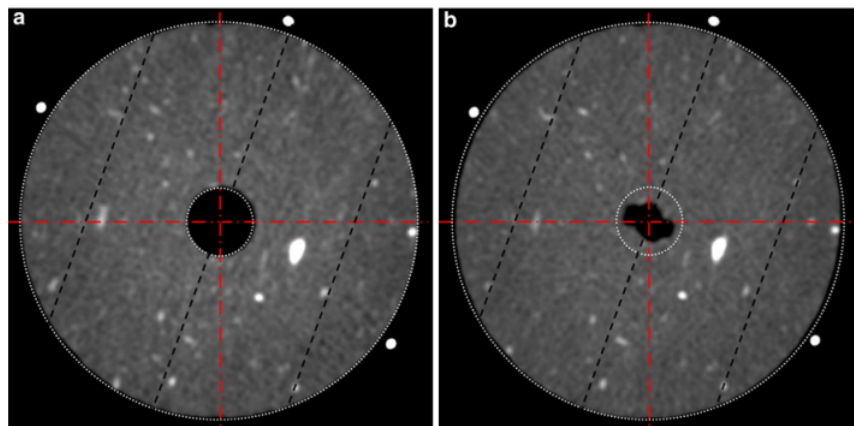


Figure 2-17: X-Ray Computed Tomography (XRCT) scans of a cross section at the mid-height of a BC sample cored parallel to the bedding (indicated by the back dashed lines), before (a) and after (b) unloading in the hollow cylinder apparatus ([Labrouse et al., 2013](#)).

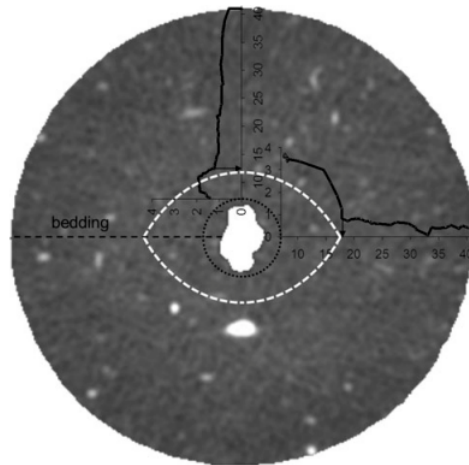


Figure 2-18: Identification of the eye-shaped Excavation Damaged Zone (EDZ), based on the radial displacements (solid black curves) measured parallel and perpendicular to the bedding (Labrouse et al., 2013).

boundaries of the damaged zone were considered to be defined by the points at which abrupt change occurred in the inclination of the displacements versus radial distance plots (solid black curves in Figure 2-18).

It was concluded that these observations may be attributed to the inherent strength and stiffness anisotropy of the material, which in turn result in the anisotropic behaviour at the central hole and the outer periphery of the sample.

François et al. (2013) developed a constitutive model for simulating the BC response, subjected to the hollow cylinder test described above. It was suggested that, as is the case for sedimentary rocks, the shear strength of the material in terms of cohesion, depends on the angle of the major principal stress with respect to the normal to the bedding: the soil manifests its largest strength for an angle of 90° , its smallest strength for an angle of 45° and an intermediate value for an angle of 0° (Figure 2-19). Based on this suggestion and by considering that the major principal stress is expected to be the one tangential to the walls of the excavation, it was deduced that the largest deviatoric plastic strains, and therefore the highest convergence, will be observed at an angle of 45° with respect to the bedding, within the plastic zone. On the contrary, the lowest strains will develop perpendicular to the bedding. Intermediate displacements are expected for an angle of 0° (Figure 2-17b).

According to Graham and Housby (1983), natural LOC clays (thus clays similar to the soil under consideration) usually exhibit elastic stiffness anisotropy. Such soils are characterised as cross-anisotropic, meaning that they demonstrate different stiffness in two directions: perpendicular and parallel to the bedding. Since the BC from Mol has larger stiffness in the direction of the bedding, the extent of the plastic zone around the central hole of the hollow cylindrical specimen will be larger parallel to the bedding and smaller perpendicular to it (Labrouse et al., 2013). That is because the soil yields earlier in the stiffer direction (for the same strain increment, a larger stress increment occurs for a stiffer material). This might explain the eye-shaped zone illustrated in Figure 2-18, which was also observed during the construction of the connecting gallery at the HADES URF (Volckaert et al., 2004). This

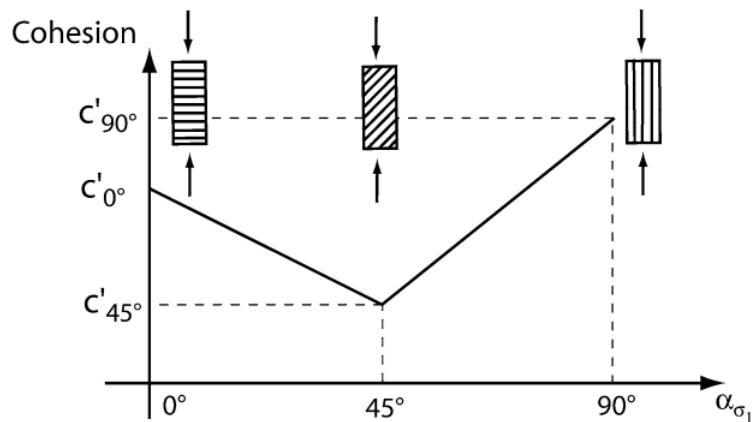


Figure 2-19: Development of the magnitude of the effective cohesion (c'), according to the angle between the major principal stress and the direction normal to the bedding (α_{σ_1}) ([François et al., 2013](#)).

shape may also be attributed to the propensity of the soil to develop shear bands (strain localisation) in the direction parallel to the bedding ([François et al., 2013](#)).

The opposite pattern observed at the outer periphery of the sample (contraction perpendicular to the bedding, Figure 2-17b) was partly explained by the elastic anisotropy of the BC material. Results of numerical analyses performed by [François et al. \(2013\)](#) showed that the part of the soil situated within the damaged zone experiences plastic swelling (displacements towards the central hole), whereas the rest of the material undergoes elastic contraction. The latter was attributed to stress redistribution from the (predominantly) plastic zone towards the (mainly) elastic zone. It was proposed that larger contraction is expected in the direction with lower stiffness, i.e. perpendicular to the bedding.

Regarding the test of the sample cored perpendicular to the bedding planes, no displacements were measured. However, the results of this test were not considered trustworthy, since it was interrupted at its first stage (generation of in-situ stress conditions).

Another test performed on a specimen cored perpendicular to the bedding, which had a distinct crack along its whole height and diameter, lead to results similar to those of the sample cored parallel to the bedding: the largest convergence in the central hole was observed in the direction of the discontinuity, whereas the displacements at the outer periphery of the sample developed perpendicular to the crack. It was deduced that, when planes of weakness (which may be either the bedding or cracks/fissures) are present, the response of BC is expected to be dominated by them, during tunnel excavation.

The anisotropic response of BC in tunnelling conditions is also expected to arise from the initial stress field and the different hydraulic conductivities (Section 2-4-7), therefore the different pore pressure distribution, in the horizontal and the vertical directions ([Bastiaens et al., 2007](#)).

2-4-7 Hydraulic conductivity

The permeability (k) of BC is low with values in the order of magnitude of 10^{-12}m/s (e.g. [Yu et al., 2013](#); [Bastiaens et al., 2007](#)), which is a crucial barrier function against radionuclide migration. The relationship between k and e may be described by an equation proposed by [Deng et al. \(2011a\)](#):

$$k = \frac{3.2 \times 10^{-9}}{w_L^{2.9}} 10^{3.56e} \quad (2-3)$$

where w_L is the liquid limit and e is the void ratio. An average value of the permeability change index was found to be $\Delta e/\Delta \log k = 0.3$.

[Deng et al. \(2011a\)](#) investigated the permeability of BC samples from Essen with three techniques: isotropic compression (in a triaxial apparatus), high pressure oedometer and constant head percolation tests. They concluded that a linear relationship exists between k and e , when the former is plotted in logarithmic scale (Figure 2-20) and they suggested that the permeability is not influenced by the loading path the material has undergone. Nevertheless, this may not hold true for the data obtained from the oedometer test (white circles, purple squares and black crosses in Figure 2-20) as a change in inclination is visible.

The conclusion drawn by [Deng et al. \(2011a\)](#) also contradicts the findings of [Bésuelle et al. \(2013\)](#), according to whom the $\log k - e$ diagram is bilinear and loading history dependent. (Figure 2-21). The data, produced by an isotropic compression test on BC samples for pressure ranging from 1MPa to 32MPa, can be fitted by two lines with different inclinations. It was suggested that the point of change in slope marks the transition from over-consolidation (smaller inclination) to normal consolidation (larger inclination), as observed in a $\log p' - e$ diagram.

[Deng et al. \(2011a\)](#) and [Bésuelle et al. \(2013\)](#) concluded that the hydraulic conductivity

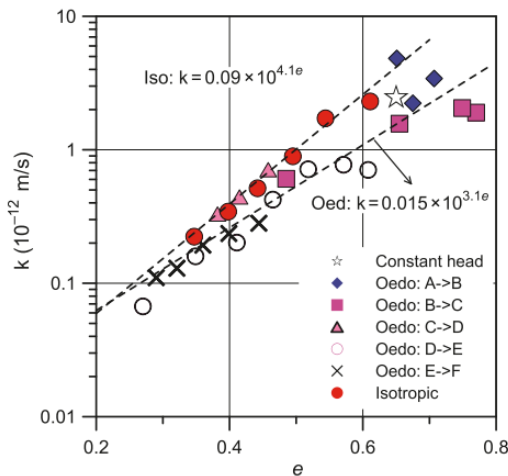


Figure 2-20: Logarithm of permeability ($\log k$) versus void ratio (e) diagram for a BC sample from Essen, derived from 3 different techniques ([Deng et al., 2011a](#)).

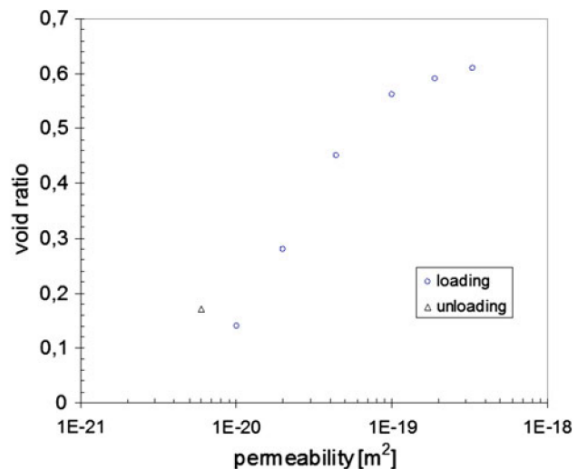


Figure 2-21: Void ratio (e) versus logarithm of permeability ($\log k$) diagram from an isotropic compression test on BC material from Mol ([Bésuelle et al., 2013](#)).

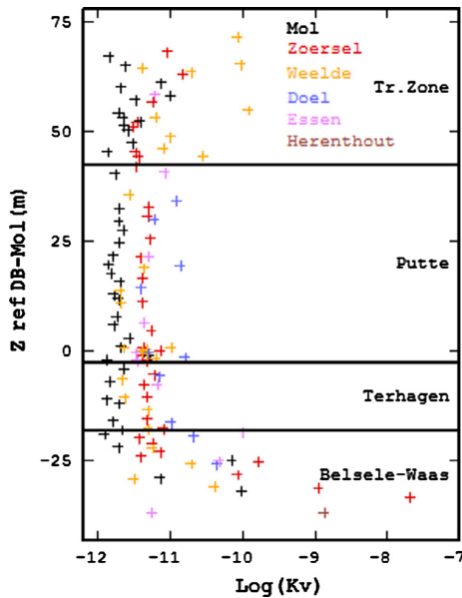


Figure 2-22: Variation of the logarithm of the vertical permeability (k_V , in m/s) in the BC formation, according to depth and location (see Figure 2-1). The reference depth is the level of the HADES URF. Tr.zone refers to the *Boeretang* member (Jeannée et al., 2013).

decreases with increasing p' (indicated by the decreasing void ratio in Figures 2-20 and 2-21). The latter mentioned that k reduces even on unloading (triangle in Figure 2-21), due to the water being adsorbed by the clay particles during swelling of the soil sample.

Measurements performed at the HADES URF, have shown that the permeability of BC is larger in the horizontal than in the vertical direction by approximately a factor of 2, i.e. $k_H \approx 2k_V$ (Bastiaens et al., 2007).

The hydraulic conductivity of BC varies according to the considered stratigraphic unit and location. Figure 2-22 shows the variation in vertical hydraulic conductivity of BC with depth, at 6 locations (shown in Figure 2-1) in Belgium. The hydraulic conductivity is expected to take larger values within the *Boeretang* and the *Belsele-Waas* members, as they contain larger fractions of silt and sand (Section 2-2-2). On the other hand, the permeability is lower in the *Putte* and *Terhagen* member, in which coarse-grained material is less present.

2-4-8 Ranges of geotechnical BC property values

In Table 2-6 ranges of geotechnical BC property values found in the literature are summarised. These values have been acquired through laboratory tests or in-situ measurements at different sites in Belgium and the Netherlands, for a depth ranging from 200m to 560m. The wide parameter ranges may be attributed to the different depths and to the varying geological settings such as different stratigraphic units or mineralogical composition.

Table 2-6: Ranges of values of the geotechnical properties of the BC material, for depth of 200m to 560m (After [Arnold et al., 2014](#)).

Definition	Symbol	Units	Range of values	Source
Strength				
Effective friction angle	φ'	[°]	2.1 – 18.0	2,5,6,7,8,9,10,11, 12,14,15,18
Drained cohesion	c'	[MPa]	0.080 – 1.818	5,6,7,8,9,11,12,15
Undrained cohesion	c_u	[MPa]	0.164 – 1.823	5,6,10,12
Stiffness				
Drained Young's modulus	E'	[MPa]	150 – 500	7,8,11,12,14,18
Undrained Young's modulus	E_u	[MPa]	200 – 400	10
Compression index	C_c	[‐]	0.123 – 0.530	1,15,17,18
Swelling index	C_s	[‐]	0.041 – 0.216	1,15,17,18
Volumetric response				
Drained Poisson's ratio	ν'	[‐]	0.125 – 0.450	2,4,5,7,8,11,14,16
Dilatancy angle	ψ	[°]	0 – 11	8,11,18
Permeability				
Horizontal permeability	k_H	[m/s]	2.00E-12 – 6.22E-10	3,10,12,13
Vertical permeability	k_V	[m/s]	1.00E-12 – 5.43E-10	3,10,12,13
k-anisotropy	-	[‐]	1.04 – 3.51	13

Sources: ¹Horseman et al. (1987), ²Laloui (1993), ³Rijkers et al. (1998), ⁴Romero (1999), ⁵Barnichon et al. (2000), ⁶Wildenborg et al. (2000), ⁷Mertens et al. (2004), ⁸Volckaert et al. (2004), ⁹Coll (2005), ¹⁰Bastiaens et al. (2006), ¹¹Bernier et al. (2007a), ¹²Li et al. (2007), ¹³Labat et al. (2008), ¹⁴François et al. (2009), ¹⁵Deng et al. (2011b), ¹⁶Lima (2011), ¹⁷Yu et al. (2012), ¹⁸Bésuelle et al. (2013)

2-5 Summary

In this chapter the hydro-mechanical response and material properties of Boom Clay was examined. It is noted that only limited information is available, especially from samples obtained at depths appropriate for disposal of radioactive waste. After briefly presenting its geological setting and its physical properties, a discussion on the geotechnical and geomechanical aspects of the soil under consideration was made by utilising the results of triaxial, oedometer and hollow cylinder tests.

First the strength parameters of the soil were considered. The magnitudes of the effective friction angle (φ') and the effective cohesion (c') of the BC material were found to be confining stress dependent in triaxial stress conditions. It was observed that for low levels of confinement the friction angle is large, accompanied with almost zero cohesion. However, when the confining stress increases beyond a certain value, φ' decreases and c' increases. This was illustrated by means of a curved failure envelope in $p' - q$ plane.

Second the evolution of the stiffness, of the mobilised shear strength and the volumetric behaviour of BC in drained triaxial conditions, was examined. It was found that the level of confinement (σ'_3) and the OCR are decisive on the response of the BC, in terms of stiffness, shear strength mobilisation and ductility. An increase in σ'_3 induces stiffer behaviour and larger shear strength of the tested specimens. The ductility of the samples increases with a decrease in OCR, which leads to more plastic volumetric strains and lower or zero dilatancy. On the contrary, an increase in OCR induces the specimens to become more brittle and dilatant. Furthermore, the OC specimens were found to manifest strain softening after the peak deviator stress was reached. A notable non-linearity of the BC was observed for all responses.

Investigation on the effect of the swelling duration before triaxial shearing on the response of BC followed. It was shown that the swelling rate of the tested specimens becomes zero only when the isotropic consolidation stress is equal to the pre-consolidation stress of the material, i.e. when $OCR = 1$. It was demonstrated via triaxial tests results, that the duration of swelling of the soil samples before shearing affected significantly the stiffness and ductility of the material. An increase in the duration of swelling induced softer and more ductile (thus less dilatant) behaviour of the specimens. The latter lead to the conclusion that an increase in the duration of swelling causes the soil to behave as if it were less over-consolidated.

Subsequently, the results of triaxial tests on BC samples from two locations (Mol and Essen) were compared. It was concluded that the non-linearity and the stress dependency of the response of the material was common in both locations. Nevertheless, differences were recognised, in terms of shear strength, stiffness and ductility.

The response of the material in oedometer stress conditions was investigated. It was observed that the soil exhibits substantial hysteresis loops when subjected to unloading-reloading paths. This was attributed to the strong swelling potential of the BC, as evident by the large values of the swelling index (C_s). Finally, it was noted that the yield stress (σ'_y) estimated from the oedometer test results should not be used for determining the OCR, as is usually the case, since it was found to be much lower than the in-situ stress, probably owing to swelling-induced destructuration. Instead, the vertical pre-consolidation stress (σ'_c) ought to be used.

The anisotropic behaviour of BC was inquired, by reviewing results of triaxial and hollow

cylinder tests. The former showed that the intrinsic anisotropy of the material is evident by a yield locus inclined towards the K_0 -line in $p' - q$ plane. However, increasing confining stress causes rotation of the yield surface (and therefore plastic anisotropy) towards the hydrostatic axis and the anisotropy diminishes. The results of hollow cylinder tests showed the dependency of the BC response on the direction at which the samples were cored with respect to the bedding plane. If the longitudinal axis of the specimen is parallel or at small angles with respect to the bedding, the convergence around the central hole of the sample is larger along this plane. On the contrary, the displacements perpendicular to the bedding are smaller. Other sources of anisotropic behaviour may be the initial stress field, the anisotropic permeability as well as the elastic cross-anisotropy, which is common for natural clays, as is the BC.

Finally the hydraulic conductivity (k) of the BC material was discussed. First an equation found in the literature was cited, which described the relationship of k with the void ratio (e). It was concluded that they are positively related. Thus, a decrease in the void ratio due to an increase in the mean effective stress leads to a drop in the value of the hydraulic conductivity. The horizontal permeability was reported to be larger than the vertical by a factor of 2, at the HADES URF. The variability of its values by stratigraphic unit and location was finally presented.

The range of values of the geotechnical properties of the BC formation were listed. Large ranges were observed, which are mainly attributed to varying depth and different geology-related attributes of the material among sites such as mineralogy.

Chapter 3

Validation of soil models for Boom Clay

3-1 Introduction

For the simulation of the tunnel excavation in the Boom Clay formation, a soil model capable of capturing the response of the material sufficiently needs to be selected. A constitutive soil model may be considered sufficient insomuch as it is able to capture adequately the most important aspects of the BC behaviour such as the dependency of the material stiffness and mobilised shear strength on the stress level (see Section 2-4-2). However, the level of complexity of the soil model needs to be acceptable both in terms of the required number of the model input parameters as well as with respect to the cost and easiness of determining them in laboratory or in-situ.

For these reasons, the response of four soil models has been evaluated by numerically simulating three drained triaxial tests and one high pressure oedometer test, performed by [Deng et al. \(2011b\)](#) on BC samples originating from Essen. These simulations have been conducted in the *lab test facility* of the *PLAXIS 2D 2011* finite element program ([Plaxis, 2011b](#)). The investigated soil models were the Linear Elastic Perfectly Plastic-Mohr Coulomb (LEPP-MC) model, the Modified Cam-Clay (MCC) model, the Soft Soil-Creep (SS-C) model and the Hardening Soil (HS) model all for which the formulation is readily available in [Plaxis \(2011a\)](#). The values of selected input parameters, of the soil model which was considered to perform the best, were varied individually in order to investigate their influence on the numerical results of the triaxial tests simulations. This aims to provide the reader with a better understanding on the response of the selected constitutive model.

A short description of the evaluated soil models is given in Section 3-2. In Section 3-3, a description of the set up of the triaxial and the oedometer tests in the lab test facility of *PLAXIS* is given. Subsequently, the capabilities and limitations of each soil model are analysed. The section concludes with the selection of the HS model, which is considered to capture the BC response the best. A detailed description of the HS soil model, with

consideration of its governing equations and its representation in stress-strain space is provided in Section 3-4. Discussion on the influence of the advanced input parameters of the HS model on the results of the triaxial tests simulations is made in Section 3-5. In Section 3-6 a brief discussion on the limitations of the laboratory tests and of the numerical tool used, with respect to the conditions expected during a tunnel excavation, is made. The chapter is concluded with a summary in Section 3-7.

3-2 Brief description of the evaluated soil models

In this section the main aspects and the most usual applications of the evaluated soil models are briefly discussed, that is, without considering their governing equations and their representation in stress-strain space. Further information on these models can be found in [Plaxis \(2011a\)](#).

The LEPP-MC model

In the LEPP-MC model failure is characterised by the Mohr-Coulomb (MC) criterion. The model response is linear elastic perfectly plastic, i.e. no elastic strains are generated after yield. This model is considered to predict well the failure of soils ([Brinkgreve, 2011](#)). It may be used in those failure problems, in which the previous strains are of limited relevance and/or when unloading-reloading is not expected.

The MCC model

The MCC model was developed by [Roscoe and Burland \(1968\)](#) in the framework of critical state soil mechanics. Its formulation is based on a logarithmic stress-strain relationship in isotropic loading and unloading. The model is characterised by stress-dependency of stiffness (linear relationship with stress) and by the generation of elasto-plastic strains after yield. The evolution of the plastic strains is predicted with the use of a yield locus which forms an ellipse in the $p' - q$ plane. The MCC model is deemed to perform best for NC clays and soft soils ([Brinkgreve, 2011](#)).

The SS-C model

The SS-C model was developed by [Vermeer and Neher \(1999\)](#) in order to account for the time-dependent behaviour of soft soils with low OCR, and is based on a logarithmic creep law for 1-dimensional loading. The main aspects of the model response are the stress-dependency of stiffness (linear relationship with stress), the development of creep strains with the use of two MCC-type yield surfaces and the use of the MC criterion for predicting the material failure and the evolution of perfectly plastic strains. According to [Vermeer and Neher \(1999\)](#), the SS-C model is suitable for predicting the settlement of soft soils due to secondary compression as well as for predicting their creep behaviour when present in slopes.

The HS model

The HS model was formulated by [Schanz et al. \(1999\)](#) and it is based on the hyperbolic stress-strain relationship for drained triaxial conditions proposed by [Duncan and Chang \(1970\)](#). It is mainly characterised by a non-linear stress-dependency of stiffness. The model comprises two yield surfaces for predicting the development of plastic strains in compressive and deviatoric stress paths. The MC criterion is used to define failure. The HS model is considered suitable

for geotechnical engineering applications, where unloading accompanied with shearing occurs such as in tunnelling or deep excavation projects ([Brinkgreve, 2011](#)).

3-3 Evaluation of soil models with the lab test facility of *PLAXIS*

In this section the four soil models are evaluated regarding their ability to capture the BC response by numerically simulating three triaxial tests and one oedometer test performed by [Deng et al. \(2011b\)](#). First, the set up of the laboratory tests simulations is described. The assessment of the performance of the models follows. Finally, the selection of the HS model, which is deemed to reproduce the BC material behaviour the best, is explained.

3-3-1 Set up of the laboratory tests simulations

The laboratory tests used for the simulations were performed by [Deng et al. \(2011b\)](#) on intact BC samples taken from cores originating from Essen. A detailed description of the triaxial tests and the oedometer test specifications was given in Sections 2-4-2-2 and 2-4-5-1, respectively. The results of the triaxial tests were presented by means of a $\varepsilon_a - q$ plot (Figure 2-6b) and a $\varepsilon_a - \varepsilon_v$ plot (Figure 2-6d). The outcomes of the high pressure oedometer test were illustrated by $\sigma'_v - e$ and time – displacement diagrams in Figures 2-11 and 2-12b, respectively. These four plots have been digitised in order to obtain the input data required for setting up the numerical simulations in the lab test facility of *PLAXIS* as well as to serve as a basis for comparison with the later numerical results (see Sections 3-3-3 to 3-3-6). It is noted that in the performed simulations one soil element is considered, i.e. no mesh is generated. Further information on the lab test facility of *PLAXIS* can be found in [Plaxis \(2011b\)](#).

Set up of the triaxial tests

Figure 3-1 shows the set up of the *Ess75Tr01* triaxial test in the interface of the lab test facility of *PLAXIS*. For all cases the test type was set to drained conditions, the direction

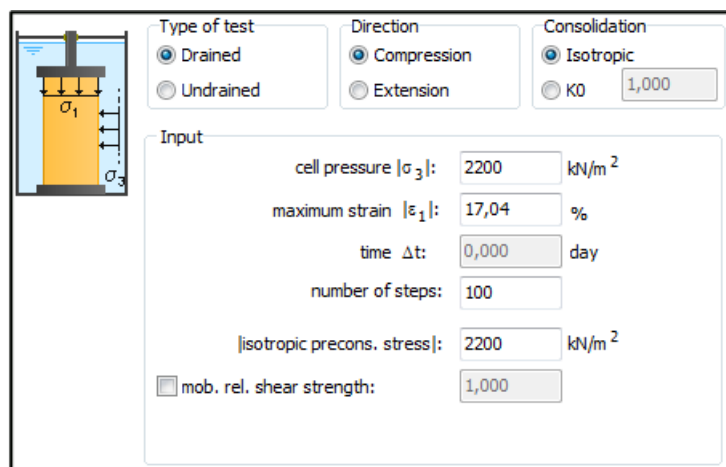


Figure 3-1: Example of input in the lab test facility of *PLAXIS* for the set up of the simulation of the triaxial test *Ess75Tr01* performed by [Deng et al. \(2011b\)](#).

Table 3-1: Set up of the drained triaxial tests performed by [Deng et al. \(2011b\)](#) for the simulations with the lab test facility of *PLAXIS*.

Test ID	Cell pressure $ \sigma_3 $ [kPa]	Isotropic consolidation stress p_c [kPa]	Maximum axial strain $ \varepsilon_1 $ [%]
<i>Ess75Tr01</i>	2200	2200/2400(for SS-C)	17.04
<i>Ess75Tr02</i>	1000	2200	18.87
<i>Ess75Tr03</i>	500	2200	18.48

of loading to compression and the type of consolidation to isotropic. The elapsed time was introduced only for the case of the SS-C model as it is the only model which accounts for time-dependency. The level of mobilised relative shear strength (mob. rel. shear strength in Figure 3-1), which was entered for the simulations with the HS model, was set to 0 (see later Section 3-4-6-1). The isotropic consolidation stress before shearing, the (constant) cell pressure during shearing and the maximum axial strains reached at the completion of tests *Ess75Tr01*, *Ess75Tr02* and *Ess75Tr03* are presented in Table 3-1. It should be noted that a value for the p'_c could be introduced for the analyses with the LEPP-MC model. Moreover, the p'_c in the case of the simulation of the *Ess75Tr01* test with the SS-C model was set to 2.4MPa ($\text{OCR} \approx 1.1$) in order to prevent the model from predicting excessive creep volumetric strains ([Brinkgreve, 2011](#)).

Set up of the oedometer test

In Figure 3-2 a part of the set up of the *Ess75Oedo1* high pressure oedometer test in the lab test facility of *PLAXIS* is shown. The total number of phases introduced is 65. The duration of the phases, which was determined by digitising the σ'_v – elapsed time plot (Figure 2-12a), is relevant only for the simulations with the SS-C model. The configuration was kept constant for the analyses with all other models, although they do not include time-dependency, in

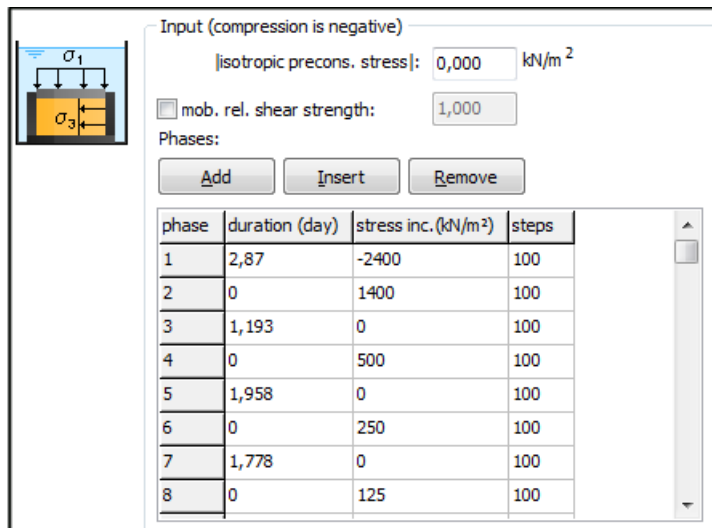


Figure 3-2: Input in the lab test facility of *PLAXIS* for the set up of the simulation of the oedometer test *Ess75Oedo1* performed by [Deng et al. \(2011b\)](#).

order to retain the comparability between the results obtained by Deng et al. (2011b) and the numerical response in terms of the resulting displacements (Figure 2-12b). Furthermore, the isotropic pre-consolidation stress was set to 0kPa since the first loading step (phase 1 in Figure 3-2), which was set to $\sigma'_{v0} = 2400\text{kPa}$ (point A in Figure 2-11), was considered to account for the initial stress conditions and, therefore, the initial position of the yield surfaces of the MCC, the SS-C and the HS model. The resulting void ratio induced by this first step was not taken into account. Instead, an initial void ratio of $e = 0.7$ (point A in Figure 2-11) was considered.

3-3-2 Comments on the numerical simulations and the produced results

The calibration of the models was such that the best fit was obtained for all simulated tests with the same set of the model input parameters.

For the LEPP-MC, SS-C and HS model, all which include the MC failure criterion, a friction angle $\varphi' = 12.4^\circ$ and a cohesion $c' = 110\text{kPa}$, which were determined by Deng et al. (2011b), were used for the analyses. A dilatancy angle $\psi = 2^\circ$, which was estimated from the $\varepsilon_a - \varepsilon_v$ diagram (see Section 2-4-2-3 and Figure 2-6d), was introduced for the simulation of the *Ess75Tr03* test, while it was kept equal to $\psi = 0^\circ$ for all other tests.

The results of the triaxial tests simulations and the outcomes of Deng et al. (2011b) are compared for all models. For each of the *Ess75Tr01*, *Ess75Tr02* and *Ess75Tr03* tests, Figures 3-3 to 3-8 show the $\varepsilon_a - q$ and the $\varepsilon_a - \varepsilon_v$ diagrams. The resulting $\sigma'_v - e$ and time – displacement graphs of the *Ess75Oedo1* test are illustrated separately for every model, in Figures 3-9 to 3-14, for reasons of clarity.

3-3-3 Evaluation of the response of the LEPP-MC model

The MC failure criterion captures the value of q at the completion of the *Ess75Tr01* test with very high accuracy (Figure 3-3). It also reproduces the peak deviator stress (q_p) in tests *Ess75Tr02* (Figure 3-5) and *Ess75Tr03* (Figure 3-7) fairly well. The model accounts for the stress dependency of the peak shear strength of the material, as it decreases for a decrease in the value of the cell pressure ($q_p = 1.48\text{MPa}$ for $\sigma'_3 = 2.2\text{MPa}$, $q_p = 0.82\text{MPa}$ for $\sigma'_3 = 1.0\text{MPa}$ and $q_p = 0.55\text{MPa}$ for $\sigma'_3 = 0.5\text{MPa}$).

However, the LEPP-MC model cannot capture the dependency of the mobilised shear strength and stiffness of the BC material on the confining pressure and the value of the OCR (see Section 2-4-2). The non-linear response of the soil is not reproduced, as the model does not predict elastoplastic strains after yield.

Furthermore, whereas the ε_v at the end of test *Ess75Tr01* are captured with a good accuracy (Figure 3-4), this does not hold true for the other tests (Figures 3-6 and 3-8). The results of the simulation of the *Ess75Oedo1* test are not presented since the calibration of the LEPP-MC model with respect to this type of test had not been possible.

The best fit to the triaxial tests results was obtained with a value of $E' = 40\text{MPa}$ and a value of $\nu' = 0.25$. The values of φ' and c' have been kept constant to the ones obtained by Deng et al. (2011b) (Section 3-3-2).

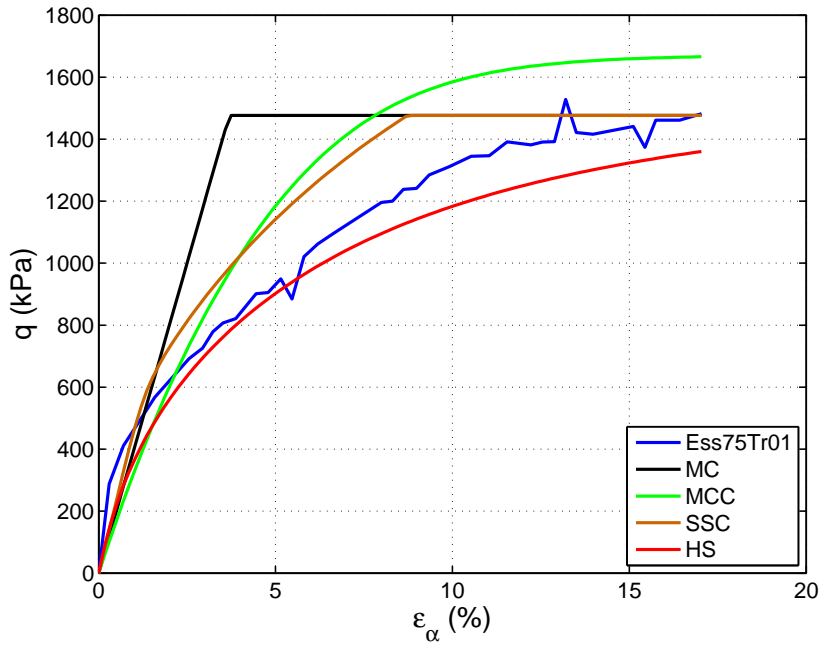


Figure 3-3: Deviator stress (q) versus axial strain (ε_a) for the numerical simulations of the *Ess75Tr01* test with four soil models. The triaxial data (blue curve) have been digitised from [Deng et al. \(2011b\)](#).

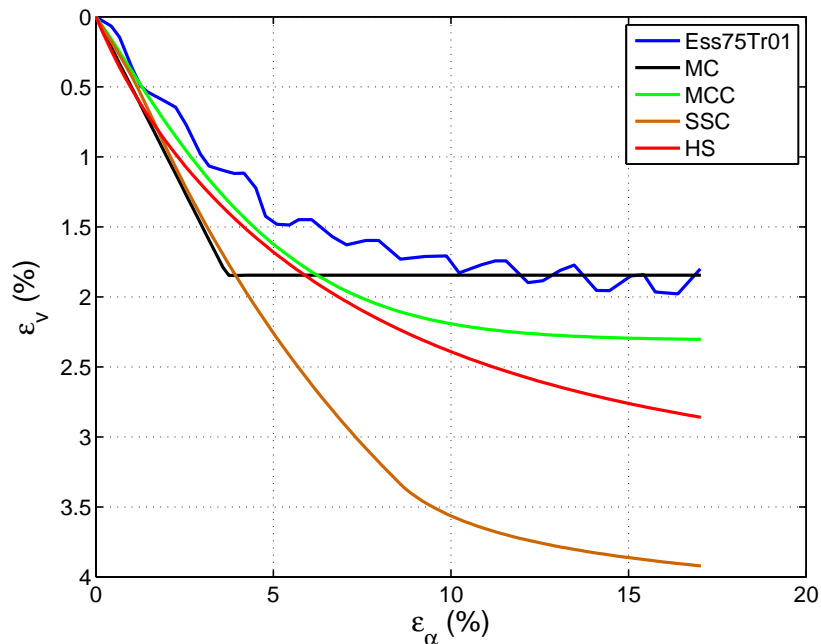


Figure 3-4: Volumetric strains (ε_v) versus axial strain (ε_a) for the numerical simulations of the *Ess75Tr01* test with four soil models. The triaxial data (blue curve) have been digitised from [Deng et al. \(2011b\)](#).

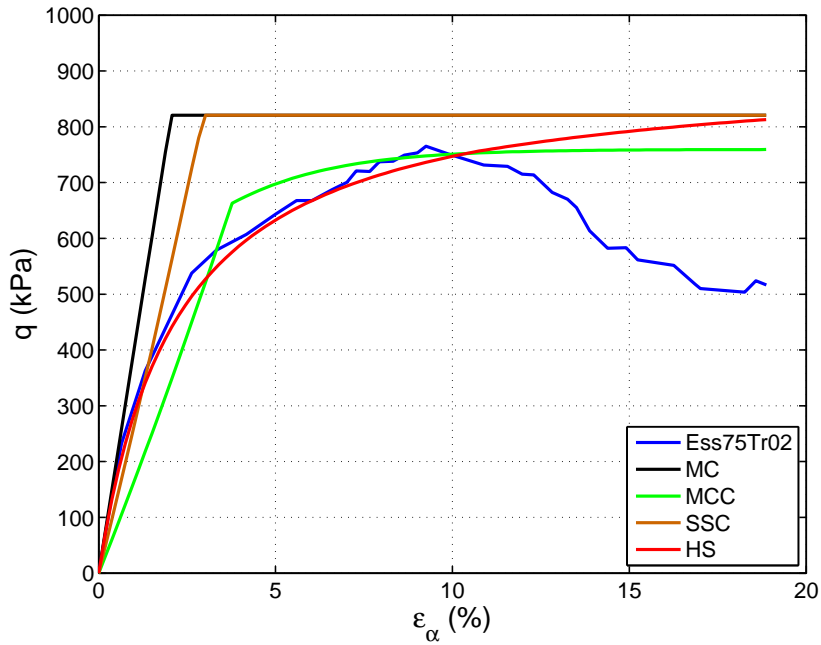


Figure 3-5: Deviator stress (q) versus axial strain (ε_a) for the numerical simulations of the *Ess75Tr02* test with four soil models. The triaxial data (blue curve) has been digitised from [Deng et al. \(2011b\)](#).

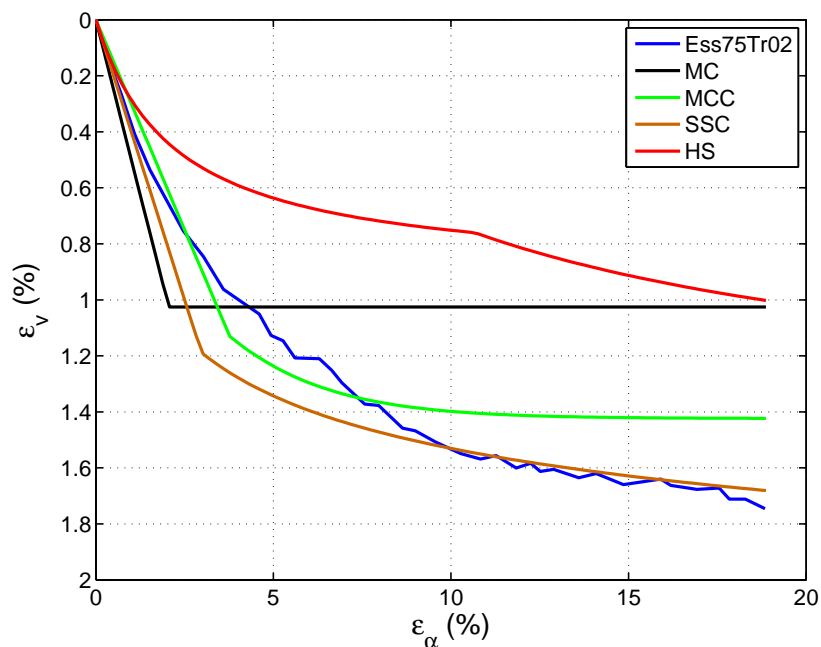


Figure 3-6: Volumetric strains (ε_v) versus axial strain (ε_a) for the numerical simulations of the *Ess75Tr02* test with four soil models. The triaxial data (blue curve) have been digitised from [Deng et al. \(2011b\)](#).

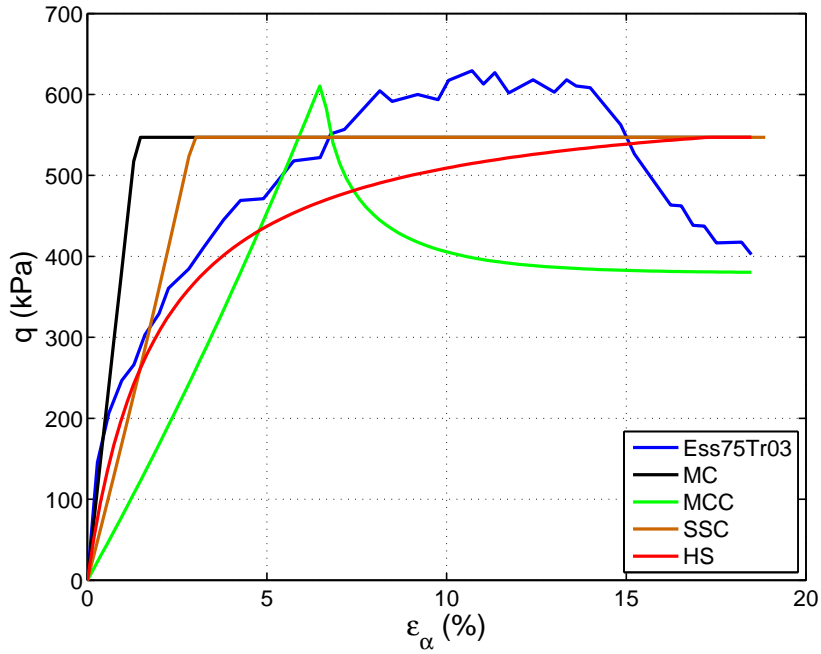


Figure 3-7: Deviator stress (q) versus axial strain (ε_a) for the numerical simulations of the *Ess75Tr03* test with four soil models. The triaxial data (blue curve) have been digitised from [Deng et al. \(2011b\)](#).

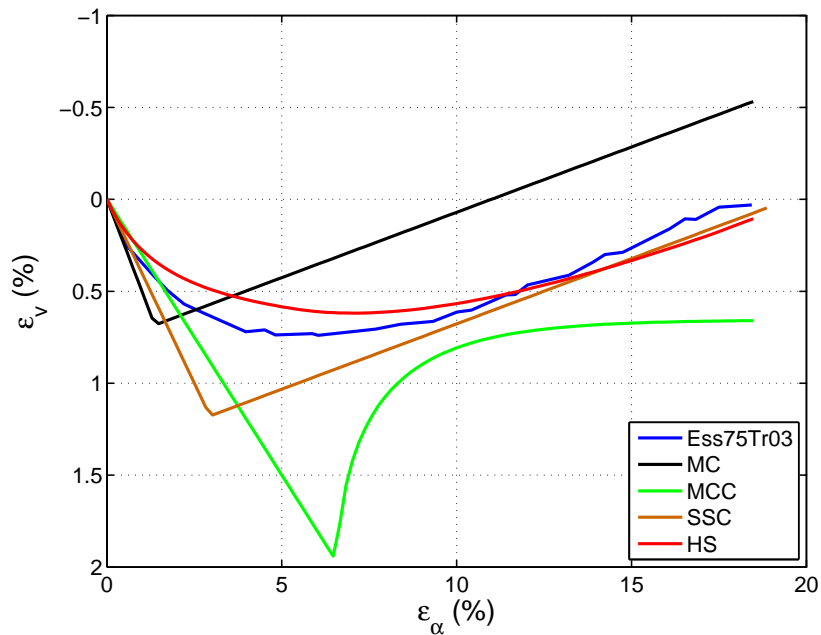


Figure 3-8: Volumetric strains (ε_v) versus axial strain (ε_a) for the numerical simulations of the *Ess75Tr03* test with four soil models. The triaxial data (blue curve) have been digitised from [Deng et al. \(2011b\)](#).

3-3-4 Evaluation of the response of the MCC model

The MCC model is capable of capturing the non-linear response of the soil in the *Ess75Tr01* test (Figure 3-3), with the BC being NC. Even though the stiffness and mobilised shear strength of the material are initially underestimated and later overestimated by the MCC model, the shape of the $\varepsilon_a - q$ curve is similar to that of the real test. Furthermore, a slight overestimation of ε_v can be observed in the $\varepsilon_a - \varepsilon_v$ plot (Figure 3-4).

For the *Ess75Tr02* test ($OCR = 2.2$), the evolution of the mobilised shear strength and stiffness of the soil is not reproduced well before yield in either the $\varepsilon_a - q$ space (Figure 3-5) or the $\varepsilon_a - \varepsilon_v$ space (Figure 3-6). On the other hand, strain hardening develops after yield and the peak strength of the sample is predicted accurately. Moreover, the evolution of volumetric strains is fairly well captured, as in the case of the *Ess75Tr01* test.

In the case of the *Ess75Tr03* test ($OCR = 4.4$) the material non-linearity is not captured well before yield (Figures 3-7 and 3-8). The inclination of the $\varepsilon_a - q$ curve ($\delta q / \delta \varepsilon_a \approx 9.25 \text{ MPa}$ in Figure 3-7) has decreased with respect to the *Ess75Tr02* test ($\delta q / \delta \varepsilon_a \approx 17.43 \text{ MPa}$, see Figure 3-5), which indicates the dependency of the stiffness on the level of confinement ($\sigma'_3 = 1.0 \text{ MPa}$ for the *Ess75Tr02* test and $\sigma'_3 = 0.5 \text{ MPa}$ for the *Ess75Tr03* test). The value of the peak strength is very similar to that of the real test however, it is exhibited at much smaller ε_a and therefore the predicted soil stiffness is very low. Strain softening occurs after yield, an aspect of the BC which is accounted for, qualitatively, only by the MCC model. The response in the $\varepsilon_a - \varepsilon_v$ diagram (Figure 3-8) is not well reproduced.

The response of the MCC model for the *Ess75Oedo1* test, in terms of $\sigma'_v - e$ and time – displacement plots is shown in Figures 3-9 and 3-10. The inclination of the virgin compression line is very similar to that of the real data (Figure 3-9). The same holds true for the void ratio and the displacements (Figures 3-9 and 3-10, respectively) at the points C, D and E. Nevertheless, the model predicts very strong swelling during the first unloading path (A–B). Also, the significant hysteresis of the BC material during the unloading-reloading loops (Section 2-4-5-2) is not captured (Figure 3-9).

The best fit for the MCC model was obtained for a slope of the normal compression line $\lambda = 0.12$, a slope of the un-/reloading line $\kappa = 0.10$, a slope of the critical state line $M = 0.606$ and an unloading-reloading Poisson's ratio $\nu_{ur} = 0.35$.

3-3-5 Evaluation of the response of the SS-C model

The SS-C model predicts initially a softer and afterwards a stiffer response of the material in the $\varepsilon_a - q$ diagram for the *Ess75Tr01* test (Figure 3-3). The non-linear response of the soil is reproduced however, failure of the material is reached at a lower level of ε_a . Severe divergence from the results obtained by [Deng et al. \(2011b\)](#) is observed in the $\varepsilon_a - \varepsilon_v$ plot (Figure 3-4), even though an $OCR \approx 1.1$ (larger than $OCR = 1.0$, which is the case for the *Ess75Tr01* test) has been used (see Section 3-3-1). This may attributed to the prediction of large initial creep strain rates by the SS-C model for near-NC soils ([Brinkgreve, 2011](#)).

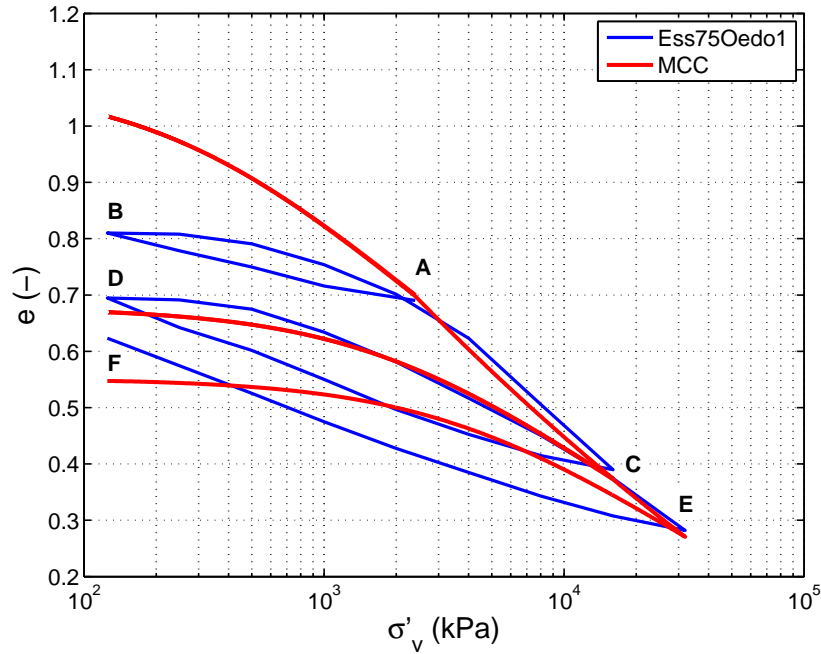


Figure 3-9: Void ratio (e) versus vertical effective stress (σ'_v) for the numerical simulation of the *Ess75Oedo1* test with the MCC model. The oedometer test results (blue curve) have been digitised from [Deng et al. \(2011b\)](#).

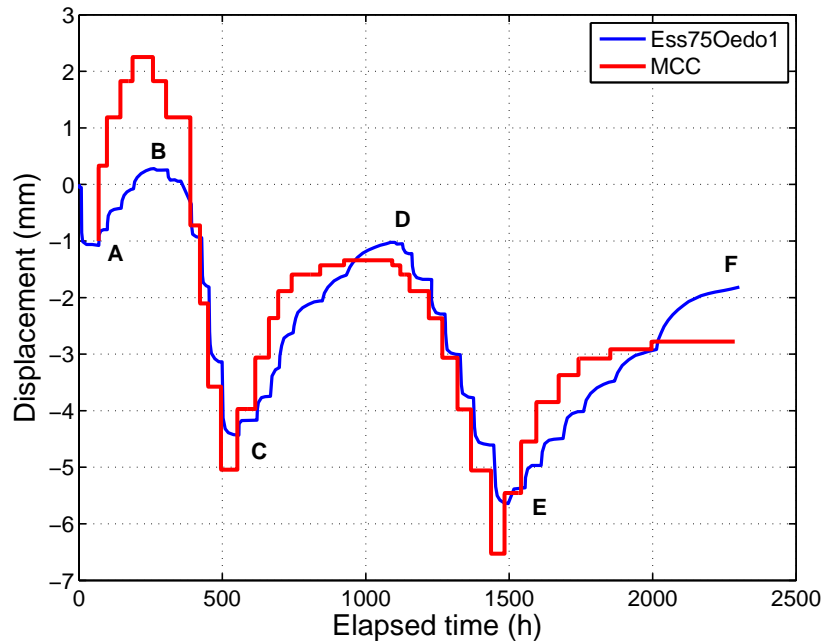


Figure 3-10: Displacement versus elapsed time for the numerical simulation of the *Ess75Oedo1* test with the MCC model. The oedometer test results (blue curve) have been digitised from [Deng et al. \(2011b\)](#). It is noted that, although the MCC model does not account for the time dependent response of the material, this figure is utilised for the comparison of the actual displacements with the ones that are numerically predicted.

For the *Ess75Tr02* test ($\text{OCR} = 2.2$) and the *Ess75Tr03* test ($\text{OCR} = 4.4$), the response of the model is similar to that of a LEPP model, especially in terms of the $\varepsilon_a - q$ plots (Figures 3-5 and 3-7). The stiffness in the elastic domain is confining stress-dependent as it decreases for a decrease in σ'_3 ($\delta q/\delta\varepsilon_a \approx 27.70\text{MPa}$ for test *Ess75Tr02* and $\delta q/\delta\varepsilon_a \approx 18.60\text{MPa}$ for test *Ess75Tr03*). The volumetric response is well simulated for $\text{OCR} = 2.2$ (Figure 3-6) and $\text{OCR} = 4.4$ (Figure 3-8) after q_p is exhibited (Figures 3-5 and 3-7, respectively).

The performance of the SS-C model for the simulation of the *Ess75Oedo1* test is considered to be very good. The resulting $\sigma'_v - e$ graph (Figure 3-11) and elapsed time – displacement plot (Figure 3-12) are very similar to the test results obtained by Deng et al. (2011b). In addition, the hysteresis is predicted well, especially for the second unloading-reloading loop (path C–D, Figure 3-11). The change in slope of the unloading and reloading branches (Section 2-4-5-2) is also predicted. The time effect, which can be identified by the curvature of the elapsed time – displacement graph for the reloading paths B–C and D–E in Figure 3-12, is predicted by the model. This is not the case, however, for the unloading paths, where the time-dependency has not been captured. This is due to the generation of purely elastic strains on unloading, in addition to the stress path not reaching the yield locus of the SS-C model.

The best fit for the SS-C model was achieved with a modified compression index $\lambda^* = 0.12$, a modified swelling index $\kappa^* = 0.07$, a modified creep index $\mu^* = 0.00172$, a $\nu_{ur} = 0.30$, a K_0 -value for normal consolidation $K_0^{NC} = 0.7853$ and a K_0^{NC} -related parameter $M = 0.6595$.

3-3-6 Evaluation of the response of the HS model

The HS model seems to perform well for all analyses, in the deviatoric response ($\varepsilon_a - q$ plots, Figures 3-3, 3-5 and 3-7). The process of strain hardening of the BC samples is very well reproduced for all triaxial tests, although the predicted stiffness is somewhat lower than that of the soil specimens for the *Ess75Tr01* and *Ess75Tr03* tests. It can be concluded that the performance of the model is good for OC conditions, especially at low ranges of ε_a , which is not observed for the other evaluated models. However, the strain softening response of the material is not predicted.

The volumetric behaviour of the BC is fairly well captured for the simulation of the *Ess75Tr01* test (Figure 3-4) and very well reproduced for the *Ess75Tr03* test (Figure 3-8). Nevertheless, the model response is much different from the soil behaviour for the *Ess75Tr02* test where $\text{OCR} = 2.2$ (Figure 3-6).

The BC response in oedometer stress conditions is well reproduced by the HS model. The slope of the virgin compression line and the values of the void ratio at the end of the unloading and reloading paths predicted by the model are similar to those of the tested samples (Figure 3-13). Furthermore, the hysteresis exhibited by the specimen is captured qualitatively. The change in slope of the unloading and reloading branches is fairly well simulated. The produced displacements are similar to the ones of the soil sample, except for point E (Figure 3-14).

The best fit for the HS model was obtained for a reference secant modulus $E_{50}^{ref} = 8.53\text{MPa}$, a reference un-/reloading modulus $E_{ur}^{ref} = 20.94\text{MPa}$, a reference oedometer modulus $E_{oed}^{ref} = 11.00\text{MPa}$ at a reference stress of $p^{ref} = 0.10\text{MPa}$, a rate of stress dependency of stiffness $m = 0.7$ and a $\nu_{ur} = 0.30$.

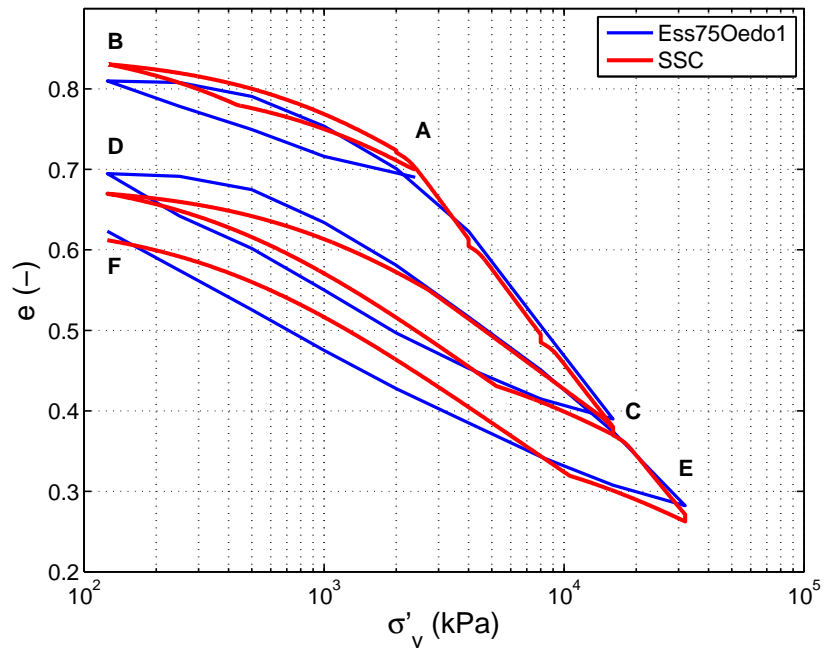


Figure 3-11: Void ratio (e) versus vertical effective stress (σ'_v) for the numerical simulation of the *Ess75Oedo1* test with the SS-C model. The oedometer test results (blue curve) have been digitised from [Deng et al. \(2011b\)](#).

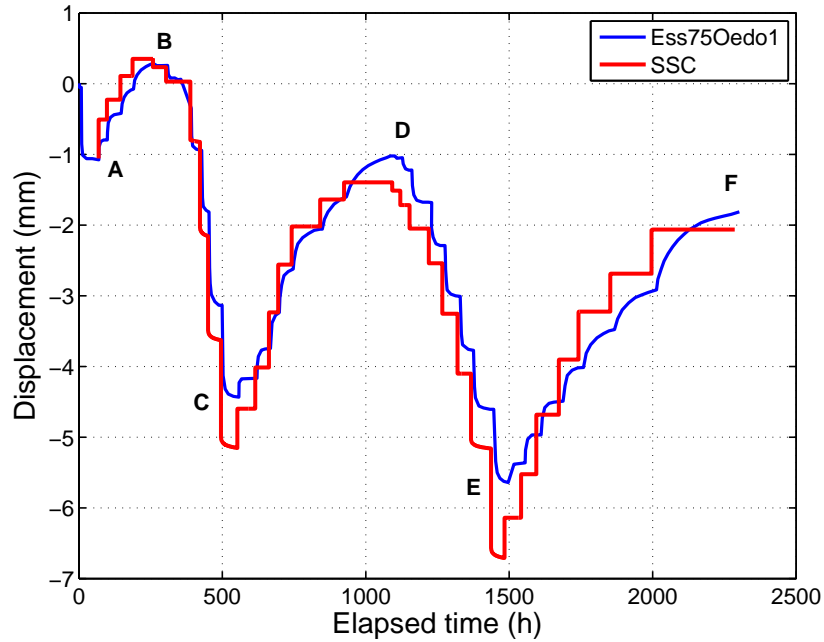


Figure 3-12: Displacement versus elapsed time for the numerical simulation of the *Ess75Oedo1* test with the SS-C model. The oedometer test results (blue curve) have been digitised from [Deng et al. \(2011b\)](#).

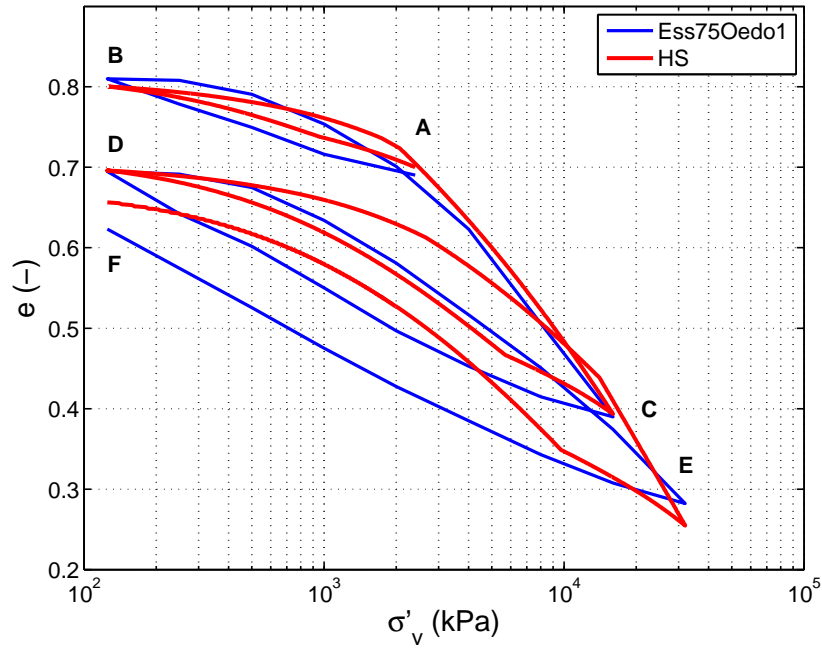


Figure 3-13: Void ratio (e) versus vertical effective stress (σ'_v) for the numerical simulation of the *Ess75Oedo1* test with the HS model. The oedometer test results (blue curve) have been digitised from [Deng et al. \(2011b\)](#).

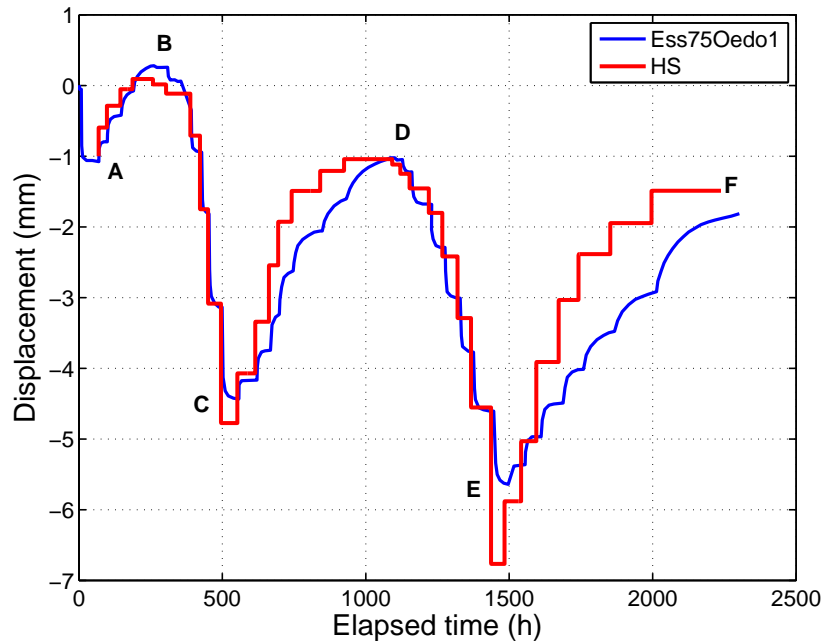


Figure 3-14: Displacement versus elapsed time for the numerical simulation of the *Ess75Oedo1* test with the HS model. The oedometer test results (blue curve) have been digitised from [Deng et al. \(2011b\)](#). It is noted that, although the HS model does not account for the time dependent response of the material, this figure is utilised for comparing the actual displacements with the ones that are numerically predicted.

3-3-7 Selection of the model that captures the BC response the best

The LEPP-MC model captures the failure of BC fairly well. However, the strain hardening process observed in the results of the triaxial tests is not reproduced. Moreover, the model does not hold any memory of the pre-consolidation of the material. On the other hand, the performance of the LEPP-MC model in triaxial stress conditions seems to be reasonable to some extent (provided that un-/reloading does not occur), despite being the simplest among the investigated models and in spite of the small number of the required input parameters. Calibration of the model for the oedometer test was not possible due to its inability to capture the material response in un-/reloading paths.

The MCC model performs well in drained triaxial compression for NC conditions. It also holds memory of the pre-consolidation of the soil. Moreover, it is the only model that accounts for strain softening (qualitatively) for the case where $\text{OCR} = 4.4$. However, the model does not capture well the BC response for $\text{OCR} = 2.2$ and $\text{OCR} = 4.4$ in the $\varepsilon_a - q$ space. The model prediction for the simulation of the oedometer test might be considered adequate as far as the evolution of the void ratio with respect to the vertical effective stress on the reloading paths is concerned.

The SS-C model does not show very good performance with regards to the $\varepsilon_a - q$ plots in simulating the triaxial tests. Also, the predicted volumetric strains are very high for the near-NC case with $\text{OCR} \approx 1.1$. On the other hand, the volumetric response of the BC is well simulated for OCR equal to 2.2 and 4.4. Moreover, the best fit, among the tested models, is obtained for the behaviour of the soil in 1-dimensional loading. The SS-C is the only model that accounts for the viscous (time-dependent) response of BC.

The HS model is considered to have performed the best for the simulations of the triaxial tests, that is, with respect of computing the mobilised shear strength, the change in stiffness and the non-linearity of BC. These aspects of the soil response are well predicted for both NC and OC conditions. The performance of the model is also deemed to be very good for the simulation of the oedometer test. However, the volumetric response of the soil is not well predicted for the *Ess75Tr02* test with an intermediate $\text{OCR} = 2.2$. The HS model does not as well account for strain softening.

Even though the SS-C model captured very well the response of BC in oedometer loading, in addition to being the only model that accounts for the material time-dependency, its performance in shearing, which is expected to be a dominant process in tunnelling conditions, is considered to be not sufficient to outperform the HS model.

Based on the aforementioned, it seems that the overall performance of the HS model is better than that of the other three tested models, as it captures sufficiently most aspects of the BC response under drained triaxial compression and 1-dimensional loading. It is noted that from all simulated tests the oedometer test is the only that includes also unloading, which might be of interest for the simulation of a tunnel excavation.

In Section 3-4 a detailed description of the HS model is given in order to provide the reader with the information required to gaining a more critical view on the results of varying the model input parameters (Section 3-5) as well as the later finite element calculations (Chapter 4).

A summary of the values of the input parameters of the evaluated soil models, which gave the best fit with the test data, is shown in Table 3-2.

Table 3-2: Values of the input parameters of the assessed soil models that gave the best fit with the test data.

Model	Definition	Symbol	Unit	Value
LEPP-MC	Drained Young's modulus	E'	[MPa]	40.0
	Poisson's ratio	ν	[\cdot]	0.25
MCC	Swelling index	κ	[\cdot]	0.10
	Compression index	λ	[\cdot]	0.12
	Slope of the critical state line	M	[\cdot]	0.606
	Un-/reloading Poisson's ratio	ν_{ur}	[\cdot]	0.35
SS-C	Modified swelling index	κ^*	[\cdot]	0.07
	Modified compression index	λ^*	[\cdot]	0.12
	Modified creep index	μ^*	[\cdot]	0.00172
	Un-/reloading Poisson's ratio	ν_{ur}	[\cdot]	0.30
	K_0 -value for normal consolidation	K_0^{NC}	[\cdot]	0.7853
	K_0^{NC} -related parameter	M	[\cdot]	0.6595
HS	Reference secant modulus	E_{50}^{ref}	[MPa]	8.53
	Reference oedometer modulus	E_{oed}^{ref}	[MPa]	11.00
	Reference un-/reloading modulus	E_{ur}^{ref}	[MPa]	20.94
	Rate of stress dependency of stiffness	m	[\cdot]	0.70
	Un-/reloading Poisson's ratio	ν_{ur}	[\cdot]	0.30
	Reference stress for stiffness	p^{ref}	[MPa]	0.10
	Effective friction angle ^(a)	φ'	[$^\circ$]	12.4
	Effective cohesion ^(a)	c'	[MPa]	0.11
	Dilatancy angle ^(a)	ψ	[$^\circ$]	0 ^(b) / 2 ^(c)

^(a)Common for the LEPP-MC model, the SS-C model and the HS model.

^(b)Used for the *Ess75Tr01* test, the *Ess75Tr02* test and the *Ess75Oedo1* test.

^(c)Used for the *Ess75Tr03* test.

3-4 The Hardening Soil model

The Hardening Soil (HS) model is an advanced constitutive soil model formulated by [Schanz et al. \(1999\)](#), appropriate to simulate the response of both cohesive (soft or stiff) and non-cohesive soils. In this section the general features of the model are given at first. Then, the governing equations and its representation in stress-strain space are summarised. Finally, important specifications of the model, in conjunction with its use in the *PLAXIS* finite element program, are described. For further information on the HS model, the reader is referred to [Schanz et al. \(1999\)](#), [Benz \(2006\)](#) and [Plaxis \(2011a\)](#).

3-4-1 General description

Some of the most important features of the HS model are the introduction of stress-dependent stiffness evolution equations, for both loading and un-/reloading, and the use of two yield surfaces for predicting the development of plastic strains upon primary compression and shearing.

The HS model comprises an isotropic, compression hardening cap yield surface, a shear hardening yield surface and the MC failure criterion. The cap yield concerns the better prediction of the evolution of plastic strains for radial stress paths and the shear yield is responsible for the evolution of plastic strains due to deviatoric stress paths. The MC criterion forms the limiting boundary (failure) as a function of the shear strength of the material.

It should be noted that the formulas presented in this section refer to triaxial stress conditions.

3-4-2 Yield function for shear hardening

The formulation of the yield function of the HS model for shear hardening is based on the hyperbolic stress-strain relationship for a standard drained triaxial test, originally developed by [Kondner \(1963\)](#) and adapted by [Duncan and Chang \(1970\)](#), in the context of elasticity. This formulation was extended to the elasto-plastic framework by [Schanz \(1998\)](#) and the shear yield function is given by:

$$f^s = \bar{f} - \gamma^p \quad (3-1)$$

where γ^p is a strain hardening parameter, and

$$\bar{f} = \frac{2}{E_i} \frac{q}{1 - q/q_a} - \frac{2q}{E_{ur}} \quad \text{and} \quad \gamma^p = 2\varepsilon_1^p - \varepsilon_v^p \approx 2\varepsilon_1^p \quad (3-2)$$

with E_i being the initial secant stiffness (see Figure 3-15), q being the deviator stress and the superscript s denotes shearing. The first is calculated according to:

$$E_i = \frac{2E_{50}}{2 - R_f} \quad (3-3)$$

$R_f = q_f/q_\alpha$ is the failure ratio and q_α is a quantity relating R_f with the ultimate deviator stress, (q_f). The latter is determined by:

$$q_f = (c \cot \varphi - \sigma'_3) \frac{2 \sin \varphi}{1 - \sin \varphi} \quad (3-4)$$

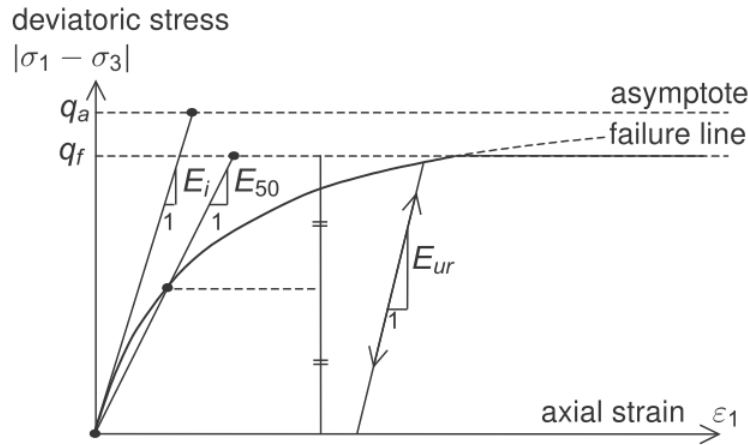


Figure 3-15: Hyperbolic stress-strain relationship in a deviator stress (q) versus axial strain ($\varepsilon_a = \varepsilon_1$ for triaxial compression) plot for a standard drained triaxial test. E_i is the initial secant modulus, E_{50} is the stress-dependent secant modulus, E_{ur} is the stress-dependent unloading-reloading modulus, q_a is the asymptotic value of the shear strength and q_f is the ultimate deviator stress (Plaxis, 2011a).

E_{50} is the stress-dependent secant stiffness for primary deviatoric loading given by:

$$E_{50} = E_{50}^{ref} \left(\frac{c \cos \varphi - \sigma'_3 \sin \varphi}{c \cos \varphi + p^{ref} \sin \varphi} \right)^m \quad (3-5)$$

where E_{50}^{ref} is the reference secant modulus, intersecting the $\varepsilon_a - q$ curve at $q_f/2$ (Figure 3-15), in a drained triaxial test conducted under constant confining stress. p^{ref} is a reference pressure, usually taken equal to 0.1 MPa.

The quantity E_{ur} , in the first part of Equation 3-2, is the unloading-reloading modulus:

$$E_{ur} = E_{ur}^{ref} \left(\frac{c \cos \varphi - \sigma'_3 \sin \varphi}{c \cos \varphi + p^{ref} \sin \varphi} \right)^m \quad (3-6)$$

where E_{ur}^{ref} is the inclination of an unloading-reloading path in a drained triaxial test (Figure 3-15), performed at a constant confining pressure.

The constant m represents the level of stress dependency of stiffness of a material and usually ranges from 0.5 for sands to 1 for soft soils (Brinkgreve, 2011). It is determined from two triaxial tests, carried out on the same material at different confining pressures, for instance $\sigma'_3^{(1)}$ and $\sigma'_3^{(2)}$ (Figure 3-16). Once the secant moduli corresponding to each confining pressure ($E_{50}^{(1)}$ and $E_{50}^{(2)}$) are estimated, m can be calculated as follows (Brinkgreve, 2011):

$$\frac{E_{50}^{(1)}}{E_{50}^{(2)}} = \left(\frac{\sigma'_3^{(1)}}{\sigma'_3^{(2)}} \right)^m \Rightarrow m = \frac{\ln \left(E_{50}^{(1)} / E_{50}^{(2)} \right)}{\ln \left(\sigma'_3^{(1)} / \sigma'_3^{(2)} \right)} \quad (3-7)$$

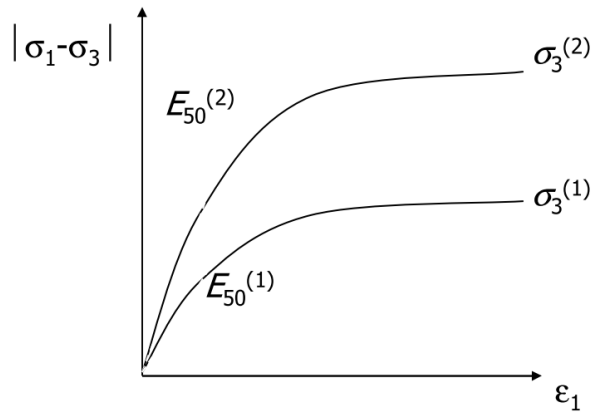


Figure 3-16: Deviator stress, $|\sigma_1 - \sigma_3|$, versus axial strain ($\varepsilon_1 = \varepsilon_a$ for triaxial compression) diagrams resulting from 2 drained triaxial tests at different confining pressures (σ_3), for determining the stress dependency of stiffness (m). E_{50} is the secant modulus (Brinkgreve, 2011).

In the principal stress space Equation 3-1 becomes (Schanz et al., 1999):

$$\begin{aligned} f_{12}^s &= \frac{2q_a}{E_i} \frac{(\sigma_1 - \sigma_2)}{q_a - (\sigma_1 - \sigma_2)} - \frac{2(\sigma_1 - \sigma_2)}{E_{ur}} - \gamma^p \quad \text{and} \\ f_{13}^s &= \frac{2q_a}{E_i} \frac{(\sigma_1 - \sigma_3)}{q_a - (\sigma_1 - \sigma_3)} - \frac{2(\sigma_1 - \sigma_3)}{E_{ur}} - \gamma^p \end{aligned} \quad (3-8)$$

For predicting plastic strains due to shear hardening, a non-associated flow rule is used, namely the plastic potential surface is different from the one described by Equation 3-8. The plastic potential functions are given by (Schanz et al., 1999):

$$\begin{aligned} g_{12}^s &= \frac{\sigma_1 - \sigma_2}{2} - \frac{\sigma_1 + \sigma_2}{2} \sin \psi_m \quad \text{and} \\ g_{13}^s &= \frac{\sigma_1 - \sigma_3}{2} - \frac{\sigma_1 + \sigma_3}{2} \sin \psi_m \end{aligned} \quad (3-9)$$

where ψ_m is the mobilised dilatancy angle (Section 3-4-4) and σ_1 , σ_2 and σ_3 are the major, intermediate and minor principal stresses, respectively.

It is noted that for calculating γ^p in Equation 3-2, Schanz et al. (1999) assumed that, for hard soils, the plastic volumetric strains (ε_v^p) are very low compared to the plastic major principal strains (ε_1^p). Therefore the latter falls out in the formula.

In Figure 3-17 the cone-type shear hardening loci are presented, for $m = 0.5$ and for various values of γ^p . The shear hardening locus can be plotted on the $p' - q$ plane by utilising Equations 3-2, 3-5 and 3-6.

3-4-3 Calculation of the axial strains

The relationship for calculating ε_1^p (which are equal to the plastic axial strains, ε_α^p , for triaxial conditions) upon primary deviatoric loading is derived by satisfying the yield condition, that

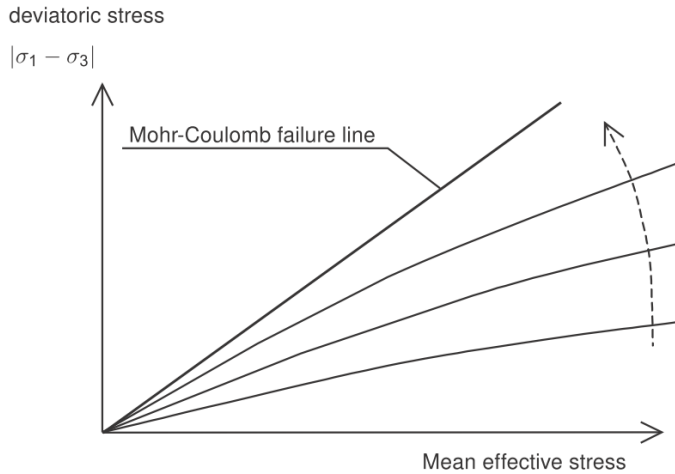


Figure 3-17: Shear hardening loci in a deviatoric stress, $|\sigma_1 - \sigma_3|$, versus mean effective stress plot for cohesionless soil, for stress dependency of stiffness $m = 0.5$ and for different values of the shear hardening parameter (γ^p). The locus moves upwards with increasing γ^p (Plaxis, 2011a).

is by setting $f^s = 0$ (Equation 3-1). Then, from Equation 3-2 it follows that:

$$\varepsilon_1^p \approx 1/2\bar{f} = \frac{1}{E_i} \frac{q}{1 - q/q_a} - \frac{q}{E_{ur}} \quad (3-10)$$

The elastic major, intermediate and minor principal strains (ε_1^e , ε_2^e and ε_3^e , respectively) upon primary loading or unloading-reloading are calculated, according to:

$$\varepsilon_1^e = \frac{q}{E_{ur}} \quad \text{and} \quad \varepsilon_2^e = \varepsilon_3^e = -\nu_{ur} \frac{q}{E_{ur}} \quad (3-11)$$

where ν_{ur} is the unloading/reloading Poisson's ratio.

For determining the total major principal strains (ε_1), Equations 3-10 and 3-11 need to be considered:

$$\varepsilon_1 = \varepsilon_1^e + \varepsilon_1^p \approx \frac{1}{E_i} \frac{q}{1 - q/q_a} \quad (3-12)$$

3-4-4 Evolution of plastic volumetric strains due to shear hardening

The flow rule for the development of plastic volumetric strains in triaxial stress conditions is given by:

$$\dot{\varepsilon}_v^p = \sin \psi_m \dot{\gamma}_s^p \quad (3-13)$$

with $\dot{\varepsilon}_v^p$ being the rate of plastic volumetric strains and $\dot{\gamma}_s^p$ being the rate of plastic deviatoric strains. The value of ψ_m in Equation 3-13 varies according to the level of the mobilised friction in the material during the numerical analysis, similarly to the stress-dilatancy theory

proposed by [Rowe \(1962\)](#) and adapted by [Schanz and Vermeer \(1996\)](#):

$$\begin{aligned}
 \text{For } \sin \varphi_m < 3/4 \sin \varphi & \quad \psi_m = 0^\circ \\
 \text{For } \sin \varphi_m \geq 3/4 \sin \varphi \text{ and } \psi > 0^\circ & \quad \sin \psi_m = \max \left(\frac{\sin \varphi_m - \sin \varphi_{cv}}{1 - \sin \varphi_m \sin \varphi_{cv}}, 0 \right) \\
 \text{For } \sin \varphi_m \geq 3/4 \sin \varphi \text{ and } \psi \leq 0^\circ & \quad \psi_m = \psi \\
 \text{For } \varphi = 0^\circ & \quad \psi_m = 0^\circ
 \end{aligned} \tag{3-14}$$

where φ_{cv} and φ_m are the critical state (or constant volume) and the mobilised friction angle, respectively. From the second row of Equation 3-14, it can be concluded that, for $\varphi_m < \varphi_{cv}$ the material contracts ($\psi = 0^\circ$), whereas it dilates for $\varphi_m > \varphi_{cv}$ (as $\psi > 0^\circ$). φ_m is calculated as follows:

$$\sin \varphi_m = \frac{\sigma'_1 - \sigma'_3}{\sigma'_1 + \sigma'_3 - 2c \cot \varphi} \tag{3-15}$$

The critical state friction angle is calculated automatically by *PLAXIS*, according to the following equation:

$$\sin \varphi_{cv} = \frac{\sin \varphi_f - \sin \psi_f}{1 - \sin \varphi_f \sin \psi_f} \tag{3-16}$$

where φ_f and ψ_f are the friction and dilatancy angle at failure, respectively. Equation 3-16 is derived by Equation 3-14 for failure conditions ($\varphi_m = \varphi_f$), which results in:

$$\sin \psi_f = \frac{\sin \varphi_f - \sin \varphi_{cv}}{1 - \sin \varphi_f \sin \varphi_{cv}} \tag{3-17}$$

It is noted that, according to Equations 3-13 to 3-17, when $\psi = 0^\circ$ is introduced, no plastic volumetric strains develop in triaxial stress conditions. They occur only when the cap yield surface is met (Section 3-4-5).

3-4-5 Cap yield surface

The yield function for the cap is given by:

$$f^c = \frac{\tilde{q}^2}{\alpha^2} + p'^2 - p_c^2 \tag{3-18}$$

where p_c is the isotropic pre-consolidation pressure, the superscript c denotes the cap and \tilde{q} is a stress measure of the hardening soil model:

$$\tilde{q} = \sigma_1 + (\delta - 1) \sigma_2 - \delta \sigma_3 \quad \text{with} \quad \delta = \frac{3 + \sin \varphi}{3 - \sin \varphi} \tag{3-19}$$

For triaxial compression it is $\sigma_1 > \sigma_2 = \sigma_3$ and Equation 3-19 results in $\tilde{q} = \sigma_1 - \sigma_3$. For triaxial extension, where $\sigma_1 = \sigma_2 > \sigma_3$, it is $\tilde{q} = \delta(\sigma_1 - \sigma_3)$.

The parameter α is a quantity determined by the coefficient of earth pressures for normal consolidation, $K_0^{NC} = 1 - \sin \varphi$ ([Jaky, 1944](#)). This parameter controls the steepness of the cap, which in turn affects the orientation of the rate of plastic strains vector (thus, $\dot{\varepsilon}_v^p / \dot{\gamma}_s^p$).

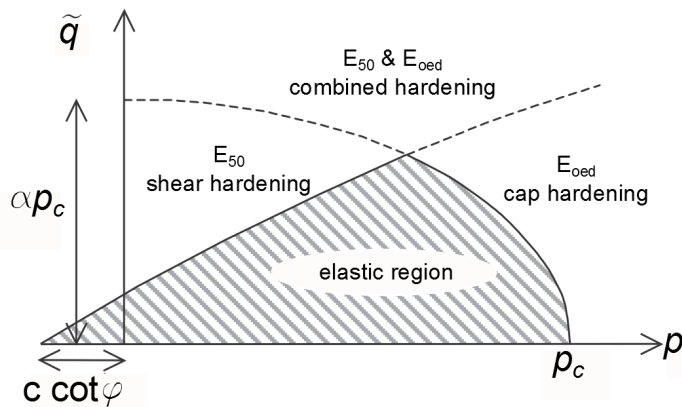


Figure 3-18: Cap and shear hardening loci in the deviator stress of the HS model (\tilde{q}) versus mean stress (p) graph, with indication of the stiffness zones and the related moduli. α is the cap parameter of the HS model, p_c is the isotropic pre-consolidation stress, c is the cohesion, φ is the friction angle, E_{50} is the stress-dependent secant modulus, E_{oed} is the stress-dependent oedometer modulus and E_{ur} is the stress-dependent un-/reloading modulus (After Plaxis, 2011a and Karstunen, 2013).

Figure 3-18 depicts the influence of the values of the α parameter and of p_c on the steepness and the size of the cap, respectively.

The law that describes the cap hardening process due to the generation of plastic volumetric cap strains (ε_v^{pc}) is given below:

$$\varepsilon_v^{pc} = \frac{\beta}{1-m} \left(\frac{p_c}{p^{ref}} \right)^{1-m} \quad (3-20)$$

where β is an internal model parameter, controlled by the reference oedometer modulus (E_{oed}^{ref}). The latter determines the value of the stress-dependent oedometer modulus:

$$E_{oed} = E_{oed}^{ref} \left(\frac{c \cos \varphi - \frac{\sigma'_3}{K_0^{NC}} \sin \varphi}{c \cos \varphi + p^{ref} \sin \varphi} \right)^m \quad (3-21)$$

E_{oed}^{ref} is determined from the tangent to the $\varepsilon_1 - \sigma'_v$ plot of an oedometer test, at a reference pressure (Figure 3-19).

For calculating the rate of plastic cap strains, an associated flow rule is adopted, i.e. the yield surface is used as plastic potential surface, too:

$$\dot{\varepsilon}^{pc} = \lambda \frac{\partial f^c}{\partial \underline{\sigma}} \quad \text{with} \quad \lambda = \frac{\beta}{2p'} \left(\frac{p_c}{p^{ref}} \right)^m \frac{\dot{p}_c}{p^{ref}} \quad (3-22)$$

where λ is the plastic multiplier.

The yield contour of the HS model in the principal stress space is shown in Figure 3-20.

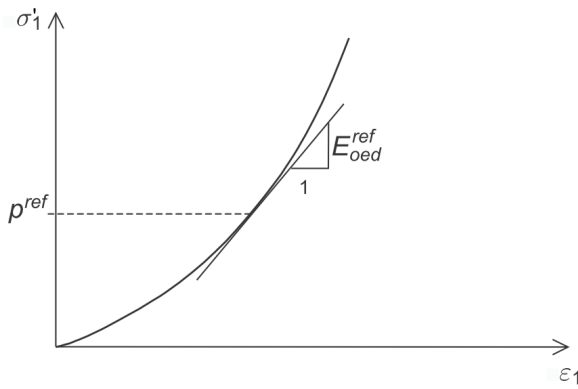


Figure 3-19: Determination of the reference oedometer modulus (E_{oed}^{ref}) from the resulting major principal (vertical) effective stress (σ'_1) versus major principal (vertical) strain (ε_1) plot of an oedometer test at a reference pressure (p^{ref}) (After [Plaxis, 2011a](#)).

3-4-6 Specifics of the HS model

3-4-6-1 Initial position of the shear hardening locus

When the lab test facility of *PLAXIS* is used, the state consequent to the previous stress history has to be assigned. This is possible by an option, which reads "mobilised relative shear strength" (*mob. rel. shear strength*, see Figure 3-1). Its value ranges from 0, where the initial yield locus is coincident with the hydrostatic axis (p'), to 1, where the yield surface is at its maximum located at the MC failure criterion. For the latter case as well as for any intermediate values, the stress paths within the area bounded by the cap and the shear hardening surface induce elastic behaviour of the material (Figure 3-18). For full mesh analyses, the yield surface is initialised along the K_0^{NC} line (Figure 3-22).

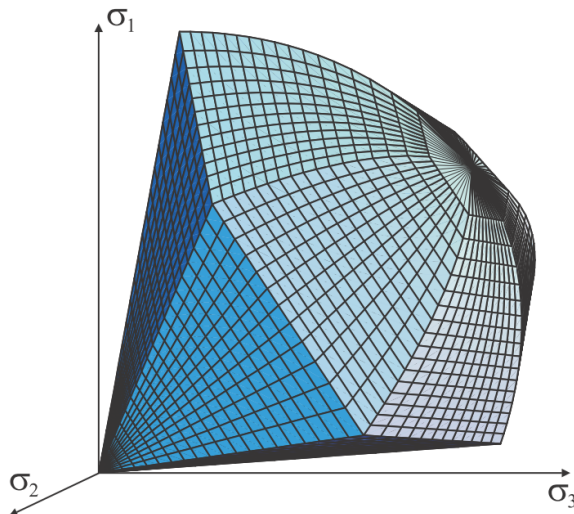


Figure 3-20: Yield contour of the HS model in the principal stress space. The soil cohesion is zero and the shear hardening locus coincides with the MC failure surface. σ_1 , σ_2 and σ_3 are the major, intermediate and minor principal stresses, respectively ([Benz, 2006](#)).

3-4-6-2 Stiffness zones on the $p' - \tilde{q}$ plane

The HS model comprises two yield surfaces for predicting the development of plastic strains for both radial and deviatoric stress paths (Sections 3-4-2, 3-4-5). The amount of the former is mainly controlled by the input value of E_{oed}^{ref} (influences the cap) and the amount of the latter is predominantly influenced by E_{50}^{ref} (affects the shear hardening surface).

According to the position of the stress path on the $p' - \tilde{q}$ plane, the examined soil may behave (Figure 3-18):

1. non-linear elastic, the stress path is located within the area bounded by the shear hardening and cap yield loci,
2. pure shear hardening, the stress state is situated within the area bounded by the cap and lies on the shear hardening yield locus,
3. pure cap hardening, the stress state lies below the shear hardening yield surface and moves with the cap, and
4. combined hardening, the stress state lies on both yield surfaces.

3-4-6-3 Initial conditions

For a finite element full mesh analysis the initial horizontal stresses (σ'_{h0}) are determined from the initial vertical effective stresses σ'_{v0} by a procedure which is based on entering either the value of the Pre-Overburden Pressure (POP) or the value of the OCR (Figure 3-21). These quantities are given by (Brinkgreve, 2011):

$$POP = |\sigma'_c - \sigma'_{v0}| \quad \text{and} \quad OCR = \sigma'_c / \sigma'_{v0} \quad (3-23)$$

Then, the initial horizontal effective stresses will be (see Figure 3-22):

$$\sigma'_{h0} = K_0 \sigma'_{v0} \quad (3-24)$$

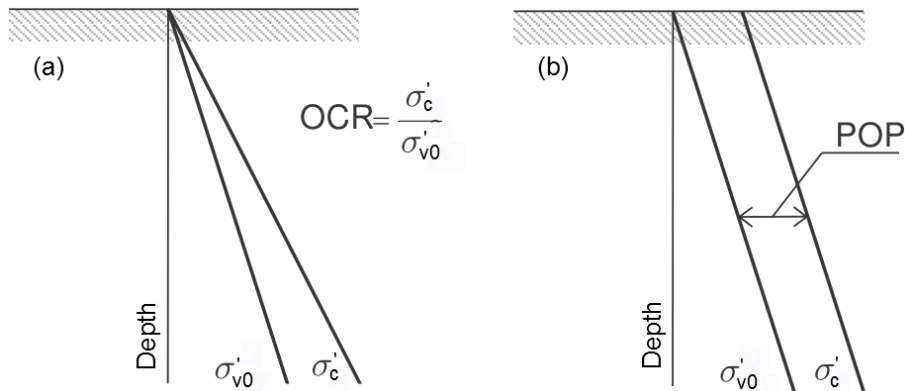


Figure 3-21: Illustration of the in-situ stress state for calculating the Over-Consolidation ratio (OCR) (a) and the Pre-Overburden Pressure (POP) (b). σ'_{v0} is the initial vertical effective stress and σ'_c is the vertical pre-consolidation stress (After Plaxis, 2013).

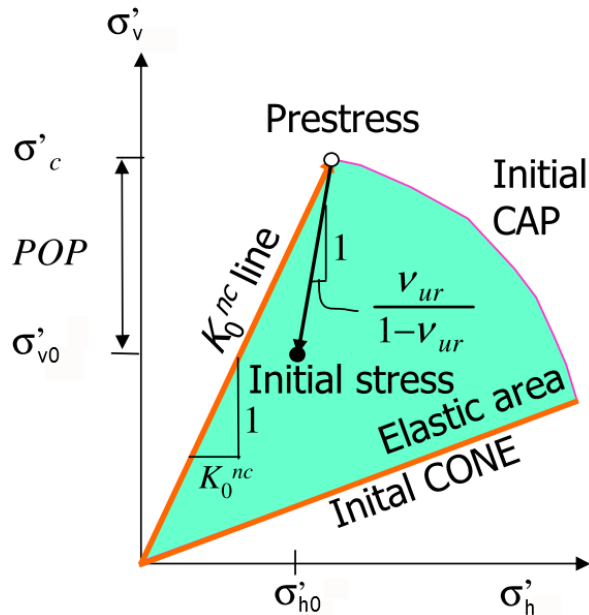


Figure 3-22: Determination of the initial horizontal effective stresses (σ'_{h0}) in a finite element mesh for the HS model. σ'_{v0} is the initial vertical effective stress, σ'_c is the vertical pre-consolidation stress, K_0^{NC} is the coefficient of earth pressures in NC conditions, ν_{ur} is the unloading-reloading Poisson's ratio and POP is the Pre-Overburden Pressure (After Brinkgreve, 2011).

with:

$$K_0 = \frac{K_0^{NC} (|\sigma'_{v0}| + POP) - \frac{\nu_{ur}}{1-\nu_{ur}} POP}{|\sigma'_{v0}|} \quad \text{or} \quad K_0 = OCR K_0^{NC} - \frac{\nu_{ur}}{1-\nu_{ur}} (OCR - 1) \quad (3-25)$$

3-4-7 HS model input parameters

The input parameters of the HS model are listed in Table 3-3. It is noted that the input value of E_{ur}^{ref} must be larger than $2E_{50}^{ref}$. Furthermore, values of the input parameter K_0^{NC} which do not lie within an admissible range are rejected by the program. This range is controlled by the values of E_{50}^{ref} , E_{ur}^{ref} , E_{oed}^{ref} and ν_{ur} . In such cases, either the input value of K_0^{NC} or the values of the aforementioned parameters need to be changed.

Instead of the standard stiffness parameters E_{50}^{ref} , E_{oed}^{ref} and E_{ur}^{ref} , the compression and the swelling indices, determined from oedometer or isotropic compression tests, may be used. In such cases, the program still uses the standard parameters which, however, are calculated automatically, according to:

$$C_c = \frac{2.3 (1 + e_0) p^{ref}}{E_{oed}^{ref}} \quad (3-26)$$

and

$$C_s \simeq \frac{2.3 (1 + e_0) (1 + \nu_{ur}) (1 - 2\nu_{ur}) p^{ref}}{(1 - \nu_{ur}) E_{ur}^{ref}} \quad (3-27)$$

Table 3-3: Input parameters for the HS model ([Plaxis, 2011a](#)).

Definition	Symbol	Unit
Mohr-Coulomb criterion		
(Effective) friction angle	φ	[°]
(Effective) cohesion	c	[kN/m ²]
Dilatancy angle	ψ	[°]
Standard Stiffness		
Reference secant modulus	E_{50}^{ref}	[kN/m ²]
Reference un-/reloading modulus	E_{ur}^{ref}	[kN/m ²]
Reference oedometer modulus	E_{oed}^{ref}	[kN/m ²]
Rate of stress dependency of stiffness	m	[‐]
Alternative Stiffness*		
Compression index	C_c	[‐]
Swelling index	C_s	[‐]
Initial void ratio	e_0	[‐]
Advanced		
Un-/reloading Poisson's ratio	ν_{ur}	[‐]
Reference stress for stiffness	p^{ref}	[kN/m ²]
K_0 -value for normal consolidation	K_0^{NC}	[‐]
Failure ratio	R_f	[‐]
Tensile strength	σ_t	[kN/m ²]
Increase of cohesion per unit depth	c_{inc}	[kN/m ³]

*The alternative stiffness parameters may be used instead of the standard stiffness parameters. In such cases the program considers $m = 1$.

The value of the reference secant modulus is automatically set to $E_{50}^{ref} = 1.25E_{oed}^{ref}$. Also, when C_c and C_s are used instead of the standard stiffness parameters a value of $m = 1$ is used by the program.

3-4-8 On the internal algorithm and the internal parameters of the HS model

Every time an input parameter of the HS model is altered, *PLAXIS* performs an internal algorithm in order to determine the values of some internal parameters, which control the magnitude and the evolution of the generated plastic strains. A comment made by [Calvello and Finno \(2004\)](#) (p. 417), regarding this algorithm, is cited below:

"The HS model implemented in PLAXIS has an internal algorithm that runs every time a new set of input parameters is specified. This algorithm considers the deviatoric stress response of an internally modelled compression test and "adjusts" the values of parameter E_{oed}^{ref} to produce a hyperbolic curve in a triaxial stress-strain space."

However, according to the findings of Section 3-5 the value of E_{oed}^{ref} does not seem to be changed.

As reported by Benz (2006), in cases of combined hardening (Figure 3-18) the internal parameters of the HS model are determined through an iterative procedure, during which numerical simulations of triaxial and oedometer element tests are performed in the background. According to the findings of Section 3-5, a similar process seems to be followed by the program before the commencement of any numerical analysis.

In Plaxis (2011a) it is mentioned that the internal parameters α and β are used for predicting the generated plastic strains (Section 3-4-5). Whereas in the material models manual of PLAXIS the β parameter is used for describing the cap hardening law (Equation 3-20), Schanz et al. (1999) and Benz (2006) use a slightly different formulation:

$$\varepsilon_v^{pc} = \frac{H}{m+1} \left(\frac{p_c}{p^{ref}} \right)^{(m+1)} \quad (3-28)$$

with

$$H = \frac{K_c}{K_s - K_c} K_s \quad (3-29)$$

with H being a hardening modulus of the HS model and K_c being the elastoplastic compression modulus for isotropic compression (Schanz et al., 1999). K_s is the swelling modulus for isotropic compression, calculated as follows:

$$K_s = \frac{E_{ur}}{3(1-2\nu_{ur})} \quad (3-30)$$

A comparison of Equation 3-20 with Equations 3-28 to 3-30 suggests that β , aside from E_{oed}^{ref} , is also be dependent on K_c , E_{ur}^{ref} and ν_{ur} .

Benz (2006) mentions another internal parameter, the initial secant stiffness (E_i^{ref}), which seems to be related to the E_i parameter of Equation 3-3 via the equation below:

$$E_i = E_i^{ref} \left(\frac{\sigma_3 + c \cot \varphi}{p^{ref} + \cot \varphi} \right)^m \quad (3-31)$$

Table 3-4: Summary of the *internal* parameters of the HS model with their (possible) dependency and influence, as inferred from the literature.

Definition	Symbol	Unit	Dependency	Influence
Cap parameter ⁽¹⁾	α	[-]	K_0^{NC}	$\dot{\varepsilon}_v^{pc}/\dot{\gamma}_s^{pc}$
Cap parameter ⁽¹⁾	β	[-]	K_s/K_c	ε^{pc}
Bulk modulus in primary loading ⁽²⁾	K_c	[kN/m ²]	E_{oed}^{ref}	ε^{pc} (through β)
Bulk modulus in un-/reloading ⁽²⁾	K_s	[kN/m ²]	ν_{ur}, E_{ur}^{ref}	ε^{pc} (through β)
Initial secant stiffness ⁽³⁾	E_i^{ref}	[kN/m ²]	-	E_i

Sources: ⁽¹⁾ Plaxis (2011a), ⁽²⁾ Schanz et al. (1999), ⁽³⁾ Benz (2006)

Table 3-4 shows the internal parameters of the HS model, their possible dependency on other parameters and their possible influence on the numerical results, as inferred from the literature.

On the other hand, the findings of Section 3-5 suggest that *PLAXIS* uses the α parameter, the swelling to compression ratio (K_s/K_c) and the reference shear modulus in primary loading (G_{50}^{ref}) for predicting the amount and the evolution of the produced plastic strains. The values of these parameters are determined via the internal algorithm and depend on the values of E_{50}^{ref} , E_{oed}^{ref} , E_{ur}^{ref} , m , ν_{ur} , φ' and K_0^{NC} (for the two latter see Section 4-3-2-5). The value of the β parameter was not identified in the .vlt file where the numerical results of the triaxial tests simulations were saved.

3-5 Investigating the influence of the HS model input parameters

In this section the influence of changing selected input parameters of the HS model on the results of the triaxial tests simulations, described in Section 3-3-1, is investigated. This is achieved by comparing the results obtained for the best fit of the model (red curves in Figures 3-3 to 3-8), with the ones acquired by changing, individually, each input parameter.

Table 3-5 shows the values of the parameters that have given the best fit of the HS model (Section 3-3-6) with the data obtained by [Deng et al. \(2011b\)](#). For the failure ratio and the reference stress for stiffness the default values were used, i.e. $R_f = 0.9$ and $p^{ref} = 0.1\text{MPa}$ ([Plaxis, 2011a](#)). The value of K_0^{NC} was set to 0.7853, which resulted from Jaky's formula ($K_0^{NC} = 1 - \sin\varphi'$) ([Jaky, 1944](#)). It is noted that the former should be calculated based on the critical state friction angle. The value of φ' used was determined by [Deng et al. \(2011b\)](#) from the inclination of the second branch of the failure envelope of the material (see Section 2-4-2-3 and Figure 2-4). Nevertheless, the considered part of the failure envelope does not intersect with the origin in the $p' - q$ plane (i.e. cohesion is present), which is not consistent with the critical state theory. The dilatancy angle for the simulation of the *Ess75Tr03* test was determined to be $\psi = 2^\circ$. The set of parameters listed in Table 3-5 will henceforth be referred to as *Initial data*.

The value of the mobilised relative shear strength was set to 0 in all analyses. Therefore, the shear hardening contour was initialised on the hydrostatic axis (Section 3-4-6) at the beginning of the simulations, leading to an immediate generation of plastic deviatoric strains.

The simulations for investigating the effect of the model input parameters on the numerical results have been performed with the lab test facility of *PLAXIS 2d 2010* ([Plaxis, 2010](#)). A specificity of this version is that, even though the value of the isotropic pre-consolidation pressure is asked as input for the simulation of a triaxial test (see Figure 3-1), the value of the equivalent pre-consolidation pressure (p_c^{eq}) is actually needed, in order for the correct initial cap of the HS model to be generated. This particularity is also present in the lab

Table 3-5: Values of the input parameters of the HS model obtained by the best fit of the results of some triaxial and oedometer tests performed by [Deng et al. \(2011b\)](#).

Definition	Symbol	Unit	Value	Obtained by
Effective friction angle	φ'	[°]	12.40	Deng et al. (2011b)
Effective cohesion	c'	[MPa]	0.11	Deng et al. (2011b)
Reference secant modulus	E_{50}^{ref}	[MPa]	8.53	Calibration
Reference oedometer modulus	E_{ref}^{oed}	[MPa]	11.00	Calibration
Reference un-/reloading modulus	E_{ur}^{ref}	[MPa]	20.94	Calibration
Stress dependency of stiffness	m	[‐]	0.70	Calibration
Un-/reloading Poisson's ratio	ν_{ur}	[‐]	0.30	Calibration
Failure ratio	R_f	[‐]	0.90	Plaxis (2011a)
Reference stress for stiffness	p^{ref}	[MPa]	0.10	Plaxis (2011a)
K_0 -value for normal consolidation	K_0^{NC}	[‐]	0.7853	$1 - \sin\varphi'$ (Jaky, 1944)

test facility of the *PLAXIS 2d 2011* version. The equivalent pre-consolidation pressure varies for different values of the model input parameters, and is calculated from the vertical pre-consolidation stress (σ'_c), which in the considered case is equal to 2200kPa. The stress state that corresponds to σ'_c , in terms of p' and q , is given by (Plaxis, 2014a):

$$p' = \frac{1}{3} (1 + 2K_0^{NC}) \sigma'_c \quad \text{and} \quad q = (1 - K_0^{NC}) \sigma'_c \quad (3-32)$$

and the equivalent stress is calculated according to:

$$p_c^{eq} = \sqrt{(p')^2 + \frac{q^2}{\alpha^2}} \quad (3-33)$$

where α is the internal parameter of the HS model which controls the steepness of the cap.

In order to overcome the aforementioned particularity of the lab test facility a procedure, for performing the numerical simulation of a triaxial test each time a model input parameter was changed, was followed:

1. A triaxial test was performed with the desired values of the HS model input parameters. The numerical results were saved by means of a .vlt file.
2. The value of the α parameter, which resulted from the internal algorithm performed by the program, was obtained from the saved .vlt file.
3. The value of p_c^{eq} was determined via Equations 3-32 and 3-33.
4. The numerical simulation of the triaxial test, with the required boundary conditions and the same values of the model input parameters, was performed by introducing the value of p_c^{eq} instead of the value of the isotropic pre-consolidation pressure.

This procedure was validated by numerically simulating triaxial tests, with the same sets of input parameters and the same boundary conditions, in the lab test facility of *PLAXIS 2D Anniversary Edition* (Plaxis, 2014b), where the aforementioned specificity is not present. The numerical results were found to be identical between the two methods.

3-5-1 Changes in the values of the HS model input parameters

The changes in the input parameters of the HS model for examining, separately, their influence on the numerical results were:

- A decrease in E_{50}^{ref} from 8.53MPa to 6MPa,
- an increase in E_{oed}^{ref} from 11MPa to 15MPa,
- an increase in E_{ur}^{ref} from 20.94MPa to 25MPa,
- a decrease in m from 0.7 to 0.55, and
- a decrease in ν_{ur} from 0.3 to 0.25.

These changes imply different values of the internal parameters of the HS model (Tables 3-6 to 3-10), which control the response of the shear and the compression hardening loci,

and therefore the evolution of the plastic deviatoric and volumetric strains. These are the α parameter, which controls the steepness of the cap (Section 3-4-5), the swelling to compression ratio (K_s/K_c) which, presumably, is positively related to the β parameter (Section 3-4-8) and affects the magnitude of the plastic cap strains (Equation 3-22), and the reference shear modulus in primary loading (G_{50}^{ref}). The latter is an elasto-plastic shear modulus, which influences the evolution of plastic deviatoric strains due to shear hardening. The calculated values of the internal parameters were obtained from the output file of the lab test facility of *PLAXIS* after saving the results of the numerical simulations.

It is noted that the changes in the values of the HS model input parameters have been chosen arbitrarily as this section only aims at understanding the response of the model in drained triaxial compression.

3-5-2 Effects of the model input parameters on the results of the simulation of the *Ess75Tr01* test

The numerical results of the simulations of the *Ess75Tr01* test are presented in terms of $\varepsilon_a - q$ and $\varepsilon_a - \varepsilon_v$ diagrams in Figures 3-23 and 3-24, respectively. The outcomes of changing the values of E_{oed}^{ref} , E_{ur}^{ref} and ν_{ur} are not presented in Figure 3-23, as they coincide with the curve that corresponds to the analysis with the *Initial data*.

It should be noted that, in the considered simulations, the double hardening process (Figure 3-18) initiates from the first steps of the analysis as NC conditions are imposed. Therefore, the stress path lies on both yield loci almost immediately after the beginning of the simulations.

3-5-2-1 Investigation on the influence of E_{50}^{ref}

A decrease in E_{50}^{ref} to 6 MPa leads to a softer material response (green curve in Figure 3-23) and to larger ε_a at the same level of ε_v (green curve in Figure 3-24). This is attributed to the reduction in E_{50} (Equation 3-5) and subsequently to the decrease in E_i (Equation 3-3). Consequently, the generated ε_1^p ($= \varepsilon_a^p$) increase (Equation 3-10), leading to a smaller inclination of the curves in the $\varepsilon_a - q$ and the $\varepsilon_a - \varepsilon_v$ plots. It should be noted that the produced plastic axial strains are not expected to contribute to the generated total volumetric strains. [Schanz et al. \(1999\)](#) assumed that $\varepsilon_v^p \approx 0$ when deriving the shear hardening parameter γ^p for the formulation of the related yield function (Section 3-4-2). This can also be deduced by introducing $\psi = 0^\circ$ in Equations 3-14 to 3-17.

Table 3-6 shows the changes in the internal parameters of the HS model for decreasing values of E_{50}^{ref} . It can be observed that G_{50}^{ref} (and thus the shear stiffness in the elasto-plastic domain) decreases. Also, a slight increase in the α parameter and the ratio K_s/K_c occurs. The first implies an imperceptible increase in the steepness of the cap (thus, $\dot{\varepsilon}_v^{pc}$ becomes somewhat larger, Section 3-4-5) and the second induces insignificantly higher ε_v^{pc} (Equation 3-22). This is in accordance with the assumption of [Schanz et al. \(1999\)](#) that $\varepsilon_v^p \approx 0$ during shear hardening (provided that $\psi = 0^\circ$).

Table 3-6: Effect of changing the value of the reference secant modulus (E_{50}^{ref}) on the values of the internal parameters of the HS model. The value in red colour concerns the *initial data*.

E_{50}^{ref} [MPa]	G_{50}^{ref} [MPa]	α [-]	K_s/K_c [-]
10.00	10.84	0.411	1.486
8.53	8.38	0.418	1.488
7.00	6.31	0.427	1.491
6.00	5.13	0.436	1.494
5.00	4.07	0.451	1.497

3-5-2-2 Investigation on the influence of E_{oed}^{ref}

An increase in E_{oed}^{ref} to 15 MPa leads to lower ε_v (brown curve in Figure 3-24). The model response seems to be logical since the soil is expected to react stiffer, in terms of cap hardening, for a larger oedometer modulus. Further justification can be given by observing the resulting internal model parameters, shown in Table 3-7. The cap becomes shallower as α decreases, inducing a smaller rate of $\dot{\varepsilon}_v^{pc}$ (Section 3-4-5). The swelling to compression ratio reduces, leading to smaller ε_v^{pc} (Equation 3-20). The reduction in ε_v is significant for the particular analysis. This may be attributed to the stress path lying on the cap from the beginning of the simulation due to the imposed NC conditions. Therefore, the volumetric behaviour of the material is expected to be dominated by the response of the cap.

In Table 3-7, a small decrease in the value of G_{50}^{ref} is observed. A slightly softer response in

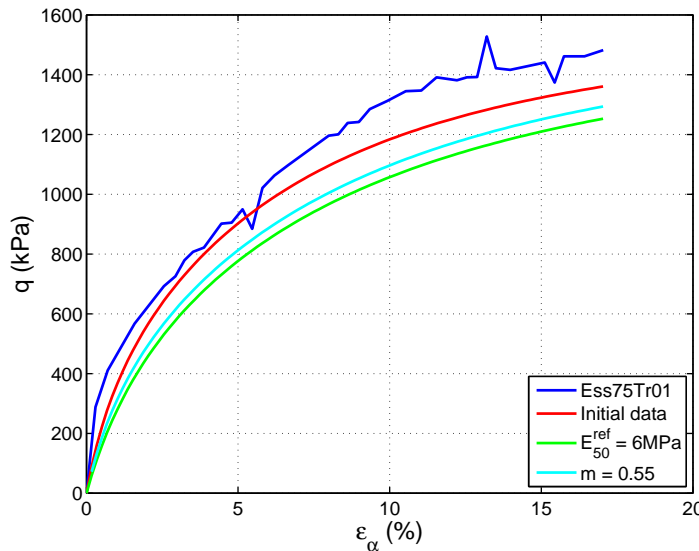


Figure 3-23: Deviator stress (q) versus axial strain (ε_a) resulting from varying some of the input parameters of the HS model, for the numerical simulation of the *Ess75Tr01* test. E_{50}^{ref} is the reference secant modulus and m is a measure of the stress dependency of stiffness. The triaxial data (blue curve) have been digitised from [Deng et al. \(2011b\)](#).

Table 3-7: Effect of changing the value of the reference oedometer modulus (E_{oed}^{ref}) on the values of the internal parameters of the HS model. The value in red colour concerns the *initial data*.

E_{oed}^{ref} [MPa]	G_{50}^{ref} [MPa]	α [-]	K_s/K_c [-]
9.00	9.27	0.466	1.808
11.00	8.38	0.418	1.488
13.00	7.96	0.355	1.268
15.00	7.94	0.266	1.110
16.00	6.05	0.868	1.059

terms of a $\gamma_s - q$ graph may be expected. Also, it can be observed that an increase in E_{oed}^{ref} to 16MPa leads to a larger value of the α parameter ($=0.868$). This would induce a steeper cap, which does not seem to be realistic. In addition, a value of $E_{oed}^{ref} = 17$ MPa is rejected by the program, indicating that a $E_{oed}^{ref} = 16$ MPa is already very large for the particular set of the model input parameters.

3-5-2-3 Investigation on the influence of E_{ur}^{ref}

An increase in E_{ur}^{ref} to 25MPa (thus, an increase in E_{ur} , Equation 3-6) does not induce any changes in the $\varepsilon_a - q$ plot of Figure 3-23. This may be attributed to the interplay between the decrease in the elastic axial strains (Equation 3-11) and the increase in the plastic axial

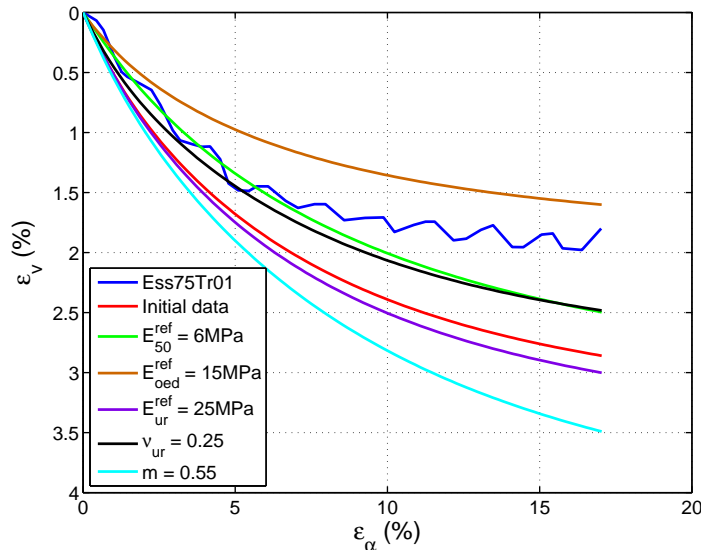


Figure 3-24: Volumetric strain (ε_v) versus axial strain (ε_a) resulting from varying some of the input parameters of the HS model, for the simulation of the *Ess75Tr01* test. E_{50}^{ref} is the reference secant modulus, E_{oed}^{ref} is the reference oedometer modulus, E_{ur}^{ref} is the reference unloading-reloading modulus, ν_{ur} is the unloading-reloading Poisson's ratio and m is a measure of the stress dependency of stiffness. The triaxial data (blue curve) have been digitised from [Deng et al. \(2011b\)](#).

Table 3-8: Effect of changing the value of the reference un-/reloading modulus (E_{ur}^{ref}) on the values of the internal parameters of the HS model. The value in red colour concerns the *initial data*.

E_{ur}^{ref} [MPa]	G_{50}^{ref} [MPa]	α [-]	K_s/K_c [-]
18.00	8.60	0.356	1.285
20.94	8.38	0.418	1.488
25.00	8.29	0.468	1.770
30.00	8.28	0.506	2.118
40.00	8.31	0.548	2.816

strains (Equation 3-10). It seems that these effects cancel each other, leading to no observable change in the development of the mobilised shear strength and stiffness of the material. The value of G_{50}^{ref} is practically unaffected by the change in E_{ur}^{ref} (Table 3-8).

The aforementioned model response may be justified by the notion that a stiffer elastic behaviour of the material (therefore smaller ε_1^e) will cause larger ε_1^p after it yields, for a pre-defined amount of ε_1 (= 17.04% in the case under consideration). That is because $\varepsilon_1 = \varepsilon_1^e + \varepsilon_1^p$. Note that $\varepsilon_1 = \varepsilon_a$ and $\varepsilon_3 = \varepsilon_r$, where the subscript r denotes radial strain.

The values of the α parameter and the swelling to compression ratio rise for an increase in E_{ur}^{ref} (Table 3-8). The first induces a steeper cap (thus, larger $\dot{\varepsilon}_v^{pc}$) and the second leads to higher $\dot{\varepsilon}_v^{pc}$ (Table 3-4 and Equation 3-22). On the other hand, an increase in E_{ur}^{ref} causes a larger E_{ur} (Equation 3-6) and, therefore, smaller ε_v^e (Equation 3-11). Note that for triaxial compression $\varepsilon_v^e = \varepsilon_1^e - 2\varepsilon_3^e$. The two counter-acting processes lead to larger total volumetric strains (purple curve in Figure 3-24), with respect to the ones resulting from the analysis with the *Initial data* (red curve in Figure 3-24). This may be attributed to the fact that the material behaviour is dominated by the response of the cap, as mentioned in Section 3-5-2-2. The generated plastic volumetric cap strains are expected to be prevalent in the considered case.

The increase in the α and the K_s/K_c parameters (therefore the increase in $\dot{\varepsilon}_v^{pc}$ and ε_v^{pc} , respectively), caused by the increase in E_{ur}^{ref} (Table 3-8), seems to be the outcome of the internal algorithm performed by the program (Section 3-4-8).

3-5-2-4 Investigation on the influence of ν_{ur}

A decrease in ν_{ur} to 0.25 does not induce visible changes in the $\varepsilon_a - q$ diagram of Figure 3-23. The program calculates a larger value of G_{50}^{ref} than that of the *Initial data* (Table 3-9). Thus, the material is expected to exhibit stiffer behaviour by means of a $\gamma_s - q$ plot.

The total volumetric strains decrease for a smaller value of ν_{ur} (black curve in Figure 3-24). It seems that the effect of the smaller ε_v^{pc} is more significant than that of the larger ε_v^e . The former are lower due to the smaller value of the α parameter, which causes the cap to be shallower (thus, $\dot{\varepsilon}_v^{pc}$ decrease) and owing to the smaller K_s/K_c (Table 3-9), which controls the magnitude of ε_v^{pc} through the β parameter (Equation 3-20). The elastic volumetric strains are larger since ε_3^e ($=\varepsilon_r^e$) decrease, ε_1^e ($=\varepsilon_a^e$) are not influenced (Equation 3-11), and for triaxial

Table 3-9: Effect of changing the value of the un-/reloading Poisson's ratio (ν_{ur}) on the values of the internal parameters of the HS model. The value in red colour concerns the *initial data*.

ν_{ur} [-]	G_{50}^{ref} [MPa]	α [-]	K_s/K_c [-]
0.33	8.01	0.471	1.747
0.30	8.38	0.418	1.488
0.25	9.56	0.310	1.198
0.23	10.65	0.255	1.116
0.20	6.46	0.029	1.000

compression $\varepsilon_v^e = \varepsilon_1^e - 2\varepsilon_3^e$ applies. As mentioned in Sections 3-5-2-2 and 3-5-2-3, it seems that the response of the cap is the most influential on the model performance, for NC conditions.

A further decrease in ν_{ur} to 0.20 results in a value of the α parameter which seems unrealistic (Table 3-9). Such low α -value (=0.029) would lead to an exceedingly shallow cap. Moreover, the change in G_{50}^{ref} is not in accordance with the ones induced by decreasing ν_{ur} from 0.30 to 0.25 and to 0.23. It seems that a value of $\nu_{ur} = 0.20$ is considered very low for the particular set of the input model parameters. A decrease of ν_{ur} to 0.19 is rejected by the program.

3-5-2-5 Investigation on the influence of the m parameter

A decrease in the value of m to 0.55 induces a softer response in the $\varepsilon_a - q$ curve (cyan curve in Figure 3-23). This model response may be explained by the effect of a reduction in m on the value of E_{50} . A decrease in m (which is always ≤ 1) leads to a smaller value of E_{50} since the numerator in Equation 3-5 is always larger than the denominator. Consequently, E_i decreases (Equation 3-3) and ε_1^p ($= \varepsilon_a^p$) increases (Equation 3-10), inducing a smaller inclination in the $\varepsilon_a - q$ plot. The reduction in E_{ur}^{ref} (Equation 3-6) may not have affected the results since the increase in the ε_1^e and the decrease in ε_1^p might have cancelled each other (Section 3-5-2-3). The calculated value of G_{50}^{ref} is not altered for a decrease in m to 0.55 and 0.40. However, it reduces noticeably for $m = 0.30$ (Table 3-10). Also, the resulting α parameter seems to be unrealistic, since it leads to an excessively steep cap.

The total volumetric strains increase for a decrease in m (cyan curve in Figure 3-24). This may be attributed to the lower value of E_{oed} (Equation 3-21) which, even though does not influence the internal parameters of the HS model (E_{oed}^{ref} does), might be considered equivalent to a somewhat steeper cap (larger α parameter), thus higher $\dot{\varepsilon}_v^{pc}$, and a slightly larger K_s/K_c (higher ε_v^{pc} , Equation 3-20), as observed in Table 3-10. The change in E_{oed} is deemed to be the most influential since it mainly controls the response of the cap of the HS model (Section 3-4-6-2). In addition, a reduction in m leads to larger ε_v^{pc} , according to Equation 3-20. Moreover, the induced decrease in E_{ur} causes larger ε_v^e (Equation 3-11). Both generated strains add up to result in the highest ε_v , with respect to the other analyses.

Values of $m > 0.90$ are rejected for the considered set of the model input parameters.

Table 3-10: Effect of changing the value of the rate of stress dependency of stiffness (m) on the values of the internal parameters of the HS model. The value in red colour concerns the *initial data*.

m [-]	G_{50}^{ref} [MPa]	α [-]	K_s/K_c [-]
0.80	8.39	0.406	1.453
0.70	8.38	0.418	1.488
0.55	8.38	0.434	1.542
0.40	8.39	0.450	1.598
0.30	6.32	1.516	1.762

3-5-3 Effects of the model input parameters on the results of the simulation of the *Ess75Tr02* test

The resulting $\varepsilon_a - q$ and $\varepsilon_a - \varepsilon_v$ diagrams for the simulations of the *Ess75Tr02* test are depicted in Figures 3-25 and 3-26, respectively. The former does not include the results obtained by changing the values of E_{ur}^{ref} , ν_{ur} and m since the first two practically coincide with the ones of the *Initial data* and the last one coincides with the curve corresponding to the simulation with $E_{oed}^{ref} = 15\text{ MPa}$.

It should be mentioned that in the considered case, where OCR 2.2, the stress path lies on the shear hardening locus immediately at the beginning of the analysis. The cap is met at later steps during the simulation. The intersection of the stress path with the cap (see Figure 3-27)

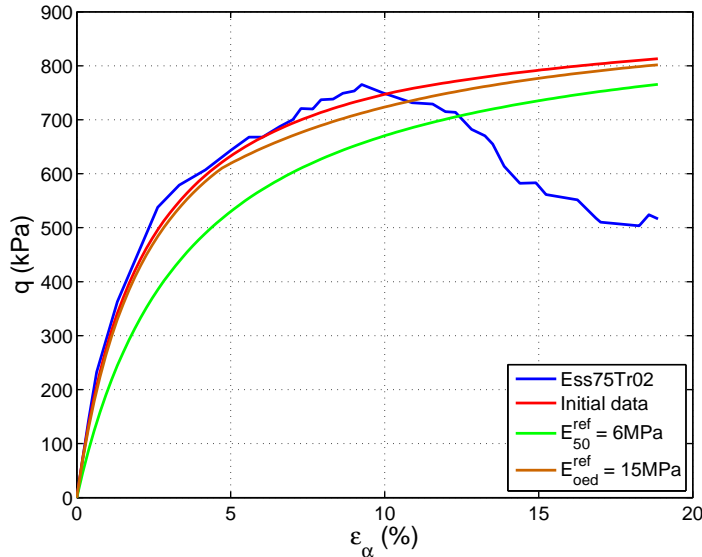


Figure 3-25: Deviator stress (q) versus axial strain (ε_a) resulting from varying some of the input parameters of the HS model, for the simulation of the *Ess75Tr02* test. E_{50}^{ref} is the reference secant modulus and E_{oed}^{ref} is the reference oedometer modulus. The triaxial data (blue curve) have been digitised from [Deng et al. \(2011b\)](#).

is identified by a "kink" observed in either the $\varepsilon_a - q$ (Figure 3-25) or the $\varepsilon_a - \varepsilon_v$ (Figure 3-26) plots. It should be noted that the stress ratio for a conventional drained triaxial test is $\eta = q/p' = 3/1$ (Figure 3-27).

The cap for the case of the reduction of E_{50}^{ref} to 6MPa is not discernible in Figure 3-27, as it coincides with the one resulting for a decrease in the m parameter to 0.55 (cyan curve).

The influence of changing the value of E_{50}^{ref} is not discussed as the same explanations given in Section 3-5-2-1 apply here.

3-5-3-1 Investigation on the influence of E_{oed}^{ref}

An increase in E_{oed}^{ref} to 15MPa induces a slightly softer response in the $\varepsilon_a - q$ graph before the cap is reached ($\varepsilon_a < 5\%$, Figure 3-25). After the stress path has reached the cap ("kink" observed at $\varepsilon_a \approx 5\%$ in Figures 3-25 and 3-26) the rate of strain hardening in the $\varepsilon_a - q$ plot reduces further. This may be attributed to the double hardening process, as additional ε_1^p are produced due to cap hardening. Such a decrease in the stiffness evolution of the material has not been observed in the case of simulating the *Ess75Tr01* test (Section 3-5-2-2), where the double hardening procedure initiates from the first steps of the analysis.

Before the stress path reaches the cap the total volumetric strains are almost identical to the ones of the analysis with the *Initial data*. This can be explained by the assumption that during shear hardening no ε_v^p are generated (Section 3-5-2-1). As a result, $\varepsilon_v = \varepsilon_v^e$. Since a change in E_{oed}^{ref} is not expected to induce the generation of elastic volumetric strains, ε_v will

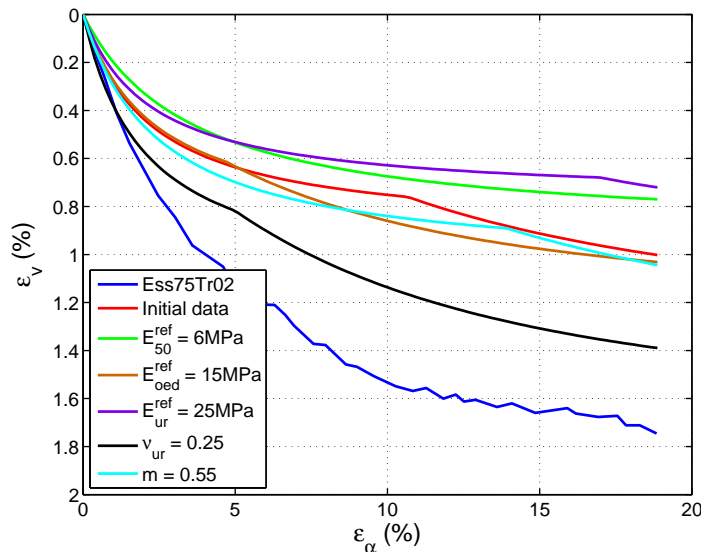


Figure 3-26: Volumetric strain (ε_v) versus axial strain (ε_a) resulting from varying some of the input parameters of the HS model, for the simulation of the *Ess75Tr02* test. E_{50}^{ref} is the reference secant modulus, E_{oed}^{ref} is the reference oedometer modulus, E_{ur}^{ref} is the reference unloading-reloading modulus, ν_{ur} is the unloading-reloading Poisson's ratio and m is a measure of the stress dependency of stiffness. The triaxial data (blue curve) have been digitised from [Deng et al. \(2011b\)](#).

remain unchanged.

After the stress path has intersected the cap (Figure 3-27) the rate of the generated ε_v increases (Figure 3-26) due to the additional plastic volumetric cap strains. Even though for $E_{oed}^{ref} = 15\text{MPa}$ the value of the α parameter is smaller than that of the *Initial data* (Table 3-7), the rate of increase of ε_v is initially larger in the former case ($\delta\varepsilon_v/\delta\varepsilon_a \approx 0.048$ compared to $\delta\varepsilon_v/\delta\varepsilon_a \approx 0.035$ for the simulation with the *Initial data*, Figure 3-26). This may be explained by the reduction of the plastic multiplier (λ) for a lower stress level, which induces a larger rate of $\dot{\varepsilon}^{pc}$, according to Equation 3-22. In Figure 3-27 it can be observed that p' is smaller at the point of the intersection of the stress path with the cap (brown curve) for $E_{oed}^{ref} = 15\text{MPa}$, compared to the case of the *Initial data* (red curve).

On the contrary, the rate of increase of ε_v is lower at the end of the analysis for $E_{oed}^{ref} = 15\text{MPa}$ ($\delta\varepsilon_v/\delta\varepsilon_a \approx 0.013$ compared to $\delta\varepsilon_v/\delta\varepsilon_a \approx 0.021$ for the simulation with the *Initial data*), probably owing to the fact that the cap hardening process starts at earlier calculation steps in the case of $E_{oed}^{ref} = 15\text{MPa}$, leading to a lower rate of cap expansion (thus smaller λ and lower $\dot{\varepsilon}^{pc}$, Equation 3-22), in addition to the cap being shallower. At the end of the analysis the resulting volumetric strains are larger for $E_{oed}^{ref} = 15\text{MPa}$ (Figure 3-26).

The fact that the cap is shallower for a larger E_{oed}^{ref} (Figure 3-27), which leads to an intersection with the stress path at smaller ε_a (Figure 3-26), may be explained by the notion that a stiffer soil is expected to yield at lower level of strains. That is because for the same strain increment, a larger stress increment occurs for a stiffer material.

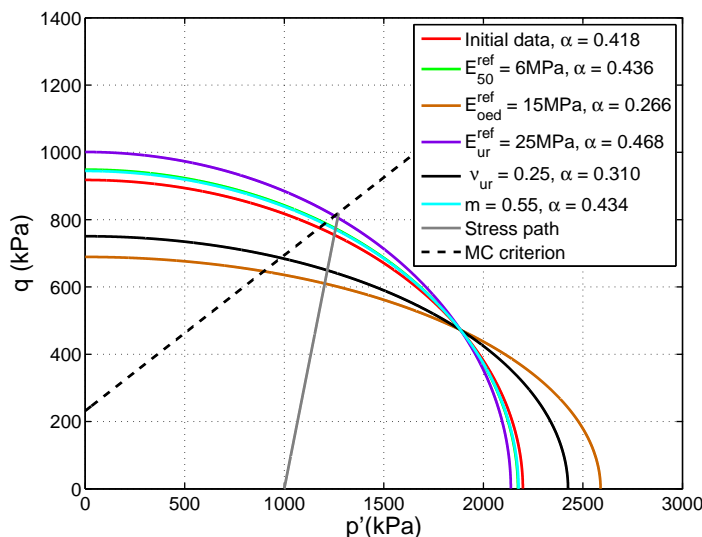


Figure 3-27: Representation, on the deviator stress (q) versus mean effective stress (p') plane, of the initial caps of the HS model resulting from changing some of the model input parameters. The grey line concerns the stress path of the *Ess75Tr02* test. E_{50}^{ref} is the reference secant modulus, E_{oed}^{ref} is the reference oedometer modulus, E_{ur}^{ref} is the reference unloading-reloading modulus, ν_{ur} is the unloading-reloading Poisson's ratio, m is a measure of the stress dependency of stiffness and α is an internal model parameter which determines the steepness of the caps. MC denotes Mohr Coulomb. The resulting cap for $E_{50}^{ref} = 6\text{MPa}$ is not visible since it coincides with that of $m = 0.55$.

3-5-3-2 Investigation on the influence of E_{ur}^{ref}

An increase in E_{ur}^{ref} does not induce any changes in the $\varepsilon_a - q$ graph for the reasons explained in Section 3-5-2-3.

The generated ε_v reduce significantly for an increase in E_{ur}^{ref} to 25MPa. This is ascribed to the fact that the steepness of the cap increases substantially (α rises, Table 3-8), leading to a material behaviour which is almost exclusively dominated by shear hardening. The stress path in Figure 3-27 intersects the related cap (purple curve) at a very large q and therefore close to the end of the simulation. Consequently, the "kink" (thus, the generation of ε_v^{pc}) in the $\varepsilon_a - \varepsilon_v$ diagram (Figure 3-26) occurs at large axial strains. Therefore, the volumetric response of the material is governed by elasticity, as no ε_v^p are generated due to shear hardening (Section 3-5-2-1). From Equations 3-6 and 3-11 it can be concluded that an increase in E_{ur}^{ref} leads to smaller ε_v^e .

3-5-3-3 Investigation on the influence of ν_{ur}

A decrease in ν_{ur} to 0.25 does not alter the evolution of stiffness and mobilised shear strength of the material, which has also been observed for the simulation of the *Ess75Tr01* test (Section 3-5-2-4).

Nevertheless, the volumetric response of the soil is altered considerably (Figure 3-26). A decrease in ν_{ur} leads to a smaller value of the α parameter (Table 3-9), which implies that the cap becomes shallower than the one corresponding to the *Initial data* (black curve in Figure 3-27). In Section 3-5-3-2 it was shown that only elastic volumetric strains develop before the stress path reaches the cap. A decrease in ν_{ur} induces larger elastic volumetric strains before the "kink" occurs (Figure 3-26) since ε_3^e reduce (Equation 3-11) and $\varepsilon_v^e = \varepsilon_1^e - 2\varepsilon_3^e$.

After the stress path intersects with the cap, the rate of the generated volumetric strains for $\nu_{ur} = 0.25$ is larger than that of the simulation with the initial data ($\delta\varepsilon_v/\delta\varepsilon_a \approx 0.074$ for the former and $\delta\varepsilon_v/\delta\varepsilon_a \approx 0.035$ for the latter), although the cap steepness and the swelling to compression ratio are smaller for the former (Table 3-9). This may be attributed to the lower p' at which the stress path meets the cap, as explained in Section 3-5-3-1. The rate of increase of ε_v at yield is even larger than the one for the simulation with $E_{oed}^{ref} = 15\text{MPa}$ ($\delta\varepsilon_v/\delta\varepsilon_a = 0.048$), as the cap parameters are larger ($\alpha = 0.310$, $K_s/K_c = 1.198$ for $\nu_{ur} = 0.25$ and $\alpha = 0.266$, $K_s/K_c = 1.110$ for $E_{oed}^{ref} = 15\text{MPa}$). At the end of the analysis with $\nu_{ur} = 0.25$, $\delta\varepsilon_v/\delta\varepsilon_a = 0.019$, which is lower than that of the analysis with the *Initial data* ($\delta\varepsilon_v/\delta\varepsilon_a = 0.021$). This may be explained by the arguments developed in Section 3-5-3-1.

3-5-3-4 Investigation on the influence of the m parameter

A decrease in m to 0.55 causes a softer response of the material in the $\varepsilon_a - q$ graph. The resulting curve is not presented in Figure 3-25 since it coincides with the one of the simulation with $E_{oed}^{ref} = 15\text{MPa}$. An explanation for this response was given in Section 3-5-2-5.

A possible explanation for the increase in the α and the K_s/K_c parameters, due to a decrease in m (Table 3-10), was given in Section 3-5-2-5. Before the stress path reaches the cap of the HS model the volumetric strains are larger than the ones resulting from the simulation with the *Initial data* (Figure 3-26). This is attributed to the generation of larger ε_v^e , induced by the

lower value of E_{ur} (Section 3-5-2-5). Consequently, ε_v will be larger since they are equal to the elastic volumetric strains when the stress path lies below the cap (Section 3-5-3-2). The generated ε_v^{pc} are not significant as cap hardening occurs at a late stage during the analysis (see Figure 3-27).

3-5-4 Effects of the model input parameters on the results of the simulation of the *Ess75Tr03* test

The numerical results for the simulation of the *Ess75Tr03* test are shown, by means of $\varepsilon_a - q$ and $\varepsilon_a - \varepsilon_v$ diagrams, in Figures 3-28 and 3-29, respectively. The former does not include the results obtained by changing the values of E_{oed}^{ref} , E_{ur}^{ref} and ν_{ur} since they coincide with the ones acquired from the simulation with the *Initial data*. Even though the resulting $\varepsilon_a - q$ plot for the simulation with $m = 0.55$ almost coincides with the red curve, it is presented in order to compare it with the respective diagrams of the analyses of the *Ess75Tr01* and *Ess75Tr02* tests.

In the case of the simulation of the *Ess75Tr03* test an $OCR = 4.4$ is imposed. This leads to a stress path which does not intersect with any of the initial caps (Figure 3-30). Hence, in all considered cases, only shear hardening occurs and the volumetric response is governed entirely by the generated ε_v^e .

3-5-4-1 Investigation on the influence of E_{50}^{ref}

For a reduction in E_{50}^{ref} to 6MPa the model response is softer in the $\varepsilon_a - q$ plot (Figure 3-28) for the reasons explained in Section 3-5-2-1.

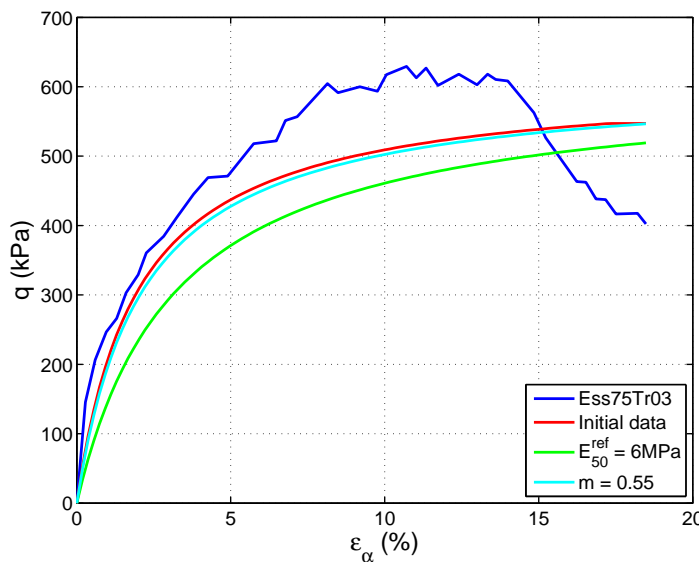


Figure 3-28: Deviator stress (q) versus axial strain (ε_a) resulting from varying some of the input parameters of the HS model, for the numerical simulation of the *Ess75Tr03* test. E_{50}^{ref} is the reference secant modulus and m is a measure of the stress dependency of stiffness. The triaxial data (blue curve) have been digitised from [Deng et al. \(2011b\)](#).

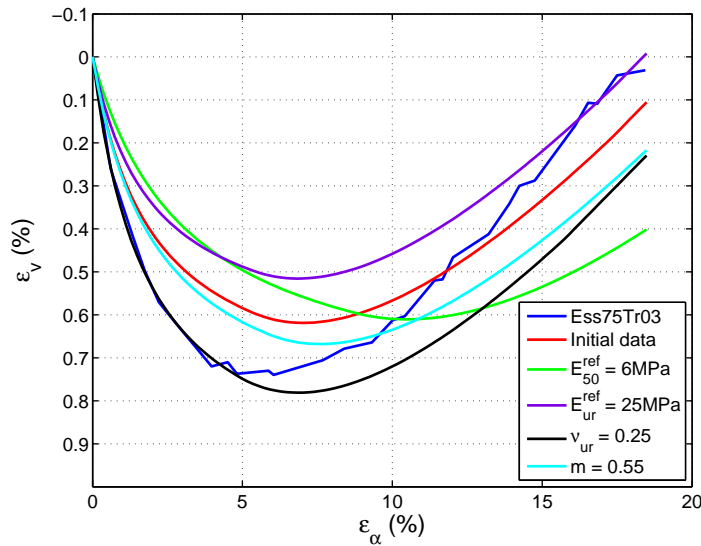


Figure 3-29: Volumetric strain (ε_v) versus axial strain (ε_a) resulting from varying some of the input parameters of the HS model, for the simulation of the *Ess75Tr03* test. E_{50}^{ref} is the reference secant modulus, E_{ur}^{ref} is the reference unloading-reloading modulus, ν_{ur} is the unloading-reloading Poisson's ratio and m is a measure of the stress dependency of stiffness. The triaxial data (blue curve) have been digitised from [Deng et al. \(2011b\)](#).

In the $\varepsilon_a - \varepsilon_v$ graph (Figure 3-29), it is observed that larger ε_a for the same level of ε_v are produced, due to the increase in ε_1^p (Section 3-5-2-1). The peak value of the generated total volumetric strains is transferred to the right. In the case of the simulation with the reduced E_{50}^{ref} (green curve), the peak value of ε_v is marginally lower than that corresponding to the analysis with the *Initial data*. This indicates that the assumption $\varepsilon_v^p \approx 0$ during shear hardening holds true (Section 3-5-2-1).

The transition from compression to dilatancy does not occur abruptly as the latter develops before the stress path meets the MC criterion, according to Equations 3-14 to 3-17. The resulting $\varepsilon_a - \varepsilon_v$ curve for the simulation with the *Initial data* ends at a smaller level of compressive ε_v (Figure 3-29) since the the MC criterion is met at smaller ε_a . Thus, the stress path will travel longer (towards a larger p' in Figure 3-30) along the MC surface.

3-5-4-2 Investigation on the influence of E_{oed}^{ref}

An increase of E_{oed}^{ref} to 15MPa does not cause any changes in the $\varepsilon_a - q$ graph. The same applies for the volumetric response of the model, where the resulting curve almost coincides with that of the *Initial data* (Figure 3-29). This supports the suggestion that a change in E_{oed}^{ref} does not induce the generation of ε_v^e (Section 3-5-3-1).

3-5-4-3 Investigation on the influence of E_{ur}^{ref}

An increase in E_{ur}^{ref} to 25MPa does not lead to a change in the model response, in terms of the evolution of the mobilised shear strength and stiffness, for the reasons explained in Section 3-5-2-3.

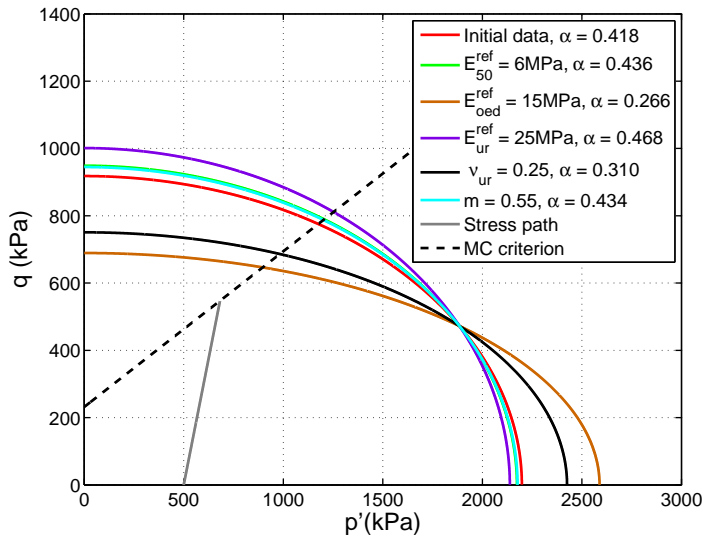


Figure 3-30: Representation, on the deviator stress (q) versus mean effective stress (p') plane, of the initial caps of the HS model resulting from changing some of the model input parameters. The grey line concerns the stress path of the *Ess75Tr03* test. E_{50}^{ref} is the reference secant modulus, E_{oed}^{ref} is the reference oedometer modulus, E_{ur}^{ref} is the reference unloading-reloading modulus, ν_{ur} is the unloading-reloading Poisson's ratio, m is a measure of the stress dependency of stiffness and α is an internal model parameter which determines the steepness of the caps. MC denotes Mohr Coulomb. The resulting cap for $E_{50}^{ref} = 6\text{ MPa}$ is not visible since it coincides with that of $m = 0.55$.

On the other hand, the generated ε_v are substantially lower (3-29) as the ε_v^e , which are equal to the total volumetric strains, decrease for an increase in E_{ur}^{ref} (Section 3-5-2-3).

3-5-4-4 Investigation on the influence of ν_{ur}

As in the previous cases (Sections 3-5-2-4 and 3-5-3-3), no substantial change is observed in the $\varepsilon_a - q$ diagram for a decrease in ν_{ur} to 0.25. The value of G_{50}^{ref} , as calculated by the internal algorithm of the program, is slightly larger with respect to the one of the *Initial data* (Table 3-9).

The generated volumetric strains are larger than the ones of the analysis with the *Initial data*, due to the smaller elastic radial strains, according to Equation 3-11 ($\varepsilon_v^e = \varepsilon_a^e - 2\varepsilon_r^e$ for triaxial compression).

3-5-4-5 Investigation on the influence of the m parameter

The model response is softer for a reduction in the value of the m parameter, in terms of the $\varepsilon_a - q$ plot, for the simulations of the *Ess75Tr01*, *Ess75Tr02* and *Ess75Tr03* tests, due to the lower value of E_{50}^{ref} (Section 3-5-2-5). However, the stiffness reduction becomes less significant as the OCR increases (Figures 3-23, 3-25 and 3-28). It should be reminded that the curve in Figure 3-25 coincides with the one of $E_{oed}^{ref} = 15\text{ MPa}$. The less significant stiffness reduction with increasing value of the OCR may be ascribed to the decrease of the generated plastic axial strains with higher level of over-consolidation. For the simulation where NC conditions

are imposed, ε_a^p due to cap and shear hardening develop from the beginning of the analysis since the stress path lies on both loci. For the simulation with $OCR = 2.2$, the plastic axial cap strains are added at a later stage during the analysis since the stress path does not reach the cap immediately. For the analysis with $OCR = 4.4$ the stress path does not intersect with the cap, leading only to the generation of shear hardening-induced ε_a^p . This line of reasoning may hold true if the model considers that the total ε_a^p result from adding the compression- and shear hardening-induced plastic axial strains in double hardening situations.

The produced ε_v are larger for a reduction in m to 0.55 (Figure 3-29) as the volumetric response of the material is dominated by ε_v^e , which increase for a decrease in E_{ur} (Equations 3-6 and 3-11).

3-5-5 On the response of the cap of the HS model

In this section an attempt is made to explain the influence of E_{ur}^{ref} and ν_{ur} on the steepness of the cap of the HS model. The effects of E_{50}^{ref} , E_{oed}^{ref} and m are deemed to have been explained sufficiently in Sections 3-5-2-1, 3-5-2-2 and 3-5-2-5, respectively.

In Table 3-8 it is observed that an increase in E_{ur}^{ref} induces a steeper cap and a larger swelling to compression ratio, which entail the generation of larger ε_v^{pc} . This may be explained by the notion that a stiffer elastic response of the material, which induces smaller ε_v^e , will cause larger ε_v^p after it yields, for a predefined amount of strains. For the HS model, E_{ur} controls the magnitude of the elastic volumetric strains through Equation 3-11. In addition, E_{ur} is positively related to E_{oed} in the context of elasticity, according to the equation below:

$$E_{oed,ur} = \frac{E_{ur} (1 - \nu_{ur})}{(1 - 2\nu_{ur})(1 + \nu_{ur})} \quad (3-34)$$

where $E_{oed,ur}$ is the unloading-reloading (elastic) stress-dependent oedometer modulus. According to this equation, an increase in E_{ur} causes a larger $E_{oed,ur}$. The line of reasoning expressed before leads to the conclusion that an increase in $E_{oed,ur}$ (thus a lower compressibility in the elastic domain) will induce a more plastic response after yield. Consequently, the cap of the HS model will become steeper (the α parameter will increase), leading to larger ε_v^{pc} , and ε^{pc} will be higher (K_s/K_c will increase).

A similar explanation can be given for the effect of ν_{ur} on the response of the cap of the HS model. In Table 3-9 it is observed that a decrease in ν_{ur} induces a shallower cap and smaller K_s/K_c . The unloading-reloading Poisson's ratio controls the generation of ε_v^e , through Equation 3-11, as is the case for E_{ur} . According to Equation 3-34, a decrease in ν_{ur} leads to a reduction in $E_{oed,ur}$ and, therefore, the compressibility in the elastic domain increases. Consequently, a less plastic response will be exhibited after yield, which implies a shallower cap and a smaller K_s/K_c .

The aforementioned hold true for NC conditions, where the stress path lies on the cap from the beginning of the simulations. However, for OC conditions a steeper cap does not necessarily lead to larger ε_v at the end of the analysis, since the stress path may not meet the yield locus. Furthermore, initial yield may take place at a late stage during the simulations, i.e. at a large value of p' , leading to a low value of λ and thus, to low $\dot{\varepsilon}^{pc}$ (see Sections 3-5-3-1 and 3-5-3-3).

3-6 Limitations of the laboratory tests and the numerical tool

The evaluation of the soil models, regarding their ability to capture the BC response, has been based on the results of the simulations of triaxial and oedometer tests (Section 3-3) with the lab test facility of *PLAXIS*. Nevertheless, the conditions met during the laboratory tests are expected to be different than the ones found in the course of a tunnel excavation.

Limitations of the simulated laboratory tests

For the investigated triaxial tests it holds $\sigma'_2 = \sigma'_3$ (which implies triaxial compression), whereas general stress states, including extension, apply during a tunnelling project. Therefore, the stress paths followed by the soil close to the excavation are expected to be different than the ones followed in a triaxial test. Moreover, during a triaxial test the level of confinement and the magnitude of the OCR are pre-defined, leading to a specific evolution of the stiffness and the mobilised shear strength of the material (Section 2-4-2). However, the values of σ'_3 and the OCR may be different and may vary during a tunnel excavation. In addition, the considered triaxial tests were performed in drained conditions. Nevertheless, undrained conditions in the short term, and consolidation, accompanied by unsaturated soil behaviour, are expected in the long term, for a tunnel excavation in the BC formation (Section 1-2). The duration of swelling of the BC before shearing may be different between the triaxial tests and an actual project, which may lead to different soil behaviour, in terms of the stiffness and ductility of the material (see Section 2-4-3). Furthermore, this effect has not been considered in the numerical simulations. Finally, the BC specimens originating from Essen were isotropically consolidated before shearing, i.e. a $K_0 = 1$ was assumed (Section 2-4-2-2). Consequently, the influence of an initially anisotropic stress field on the behaviour of the soil has not been considered ($K_0 \approx 0.3 - 0.9$ at the HADES URF, [Bernier et al., 2007a](#)).

The different boundary conditions that are present in oedometer loading and during a tunnel excavation implies different stress paths, and therefore different material response between the two cases.

The triaxial stress conditions might be closer to the ones met during tunnelling as shearing is likely to be the most predominant process. However, investigation on the response of the BC on unloading and reloading has been possible only via one-dimensional loading, as far as the laboratory tests performed by [Deng et al. \(2011b\)](#) are concerned. The simulation of triaxial tests conducted on BC samples, which include unloading-reloading loops ([Barnichon et al., 2000](#)) could be useful.

Limitations of the numerical tool

In the lab test facility of *PLAXIS* the response of a soil element is considered, i.e. no finite element mesh is generated. As a result, investigation on the interaction among the soil elements of the modelled sample is not possible. Such an interaction may include stress redistribution and strain localisation.

Calibration of the HS model with $\nu_{ur} = 0.25$

From Figures 3-23 to 3-26 and Figures 3-28, 3-29 it can be observed that a value of $\nu_{ur} = 0.25$ leads to a better calibration of the HS model with the triaxial tests results. However, severe divergence for the resulting C-D and E-F paths of the simulation of the *Ess75Oedo1* test occurs (Figure 3-31). That is because a lower value of ν_{ur} induces a larger inclination in the

unloading branch of the $\sigma'_h - \sigma'_v$ curve, leading to an earlier intersection with the yield function of the MC criterion. Once this diagram meets with the MC criterion fully plastic unloading occurs. This intersection is marked by the change in slope of the resulting unloading C–D and E–F paths (red curve in Figure 3-31), of which the steeper branches coincide. As a result, they end at the same value of the void ratio (the resulting points D and F coincide).

It is noted that the inclination of the $\sigma'_h - \sigma'_v$ plot ($=\delta\sigma'_v/\delta\sigma'_h$) on unloading is equal to $(1 - \nu_{ur})/\nu_{ur}$. The latter is equal to 2.333 and 3 for $\nu_{ur} = 0.3$ and $\nu_{ur} = 0.25$, respectively.

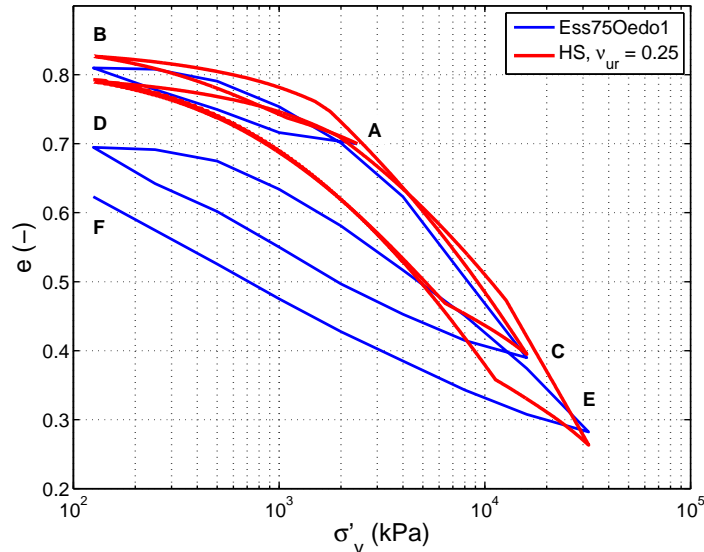


Figure 3-31: Void ratio (e) versus vertical effective stress (σ'_v) for the numerical simulation of the *Ess75Oedo1* test with the *Initial data* of the HS model, for $\nu_{ur} = 0.25$. The oedometer test results (blue curve) have been digitised from [Deng et al. \(2011b\)](#).

3-7 Summary

In this chapter four soil models were evaluated, regarding their ability to capture the Boom Clay (BC) response in three drained triaxial tests and in one oedometer test, performed on BC samples, found from the literature. This assessment aimed at selecting an appropriate material model for modelling the behaviour of BC in tunnelling conditions. To this purpose, the Linear Elastic Perfectly Plastic-Mohr Coulomb (LEPP-MC) model, the Modified Cam-Clay (MCC) model, the Soft Soil-Creep (SS-C) model and the Hardening Soil (HS) model were calibrated on the basis of the test results. The tests were numerically simulated in the lab test facility of the *PLAXIS 2D 2011* finite element program. The models were evaluated by comparing the numerical results with the test data.

Information on the theoretical background and the most usual geotechnical engineering applications of the evaluated models was first given. Then, the ability of the soil models to reproduce the most important aspects of the BC behaviour, which were observed in the considered tests, was assessed.

The LEPP-MC model was found not to capture the BC response in triaxial stress conditions sufficiently, as the dependency of the mobilised shear strength and stiffness of the soil on the stress level and the value of the Over-Consolidation Ratio (OCR) was not reproduced. Moreover calibration of the model based on the oedometer test results could not be achieved. Nevertheless, the model performance was considered to be acceptable for the simulations of the triaxial tests, given its low level of intricacy and the limited number of the required input parameters.

The MCC model was found to be capable of capturing the deviatoric and the volumetric response of BC in Normally Consolidated (NC) conditions, in drained triaxial compression. In addition, it was found to be the only model that accounts for the strain softening response of the soil, but only qualitatively and not after strain hardening for the considered stress path, for high values of the OCR. The non-linear material behaviour was not well captured in OC conditions. The hysteresis exhibited by the BC in oedometer loading was not reproduced, in addition to the resulting void ratio being much different from the test data at the end of the unloading branches.

The SS-C model, as in the case of the MCC model, was found to perform well in NC conditions, in the deviator stress (q) versus axial strain (ε_a) space. This was not the case for OC conditions. Moreover, it was observed that exceedingly large volumetric strains were produced for low values of OCR. The SS-C model was found to capture the BC response in oedometer loading the best, compared to all other models.

The performance of the HS model was considered to be the most adequate in drained triaxial compression as the mobilised shear strength and the evolution of the stiffness of BC was very well captured for NC and OC conditions. In addition, the volumetric response was well reproduced, except for intermediate values of the OCR. The model response in oedometer stress conditions was also considered to be sufficiently captured. Based on the suggestion that the deviatoric response of the BC would be the most relevant in tunnelling conditions, the HS model was selected as the most appropriate to numerically simulate a tunnel excavation in the BC formation.

A detailed description of the HS model followed, by means of its governing equations for

drained triaxial compression and its representation in stress-strain space.

Subsequently, the lab test facility of *PLAXIS 2D 2010* was used in order to investigate the influence of varying selected HS model input parameters on the model response in the triaxial tests simulations. This study was complemented by inspecting the changes in the model internal parameters, which control the evolution of the generated plastic strains, induced by varying the input parameters. For all simulations it was found that the response of the model in the $\varepsilon_a - q$ space was almost exclusively influenced by the value of the reference secant modulus (E_{50}^{ref}) as it affected the generated plastic axial strains (ε_a^p). An effect of the level of the stress dependency of stiffness (m) was also identified, attributed to the changes it induces in the value of the stress dependent secant modulus, E_{50} , (thus, in the generated ε_a^p).

For NC conditions, it was found that the volumetric behaviour of the material was governed by the response of the cap of the model. The latter concerns the produced plastic volumetric cap strains (ε_v^{pc}), which are controlled by the internal cap parameters, as well as by the current stress state (p'). For intermediate values of the OCR the volumetric response of the soil was found to depend mainly on the initial position of the cap in the $p' - q$ plane. For stress paths lying below the yield locus, only elastic volumetric strains (ε_v^e) are produced. If the stress path meets the cap ε_v^{pc} are also generated. For the latter case it was observed that a stiffer cap response (i.e. a shallower cap) leads to an initially larger rate of produced volumetric strains ($\dot{\varepsilon}_v$), probably owing to the lower p' at initial yield, which causes a larger plastic multiplier (λ). For large values of the OCR the stress path did not meet the cap of the HS model, leading to an elastically dominated volumetric response of the material.

Finally, a discussion on the possible limitations of the laboratory tests and the numerical tool, employed for the purpose of this chapter, was made. It was mentioned that the boundary conditions, which are present in the considered laboratory tests, are expected to be different than the ones met during a tunnel excavation, leading to different stress paths and, therefore, to a distinct response of the BC material between the two cases. It was noted that the limitation of the numerical tool may lie in the fact that only one soil element was considered during the simulations of the laboratory tests. As a result, research on stress redistribution and strain localisation effects was not made.

Chapter 4

Modelling a deep tunnel excavation in the Boom Clay formation

4-1 Introduction

In this chapter a simulation of an undrained tunnel excavation in the BC formation is presented, with the use of the *PLAXIS 2D 2011* finite element program ([Plaxis, 2011b](#)), in plane strain conditions. The BC response has been modelled with the HS model, which was considered to perform the best, among the investigated soil models, in simulated drained triaxial compression and in oedometer loading (Section 3-3-7).

The scope of this chapter is the investigation on the influence of selected input parameters of the HS model on the extent of the hydro-mechanical disturbance in the soil around the excavation and on the magnitude of the internal forces acting on the tunnel liner. This investigation also includes a preliminary estimation of the level of influence of the model input parameters. To this purpose, a mechanical sensitivity analysis has been conducted, during which these parameters are changed to an upper and a lower bound value, which are found from the literature regarding the BC formation. The results of these analyses were compared to the ones of a simulation with the mean of the values of the model input parameters.

The aforementioned results have been explained by examining the stress paths and the evolution of the elastic and the elastoplastic shear stiffness of the material in the proximity of the excavation. Furthermore, the profiles of the stresses and the pore water pressures along a radial line have been utilised.

In Section 4-2 the set up of the geotechnical model, of the calculation phases and of the mechanical sensitivity analysis are described. The results of the latter are presented, investigated and explained in Section 4-3. A preliminary estimation on the level of influence of the varied model input parameters is made in Section 4-4 and finally, a summary for this chapter is given in Section 4-5.

4-2 Set up of the numerical simulations

In this section the set up of the geotechnical model is described first. Then, the calculation phases of the numerical analyses with the *PLAXIS 2D 2011* finite element program are presented. Finally, the process of the mechanical sensitivity analysis is outlined.

4-2-1 Set up of the geotechnical model

Outline of the finite element mesh

The simulated tunnel excavation has been based upon the case of the construction of the connecting gallery at the HADES URF ([Bernier et al., 2007b](#)). The geotechnical domain used for all simulations is shown in Figure 4-1a. The tunnel centerline is located at a depth of 225m below the ground surface. As mentioned in Section 4-1, plane strain conditions have been assumed, as the tunnel is long. Therefore, only a vertical cross section perpendicular to the tunnel centerline has been considered for the analyses. Symmetry has been assumed with respect to the vertical plane along the axis of the excavation as strain localisation and fracture propagation effects due to pre-existing planes of weakness or owing to the local material heterogeneity, which may induce a non-symmetric extent of the hydro-mechanical disturbance, have not been considered for reasons of simplicity. As a result, only half of the problem has been modelled.

The part above a depth of -165m has not been considered relevant for the analyses. The term "relevant" denotes the extent of the domain beyond which its boundaries are deemed not to affect significantly the results of the numerical analyses. The relevant part of the domain extends 60m above and below the tunnel centerline. The same applies for the vertical boundary. The overburden of the part of the soil from 0m to -165m was taken into account by imposing a distributed load at the upper boundary. For a saturated unit weight of BC equal to $\gamma_{sat} = 20\text{kN/m}^3$ (see Table 2-2) and a water unit weight $\gamma_w = 10\text{kN/m}^3$, the distributed load is equal to $(\gamma_{sat} - \gamma_w) \times \text{depth} = 1650\text{kPa}$ as the level of the groundwater was set at the ground surface ([Bernier et al., 2007b](#)). Even though the extent of the relevant part of the domain is 60m above the tunnel centerline, the original finite element mesh included the depth from the ground surface (0m) until its deepest boundary (located at a depth of -285m, see Figure 4-1a), for the reasons that will be explained in Section 4-2-2.

Full fixities were imposed to the lower boundary of the domain, whereas the ones at the sides were free to move in the vertical direction (horizontal fixities, see Figure 4-1a). No fixities were introduced to the top boundary of the mesh.

The rectangle around the tunnel in Figures 4-1a and 4-1b has been introduced in order to refine the mesh in the enclosed area. That is because higher accuracy is required in the vicinity of the excavation where stress and strain gradients are expected to be higher.

The finite element mesh (from a depth of 0m to a depth of -285m) comprised of 3063 fifteen-node triangular elements with twelve Gauss (stress) points. The finite element discretisation of the relevant part of the domain (from a depth of -225m to a depth of -285m) is shown in Figure 4-1b.

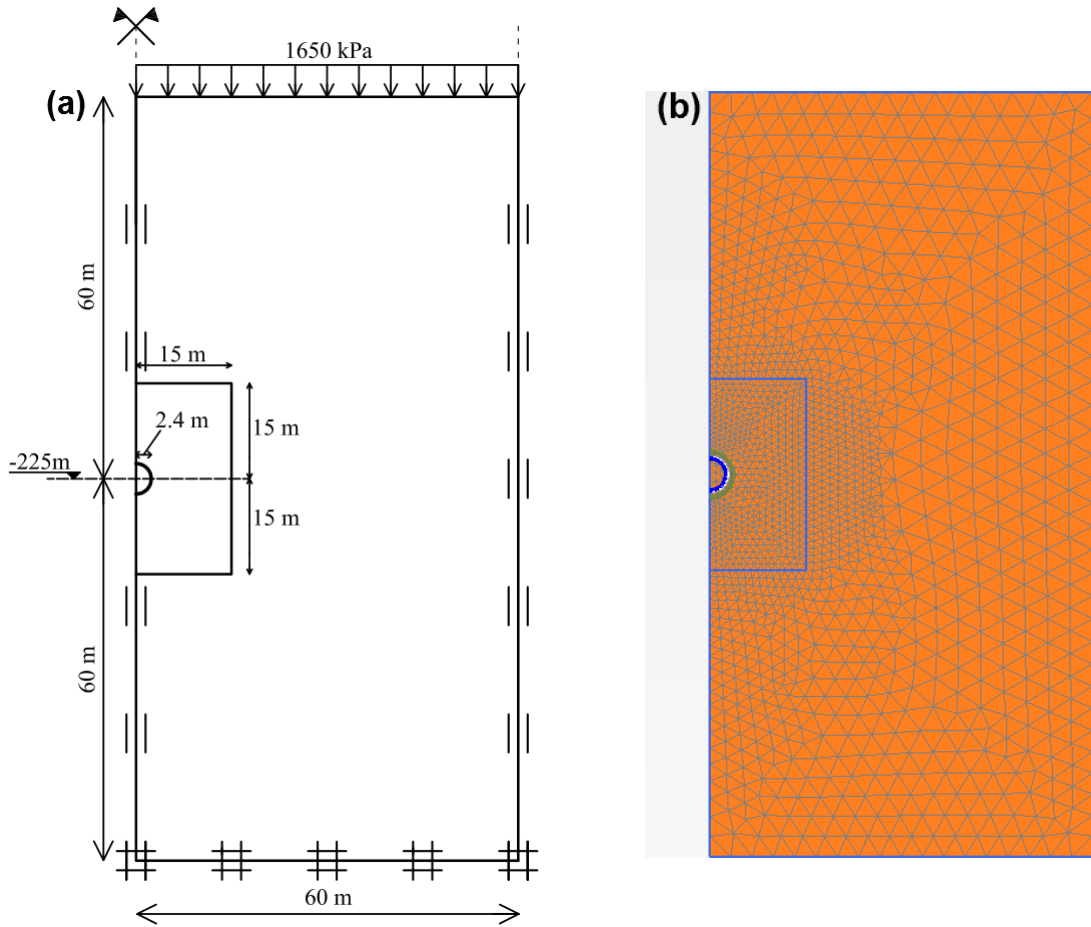


Figure 4-1: Relevant part of the geotechnical domain used for the analyses (a) and finite element discretisation of the relevant part of the geotechnical domain (b). The term "relevant" refers to the extent of the domain beyond which its boundaries are deemed not to affect significantly the results of the numerical analyses.

Tunnel geometry and liner properties

The external radius (r_{ext}) of the tunnel and the liner properties are listed in Table 4-1. The cross section of the tunnel was considered to be circular with an external diameter of 4.8m and a thickness (d) equal to 0.4m. The liner behaviour has been assumed to be linear elastic.

It is noted that the cross sectional area (A) of the liner per meter out of plane, for plane strain conditions, is equal to its thickness, i.e. $A = 0.4\text{m}^2/\text{m}$. Furthermore, the moment of inertia (I) of the liner is given by (Bakker, 2003):

$$I = \frac{1}{12}d^3 \quad (4-1)$$

Therefore, for the considered case $I = 5.33 \times 10^{-3}\text{m}^4/\text{m}$. The interface between the tunnel wall and the host rock was assumed to be rigid, i.e. it was considered to have the same strength characteristics with the surrounding soil (Plaxis, 2011b). When the HS model is used the strength of the interface is governed by the MC criterion. If a rigid interface is

Table 4-1: Characteristics of the tunnel and the tunnel liner used for the simulations of the mechanical sensitivity analysis (After Bernier et al., 2007b).

Definition	Symbol	Units	Value
Geometry			
External tunnel radius	r_{ext}	[m]	2.4
Liner properties			
Thickness	d	[m]	0.40
Young's modulus	E	[kN/m ²]	50.0×10^6
Axial stiffness	EA^*	[kN/m]	20.0×10^6
Bending stiffness	EI^{**}	[kNm ² /m]	266.7×10^3

* Cross sectional area per meter out of plane.

** Moment of inertia per meter out of plane.

selected, the strength characteristics of the interface, i.e. its friction angle (φ_i), its cohesion (c_i) and its dilatancy angle (ψ_i) are equal to the ones of the surrounding soil. The stiffness characteristics of the interface are calculated according to (Plaxis, 2011b):

$$G_i = R_{inter}^2 G_{soil} \leq G_{soil} \quad (4-2)$$

with G_i being shear modulus of the interface, G_{soil} being the shear stiffness of the soil and R_{inter} being a reduction factor. In the considered case $R_{inter} = 1$ and thus, $G_i = G_{soil}$. Also, the oedometer modulus of the interface ($E_{oed,i}$) is given by:

$$E_{oed,i} = 2G_i \frac{1 - \nu_i}{1 - 2\nu_i} \quad (4-3)$$

where ν_i is the Poisson's ratio of the interface, equal to 0.45. The elastic gap displacement of the interface is calculated as follows:

$$\text{Elastic gap displacement} = \frac{\sigma_N t_i}{E_{oed,i}} \quad (4-4)$$

with σ_N being the normal stress acting on the interface and t_i being the virtual thickness of the interface. The slip displacement is given by:

$$\text{Elastic slip displacement} = \frac{\tau t_i}{G_i} \quad (4-5)$$

where τ is the shear stress acting on the interface.

The assumption of a rigid interface may be supported by the fact that the imposed convergence is homogeneous around the tunnel periphery (see Section 4-2-2), in addition to the initial stress field being isotropic (see below). As a result, no significant shear stresses (and thus, slippage) are expected to occur between the soil and the tunnel liner.

Assumptions for the geotechnical model

The main hypotheses made for the development of the geotechnical model are listed below:

- The excavation is realised under plane strain conditions.
- The excavation is realised under undrained conditions.
- The initial stress field is isotropic ($K_0 = 1$).
- The soil is homogeneous.

The first hypothesis can be supported by the suggestion that the length of the tunnel is such that allows for considering the out of plane strains to be equal to zero for reasons of simplicity. The following three assumptions are made for reasons of reducing the level of complexity of the research under consideration.

It is noted that the value of K_0 can either be automatically determined by the values of POP , K_0^{NC} and OCR through Equation 3-25 or can be specified by the user. The latter has been applied in the considered case. This resulted in an initial isotropic stress field, i.e. $\sigma'_1 = \sigma'_2 = \sigma'_3$, which induced the stress paths to initiate from the hydrostatic axis (see later Section 4-3-1 and Figure 4-2).

4-2-2 Calculation phases

The calculation procedure, which was similar to that described in [Plaxis \(2011c\)](#), comprised four steps:

1) The initial stress field was generated (*K_0 procedure*). For calculating the initial effective stresses and the pore water pressures (u), the domain from the ground surface was considered. Consequently, the initial mesh had a height of 285m since it extended from a depth of 0m to -285m.

A coarse finite element mesh was generated for the part of the model which was not deemed to affect substantially the numerical results (i.e. the part from a depth of 0m to -165m), for reasons of reducing the calculation requirements.

The displacements produced during this calculation phase were set to zero.

2) The part of the mesh from a depth of 0m to -165m was switched off and a distributed load equal to 1650kPa was imposed on the top boundary (see Figure 4-1a), in order to account for the effective stresses which correspond to the removed overburden (see Section 4-2-1). The water level was kept at the ground surface. The generated displacements were set to zero.

3) The tunnel was introduced and the enclosed soil cluster was switched off. The external radius of the tunnel was set to 2.49m so as to account for an over-excavation of 9cm, as explained in the description of the fourth calculation phase.

4) A contraction was imposed on the tunnel, i.e. the external radius was reduced in order to account for the convergence of the walls of the excavation, which was considered to have been induced by a virtual over-excavation of 9cm. The latter resulted from adding the immediate convergence of the host rock due to an over-excavation of 4.5cm, and the radial displacement ahead of the face of the excavation ($\approx 4.5\text{cm}$), which was measured during the construction of the connecting gallery at the HADES URF ([Bastiaens et al., 2003](#)). This explains the larger

r_{ext} (2.49m instead of 2.40m) used in the third calculation phase. The decrease in the tunnel radius was imposed as a contraction, by means of the equation below:

$$\text{Contraction}(\%) = \frac{\pi r_{over}^2 - \pi r_{ext}^2}{\pi r_{over}^2} \quad (4-6)$$

where r_{over} is the radius of the over-excavation. Thus, for the considered case the contraction was equal to 7.098%.

4-2-3 Set up of the mechanical sensitivity analysis

For conducting the mechanical sensitivity analysis, five input parameters of the HS model have been varied. These are the reference secant modulus (E_{50}^{ref}), the reference unloading-reloading modulus (E_{ur}^{ref}), the rate of the level of stress dependency of stiffness (m), the effective friction angle (φ') and the effective cohesion (c'). These have been given an upper and a lower bound value for the BC material. The K_0 -value for normal consolidation was calculated by the program by default, through $K_0^{NC} = 1-\sin\varphi'$ (Jaky, 1944). Thus, it varied with changing φ' (Table 4-2).

It is noted that in a mechanical sensitivity analysis the effect of varying individual input parameters is considered to have the same weight. However, in a sensitivity analysis which is part of a probabilistic analysis the weight of an individual model input parameter on the performance incorporates both the effect of the mechanical model as well as of the parameter uncertainty. For instance, the sensitivity of a response to a variation of a model input parameter will increase for an increasing parameter uncertainty, e.g. expressed in a standard deviation.

Table 4-2 shows the values of the input parameters which have been used for the mechanical sensitivity analysis. In spite of some connection existing among the model input parameters one of them was changed in every simulation. Thus, the examination of the effect of each parameter on the numerical results is expected to be less intricate. The outcomes of the analysis where the parameters have been given the mean of the range of values used (Table 4-2), served as a basis for comparison with the results of all other simulations. This set of parameters will be henceforth referred to as *mean data*. The analyses have been carried out for dilatancy angle $\psi = 0^\circ$ and $\psi = 1^\circ$. Consequently, 22 simulations were performed.

The values of E_{50}^{ref} were back-calculated from the values of E_{50} (Table 4-2) through Equation 3-5. The value of E_{ur} was considered to be three times larger than that of E_{50} , which is equivalent to $E_{ur}^{ref} = 3E_{50}^{ref}$, suggested by Plaxis (2011a). The reference unloading-reloading modulus was calculated from the assigned value of E_{ur} via Equation 3-6. The value of E_{oed} was determined from Equation 3-21, after assuming that $E_{oed}^{ref} = E_{50}^{ref} = 145\text{ MPa}$ in order to prevent the intersection of the stress paths with the cap of the HS model (see next paragraph). In all cases $\sigma_3 = 2250\text{ kPa}$ (corresponding to a depth of -225m for $K_0 = 1.0$) was used and it was assumed that $c' = 0.25\text{ MPa}$, $\varphi' = 13^\circ$ and $m = 0.7$, which are equal to the mean values (Table 4-2). These were not varied so as to exclude their effect on the values of E_{50} and E_{ur} , and subsequently on the numerical results. The values of φ' and c' were kept equal to the mean as they were considered to be more likely to be met.

Table 4-2: Values of the input parameters of the HS model for the mechanical sensitivity analysis.

Parameter	Units	Lower bound	Mean	Upper bound
Varied				
E_{50}/E_{50}^{ref}	[MPa]	200/97	300/145	400/194
E_{ur}/E_{ur}^{ref}	[MPa]	615/298	900/436	1200/531
m	[\cdot]	0.50	0.70	0.87
φ'	[$^\circ$]	8	13	18
c'	[MPa]	0.10	0.25	0.40
K_0^{NC*}	[\cdot]	0.861	0.775	0.691
ψ	[$^\circ$]	0 and 1	0 and 1	0 and 1
Non-varied				
E_{oed}/E_{oed}^{ref}	[MPa]	-	340/145	-
ν_{ur}	[\cdot]	-	0.225	-
p^{ref}	[MPa]	-	0.1	-
R_f	[\cdot]	-	0.9	-
e_0	[\cdot]	-	0.7	-
OCR	[\cdot]	-	2.4	-

* Calculated by default from $K_0^{NC} = 1 - \sin\varphi'$ ([Jaky, 1944](#)).

It is noted that for the lower bound an $E_{ur} = 615\text{ MPa}$ was considered instead of $E_{ur} = 3E_{50} = 600\text{ MPa}$. That is because the latter led to an intersection of the paths of the stress points in the vicinity of the tunnel with the cap of the HS model. The effects of compression hardening on the numerical results have not been investigated in this chapter in order to reduce the intricacy of this study. This is also the reason why the value of E_{oed}^{ref} has not been varied as it was expected to influence significantly the steepness of the cap (Section 3-4-6-2), which would have led to intersection with the generated stress paths. The value of ν_{ur} was also not varied as it was expected to influence mainly the response of the cap (see Sections 3-5-2-4, 3-5-3-3 and 3-5-4-4) as well as in order to reduce the level of complexity of the research.

4-3 Discussion on the numerical results

This section starts with the description and the explanation of the paths, in the $p' - q$ plane, of stress points in the vicinity of the tunnel. Then, the effect of the varied HS model input parameters on the numerical results is investigated.

It is noted that the deviator stress is given by ([Plaxis, 2011a](#)):

$$q = \sqrt{\frac{1}{2}[(\sigma'_{xx} - \sigma'_{yy})^2 + (\sigma'_{yy} - \sigma'_{zz})^2 + (\sigma'_{zz} - \sigma'_{xx})^2 + 6(\sigma_{xy}^2 + \sigma_{yz}^2 + \sigma_{zx}^2)]} \quad (4-7)$$

4-3-1 Effective stress paths in the vicinity of the tunnel

Figure 4-2 shows the Effective Stress Path (ESP) of a point at a horizontal distance of 4cm from the tunnel sidewall. This plot depicts the ESP for the third (introduction of the tunnel) and the fourth (contraction of the tunnel) calculation phases of the analysis (see Section 4-2-2).

At the beginning of the third phase (point A in Figure 4-2) the ESP is situated at $p' = 2250\text{kPa}$, which corresponds to a depth of -225m, and at $q = 0\text{kPa}$, since a value of $K_0 = 1.0$ was introduced (see Section 4-2-1). The completion of this phase is marked by point B in Figure 4-2. It is observed that this branch of the ESP is practically vertical, implying that pure shearing occurs. This pattern is attributed to the fact that no coupling between $\delta\varepsilon_v^e$ and δq is considered by the HS model. In other words, the change in the elastic volumetric strains is only influenced by the increment of p' . This can be expressed in mathematical form by:

$$\begin{bmatrix} \delta\varepsilon_v^e \\ \delta\gamma_s^e \end{bmatrix} = \begin{bmatrix} 1/K' & 0 \\ 0 & 1/3G \end{bmatrix} \begin{bmatrix} \delta p' \\ \delta q \end{bmatrix} \quad (4-8)$$

where γ_s^e is the elastic deviatoric strain, K' is the drained bulk modulus, G is the shear modulus and δ denotes increment. For undrained conditions $\delta\varepsilon_v = 0$. Thus, from Equation 4-8 it can be concluded that $\delta p' = 0$, which explains the vertical ESP, on condition that the latter is situated in the elastic domain (see below).

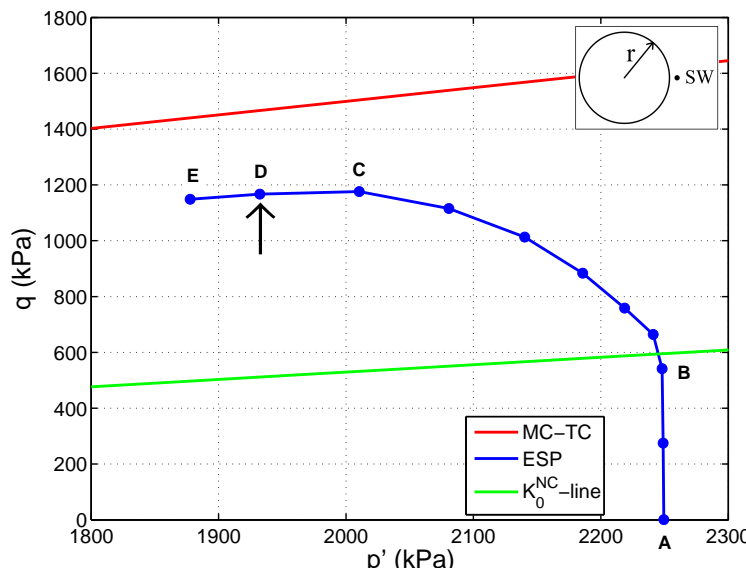


Figure 4-2: Effective Stress Path, (ESP) in the deviator stress (q) versus mean effective stress (p') plot, of a stress point next to the tunnel sidewall (SW) for the analysis with the *mean data* and for zero dilatancy angle. The red line indicates the position of the Mohr-Coulomb (MC) criterion for Triaxial Compression (TC). Point A signifies the end of the second calculation phase. Point B indicates the end of the calculation phase where the tunnel is introduced. Point C marks the peak deviator stress. The black arrow shows the position (point D) where the ESP meets the MC criterion. Point E marks the stress state at the completion of the calculation. K_0^{NC} is the coefficient of earth pressures for normal consolidation. The K_0^{NC} -line concerns triaxial compression. r is the tunnel radius.

The ESP turns to the left in the $p' - q$ plot from the onset of the last phase (after point B in Figure 4-2). This seems to signify the yield of the material and the generation of ε_v^p as the value of p' decreases. From Figure 4-2 it can be observed that the soil yields when the projection of the ESP on the $p' - q$ plane surpasses the K_0^{NC} -line. This indicates that, in general stress states, the shear hardening locus of the HS model is initiated along this line (see Figure 3-22). From this observation, a different response of the model in triaxial compression and in the case of an undrained tunnel excavation is identified: in the former case no ε_v^p were generated due to shear hardening (see Sections 3-5-2-1 and 3-5-4-1), whereas they are produced in the latter. It is noted that the ESP does not intersect with the cap of the HS model and, therefore, no plastic volumetric cap strains are generated. A flow rule for the generation of ε_v^p , in general stress states, owing to shear hardening, before dilatancy is mobilised, has not been found in the literature for the HS model. It might be said that $\varepsilon_v^p = \varepsilon_1^p$, where the latter is determined by an extended, in general stress space, version of Equation 3-10.

The MC criterion is met (point D in Figure 4-2) at a different position than that corresponding to triaxial compression, which indicates that the stress paths differ between a triaxial test and a simulation of an undrained tunnel excavation, as mentioned in Section 3-6. After the examined soil element is fully plastifies, its stress state travels along the MC surface until the completion of the calculation (marked by point E in Figure 4-2), i.e. until the total prescribed contraction is applied.

The evolution of the excess pore water pressures (u_{excess}) during the last calculation phase of the simulation with the *mean data* is illustrated in Figure 4-3. The previous phases have not been considered since $u_{excess} = 0$ kPa. It is observed that they are negative and they decrease throughout the analysis. This can be explained by considering the process that develops,

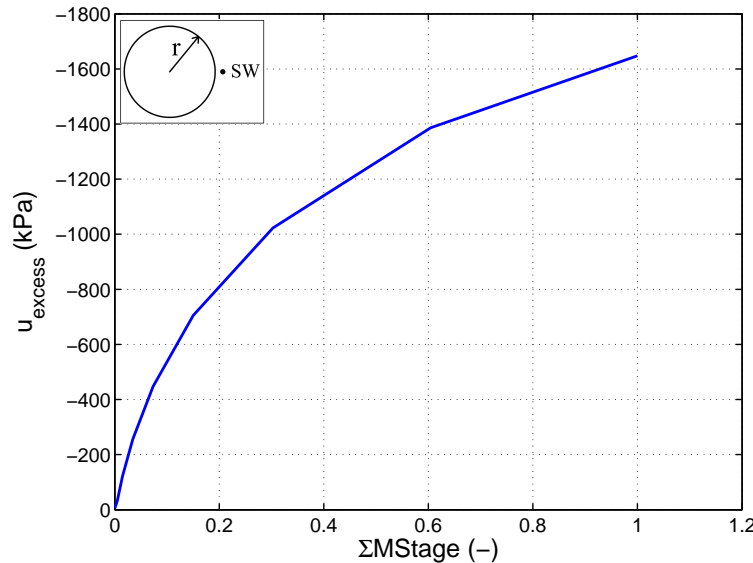


Figure 4-3: Evolution of the excess pore water pressures (u_{excess}) of a point next to the tunnel sidewall (SW), in the course of the last calculation phase (tunnel contraction), for the simulation with the *mean data* and for zero dilatancy angle. The quantity $\Sigma MStage$ denotes the percentage of the completion of the calculation phase. r is the tunnel radius.

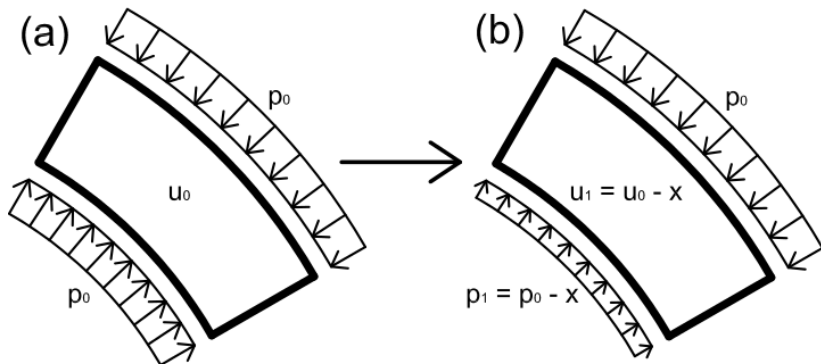


Figure 4-4: Schematic representation of the pressures acting on a soil segment situated at the walls of a circular cavity before (a) and after (b) undrained unloading.

due to undrained unloading, during an underground excavation. In Figure 4-4 an infinitely small soil segment at the wall of a circular cavity is depicted. Before the excavation takes place (Figure 4-4a) the ground pressures (p_0) acting on the segment are equal in all directions and the pore water pressures are equal to the in-situ ones (u_0). During the excavation stage (Figure 4-4b), the pressures acting on the side of the wall of the cavity (p_1) decrease by a given amount, x for instance. Since the conditions are undrained, this reduction of the isotropic part of the stress release is taken by the pore water pressures (u_1), which will decrease by x as well. The latter quantity is equal to u_{excess} , which is negative.

It should be noted that u_{excess} are not generated as long as the stress change is purely deviatoric and the material behaviour is isotropic elastic. They are produced after the soil yields. From Figure 4-3 it is observed that the rate of decrease in u_{excess} reduces as the calculation proceeds.

Figure 4-5 shows the ESP of three stress points, which are situated at different horizontal distances from the sidewall of the tunnel. It is observed that they develop in an identical manner however, they finish at larger p' and smaller q as the distance from the sidewall increases. This is attributed to the reduced level of straining that the farther soil elements are subjected to. Furthermore, the ESP of the points at $x = 2.11\text{m}$ and $x = 4.09\text{m}$ (red and green curve in Figure 4-5, respectively) from the sidewall of the excavation do not reach failure. They are situated in the elastoplastic domain, where shear hardening occurs. The lower amount of strains for these two points can also be noticed by the reduced level of shearing they experience at the end of the third calculation phase, i.e. at the completion of the emplacement of the tunnel (red and green dashed-dotted lines in Figure 4-5).

In Figure 4-6 the ESP of a point next to the sidewall of the excavation (blue curve) is compared to the ones of a point located 1cm above the crown (red curve) and a point situated 11cm below the invert (green curve). It can be observed that the ESP is similar in all directions around the tunnel as all paths lie on the same line of the MC failure surface at the end of the calculation. The difference in p' at the beginning of the third calculation phase (emplacement of the tunnel) is ascribed to the different depths of the considered stress points.

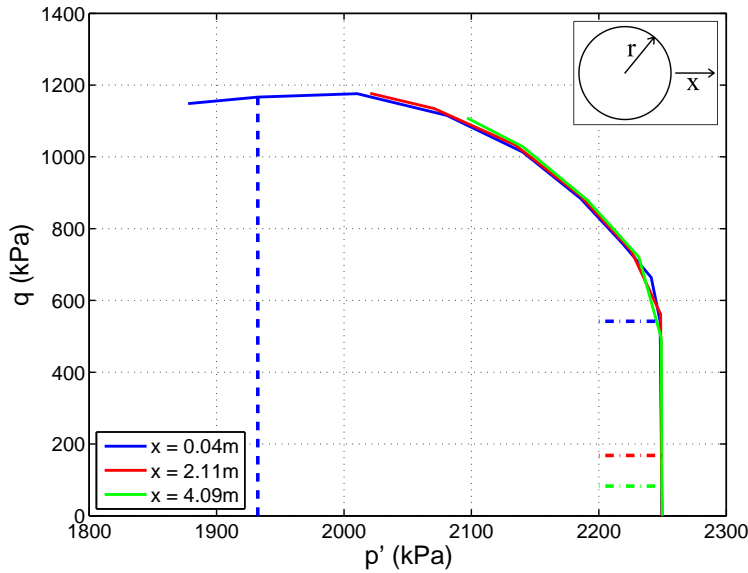


Figure 4-5: Effective Stress Paths (ESP), in a deviator stress (q) versus mean effective stress (p') plot, of three stress points located at different horizontal distances (x) from the sidewall of the tunnel, for the simulation with the *mean data* and for zero dilatancy angle. The dashed blue line indicates the position where the ESP meets the MC criterion. The dashed-dotted lines indicate the end of the calculation phase where the tunnel is introduced. r is the tunnel radius.

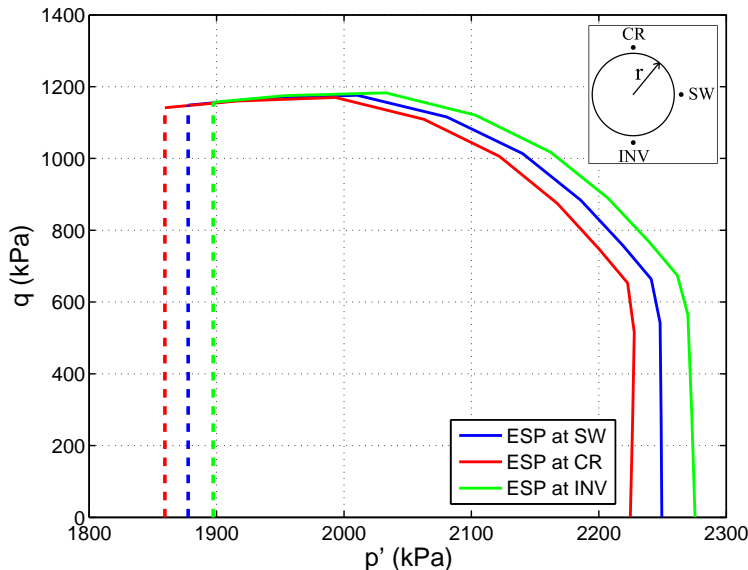


Figure 4-6: Effective Stress Paths (ESP), in a deviator stress (q) versus mean effective stress (p') plot, of three stress points located close to the sidewall (SW), the crown (CR) and the invert (INV) of the tunnel, for the simulation with the *mean data* and for zero dilatancy angle. The dashed lines indicate the position of the ESP at the end of the analyses. r is the tunnel radius.

4-3-2 Influence of the varied model input parameters on the numerical results

In this section investigation on the effects of the input parameters of the HS model on specific results of the numerical simulations of the undrained excavation is made. Also, the level of influence of each parameter is studied. The examined results concern the thickness of the fully Plastic Zone (PZ), the shear Hardening Zone (HZ) and the Disturbed Zone ($DZ = PZ + HZ$), and the hoop forces (N) in the tunnel liner.

This study has been assisted by inspecting the ESP and the deviator stress versus deviatoric strains plots of a point situated 4cm away from the sidewall of the excavation, during the third and the fourth calculation phases (see Section 4-2-2) of the analyses. The numerical results for this point have been considered to be representative of the outcomes for all other points around the excavation as the corresponding ESP were found to be similar (Figure 4-6). Moreover, the resulting stresses and the pore water pressures at the end of the calculations, along a radial line, have been utilised.

4-3-2-1 On the fully plastic and the shear hardening zones

The PZ is considered to be the part of the finite element mesh where the stress states of the soil elements lie on the MC failure criterion (red points in Figure 4-7). The HZ comprises the soil elements of which the stress states lie on the shear hardening locus of the HS model (green

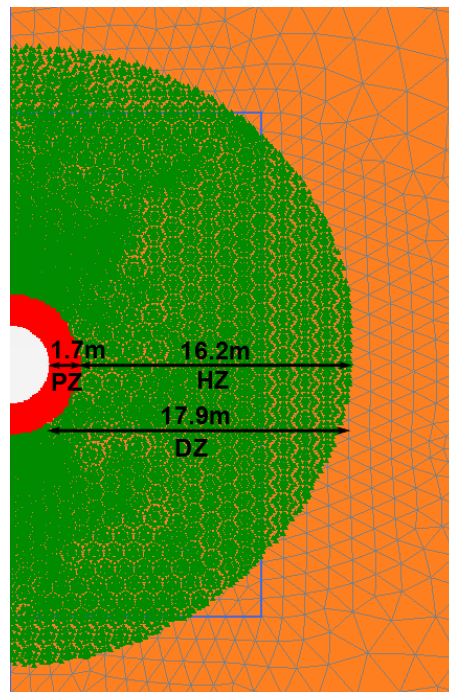


Figure 4-7: Illustration of part of the finite element mesh with the fully plastified (with red colour) stress points and the stress points of which the effective stress paths lie on the shear hardening locus of the HS model (with green colour), at the end of the analysis with the *mean data* and with zero dilatancy angle. The thickness of the fully Plastic Zone (PZ), the shear Hardening Zone (HZ) and the Disturbed Zone is indicated.

points in Figure 4-7). At the completion of the analysis with the *mean data* the thickness of the PZ and the HZ is 1.7m and 16.2m, respectively. Therefore, the hydro-mechanical disturbance in the host rock extends up to $1.7 + 16.2 = 17.9$ m away from the sidewall of the excavation. The latter concerns the thickness of the DZ.

In Figure 4-7 it is observed that the DZ is almost circular, which may be attributed to the assumed isotropic initial stress field ($K_0 = 1$, thus $\sigma'_v = \sigma'_h$, see Section 4-2-1). The latter may be responsible for the similar level of shearing (magnitude of q) experienced by the material at equal radial distances around the periphery of the excavation, which can be inferred from Figure 4-6.

4-3-2-2 Investigation on the influence of E_{50}^{ref}

In Table 4-3 it is observed that an increase in E_{50}^{ref} causes a larger thickness of the PZ. This may be attributed to the fact that the elastoplastic shear stiffness of the material increases. For E_{50}^{ref} equal to 97, 145 and 194MPa the values of the internal parameter G_{50}^{ref} , which is a measure of the elastoplastic shear stiffness of the soil (see Section 3-5-1), become 95, 178 and 317MPa, respectively. The stiffer response of the material for a rise in E_{50}^{ref} can be observed in the $\gamma_s - q$ diagrams of a stress point next to the tunnel sidewall (Figure 4-8). The inclinations of all curves are equal in the elastic domain, since the shear stiffness is controlled by E_{ur} , which remains unchanged, according to the equation below:

$$G_{ur} = \frac{E_{ur}}{2(1 + \nu_{ur})} \quad (4-9)$$

where G_{ur} is the stress-dependent unloading-reloading (elastic) shear modulus. However, the slopes change after yield. The highest slope of the $\gamma_s - q$ graph occurs for the highest value of E_{50}^{ref} (blue curve in Figure 4-8).

A stiffer material response entails a larger deviatoric stress increment for the same deviatoric strain increment. As a result, a stiffer soil element will reach the MC failure criterion at a lower level of γ_s (Figure 4-8). After the element fully plastifies, any additional load imposed during the remaining steps of the analysis will be redistributed to its surroundings. The amount of the redistributed load will be larger for the stiffer material since a larger portion of the pre-defined strains (a contraction of 7.098% is introduced, see Section 4-2-2) needs to

Table 4-3: Effect of changing the reference secant modulus (E_{50}^{ref}) on the thickness of the Plastic Zone (PZ), the Hardening Zone (HZ) and the Disturbed Zone (DZ), the hoop forces in the tunnel liner (N) and the pore water pressures (u) of a stress point next to the tunnel sidewall, at the end of the simulations.

E_{50}^{ref} [MPa]	PZ [m]	HZ [m]	DZ [m]	N [MN]		u [MPa]	
				$\psi = 0^\circ$	$\psi = 1^\circ$	$\psi = 0^\circ$	$\psi = 1^\circ$
97	0.56	17.12	17.68	4.754	4.728	0.695	0.546
145	1.70	16.20	17.90	4.382	4.297	0.568	0.275
194	3.02	13.58	16.60	4.041	3.909	0.452	0.070

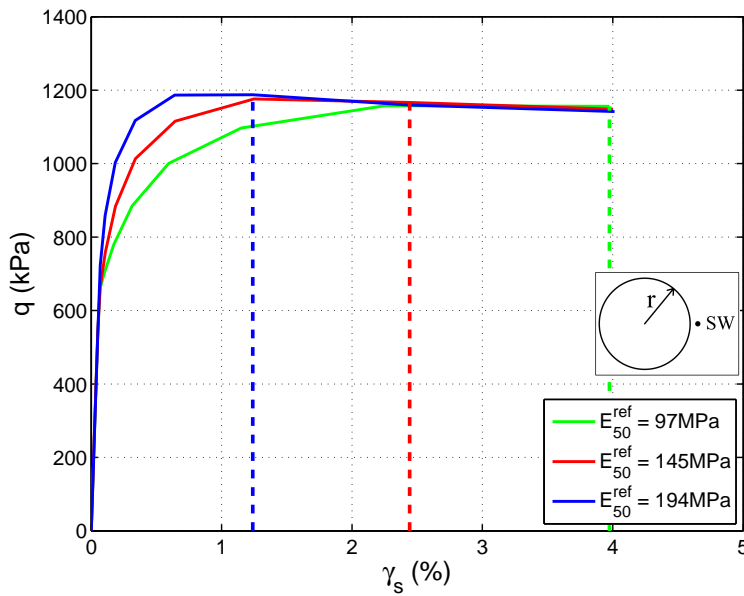


Figure 4-8: Deviator stress (q) versus deviatoric strains (γ_s) plot for a stress point 4cm away from the tunnel sidewall (SW), for different values of the reference secant modulus (E_{50}^{ref}) and for zero dilatancy angle. The dashed lines indicate the amount of strains at which the stress path meets the Mohr-Coulomb criterion. r is the tunnel radius.

be imposed until the end of the simulation. Consequently, the extent of the PZ will be larger for a higher value of E_{50}^{ref} .

The thickness of the HZ decreases for an increase in E_{50}^{ref} (Table 4-3). This is probably attributed to the smaller amount of q that is redistributed from stiffer stress points (as they experience larger δq , see Figure 4-8), that lie on the shear hardening locus, to their surroundings. Hence, the extent of the mesh where the stress states of the soil elements lie on the shear locus (green points in Figure 4-7) reduces. It can be concluded that the effect of the smaller load redistribution in the elastoplastic domain is more significant than that of the redistribution of larger q in the fully plastic domain, as the thickness of the HZ decreases (Table 4-3). No pattern is identified for the extent of the DZ (Table 4-3). It increases slightly for an increase of E_{50}^{ref} from 97 to 145MPa, whereas it reduces for a further increase of E_{50}^{ref} to 194MPa.

The hoop forces in the tunnel liner decrease for an increase in E_{50}^{ref} (Table 4-3). This is owing to the reduced total radial stresses (σ_r) and total tangential stresses (σ_t) that act on the periphery of the excavation. The profiles of the total stresses are illustrated in Figure 4-9. In this plot it is observed that the total stresses at the sidewall of the tunnel (at a distance of 2.4m from the tunnel centerline) reduce for an increase in E_{50}^{ref} , as a result of the decreased radial effective stresses (σ'_r) and pore water pressures ($\sigma_r = \sigma'_r + u$) at the same location (Figures 4-10 and 4-11, respectively).

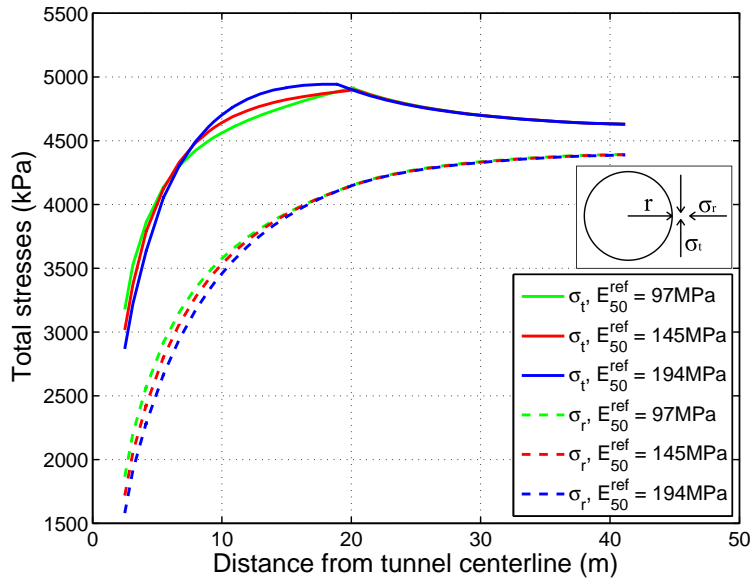


Figure 4-9: Total radial stresses (σ_r) and total tangential stresses (σ_t), along a radial line, for different values of the reference secant modulus (E_{50}^{ref}) and for zero dilatancy angle. r is the tunnel radius.

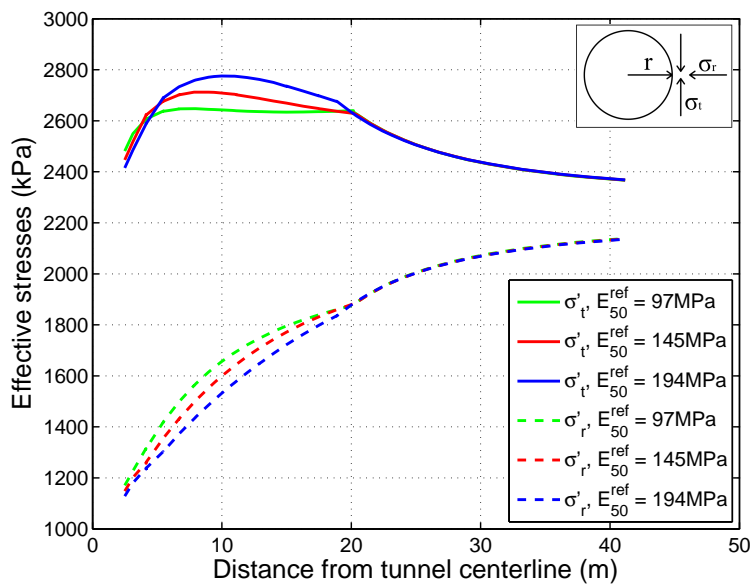


Figure 4-10: Effective radial stresses (σ'_r) and effective tangential stresses (σ'_t), along a radial line, for different values of the reference secant modulus (E_{50}^{ref}) and for zero dilatancy angle. r is the tunnel radius.

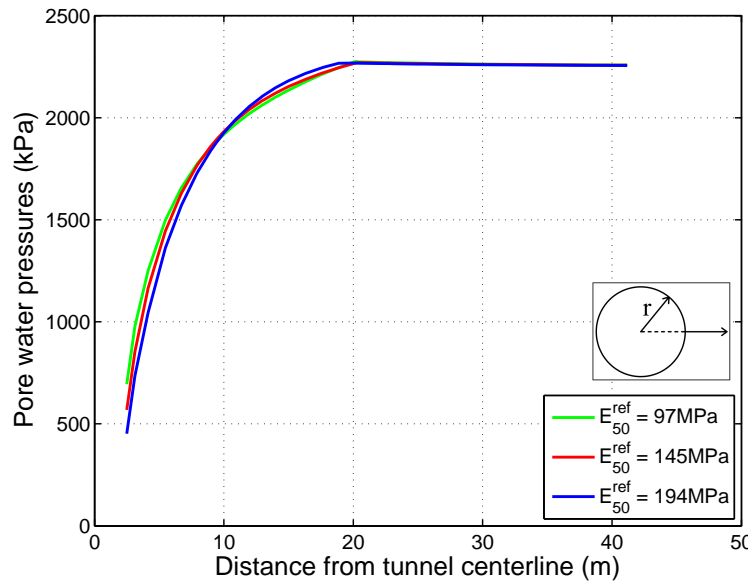


Figure 4-11: Pore water pressures, along a radial line, for different values of the reference secant modulus (E_{50}^{ref}) and for zero dilatancy angle. r is the tunnel radius.

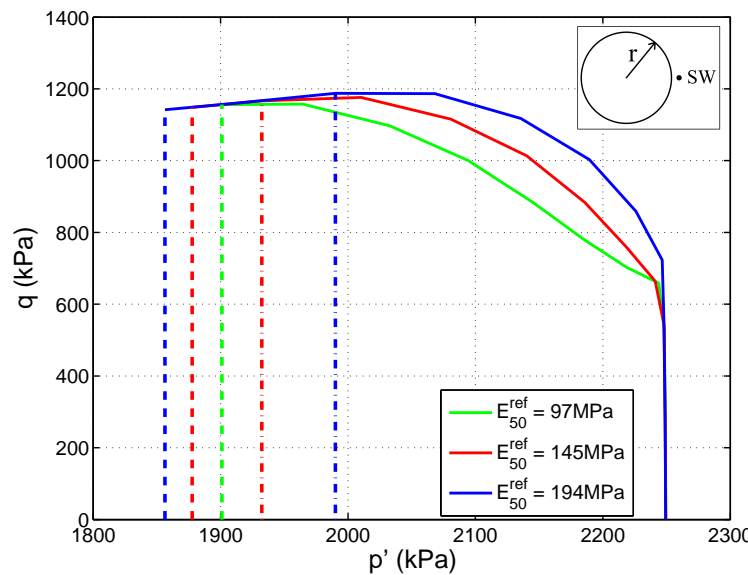


Figure 4-12: Effective Stress Paths (ESP), in a deviator stress (q) versus mean effective stress (p') plot, of a point 4cm away from the tunnel sidewall (SW), for different values of the reference secant modulus (E_{50}^{ref}) and for zero dilatancy angle. The dashed lines indicate the end of each ESP (with the corresponding colour) at the completion of the calculation. The dashed-dotted lines indicate the position at which the ESP meet the Mohr-Coulomb criterion. These lines coincide for the case of the analysis with $E_{50}^{ref} = 97\text{MPa}$. r is the tunnel radius.

The reduction in σ'_r and u may be explained by investigating the ESP of a point next to the tunnel sidewall (Figure 4-12). The latter ends at lower p' and q for an increase in E_{50}^{ref} , possibly due to the fact that a stiffer soil element meets the MC criterion at lower level of γ_s (see Figure 4-8). Thus, its path along the MC failure line until the completion of the calculation, in the $p' - q$ plane, will be longer (Figure 4-12). Smaller values of p' and q imply a decrease in the effective radial and tangential stresses (σ'_r and σ'_t , respectively). The decrease in u may be explained by the notion that a larger decrease in p' is accompanied by more negative u_{excess} . Consequently, the pore water pressures, which are derived from adding u_0 (compressive) and u_{excess} (tensile), decrease, i.e. they become less compressive for a rise in E_{50}^{ref} .

The reduction in p' is larger for a decrease in E_{50}^{ref} , in the branch of the ESP which lies between the initial yield and the MC criterion (Figure 4-12). This may imply the generation of larger ε_v^p . The hypothesis that $\varepsilon_v^p = \varepsilon_1^p$ (Section 4-3-1) might explain this observation since a decrease in E_{50}^{ref} causes larger ε_1^p in triaxial stress conditions (see Equations 3-3 and 3-10).

For the analyses with $\psi = 1^\circ$, no change is induced in the extent of the PZ, the HZ and the DZ. The effect of varying the values of E_{50}^{ref} is the same with the simulations where $\psi = 0^\circ$.

(Table 4-3). This can be inferred by the fact that the material fully plastifies at the same level of γ_s for $\psi = 0^\circ$ and $\psi = 1^\circ$ (Figures 4-8 and 4-13, respectively). On the other hand, a slight reduction in N and a more significant decrease in u occurs, compared to the analyses where no dilatancy is introduced. This is due to the increase in the tensile u_{excess} , which result from the tendency of the soil to dilate. The latter is initiated when the mobilised shear strength of the material reaches a level defined by Equations 3-14 to 3-17.

The effect of prevention of dilation of the material on the resulting values of N is limited due to the larger generated σ'_r and σ'_t than these of the analyses with the non-dilatant material. For $E_{50}^{ref} = 145\text{MPa}$ and $\psi = 0^\circ$, $\sigma'_r = 1.148\text{MPa}$ and $u = 0.568\text{MPa}$, whereas for $\psi = 1^\circ$ and for the same shear stiffness, $\sigma'_r = 1.407\text{MPa}$ and $u = 0.275\text{MPa}$. Therefore, the total radial stresses ($=\sigma'_r + u$), which predominantly affect the hoop forces in the liner, are similar in both cases ($\sigma_r = 1.717\text{MPa}$ for $\psi = 0^\circ$ and $\sigma_r = 1.682\text{MPa}$ for $\psi = 1^\circ$).

The fact that the generated effective stresses at the sidewall of the tunnel are larger for the analyses with $\psi = 1^\circ$ can be explained by comparing the resulting ESP of a point at this location, from two simulations where the dilatancy angle is changed from 0° to 1° and E_{50}^{ref} is constant (Figure 4-14). It is observed that for a dilatant material the ESP turns to the right when its tendency to dilate occurs (blue curve), i.e. p' increases due to the generation of additional tensile u_{excess} , and q increases. Consequently, the produced effective stresses are larger for $\psi = 1^\circ$ at the completion of the simulation.

The numerical results for the analyses with $\psi = 1^\circ$, in terms of effective and total stress profiles, ESP in the $p' - q$ plane, $\gamma_s - q$ plots and pore water pressures profiles, are depicted in Figures A-4, A-5, A-6, 4-13 and A-7, respectively.

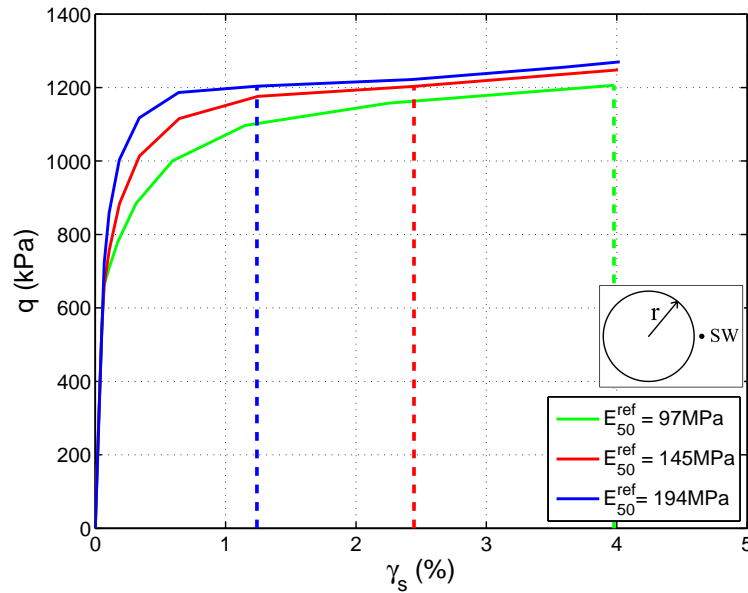


Figure 4-13: Deviator stress (q) versus deviatoric strains (γ_s) plot for a stress point next to the tunnel sidewall (SW), for different values of the reference secant modulus (E_{50}^{ref}) and for dilatancy angle equal to 1° . The dashed lines indicate the amount of strains at which the stress path meets the Mohr-Coulomb criterion. r is the tunnel radius.

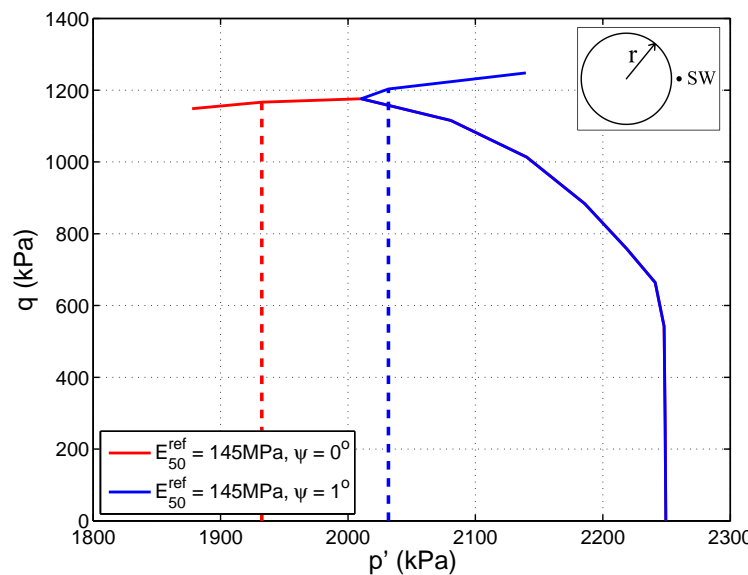


Figure 4-14: Effective Stress Paths (ESP), in a deviator stress (q) versus mean effective stress (p') plot, of a point 4cm away from the tunnel sidewall (SW), for a value of the reference secant modulus $E_{50}^{ref} = 145 \text{ MPa}$ and for values of the dilatancy angle $\psi = 0^\circ$ and 1° . The dashed lines indicate the position at which the ESP meet the Mohr-Coulomb criterion. r is the tunnel radius.

4-3-2-3 Investigation on the influence of E_{ur}^{ref}

The thickness of the PZ remains practically unchanged for a change in E_{ur}^{ref} (Table 4-4). That is because the elastoplastic shear stiffness of the material is not altered significantly, leading to a similar level of redistributed q after the ESP of the points in the vicinity of the excavation reach the MC criterion (see Section 4-3-2-2). For E_{ur}^{ref} equal to 298, 436 and 581MPa, the values of G_{50}^{ref} become 209, 178 and 175MPa, respectively. The significant change in the reference elasto-plastic shear stiffness for $E_{ur}^{ref} = 298$ MPa does not seem to be realistic. That is because a change in E_{ur}^{ref} is expected to influence only the elastic shear stiffness of the material. This inconsistency, which probably arises from the internal algorithm performed by the program (Section 3-4-8), can be inferred by inspecting the negligible effect of varying E_{ur}^{ref} on the values of G_{50}^{ref} in Table 3-8. Probably, a $E_{ur}^{ref} = 298$ MPa seems to be low for the considered set of the model input parameters.

The insignificant influence of E_{ur}^{ref} on the width of the PZ can be inferred from the $\gamma_s - q$ plot in Figure 4-15. It is observed that the stress point next to the sidewall of the excavation meets the MC failure criterion at a similar level of deviatoric strains for $E_{ur}^{ref} = 436$ and 581MPa and at slightly smaller γ_s for $E_{ur}^{ref} = 298$ MPa, which explains the somewhat larger thickness of the PZ for the latter. The curve which corresponds to $E_{ur}^{ref} = 298$ MPa (green curve) is somewhat steeper after initial yield, owing to the larger value of G_{50}^{ref} .

The thickness of the HZ increases for an increase in E_{ur}^{ref} (Table 4-4). This may be ascribed to the fact that the elastic shear stiffness of the material increases (see Equation 4-9), causing it to yield at smaller amount of deviatoric strains. This can be observed in Figure 4-15, where the inclination of the linear part of the $\gamma_s - q$ plot at low level of strains (elastic domain) increases for an increase in E_{ur}^{ref} . Consequently, the extent of the mesh where the soil elements of which the stress states meet the shear hardening locus (green points in Figure 4-7) will be larger for an increase in the elastic stiffness of the soil.

The slight change in the thickness of the PZ and the increase in the width of the HZ, due to an increase in E_{ur}^{ref} , induce a larger extent of the hydro-mechanical disturbance (thickness of DZ in Table 4-4). The thickness of the latter can also be observed in the total stresses and the pore water pressures profiles (Figures 4-16 and 4-17, respectively). In the former it is marked by the position of the peak value of σ_t and in the latter by the distance at which u stabilise.

Table 4-4: Effect of changing the reference un-/reloading modulus (E_{ur}^{ref}) on the thickness of the Plastic Zone (PZ), the Hardening Zone (HZ) and the Disturbed Zone (DZ), the hoop forces in the tunnel liner (N) and the pore water pressures (u) of a stress point next to the tunnel sidewall, at the end of the simulations.

E_{ur}^{ref} [MPa]	PZ [m]	HZ [m]	DZ [m]	N [MN]		u [MPa]	
				$\psi = 0^\circ$	$\psi = 1^\circ$	$\psi = 0^\circ$	$\psi = 1^\circ$
298	1.87	11.93	13.80	4.535	4.463	0.525	0.288
436	1.70	16.20	17.90	4.382	4.297	0.568	0.275
581	1.62	19.38	21.00	4.264	4.160	0.617	0.250

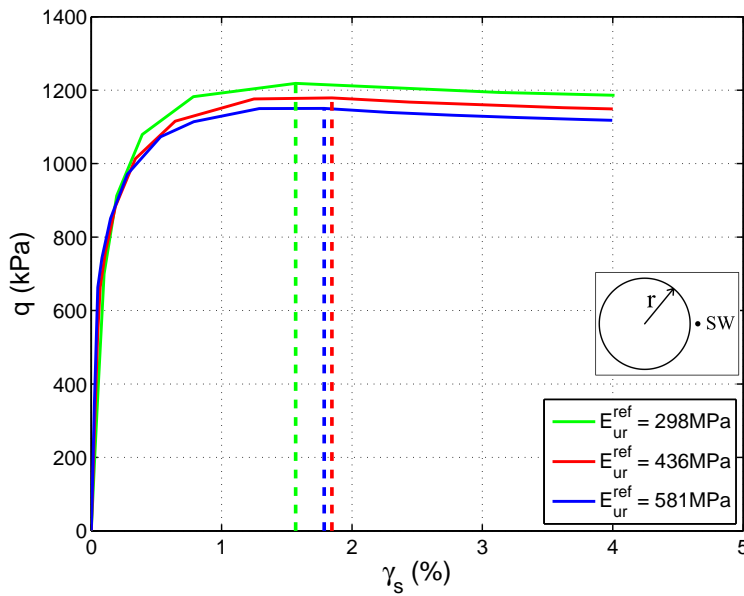


Figure 4-15: Deviator stress (q) versus deviatoric strains (γ_s) plot for a stress point next to the tunnel sidewall (SW), for different values of the reference unloading-reloading modulus (E_{ur}^{ref}) and for zero dilatancy angle. The dashed lines indicate the amount of strains at which the stress path meets the Mohr-Coulomb criterion. r is the tunnel radius. The amount of γ_s at which the material fully plastifies differs between this case and the respective case with $\psi = 1^\circ$ (Figure A-11), as the results of the former have been obtained for an increased accuracy of the analysis.

The hoop forces in the liner decrease for an increase in E_{ur}^{ref} (Table 4-4), as a result of the decrease in σ_r and σ_t (Figure 4-16) close to the excavation. The total stresses ($=\sigma' + u$) reduce as the decrease in σ'_r and σ'_t (Figure 4-18) is more significant than the increase in u (Figure 4-17) at the same position (i.e. at 2.4m from the tunnel centerline). The former can be explained by the ESP of a point next to the tunnel sidewall, which reach smaller p' and q (thus, smaller σ'_r and σ'_t) at the end of the calculation for an increase in E_{ur}^{ref} (Figure 4-19).

The line of reasoning followed in Section 4-3-2-2 cannot explain the increase in u for a rise in E_{ur}^{ref} . Even though the ESP reaches the lowest value of p' for $E_{ur}^{ref} = 581$ MPa (blue curve in Figure 4-19), the produced negative u_{excess} seem to be the lowest as the resulting compressive u ($=u_0 + u_{excess}$) are the highest (blue curve in Figure 4-17).

An increase in E_{ur}^{ref} causes a larger reduction in p' (Figure 4-19), which might imply an increase in the generated ε_v^p in the elastoplastic domain. This may be explained by the formula for the calculation of ε_1^p (Equation 3-10) if the hypothesis that $\varepsilon_1^p = \varepsilon_v^p$ (Section 4-3-1) holds true.

When dilatancy is introduced, the resulting thickness of the PZ, the HZ and the DZ remain unchanged, whereas the hoop forces and pore water pressures decrease (Table 4-4), for the reasons explained in Section 4-3-2-2. The numerical results for $\psi = 1^\circ$, in terms of effective and total stress profiles, ESP in the $p' - q$ plane, $\gamma_s - q$ plots and pore water pressures profiles, are depicted in Figures A-8, A-9, A-10, A-11 and A-12, respectively.

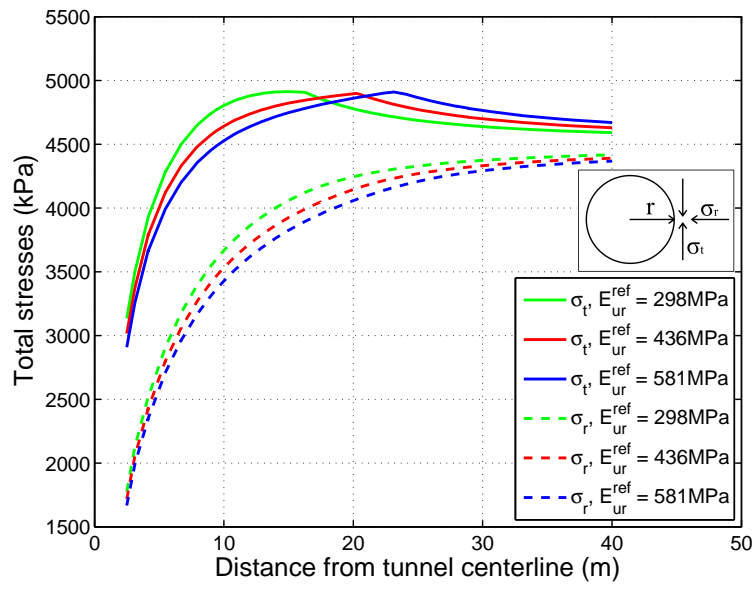


Figure 4-16: Total radial stresses (σ_r) and total tangential stresses (σ_t), along a radial line, for different values of the reference unloading-reloading modulus (E_{ur}^{ref}) and for zero dilatancy angle. r is the tunnel radius.

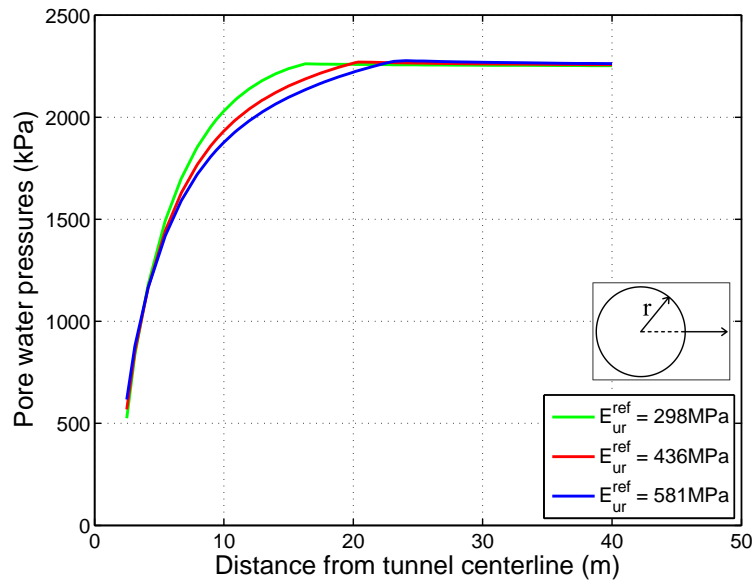


Figure 4-17: Pore water pressures, along a radial line, for different values of the reference unloading-reloading modulus (E_{ur}^{ref}) and for zero dilatancy angle. r is the tunnel radius

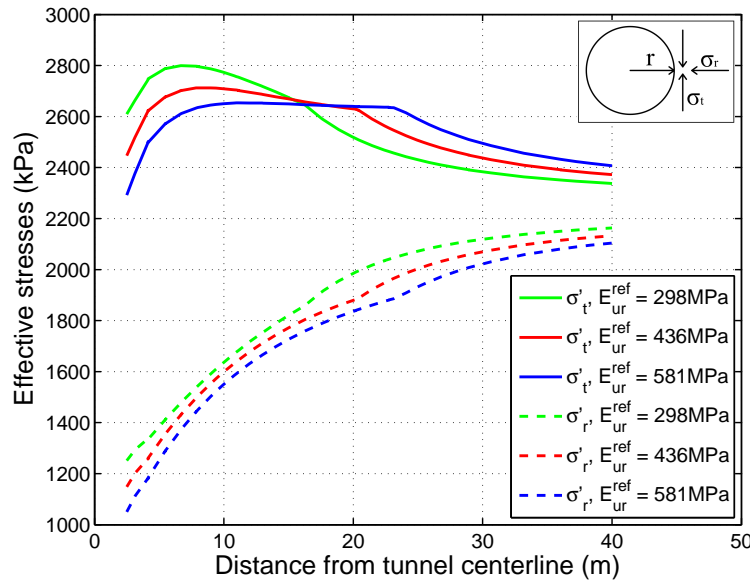


Figure 4-18: Effective radial stresses (σ'_r) and effective tangential stresses (σ'_t), along a radial line, for different values of the reference unloading-reloading modulus (E_{ur}^{ref}) and for zero dilatancy angle. r is the tunnel radius.

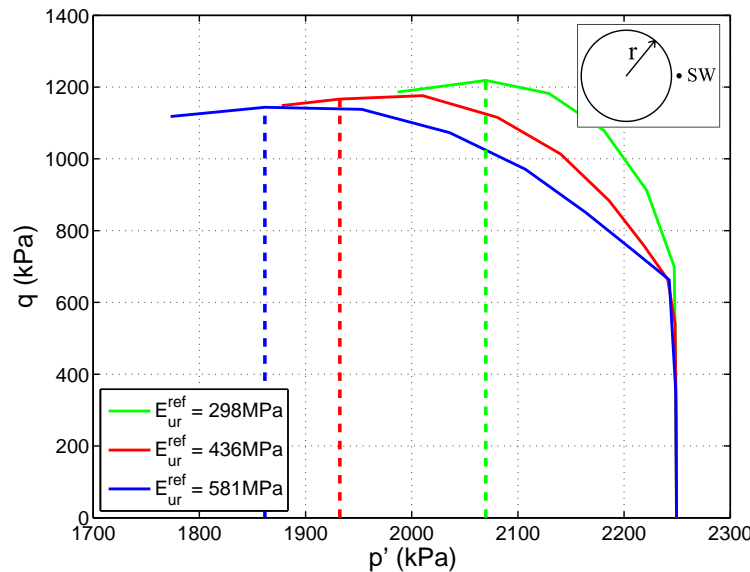


Figure 4-19: Effective Stress Paths (ESP), in a deviator stress (q) versus mean effective stress (p') plot, of a point next to the tunnel sidewall (SW), for different values of the reference unloading-reloading modulus (E_{ur}^{ref}) and for zero dilatancy angle. The dashed lines indicate the intersection of each ESP (with the corresponding colour) with the Mohr-Coulomb criterion. r is the tunnel radius.

4-3-2-4 Investigation on the influence of m

An increase in the value of m leads to a slight increase in the thickness of the PZ (Table 4-5). This may be attributed to the induced rise in the value of E_{50} (see Equation 3-5), which causes a larger elastoplastic shear stiffness of the material (the $\gamma_s - q$ curve becomes somewhat steeper after yield, Figure 4-20). On the other hand, the value of G_{50}^{ref} decreases slightly: for m equal to 0.5, 0.7 and 0.87, G_{50}^{ref} becomes 181, 178 and 176 MPa, respectively. This effect seems to be negligible. The influence of the magnitude of the elastoplastic shear stiffness on the extent of the PZ has been explained in Section 4-3-2-2.

The width of the HZ increases for a rise in m , probably due to the increase in E_{ur} and thus, in G_{ur} (Equations 3-6 and 4-9, respectively), which causes the material to yield at smaller amount of deviatoric strains, as explained in Section 4-3-2-3. The larger elastic shear stiffness for an increase in m is hardly observed in Figure 4-20, where the linear part of the curve at low level of γ_s becomes slightly steeper. It can be concluded that this particular effect is more significant than that of the smaller redistribution of q due to the larger elastoplastic shear stiffness (caused by the rise in E_{50}), which induced a smaller extent of the HZ in Section 4-3-2-2. The thickness of the DZ increases for an increase in m as the width of the PZ and the HZ becomes larger.

The hoop forces in the tunnel liner reduce for an increase in m since the total radial and tangential stresses, which result from adding the effective stresses (Figure 4-21) and the pore water pressures (Figure 4-22) close to the tunnel sidewall, decrease (Figure 4-23). Explanations for the influence of varying the values of m on the aforementioned results can be given in by inspecting the ESP in Figure 4-24, similarly to Section 4-3-2-2.

The greater decrease in p' in the elastoplastic domain for an increase in m (Figure 4-24), may imply larger produced ε_v^p (Section 4-3-2-2). Furthermore, it can be concluded that the effect of the increase in E_{ur} , on the elastoplastic branch of the ESP of a point next to the tunnel sidewall (Figure 4-19), is more significant than that of the rise in E_{50} (Figure 4-12) as the path turns more to the left in the $p' - q$ plane (Figure 4-24), which was observed in the former case (Figure 4-19). On the other hand, the influence of the rise in E_{50} is predominant in terms of the level of γ_s at failure as the soil element fully plastifies at smaller deviatoric strains (Figure 4-20).

Table 4-5: Effect of changing the level of stress dependency of stiffness (m) on the thickness of the Plastic Zone (PZ), the Hardening Zone (HZ) and the Disturbed Zone (DZ), the hoop forces in the tunnel liner (N) and the pore water pressures (u) of a stress point next to the tunnel sidewall, at the end of the simulations.

m [-]	PZ [m]	HZ [m]	DZ [m]	N [MN]		u [MPa]	
				$\psi = 0^\circ$	$\psi = 1^\circ$	$\psi = 0^\circ$	$\psi = 1^\circ$
0.50	1.40	14.30	15.70	4.585	4.521	0.595	0.356
0.70	1.70	16.20	17.90	4.382	4.297	0.568	0.275
0.87	1.88	18.12	20.00	4.220	4.114	0.553	0.212

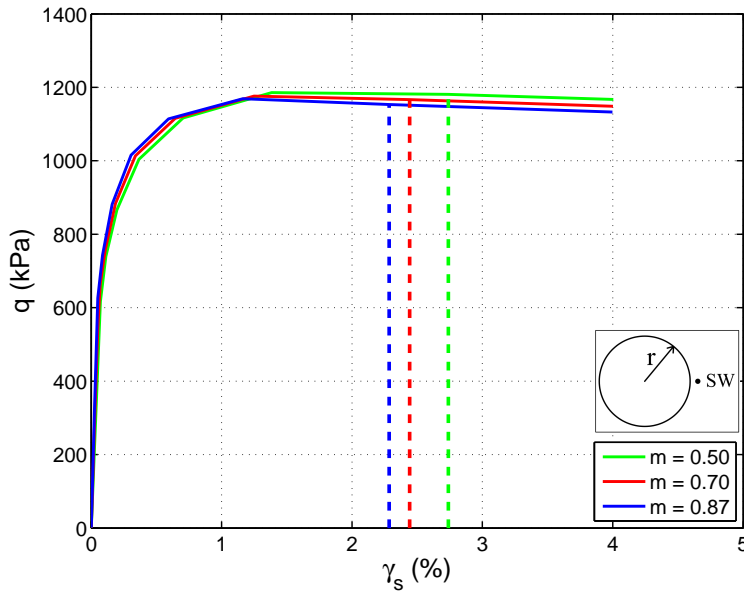


Figure 4-20: Deviator stress (q) versus deviatoric strains (γ_s) plot for a stress point next to the tunnel sidewall (SW), for different values of the rate of stress dependency of stiffness (m) and for zero dilatancy angle. The dashed lines indicate the amount of strains at which the stress path meets the Mohr-Coulomb criterion. r is the tunnel radius.

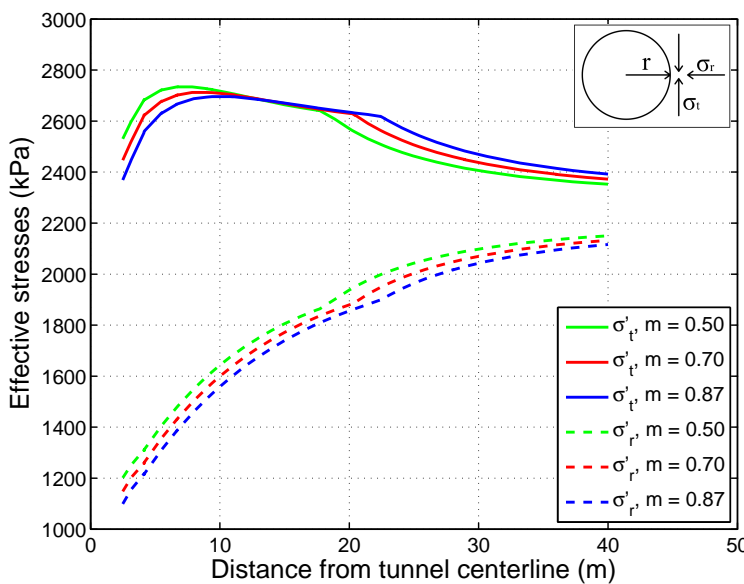


Figure 4-21: Effective radial stresses (σ'_r) and effective tangential stresses (σ'_t), along a radial line, for different values of the rate of stress dependency of stiffness (m) and for zero dilatancy angle. r is the tunnel radius.

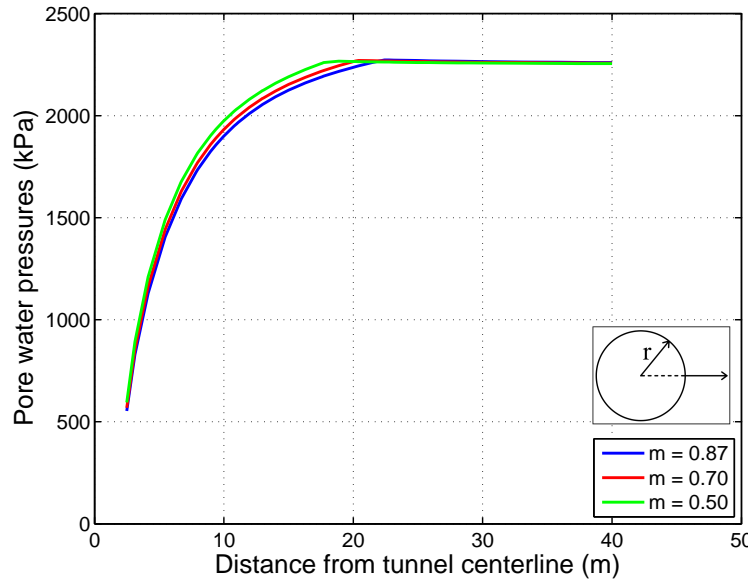


Figure 4-22: Pore water pressures, along a radial line, for different values of the rate of stress dependency of stiffness (m) and for zero dilatancy angle. r is the tunnel radius.

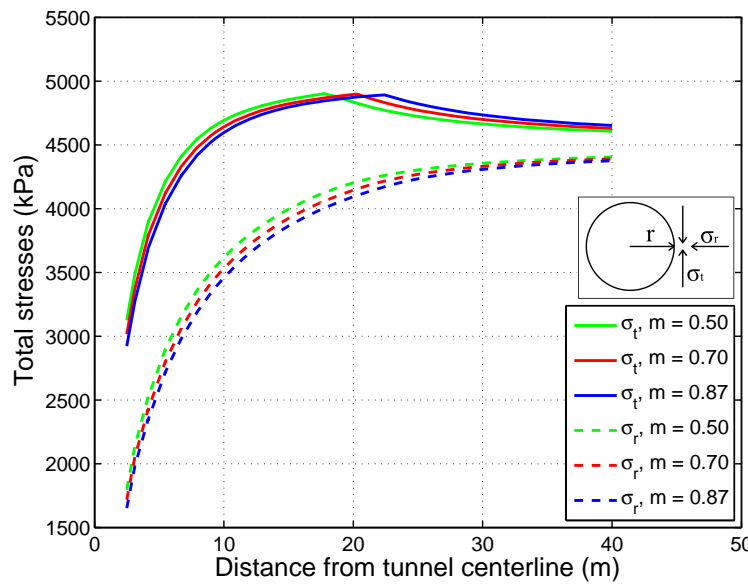


Figure 4-23: Total radial stresses (σ_r) and total tangential stresses (σ_t), along a radial line, for different values of the rate of stress dependency of stiffness (m) and for zero dilatancy angle. r is the tunnel radius.

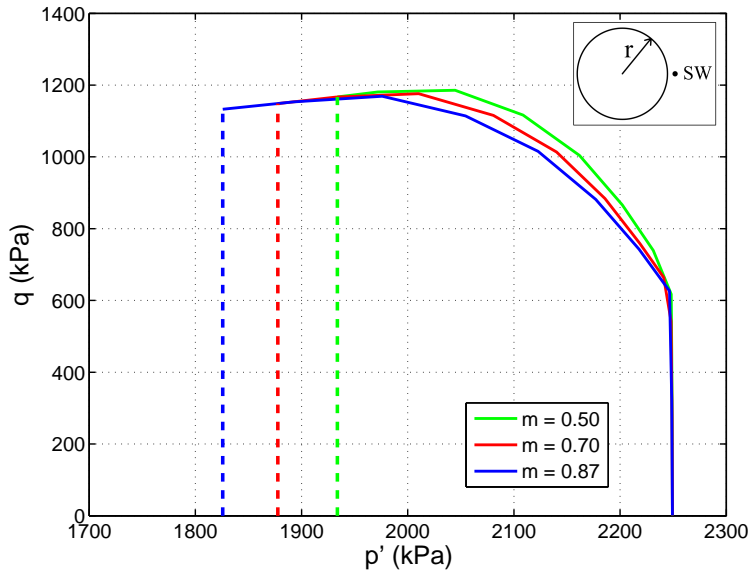


Figure 4-24: Effective Stress Paths (ESP), in a deviator stress (q) versus mean effective stress (p') plot, of a point next to the tunnel sidewall (SW), for different values of the rate of stress dependency of stiffness (m) and for zero dilatancy angle. The dashed lines indicate the end of each ESP (with the corresponding colour) at the completion of the calculation. r is the tunnel radius.

The use of $\psi = 1^\circ$ induces smaller N and u , compared to the analyses where $\psi = 0^\circ$, for the reasons explained in Section 4-3-2-2. The numerical results for $\psi = 1^\circ$, in terms of effective and total stress profiles, ESP in the $p' - q$ plane, $\gamma_s - q$ plots and pore water pressures profiles, are depicted in Figures A-13, A-14, A-15, A-16 and A-17, respectively.

4-3-2-5 Investigation on the influence of φ'

The width of the PZ decreases for an increase in φ' (Table 4-6). A rise in the effective friction angle induces an increase in E_{50} (Equation 3-5) and E_{ur} (Equation 3-6), and a decrease in G_{50}^{ref} . Regarding the latter, for φ' equal to 8, 13 and 18 degrees the value of G_{50}^{ref} becomes 203, 178 and 159 MPa, respectively. The combination of the effects of the aforementioned changes results in a larger elastoplastic shear stiffness of the material, as the inclination of

Table 4-6: Effect of changing the effective friction angle (φ') on the thickness of the Plastic Zone (PZ), the Hardening Zone (HZ) and the Disturbed Zone (DZ), the hoop forces in the tunnel liner (N) and the pore water pressures (u) of a stress point next to the tunnel sidewall, at the end of the simulations.

$\varphi' [^\circ]$	PZ [m]	HZ [m]	DZ [m]	N [MN]		u [MPa]	
				$\psi = 0^\circ$	$\psi = 1^\circ$	$\psi = 0^\circ$	$\psi = 1^\circ$
8	2.31	19.39	21.70	5.844	5.773	0.888	0.540
13	1.70	16.20	17.90	4.382	4.297	0.568	0.275
18	1.23	14.57	15.80	3.076	2.998	0.276	0.052

the $\gamma_s - q$ plot increases after yield (Figure 4-25). Thus, the influence of the rise in E_{50} , which entails a larger stress-dependent elastoplastic shear modulus (G_{50}), seems to be prevalent. Nevertheless, the MC criterion is met at larger γ_s for higher values of φ' owing to the increase in size of the failure surface in principal stress space. In other words, the soil elements with a larger φ' are able to reach a higher level of q before failure. Consequently, the extent of the PZ will be smaller since the amount of the redistributed load reduces after the soil elements fully plastify (see Section 4-3-2-2).

The extent of the HZ decreases for an increase in φ' (Table 4-6) due to the larger elastoplastic stiffness of the stress points which lie on the shear hardening locus (see Section 4-3-2-2). The influence of the larger E_{ur} , which caused a bigger thickness of the HZ in Section 4-3-2-3, seems to be outweighed by the effect of the higher value of E_{50} . As a result, the thickness of the DZ (=PZ + HZ) is also smaller for larger effective friction angle (Table 4-6).

The hoop forces in the liner and the pore water pressures decrease for larger φ' , for the reasons explained in Sections 4-3-2-2 and 4-3-2-4. The ESP, for different values of φ' , of a point located 4cm away from the sidewall of the tunnel are portrayed in Figure 4-26. It is observed that the considered stress point yields at different values of the deviator stress, which can also be inspected in the $\gamma_s - q$ plot in Figure 4-25. This is ascribed to the fact that the shear hardening locus, which is initiated along the K_0^{NC} -line (see Figure 4-2 in Section 4-3-1), is located at different positions in principal stress space since K_0^{NC} decreases for an increase in φ' (Table 4-2).

The profiles of the effective stresses, the total stresses, and the pore water pressures for the analyses with $\psi = 0^\circ$ are depicted in Figures A-1, A-2 and A-3, respectively.

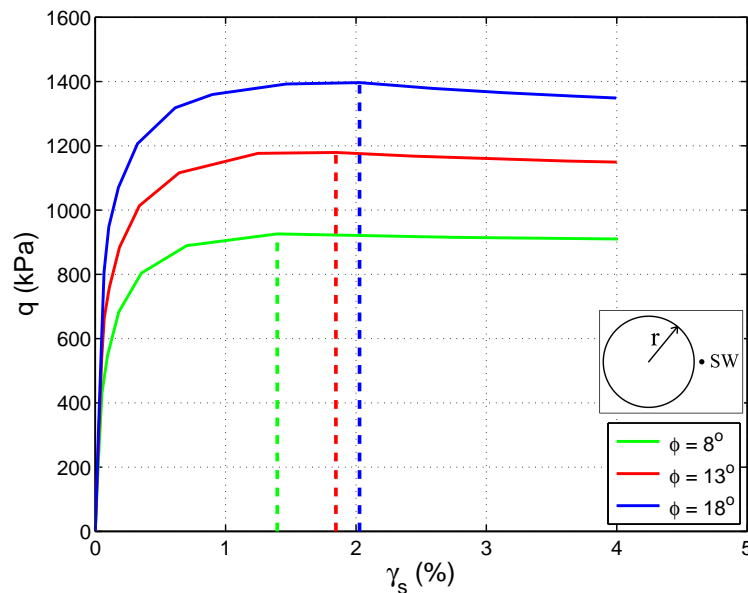


Figure 4-25: Deviator stress (q) versus deviatoric strains (γ_s) plot for a stress point next to the tunnel sidewall (SW), for different values of the effective friction angle (φ') and for zero dilatancy angle. The dashed lines indicate the amount of strains at which the stress path meets the Mohr-Coulomb criterion. r is the tunnel radius.

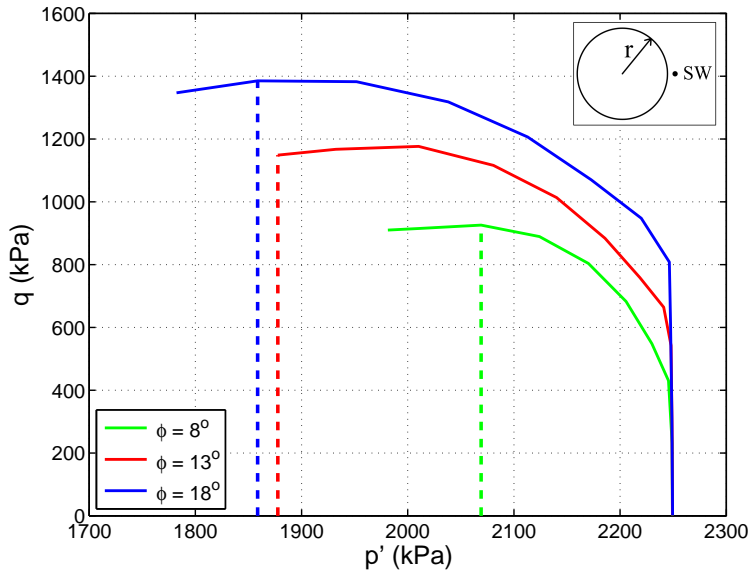


Figure 4-26: Effective Stress Paths (ESP), in a deviator stress (q) versus mean effective stress (p') plot, of a point next to the tunnel sidewall (SW), for different values of the effective friction angle (φ') and for zero dilatancy angle. The dashed lines indicate the intersection of each ESP (with the corresponding colour) with the Mohr-Coulomb criterion. r is the tunnel radius.

Similarly to the previous sections, the resulting N and u are lower for the analyses with $\psi = 1^\circ$, compared to the simulations with $\psi = 0^\circ$. The numerical results from the former, in terms of effective and total stress profiles, ESP in the $p' - q$ plane, $\gamma_s - q$ plots and pore water pressures profiles, are depicted in Figures A-18, A-19, A-20, A-21 and A-22, respectively.

4-3-2-6 Investigation on the influence of c'

An increase in the value of c' induces a reduced thickness of the PZ. The values of E_{50} and E_{ur} decrease for a rise in c' (Equations 3-5 and 3-6, respectively), which seems to be counter-intuitive, and the values of G_{50}^{ref} are not altered. Despite the first and the third, the elastoplastic stiffness of the material increases since the $\gamma_s - q$ curve becomes steeper after yield (Figure 4-27). Nevertheless, the considered stress point reaches the MC criterion at larger value of γ_s , probably owing to the fact that the failure surface increases in size in principal stress space for larger c' . Thus, the extent of the PZ decreases owing to the lower amount of redistributed q after the soil elements fully plastify (see Section 4-3-2-5).

The thickness of the HZ decreases for an increase in c' as the stiffness of the soil in the elastoplastic domain rises (Section 4-3-2-2). The decrease in the width of the PZ and the HZ result in a reduction in the extent of the hydro-mechanical disturbance (thickness of the DZ) for an increase in c' .

The forces in the tunnel liner and u decrease for an increase in c' . The former can be explained by inspecting the resulting effective and total stresses, the ESP and the pore water pressures close to the tunnel sidewall (Figures 4-28, 4-29, 4-30 and 4-31, respectively), similarly to the previous sections. Nevertheless, the smaller u cannot be explained by the notion that the tensile u_{excess} increase for a larger reduction in p' , as it is not supported by inspecting the

Table 4-7: Effect of changing the effective cohesion (c') on the thickness of the Plastic Zone (PZ), the Hardening Zone (HZ) and the Disturbed Zone (DZ), the hoop forces in the tunnel liner (N) and the pore water pressures (u) of a stress point next to the tunnel sidewall, at the end of the simulations.

c' [MPa]	PZ [m]	HZ [m]	DZ [m]	N [MN]		u [MPa]	
				$\psi = 0^\circ$	$\psi = 1^\circ$	$\psi = 0^\circ$	$\psi = 1^\circ$
0.10	3.20	21.00	24.20	5.105	4.905	0.797	0.306
0.25	1.70	16.20	17.90	4.382	4.297	0.568	0.275
0.40	0.80	14.80	15.60	3.735	3.695	0.425	0.243

ESP in Figure 4-30. The hypothesis for the evolution of the excess pore water pressures does not hold true for the analyses where the values of E_{ur}^{ref} and c' are varied.

From Figure 4-30 it can be inferred that the stress point next to the tunnel sidewall yields at different values of q when c' is varied. That is because the shear hardening locus is initiated at higher position in the $p' - q$ plane for an increase in c' owing to the intersection with the q -axis at a larger value (see Figure 3-18).

The hoop forces in the tunnel liner and the pore water pressures resulting from the analyses with $\psi = 1^\circ$ are lower than those of the simulations with $\psi = 0^\circ$ (Table 4-7), for the reasons explained in Section 4-3-2-2. The numerical outcomes of the analyses with $\psi = 1^\circ$, in terms of effective and total stress profiles, ESP in the $p' - q$ plane, $\gamma_s - q$ plots and pore water pressures profiles, are depicted in Figures A-23, A-24, A-25, A-26 and A-27, respectively.

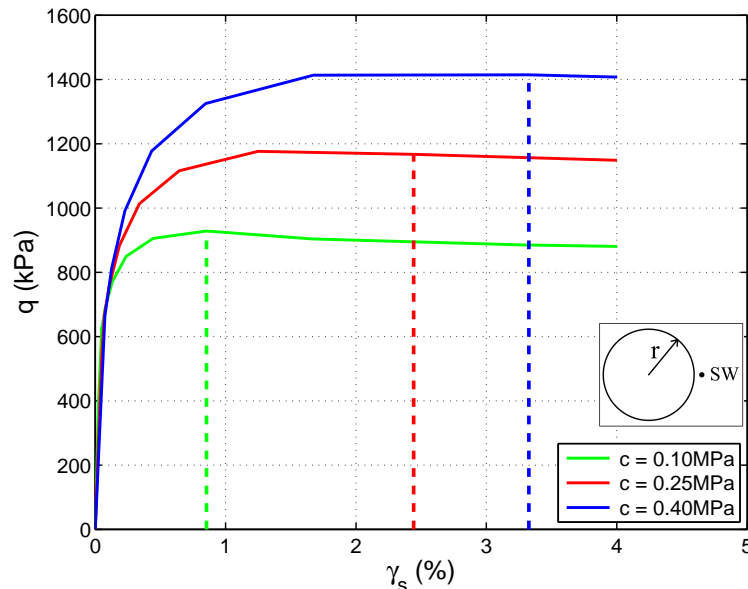


Figure 4-27: Deviator stress (q) versus deviatoric strains (γ_s) plot for a stress point next to the tunnel sidewall (SW), for different values of the effective cohesion (c') and for zero dilatancy angle. The dashed lines indicate the amount of strains at which the stress path meets the Mohr-Coulomb criterion. r is the tunnel radius.

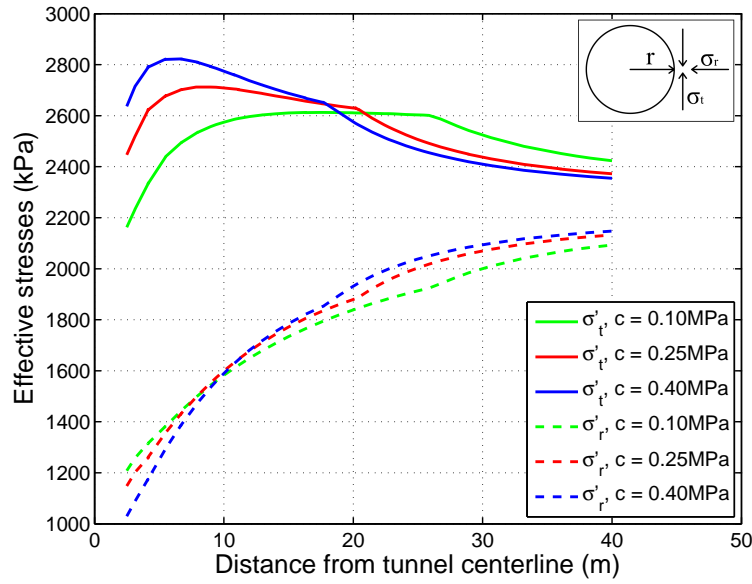


Figure 4-28: Effective radial stresses (σ'_r) and effective tangential stresses (σ'_t), along a radial line, for different values of the effective cohesion (c') and for zero dilatancy angle. r is the tunnel radius.

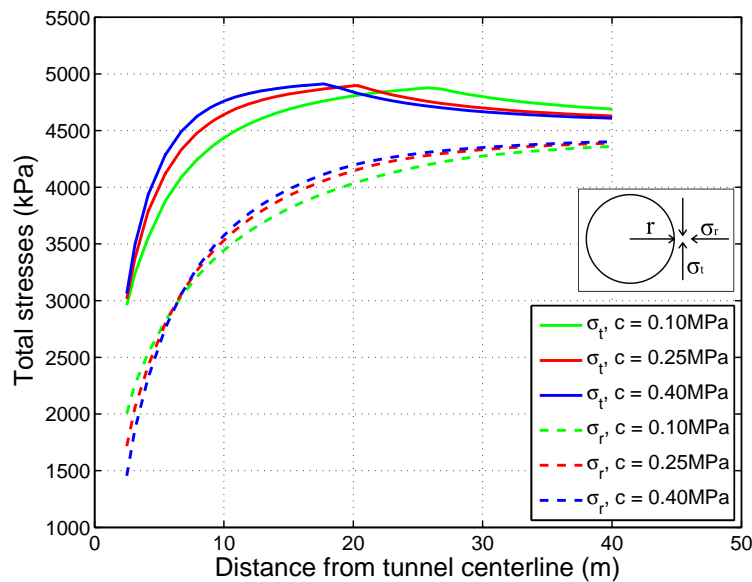


Figure 4-29: Total radial stresses (σ_r) and total tangential stresses (σ_t), along a radial line, for different values of the effective cohesion (c') and for zero dilatancy angle. r is the tunnel radius.

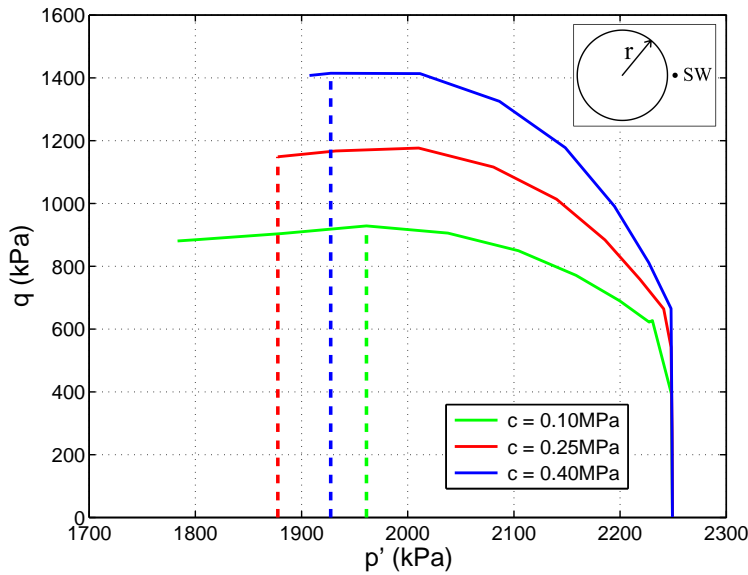


Figure 4-30: Effective Stress Paths (ESP), in a deviator stress (q) versus mean effective stress (p') plot, of a point next to the tunnel sidewall (SW), for different values of the effective cohesion (c') and for zero dilatancy angle. The dashed lines indicate the intersection of each ESP (with the corresponding colour) with the Mohr-Coulomb criterion. r is the tunnel radius.

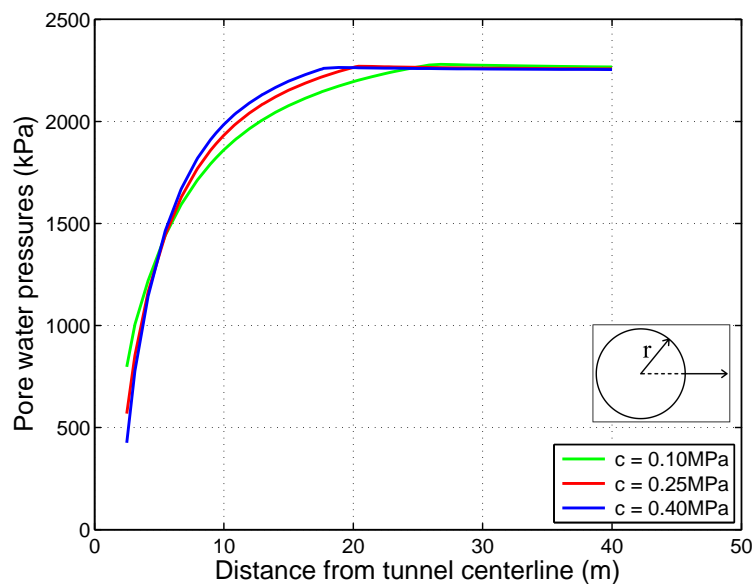


Figure 4-31: Pore water pressures, along a radial line, for different values of the effective cohesion (c') and for zero dilatancy angle. r is the tunnel radius.

4-4 Level of influence of the varied model input parameters

In this section a preliminary estimation of the level of influence of each of the varied HS model input parameters on the thickness of the PZ, the HZ and the DZ, as well as the magnitude of N and the magnitude of u at the tunnel sidewall, is made. In addition, the input parameters, which affect these results the most, are identified.

This is achieved by calculating the percentage change in the aforementioned numerical results, induced by a percentage change of each of the varied model input parameters. The calculations are made for the cases where the model input parameters are increased:

- from their lower bound value to their upper bound value
- from their lower bound value to their mean value
- from their mean value to their upper bound value

An example, for the case where the level of influence of the increase in E_{50}^{ref} from 97MPa to 194MPa (increase from the lower bound value to the upper bound value) on the change in the thickness of the PZ is investigated (see Table 4-3), is given below.

$$\text{Increase in } E_{50}^{ref} \text{ by } 100\% = \frac{194\text{MPa} - 97\text{MPa}}{97\text{MPa}} \text{ induces} \quad (4-10)$$

$$\text{Increase in PZ thickness by } 439\% = \frac{3.02\text{m} - 0.56\text{m}}{0.56\text{m}}$$

As a result, a change in the value of E_{50}^{ref} by 100% causes an increase in the thickness of the PZ by 439%. The level of influence for all other cases is determined in a similar fashion. To this purpose, the findings in Tables 4-3 to 4-7 are utilised. The results are summarised in Table 4-8.

On inspection of the results in Table 4-8, the following conclusions can be drawn:

- The thickness of the PZ is mainly influenced by E_{50}^{ref} ,
- the width of the HZ is predominantly affected by E_{ur}^{ref} ,
- the effect of E_{ur}^{ref} on the thickness of the DZ is the most prevalent,
- the magnitude of N is primarily influenced by φ' , and
- the magnitude of u is mostly affected by φ' .

The thickness of the PZ is affected, in a lower degree than that of E_{50}^{ref} , by φ' and m . The width of the HZ is influenced, in a lower level than that of E_{ur} , by m , φ' and E_{50}^{ref} . The m parameter and φ' follow after E_{ur}^{ref} , in terms of the level of influence on the extent of the hydro-mechanical disturbance (DZ). The magnitude of N and u seems to be mainly affected by E_{50}^{ref} and c' , after φ' .

As mentioned in Section 4-2-3 in a mechanical sensitivity analysis, the effect of all values assigned to the HS model input parameters (lower bound, mean and upper bound) is assumed to retain the same weight on the numerical results, which is not the case when a stochastic

Table 4-8: Percentage change in the thickness of the Plastic Zone (PZ), the Hardening Zone (HZ) and the Disturbed Zone (DZ), the magnitude of the hoop forces in the tunnel liner (N) and the pore water pressures (u) of a stress point next to the tunnel sidewall, induced by the percentage changes in the values (from lower to upper bound, from lower bound to mean and from mean to upper bound) of the HS model input parameters. The results are obtained by utilising the data of Tables 4-3 to 4-7.

Parameter	Increase by (%)	Change in (%)				
		PZ	HZ	DZ	N	u
Lower to upper bound						
E_{50}^{ref}	100	+439	-21	-6	-15	-35
E_{ur}^{ref}	95	-13	+62	+52	-6	+18
m	74	+34	+27	+27	-8	-7
φ'	125	-47	-25	-27	-47	-69
c'	300	-75	-30	-36	-27	-47
Lower bound to mean						
E_{50}^{ref}	49	+204	-5	+1	-8	-18
E_{ur}^{ref}	46	-9	+36	+30	-3	+8
m	40	+21	+13	+14	-4	-5
φ'	63	-26	-16	-18	-25	-36
c'	150	-47	-23	-26	-14	-29
Mean to upper bound						
E_{50}^{ref}	34	+78	-16	-7	-8	-20
E_{ur}^{ref}	33	-5	+20	+17	-3	+9
m	24	+11	+12	+12	-4	-3
φ'	38	-28	-10	-12	-30	-51
c'	60	-53	-9	-13	-15	-25

analysis is performed. It is noted that the current investigation concerns a deterministic study on the level of influence of the input parameters.

In Table 4-8 it is observed that a rise in c' by 60% induces a decrease in the width of the PZ by 53%, which is larger than that of an increase in c' by 150% (the thickness of the PZ reduces by 47% in this case). This indicates that the relationship between the changes in the values c' and the alterations they induce in the extent of the PZ is not linear. This seems to hold true for all the other considered parameters and numerical results.

It is noted that the effect of σ_r on the resulting hoop forces is much more significant than that of σ_t . That is because the percentage change in the values of N is found to be equal to the percentage change in the magnitude of σ_r .

4-5 Summary

In this chapter a deep tunnel excavation in the Boom Clay formation was numerically simulated in plane strain conditions and under undrained conditions, with the *PLAXIS 2D 2011* finite element program. The response of the BC material was modelled with the Hardening Soil (HS) model.

The aim of this chapter was the investigation of the individual effect and of the level of influence of particular HS model input parameters on selected numerical results, by means of a mechanical sensitivity analysis. To this purpose, 22 numerical simulations were performed, where the values of the input parameters were individually varied to an upper and a lower bound, for values of the dilatancy angle (ψ) equal to 0° and 1° . The numerical outcomes of two analyses (one with $\psi = 0^\circ$ and one with $\psi = 1^\circ$), where the values of the model input parameters were equal to the mean of the ranges used, served as a basis for comparison with the results of all other simulations. This set of parameters was referred to as *mean data*. The varied HS model input parameters were the reference secant modulus (E_{50}^{ref}), the reference un-/reloading modulus (E_{ur}^{ref}), the rate of the level of stress dependency of stiffness (m), the effective friction angle (φ') and the effective cohesion (c').

First the boundaries of the finite element mesh and the boundary conditions of the problem were outlined. The geometry of the tunnel and the liner properties were summarised. The main assumptions made for the development of the geotechnical model were listed. Subsequently, the calculation phases of the numerical simulation were described. A description of the set up of the mechanical sensitivity analysis was given.

Subsequently, the Effective Stress Paths (ESP) of stress points close to the periphery of the tunnel, resulting from the analysis with the *initial data* and for $\psi = 0^\circ$, were presented in terms of the deviator stress (q) versus the mean effective stress (p'), and explained, for investigating the HS model response in undrained excavation.

The examined numerical results concerned the thickness of the fully Plastic Zone (PZ) around the excavation, the width of the shear Hardening Zone (HZ), and the extent of the hydro-mechanical disturbance or the extent of the Disturbed Zone (DZ = PZ + HZ). Furthermore, the influence of the varied HS model input parameters on the resulting axial liner forces (N) and the generated pore water pressures (u) at the tunnel sidewall was examined.

It was found that the extent of the PZ is influenced by the magnitude of the elastoplastic shear stiffness of the material, which controls the amount of deviatoric strains (γ_s) at failure. The latter is significant as all analyses were performed by applying a constant amount of the tunnel contraction (i.e. the amount of imposed strains was kept constant). In such case, a larger shear stiffness in the elastoplastic domain entails failure of the soil elements at lower level of (γ_s). Consequently, a larger amount of q is redistributed from the fully plastified soil elements to their surroundings, as a larger portion of the prescribed γ_s needs to be applied after failure, until the completion of the simulation. Thus, the extent of the PZ increased for an increase in the elasto-plastic shear stiffness of the material. The thickness of the PZ was found to increase for a rise in the values of E_{50}^{ref} and m . On the other hand, an increase in the values of φ' and c' was found to induce a smaller extent of the PZ. The un-/reloading modulus was found not to influence the extent of the PZ.

The thickness of the HZ was found to be influenced by both the elastoplastic and the elastic

shear stiffness of the material. A rise in the first induced a smaller extent of the HZ as a lower amount of q was redistributed from stiffer stress points, of which the ESP lay on the shear hardening locus, to their surroundings. On the contrary, an increase in the elastic shear stiffness caused the ESP of the stress points which were situated in the elastic domain to yield at a smaller amount of γ_s , leading to a larger extent of the HZ. The thickness of the HZ was found to increase for a rise in the values of E_{ur}^{ref} and m . A rise in E_{50}^{ref} , φ' and c' led to a reduction in the extent of the HZ. The thickness of the DZ, which is derived by adding the width of the PZ and the HZ, increased for a rise in the values of E_{ur}^{ref} and m , whereas it reduced for an increase in the magnitudes of E_{50}^{ref} , φ' and c' .

The pore water pressures next to the sidewall of the tunnel were found to be affected by the generated negative excess pore water pressures (u_{excess}). The produced u reduced for an increase in the values of E_{50}^{ref} , m , φ' and c' , whereas they increased slightly for a rise in the magnitude of E_{ur}^{ref} .

The hoop forces in the tunnel liner were found to be mainly influenced by the magnitude of the total radial stresses (σ_r) acting on the periphery of the excavation, which result from adding the generated radial effective stresses (σ'_r) and u . For the simulations where $\psi = 0^\circ$ was used, the value of N was found to reduce for an increase in the values of all varied model input parameters. This reduction was larger for the analyses where $\psi = 1^\circ$ was used, owing to the generation of more negative u_{excess} and therefore, to the generation of less compressive u acting on the liner. Aside from the different magnitudes of N and u , the thickness of the PZ, the HZ and the DZ was found to remain constant for $\psi = 0^\circ$ and $\psi = 1^\circ$.

A preliminary estimation of the level of influence of each varied model input parameter on the numerical results followed.

Finally, the varied model input parameters which affect the investigated numerical results the most were identified. It was found that the thickness of the PZ is mainly influenced by E_{50}^{ref} . The extent of the HZ and the DZ were mostly affected by E_{ur}^{ref} . The magnitudes of N and u were predominantly influenced by φ' .

Chapter 5

Conclusions and recommendations

5-1 Conclusions

The conclusions drawn for the Hardening Soil (HS) model performance regarding the numerical simulations of the laboratory tests, presented in Chapter 3, are discussed in Section 5-1-1. Subsequently, the findings of the numerical analyses of the undrained tunnel excavation (Chapter 4) are presented in Section 5-1-2. Finally, in Section 5-1-3 the main limitations of the current research are discussed.

5-1-1 On the performance of the HS model in simulating the laboratory tests

The HS model was considered to perform best, among the assessed soil models, in simulating the triaxial tests and the oedometer test performed by [Deng et al. \(2011b\)](#).

The HS model captures well the response of the Boom Clay (BC) material of the *Ess75Tr* drained triaxial compression tests performed by [Deng et al. \(2011b\)](#). The model was found to reproduce satisfactorily the evolution of the stiffness and the mobilised shear strength of the material in Normally Consolidated (NC) and Over-Consolidated (OC) conditions, especially at a low level of axial strain ($\varepsilon_a \leq 5\%$). Furthermore, the peak deviator stress in the OC specimens was fairly well computed however, it was reached at larger ε_a than in the actual tests. The volumetric behaviour of the soil was found to be well simulated for NC conditions and for high values of the Over-Consolidation ratio (OCR). However, this did not hold true for intermediate values of the OCR. Furthermore, the HS model does not account for the strain softening exhibited by the material in OC conditions.

The HS model was found to perform competently in simulating the resulting slope of the virgin compression line and the void ratio at the end of the un-/reloading paths of the *Ess75Oedo1* oedometer test conducted by [Deng et al. \(2011b\)](#). The significant hysteresis and the swelling potential exhibited by the specimen were qualitatively well reproduced. Nevertheless, the HS model does not consider the time-dependent consolidation behaviour of the material.

5-1-2 On the findings of the numerical simulations of the undrained tunnel excavation

On the extent of the hydro-mechanical disturbance

The extent of the hydro-mechanical disturbance around the tunnel excavation was found to depend primarily on the shear stiffness of the material in the elastic domain and in the elastoplastic domain. The former, which is controlled by the elastic shear modulus (G_{ur}), determines the amount of the deviatoric strains (γ_s) at initial yield and thus, the thickness of the elastoplastic Hardening Zone (HZ). The thickness of the HZ was found to be mostly affected by the magnitude of the reference un-/reloading modulus (E_{ur}^{ref}), which determines the value of G_{ur} . The extent of the HZ was found to increase (or decrease) for a rise (or a reduction) in the value of E_{ur}^{ref} .

The elasto-plastic shear stiffness, which is determined by the elasto-plastic shear modulus (G_{50}), was found to affect the amount of γ_s at failure and therefore, the thickness of the fully Plastic Zone (PZ). The influence of G_{50} on the extent of the HZ was less significant than that of G_{ur} . The radial extent of the PZ was found to be mainly influenced by the value of the reference secant modulus (E_{50}^{ref}), which controls the magnitude of G_{50} . An increase (or a decrease) in E_{50}^{ref} induced a rise (or a decrease) in the extent of the PZ.

The dependency of the HS model response on the shear moduli is ascribed to the fact that a constant amount of the tunnel contraction was imposed in all analyses, i.e. the amount of the imposed strains was kept constant.

The extent of the Disturbed Zone ($DZ = PZ + HZ$) was found to be primarily influenced by the magnitude of E_{ur}^{ref} , that is, it increased (or reduced) for a rise (or a decrease) in E_{ur}^{ref} .

On the magnitude of the hoop liner forces and the pore water pressures

The influence of the effective friction angle (φ') on the hoop forces in the tunnel liner (N) and on the pore water pressures (u) acting on the periphery of the tunnel was found to be the most prevalent. An increase in the value of φ' induced smaller N , as the generated total radial stresses (σ_r) acting on the liner reduced. The latter resulted from the lower radial effective stresses (σ'_r) and the reduced pore water pressures ($\sigma_r = \sigma'_r + u$).

The magnitudes of u and N were found to decrease for an increase in the dilatancy angle (ψ) of the material owing to the generation of lower negative excess pore water pressures (u_{excess}) and thus, to lower compressive u . This resulted from the tendency of the material to dilate, combined with assumption of undrained conditions (no volume change).

5-1-3 On the limitations of the research

The hypothesis of the BC being in a fully saturated state and responding fully undrained may hold only true for the very first stage of the tunnel excavation.

Furthermore, the assumption of an isotropic initial stress field has led to a more isotropic radial extent of the hydro-mechanical disturbance around the excavation as one would expect, given

the K_0 -values ranging from 0.3 to 0.9 as being estimated at the HADES URF (e.g. Bernier et al., 2007a).

Moreover, the assumption of plane strain conditions did not allow for an investigation of the extent of the hydro-mechanical disturbance ahead of, and behind the tunnel face. Finally, the hypothesis that the out of plane strains are equal to zero has caused the resulting stress paths, and therefore the soil response, to be different than that of a more realistic, three-dimensional analysis.

5-2 Recommendations for further research

An investigation on the effect of an anisotropic initial stress field is expected to be of importance. It is likely to induce a different extent of the DZ in horizontal and vertical direction due to the different level of deviatoric loading in the vicinities of the crown, the sidewall and the invert of the tunnel. Furthermore, significant shear forces and bending moments might develop in the tunnel liner as a result of these differential stresses.

In addition, an examination of the effect of cap hardening, of which the response is mainly affected by the reference oedometer modulus (E_{oed}^{ref}), may be of interest. The generated plastic deviatoric cap strains, which are presumably added to the ones induced by shear hardening, might lead to a larger extent of the PZ and the HZ. Moreover, the produced plastic volumetric cap strains may influence the magnitude of the negative u_{excess} and thus, the magnitude of the hoop forces in the liner.

Moreover, an examination of the long-term response of the host rock-tunnel system through consolidation analyses is required, as the magnitude of N is expected to be different at the completion of consolidation, than that corresponding to the short term conditions, owing to the dissipation of u_{excess} .

Furthermore, a three-dimensional numerical simulation of the tunnel excavation is likely to be of importance. In such an analysis the resulting stress paths and thus, the computed soil response, is expected to be more realistic. Moreover, examination of the soil response due to the advancement of the excavation front will be feasible, e.g. the convergence of the soil ahead of the tunnel face will be numerically predicted. Also, the stress and strain concentration effects in the vicinity of the connections of the different parts of the repository will be examined.

An economical, technical and safety analysis for the selection of the optimal design of the repository is of high significance. This may be achieved by investigating the effect of varying the magnitude of the over-excavated radius, i.e. the amount of the convergence of the soil on the required tunnel liner characteristics as well as on the extent of the hydro-mechanical disturbance. The former mainly concerns the required thickness/stiffness and strength of the liner, as a result of the induced internal forces. The extent of the DZ concerns the spacing between adjacent tunnels as well as the possibility of radionuclide migration.

Finally, the safety and performance of the repository is expected to depend on other processes aside from the hydro-mechanical disturbance, especially in terms of radionuclide migration. An integrated approach assessing the long-term performance of the repository should consist of thermo-hydro-chemo-bio-mechanically coupled analyses, accounting for uncertainties in material properties and boundary conditions.

Appendix A

Numerical results of the mechanical sensitivity analysis

In this appendix the numerical results of the mechanical sensitivity analysis, performed in the context of the numerical simulations of an undrained tunnel excavation in the Boom Clay formation (see Chapter 4), are shown.

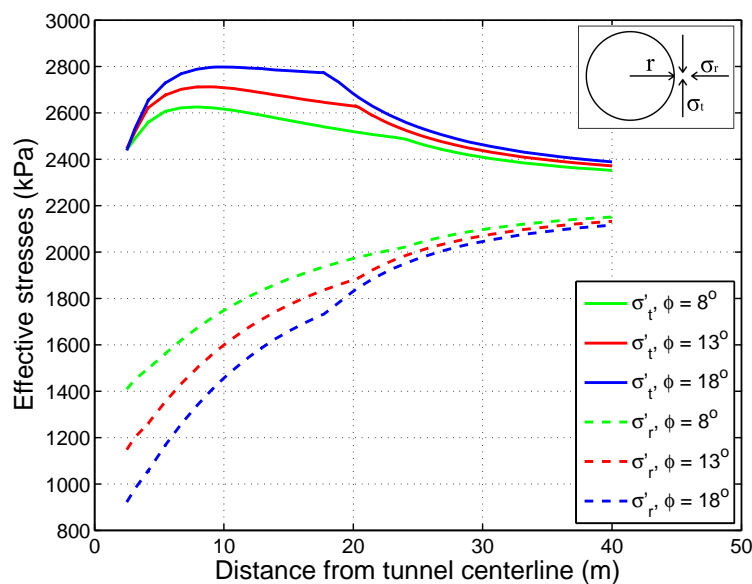


Figure A-1: Effective radial stresses (σ'_r) and effective tangential stresses (σ'_t), along a radial line, for different values of the effective friction angle (φ') and for zero dilatancy angle. r is the tunnel radius.

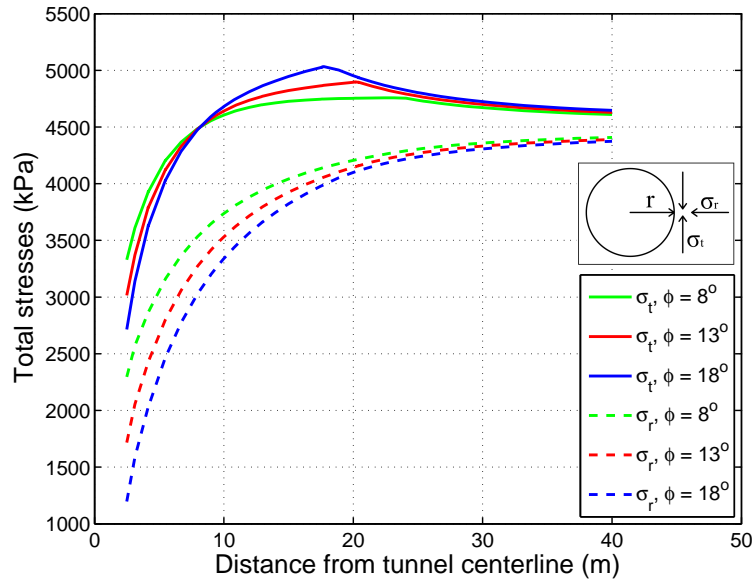


Figure A-2: Total radial stresses (σ_r) and total tangential stresses (σ_t), along a radial line, for different values of the effective friction angle (φ') and for zero dilatancy angle. r is the tunnel radius.

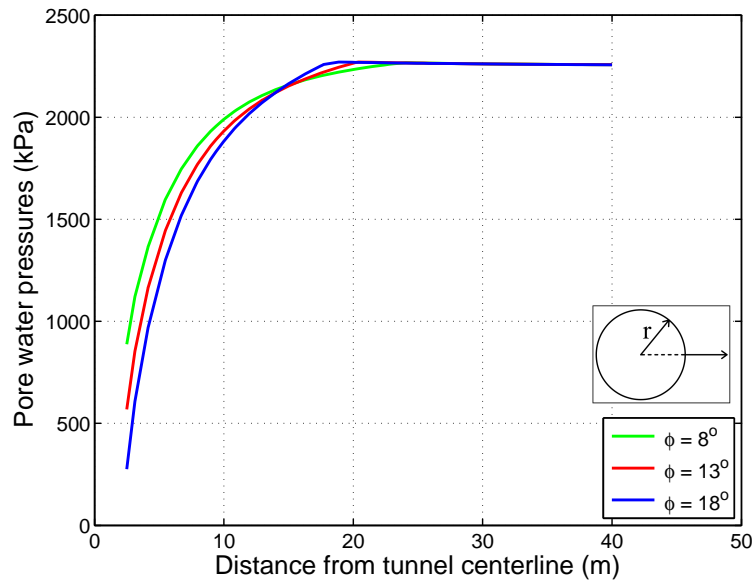


Figure A-3: Pore water pressures, along a radial line, for different values of the effective friction angle (φ') and for zero dilatancy angle. r is the tunnel radius.

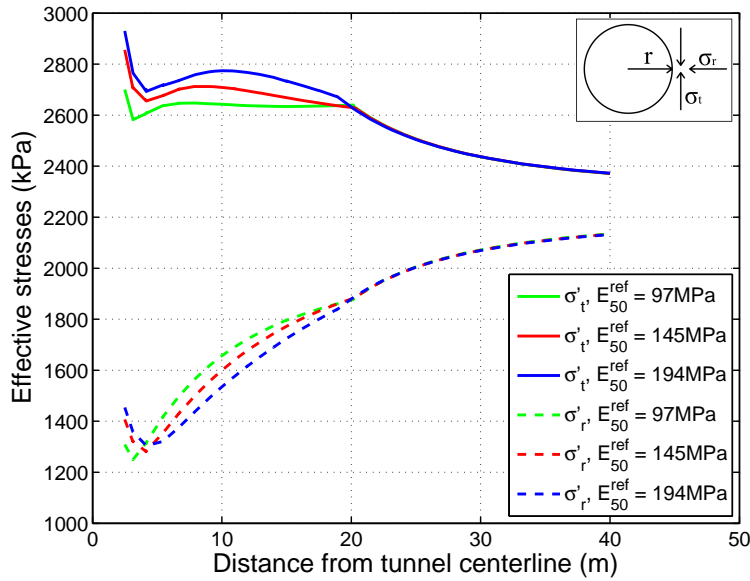


Figure A-4: Effective radial stresses (σ'_r) and effective tangential stresses (σ'_t), along a radial line, for different values of the reference secant modulus (E_{50}^{ref}) and for dilatancy angle equal to 1° . r is the tunnel radius.

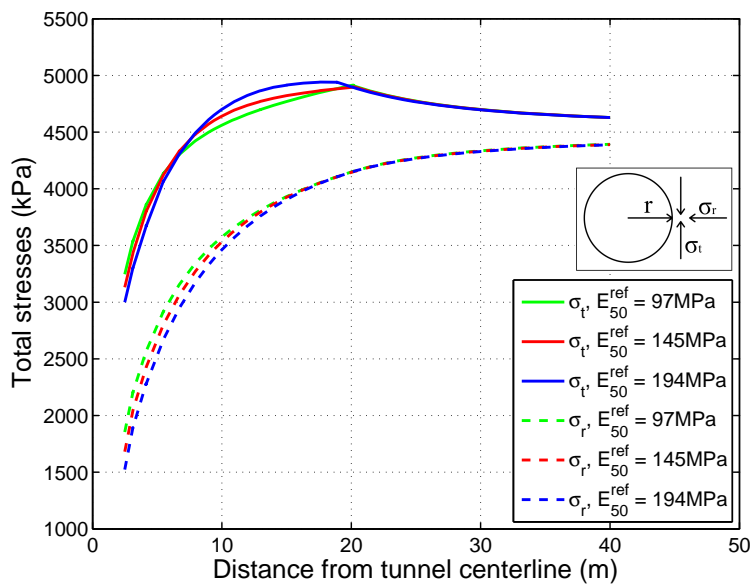


Figure A-5: Total radial stresses (σ_r) and total tangential stresses (σ_t), along a radial line, for different values of the reference secant modulus (E_{50}^{ref}) and for dilatancy angle equal to 1° . r is the tunnel radius.

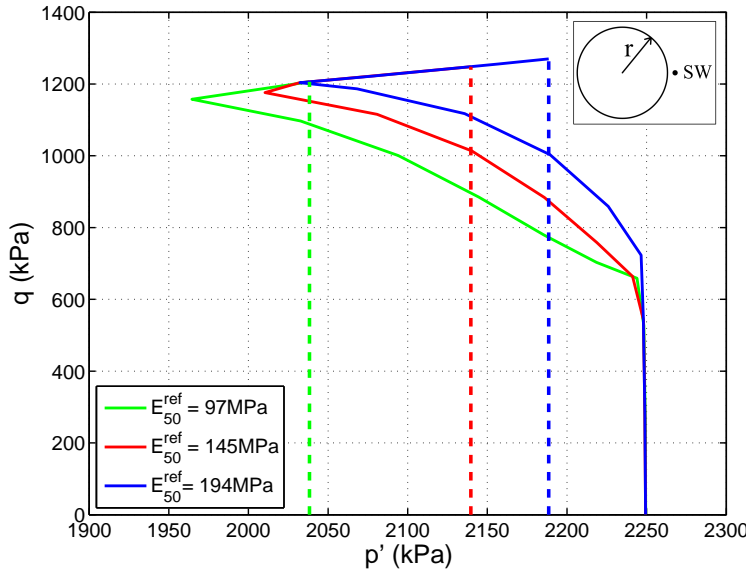


Figure A-6: Effective Stress Paths (ESP), in a deviator stress (q) versus mean effective stress (p') plot, of a point next to the tunnel sidewall (SW), for different values of the reference secant modulus (E_{50}^{ref}) and for dilatancy angle equal to 1° . The dashed lines indicate the position of each ESP (with the corresponding colour) at the completion of the calculation. r is the tunnel radius.

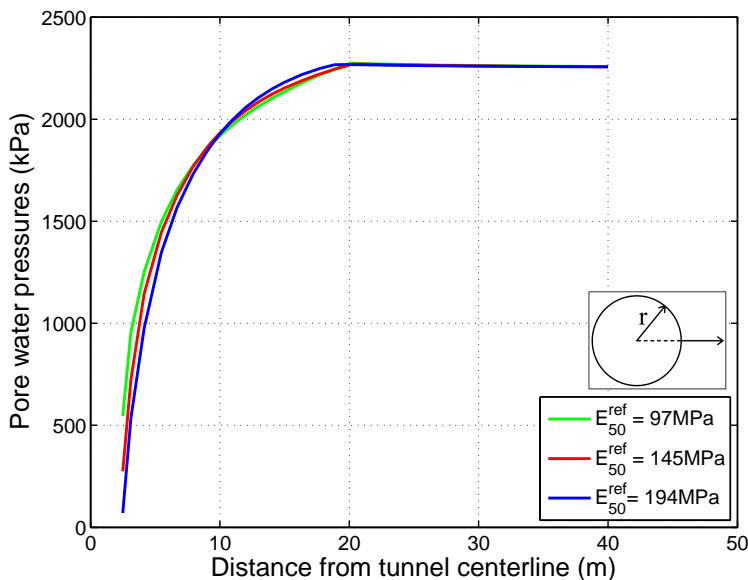


Figure A-7: Pore water pressures, along a radial line, for different values of the reference secant modulus (E_{50}^{ref}) and for dilatancy angle equal to 1° . r is the tunnel radius.

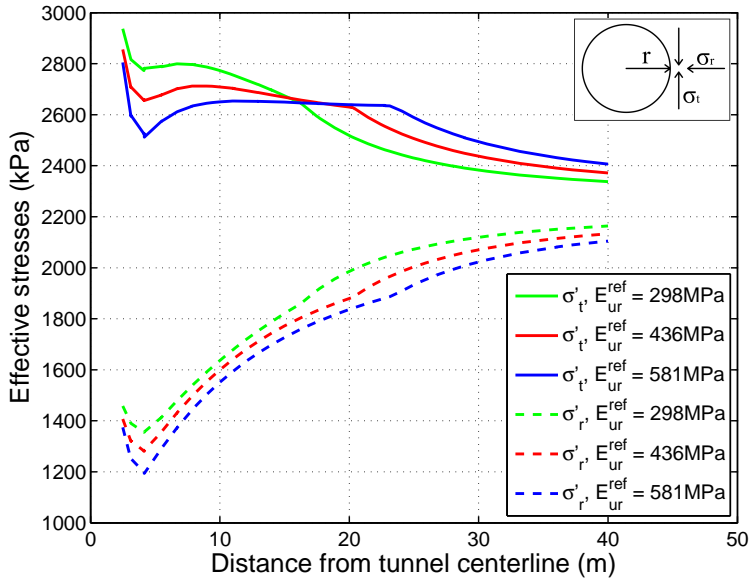


Figure A-8: Effective radial stresses (σ'_r) and effective tangential stresses (σ'_t), along a radial line, for different values of the reference unloading-reloading modulus (E_{ur}^{ref}) and for dilatancy angle equal to 1° . r is the tunnel radius.

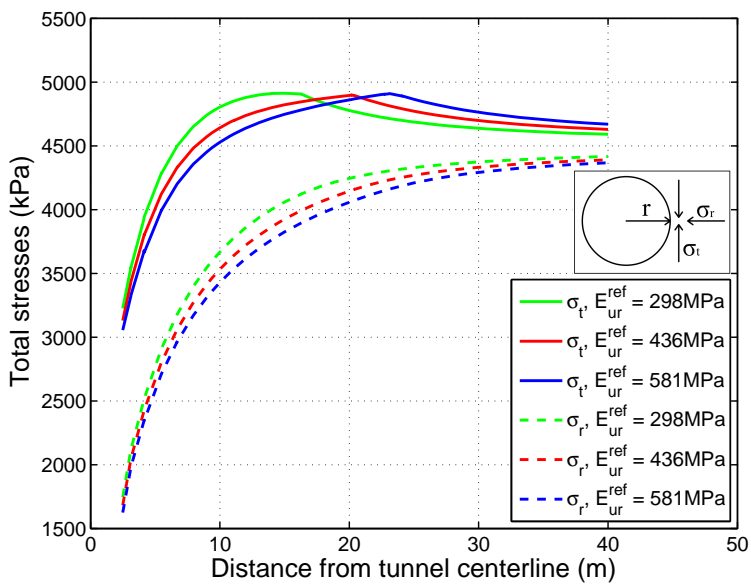


Figure A-9: Total radial stresses (σ_r) and total tangential stresses (σ_t), along a radial line, for different values of the reference unloading-reloading modulus (E_{ur}^{ref}) and for dilatancy angle equal to 1° . r is the tunnel radius.

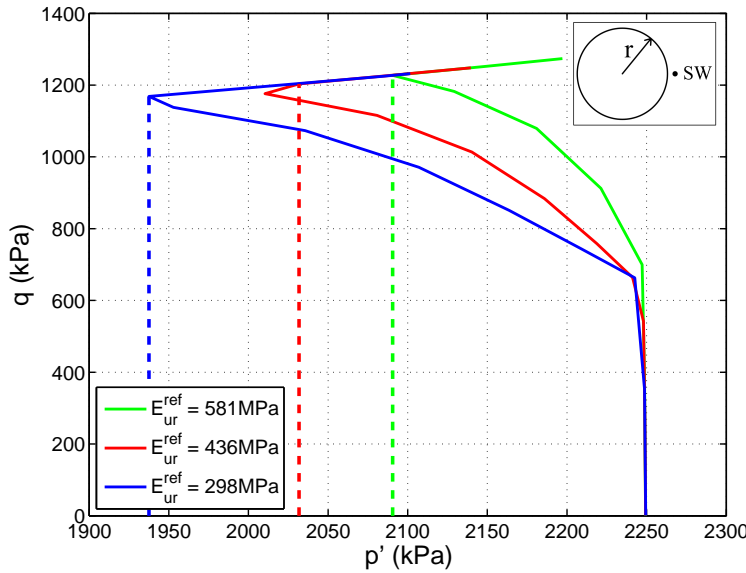


Figure A-10: Effective Stress Paths (ESP), in a deviator stress (q) versus mean effective stress (p') plot, of a point next to the tunnel sidewall (SW), for different values of the reference unloading-reloading modulus (E_{ur}^{ref}) and for dilatancy angle equal to 1° . The dashed lines indicate the intersection of each ESP with the Mohr-Coulomb criterion. r is the tunnel radius.

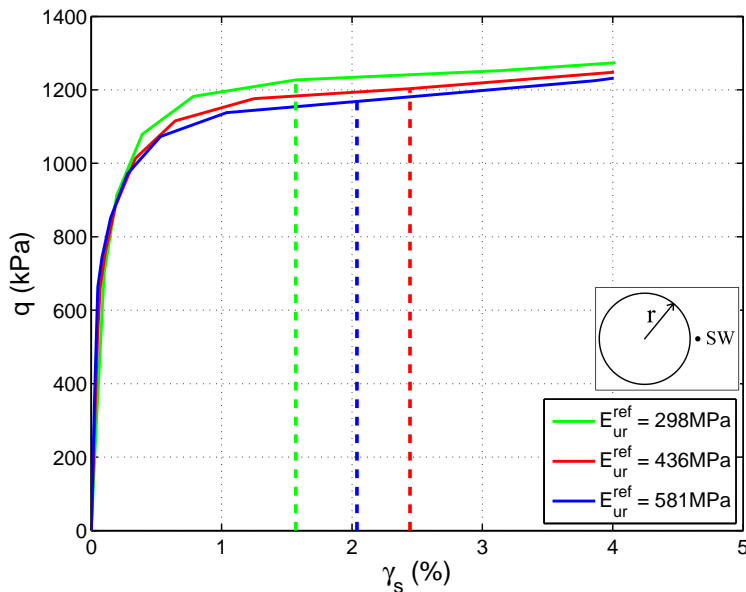


Figure A-11: Deviator stress (q) versus deviatoric strains (γ_s) plot for a stress point next to the tunnel sidewall (SW), for different values of the reference unloading-reloading modulus (E_{ur}^{ref}) and for dilatancy angle equal to 1° . The dashed lines indicate the amount of strains at which the stress path meets the Mohr-Coulomb criterion. r is the tunnel radius. The amount of γ_s at which the material fully plastifies differs between this case and the respective case with $\psi = 0^\circ$ (Figure 4-15), as the results of the latter have been obtained for an increased accuracy of the analysis.

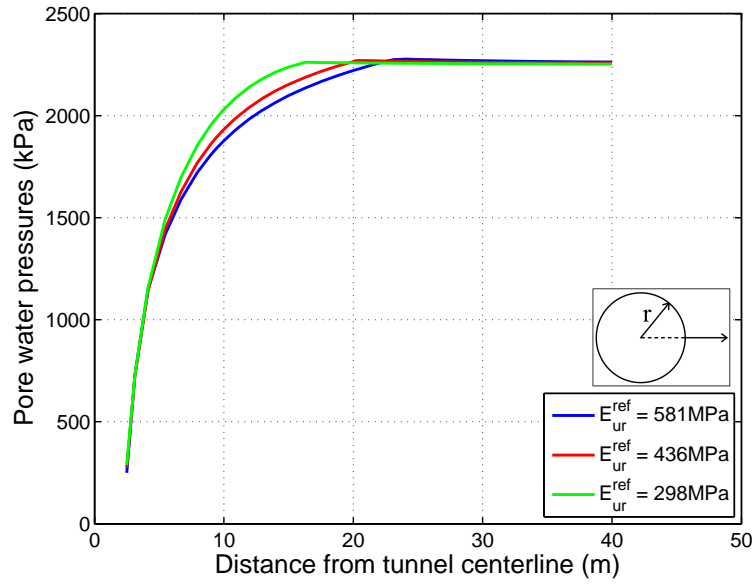


Figure A-12: Pore water pressures, along a radial line, for different values of the reference unloading - reloading modulus (E_{ur}^{ref}) and for dilatancy angle equal to 1° . r is the tunnel radius.

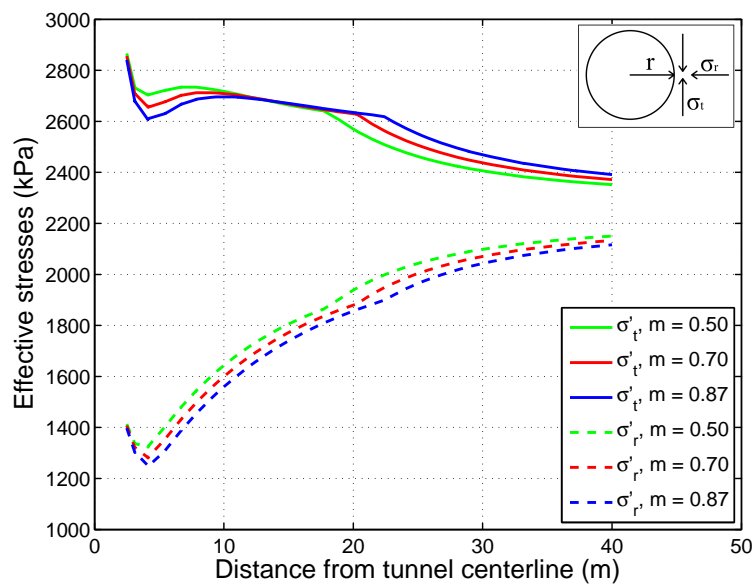


Figure A-13: Effective radial stresses (σ'_r) and effective tangential stresses (σ'_t), along a radial line, for different values of the rate of stress dependency of stiffness (m) and for dilatancy angle equal to 1° . r is the tunnel radius.

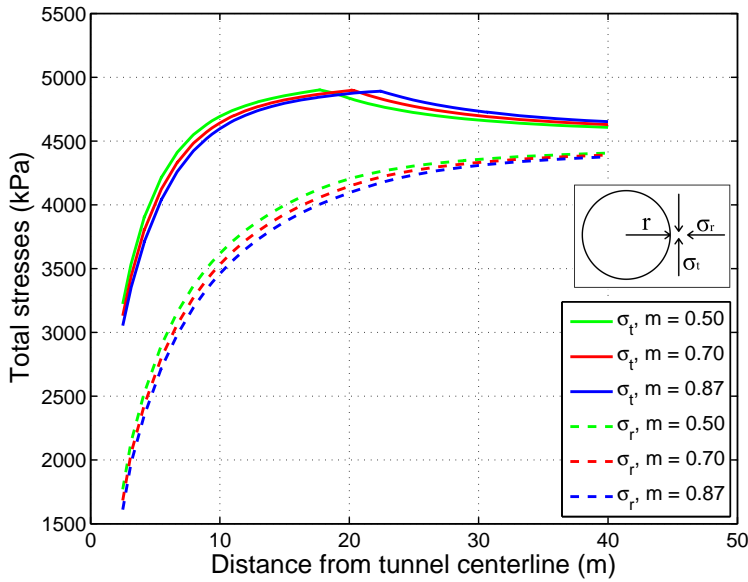


Figure A-14: Total radial stresses (σ_r) and total tangential stresses (σ_t), along a radial line, for different values of the rate of stress dependency of stiffness (m) and for dilatancy angle equal to 1° . r is the tunnel radius.

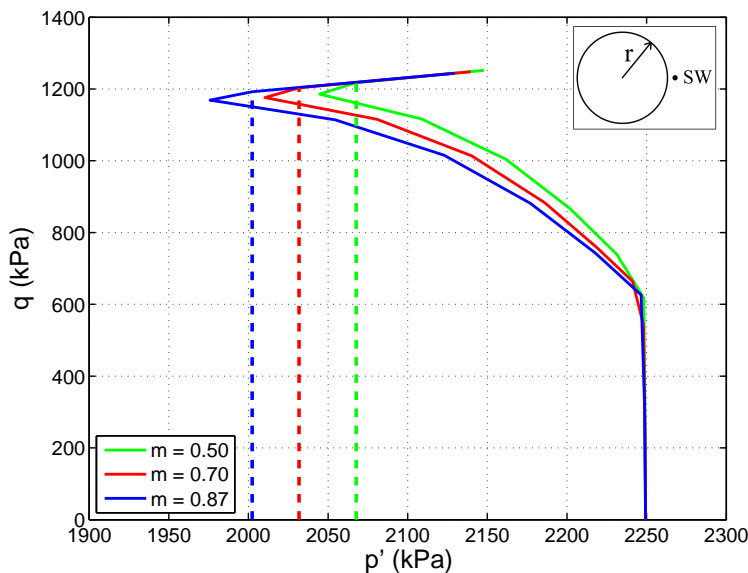


Figure A-15: Effective Stress Paths (ESP), in a deviator stress (q) versus mean effective stress (p') plot, of a point next to the tunnel sidewall (SW), for different values of the rate of stress dependency of stiffness (m) and for dilatancy angle equal to 1° . The dashed lines indicate the intersection of each ESP with the Mohr-Coulomb criterion. r is the tunnel radius.

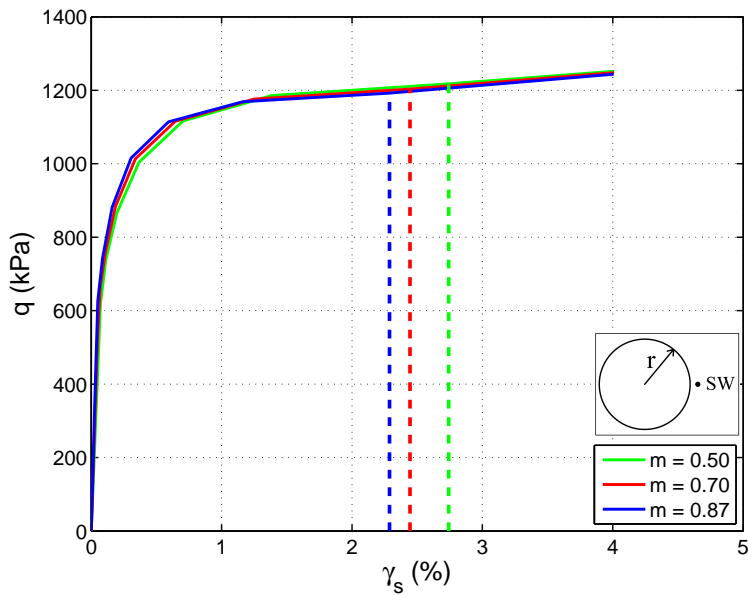


Figure A-16: Deviator stress (q) versus deviatoric strains (γ_s) plot for a stress point next to the tunnel sidewall (SW), for different values of the rate of stress dependency of stiffness (m) and for dilatancy angle equal to 1° . The dashed lines indicate the amount of strains at which the stress path meets the Mohr-Coulomb criterion. r is the tunnel radius.

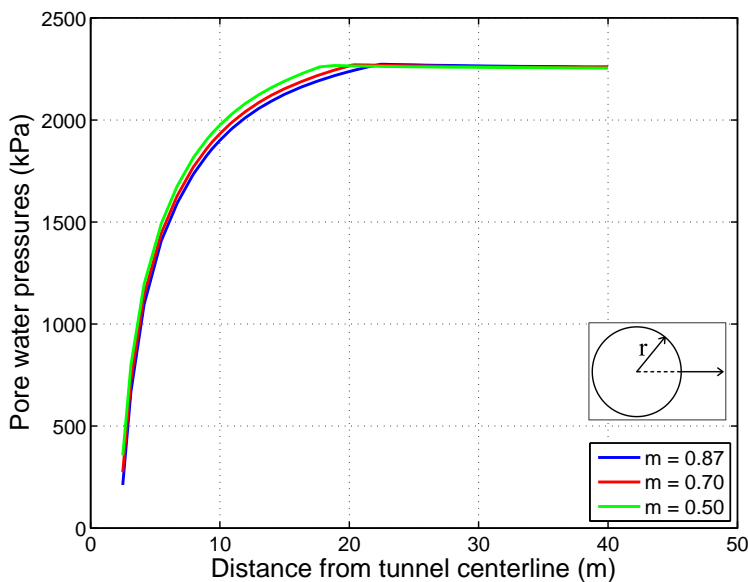


Figure A-17: Pore water pressures, along a radial line, for different values of the rate of stress dependency of stiffness (m) and for dilatancy angle equal to 1° . r is the tunnel radius.

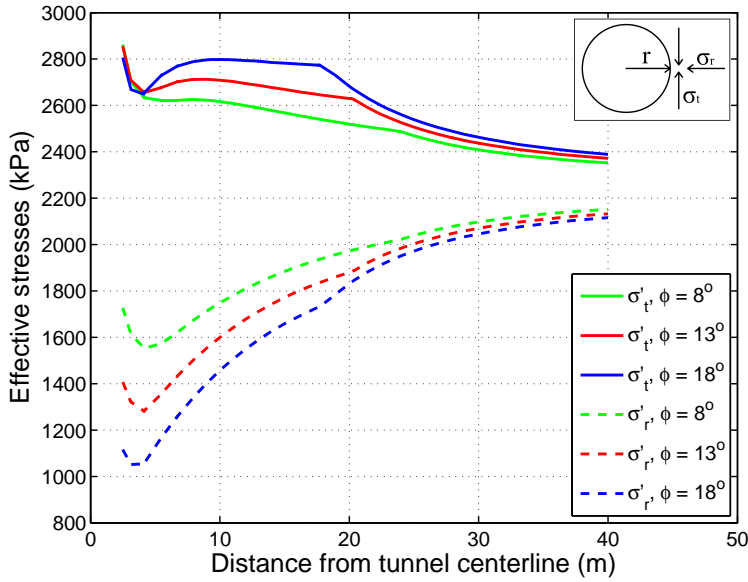


Figure A-18: Effective radial stresses (σ'_r) and effective tangential stresses (σ'_t), along a radial line, for different values of the effective friction angle (φ') and for dilatancy angle equal to 1° . r is the tunnel radius.

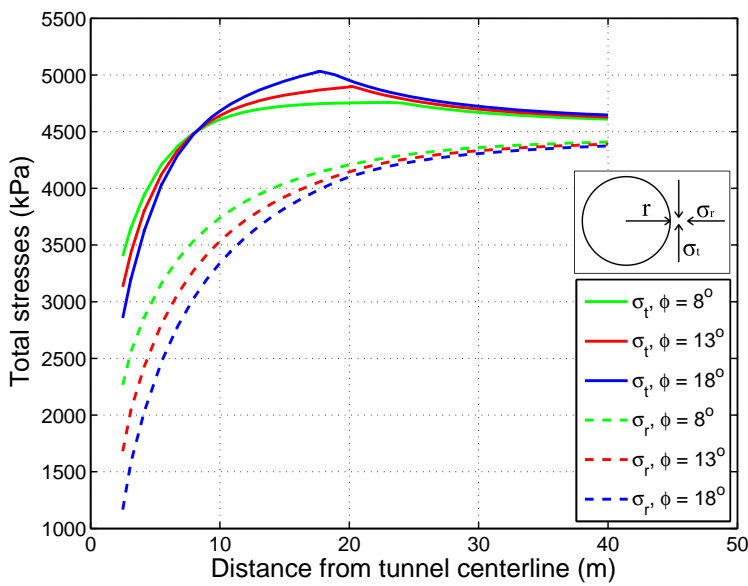


Figure A-19: Total radial stresses (σ_r) and total tangential stresses (σ_t), along a radial line, for different values of the effective friction angle (φ') and for dilatancy angle equal to 1° . r is the tunnel radius.

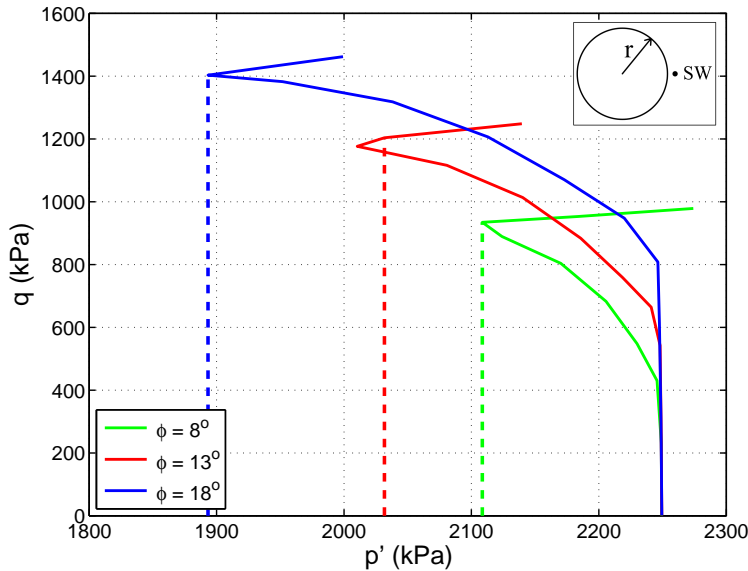


Figure A-20: Effective Stress Paths (ESP), in a deviator stress (q) versus mean effective stress (p') plot, of a point next to the tunnel sidewall (SW), for different values of the effective friction angle (φ') and for dilatancy angle equal to 1° . The dashed lines indicate the intersection of each ESP (with the corresponding colour) with the Mohr-Coulomb criterion. r is the tunnel radius.

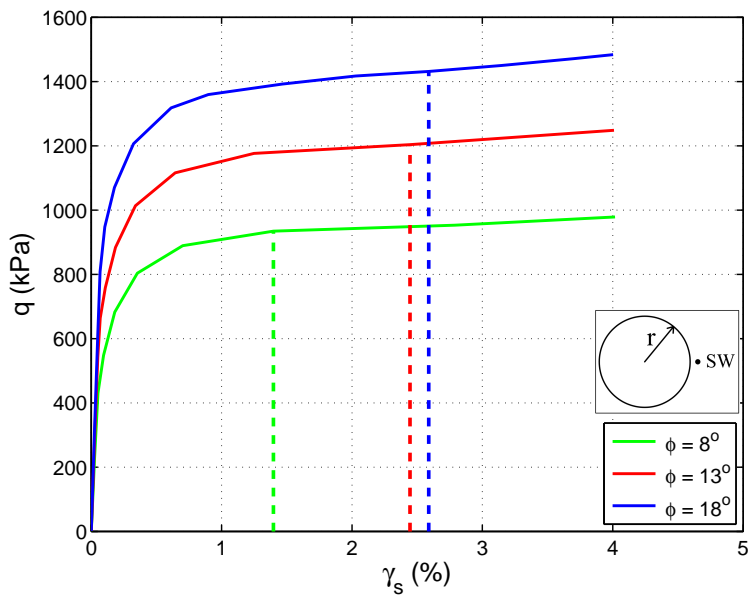


Figure A-21: Deviator stress (q) versus deviatoric strains (γ_s) plot for a stress point next to the tunnel sidewall (SW), for different values of the effective friction angle (φ') and for dilatancy angle equal to 1° . The dashed lines indicate the amount of strains at which the stress path meets the Mohr-Coulomb criterion. r is the tunnel radius.

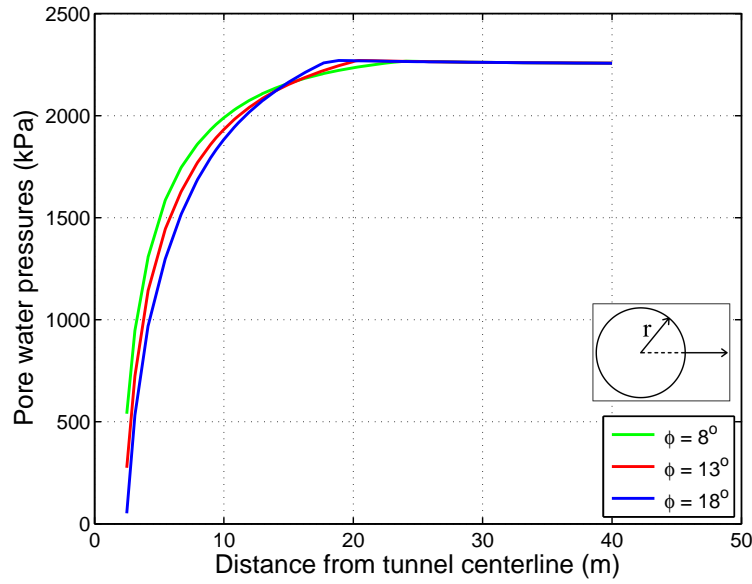


Figure A-22: Pore water pressures, along a radial line, for different values of the effective friction angle (φ') and for dilatancy angle equal to 1° . r is the tunnel radius.

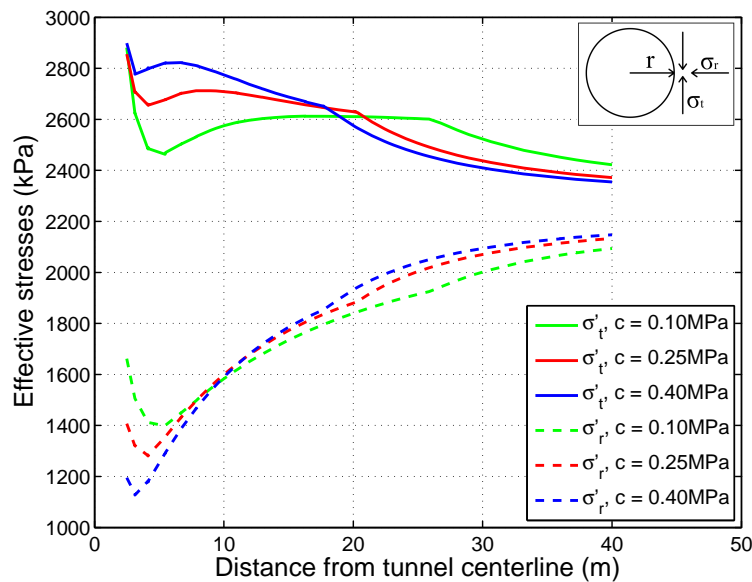


Figure A-23: Effective radial stresses (σ'_r) and effective tangential stresses (σ'_t), along a radial line, for different values of the effective cohesion (c') and for dilatancy angle equal to 1° . r is the tunnel radius.

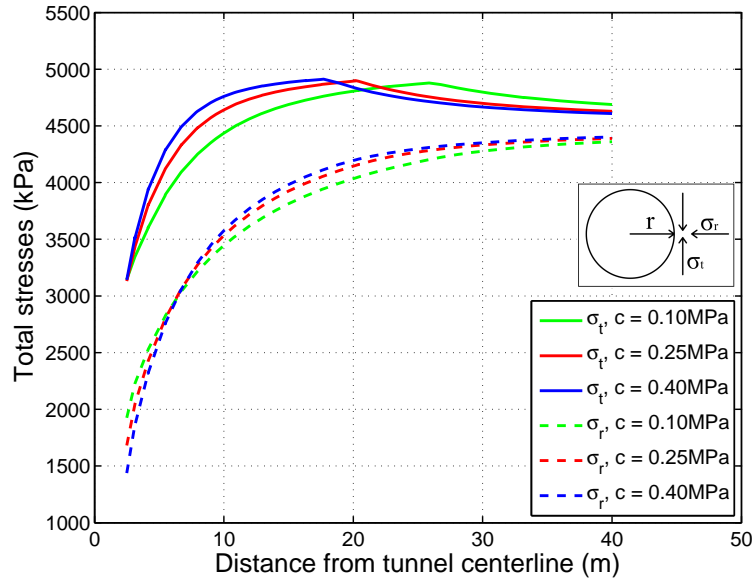


Figure A-24: Total radial stresses (σ_r) and total tangential stresses (σ_t), along a radial line, for different values of the effective cohesion (c') and for dilatancy angle equal to 1° . r is the tunnel radius.

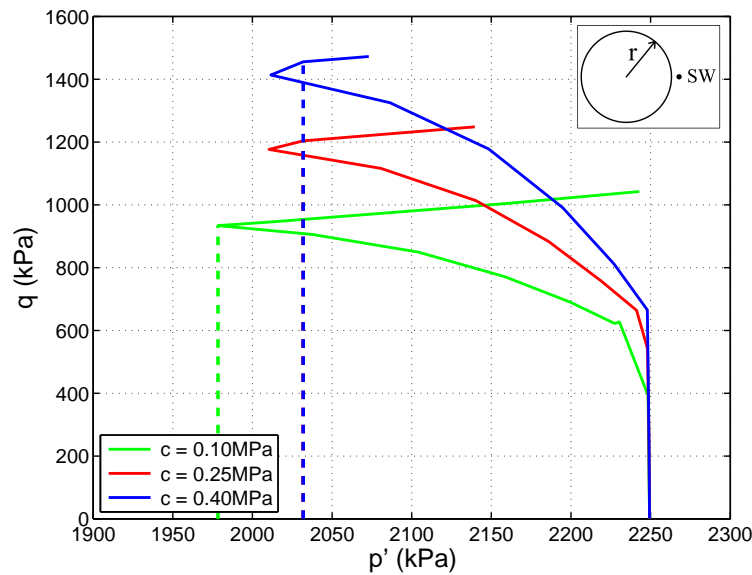


Figure A-25: Effective Stress Paths (ESP), in a deviator stress (q) versus mean effective stress (p') plot, of a point next to the tunnel sidewall (SW), for different values of the effective cohesion (c') and for dilatancy angle equal to 1° . The dashed lines indicate the intersection of each ESP (with the corresponding colour) with the Mohr-Coulomb (MC) criterion. r is the tunnel radius. The stress paths for $c = 0.25\text{MPa}$ and $c = 0.40\text{MPa}$ reach the MC criterion at the same value of p' .

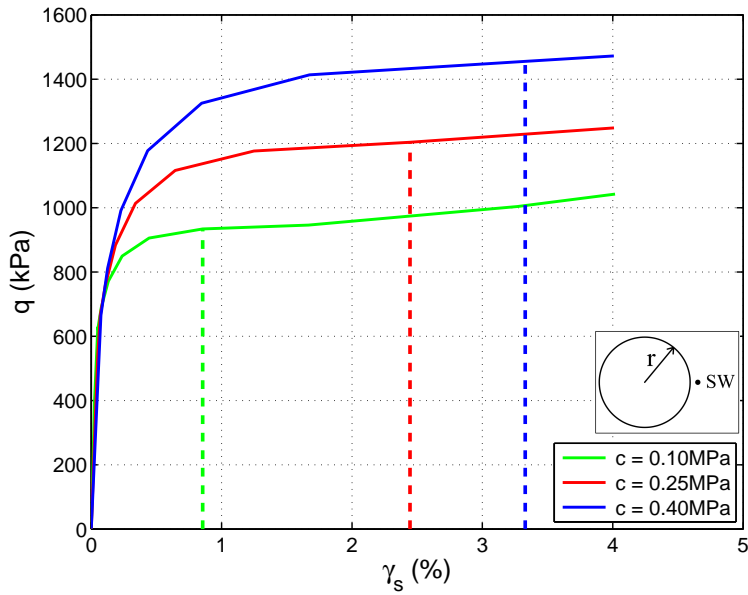


Figure A-26: Deviator stress (q) versus deviatoric strains (γ_s) plot for a stress point next to the tunnel sidewall (SW), for different values of the effective cohesion (c') and for dilatancy angle equal to 1° . The dashed lines indicate the amount of strains at which the stress path meets the Mohr-Coulomb criterion. r is the tunnel radius.

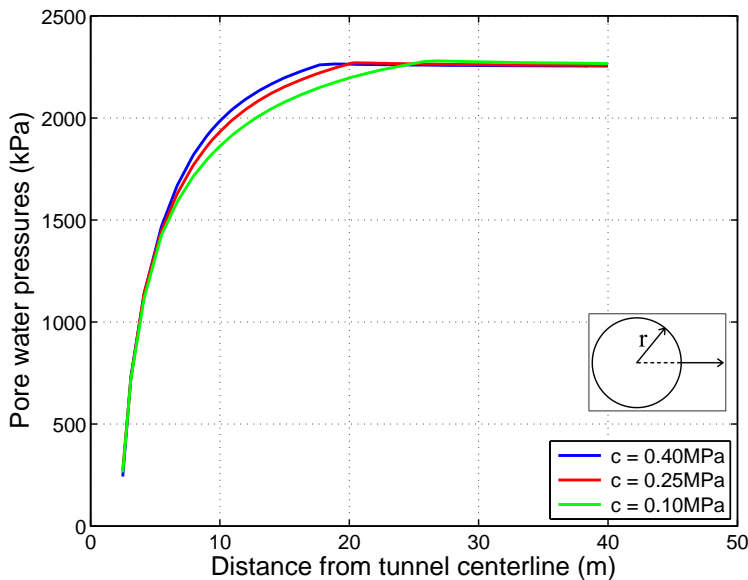


Figure A-27: Pore water pressures, along a radial line, for different values of the effective cohesion (c') and for a dilatancy angle equal to 1° . r is the tunnel radius.

Bibliography

- Aertsens, M., Maes, N., Labat, S., Van Gompel, M., and Maes, T. (2013). Vertical Distribution of HTO and $^{125}\text{I}^-$ Transport Parameters in Boom Clay in the Essen-1 Borehole. *Physics and Chemistry of the Earth, Parts A/B/C, Clays in Natural & Engineered Barriers for Radioactive Waste Confinement*, 65:90–97.
- Arnold, P., Vardon, P. J., Hicks, M. A., Fokkens, J., and Fokker, P. A. (2014). A numerical and reliability-based investigation into the technical feasibility of a Dutch radioactive waste repository in Boom Clay [In press]. Technical report, Delft University of Technology, Geo-Engineering section.
- Bakker, K. (2003). Structural design of linings for bored tunnels in soft ground. *Heron*, 48(1):33–64.
- Baldi, G., Borsetto, M., and Hueckel, T. (1987). Calibration of mathematical models for simulation of thermal, seepage and mechanical behaviour of Boom clay, Report EUR-10924. Technical report, Commission of the European Community, Luxembourg.
- Baldi, G., Hueckel, T., Peano, A., and Pellegrini, R. (1991a). Developments in modelling of thermo-hydro-geomechanical behaviour of Boom clay and clay-based buffer materials (Volume 1), Final report, Report EUR-13365/1. Technical report, Commission of the European Community, Luxembourg.
- Baldi, G., Hueckel, T., Peano, A., and Pellegrini, R. (1991b). Developments in modelling of thermo-hydro-geomechanical behaviour of Boom clay and clay-based buffer materials (Volume 2), Final report, Report EUR-13365/2. Technical report, Commission of the European Community, Luxembourg.
- Baldi, G., Hueckel, T., and Pellegrini, R. (1988). Thermal volume changes of the mineralwater system in low-porosity clay soils. *Canadian Geotechnical Journal*, 25(4):807–825. URL: <http://duke.edu/~hueckel/papers/baldihueckel88.pdf>.

- Barnichon, J. D., Neerdael, B., Grupa, J., and Vervoort, A. (2000). CORA Project TRUCK-II. Technical report, Waste & Disposal Department SCK-CEN, Mol, Belgium. URL: <http://www.covra.nl/cms-file/get/iFileId/2477>.
- Bastiaens, W., Bernier, F., Buyens, M., Demarche, M., Li, X., Linotte, J., and Verstricht, J. (2003). The connecting gallery-the extension of the HADES underground research facility at Mol, Belgium. *EURIDICE report*, pages 03–294.
- Bastiaens, W., Bernier, F., and Li, X. L. (2006). An overview of long-term HM measurements around HADES URF. In *EUROCK 2006, Multiphysics coupling and long term behaviour in rock mechanics*, pages 15–26, Liège, Belgium.
- Bastiaens, W., Bernier, F., and Li, X. L. (2007). SELFRAC: Experiments and conclusions on fracturing, self-healing and self-sealing processes in clays. *Physics and Chemistry of the Earth, Parts A/B/C, Clay in natural and engineered barriers for radioactive waste confinement - Part 2*, 32(8–14):600–615.
- Benz, T. (2006). *Small-strain stiffness of soils and its numerical consequences*. Inst. für Geotechnik, Stuttgart, Germany.
- Bernier, F., Li, X.-L., and Bastiaens, W. (2007a). Twenty-five years geotechnical observation and testing in the Tertiary Boom Clay formation. *Géotechnique*, 57(2):229–237.
- Bernier, F., Li, X. L., Verstricht, J., Barnichon, J. D., Bastiaens, W., Palut, J. M., Ben Slime, J. K., Ghoreychi, M., Gaombalet, J., Huertas, F., Galera, J. M., Merrien, K., Elorza, F. J., and Davies, C. (2007b). CLay Instrumentation Programme for the EXTension of an underground research laboratory, CLIPEX - Final Report. Technical report, EURIDICE.
- Bésuelle, P., Viggiani, G., Desrues, J., Coll, C., and Charrier, P. (2013). A laboratory experimental study of the hydromechanical behavior of Boom Clay. *Rock Mechanics and Rock Engineering*, 47(1):143–155.
- Birkholzer, J., Houseworth, J., and Tsang, C.-F. (2012). Geologic disposal of high-level radioactive waste: Status, key issues, and trends. *Annual Review of Environment and Resources*, 37:79–106.
- Bishop, A. W., Webb, D. L., and Lewin, P. I. (1965). Undisturbed samples of London clay from the Ashford common shaft: Strength-effective stress relationships. *Géotechnique*, 15(1):1–31.
- Bock, H., Dehandschutter, B., Martin, C. D., Mazurek, M., de Haller, A., Skoczylas, F., and Davy, C. (2010). Self-sealing of Fractures in Argillaceous Formations in the Context of Geological Disposal of Radioactive Waste - Review and Synthesis, No. 6148. Technical report, OECD Nuclear Energy Agency (NEA). URL: <http://www.oecd-nea.org/rwm/reports/2010/nea6184-self-sealing.pdf>.
- Brinkgreve, R. B. J. (2011). *Behaviour of Soils and Rocks*. Lecture notes (CIE 4361), Delft University of Technology, Delft, The Netherlands.
- Calvello, M. and Finno, R. J. (2004). Selecting parameters to optimize in model calibration by inverse analysis. *Computers and Geotechnics*, 31(5):410–424.

- Coll, C. (2005). *Endommagement des Roches Argileuses et Perméabilité Induite au Voisinage D'ouvrage Souterrains*. PhD thesis, Université Joseph Fourier Grenoble 1, Grenoble, France.
URL: <http://tel.archives-ouvertes.fr/docs/00/04/84/31/PDF/tel-00010193.pdf>.
- CORA (2001a). Retrievable disposal of radioactive waste in The Netherlands - Summary. Technical report, Commission of Radioactive Waste Disposal, The Hague, the Netherlands.
URL: <http://www.covra.nl/cms-file/get/i fileId/2482>.
- CORA (2001b). Terugneembare berging, een begaanbaar pad? Onderzoek naar de mogelijkheden van terugneembare berging van radioactief afval in Nederland - Eindrapport. Technical report, Commission of Radioactive Waste Disposal, The Hague, the Netherlands.
URL: <http://www.covra.nl/cms-file/get/i fileId/2458>.
- Cui, Y., Nguyen, X., Tang, A., and Li, X. (2013). An insight into the unloading/reloading loops on the compression curve of natural stiff clays. *Applied Clay Science*, 83-84:343–348.
- De Bruyn, D. and Labat, S. (2002). The second phase of ATLAS: the continuation of a running THM test in the HADES underground research facility at Mol. *Engineering Geology*, 64(2–3):309–316.
- De Craen, M. (2005). Geochemical characterisation of specific Boom Clay intervals, R-4080. Technical report, SCK·CEN, Mol, Belgium.
- De Craen, M., Delleuze, D., Volckaert, G., Sneyers, A., and Put, M. (2000). The Boom Clay as natural analogue, Final report to NIRAS/ONDRAF for the period 1997-1999, R-3444. Technical report, SCK·CEN, Mol, Belgium.
- Decleer, J., Viaene, W., and Vandenberghe, N. (1983). Relationships between chemical, physical and mineralogical characteristics of the Rupelian Boom Clay. *Clay Minerals*, 18(1):1–10.
- Dehandschutter, B., Vandycke, S., Sintubin, M., Vandenberghe, N., Gaviglio, P., Sizun, J.-P., and Wouters, L. (2004). Microfabric of fractured Boom Clay at depth: a case study of brittle-ductile transitional clay behaviour. *Applied Clay Science*, 26(1–4):389–401.
- Dehandschutter, B., Vandycke, S., Sintubin, M., Vandenberghe, N., and Wouters, L. (2005). Brittle fractures and ductile shear bands in argillaceous sediments: inferences from Oligocene Boom Clay (Belgium). *Journal of Structural Geology*, 27(5):1095–1112.
- Deng, Y.-F., Tang, A.-M., Cui, Y.-J., and Li, X.-L. (2011a). Study on the hydraulic conductivity of Boom clay. *Canadian Geotechnical Journal*, 48(10):1461–1470.
- Deng, Y. F., Tang, A. M., Cui, Y. J., Nguyen, X. P., Li, X. L., and Wouters, L. (2011b). Laboratory Hydro-mechanical Characterisation of Boom Clay at Essen and Mol. *Physics and Chemistry of the Earth, Parts A/B/C, Clays in Natural & Engineered Barriers for Radioactive Waste Confinement*, 36(17–18):1878–1890.
- Desbois, G., Urai, J. L., and Kukla, P. A. (2009). Morphology of the pore space in claystones – evidence from BIB/FIB ion beam sectioning and cryo-SEM observations. *eEarth*, 4:15–22.
URL: www.electronic-earth.net/4/15/2009/ee-4-15-2009.pdf.

- Duncan, J. M. and Chang, C.-Y. (1970). Nonlinear analysis of stress and strain in soils. *Journal of the Soil Mechanics and Foundations Division*, 96(5):1629–1653.
- François, B., Dizier, V. L. A., Marinelli, F., Charlier, R., and Collin, F. (2013). Hollow cylinder tests on Boom clay: Modelling of strain localization in the anisotropic Excavation Damaged Zone. *Rock Mechanics and Rock Engineering*, 47(1):71–86.
- François, B., Laloui, L., and Laurent, C. (2009). Thermo-hydro-mechanical simulation of ATLAS in situ large scale test in Boom Clay. *Computers and Geotechnics*, 36(4):626–640.
- Gens, A. (2012). Geomechanics of argillaceous rocks for nuclear waste disposal. In *Presentation at the International Post - TIMODAZ Workshop*, Mont Terri rock laboratory, Saint-Ursanne, Switzerland. URL: <http://www.argenco.ulg.ac.be/timodaz/pdf/session%201/S1-L1-Gens.pdf>.
- Gens, A., Vaunat, J., Garitte, B., and Wileveau, Y. (2007). In situ behaviour of a stiff layered clay subject to thermal loading: observations and interpretation. *Géotechnique*, 57(2):207–228.
- Graham, J. and Houlsby, G. (1983). Anisotropic elasticity of a natural clay. *Géotechnique*, 33(2):165–180.
- Honty, M. and De Craen, M. (2012). Boom Clay mineralogy – qualitative and quantitative aspects: Status 2011, External Report 187. Technical report, SCK-CEN, Mol, Belgium. URL: http://publications.sckcen.be/dspace/bitstream/10038/7939/1/er_194.pdf.
- Horseman, S. T., Winter, M. G., and Entwistle, D. C. (1987). Geotechnical Characterization of Boom Clay in Relation to the Disposal of Radioactive Waste. Technical report, Commission of the European Communities.
- Jaky, J. (1944). The coefficient of earth pressure at rest. *Journal of the Society of Hungarian Architects and Engineers*, 78(22):355–358.
- Jeannée, N., Berckmans, A., Wouters, L., Deraisme, J., and Chilès, J. (2013). Quantifying the transferability of hydraulic parameters using geostatistics: The boom clay case. *Physics and Chemistry of the Earth, Parts A/B/C*, 65:20–31.
- Karstunen, M. (2013). *Lecture notes*. Strathclyde University, Glasgow, Scotland, UK.
- Kondner, R. L. (1963). *A hyperbolic stress-strain formulation for sands*. Northwestern University, Evanston, USA.
- Labat, S., Marivoet, J., Wemaere, I., and Maes, T. (2008). Essen-1 borehole of the hydro/05neb campaign: technical aspects and hydrogeological investigations, External Report ER-68. Technical report, SCK-CEN, Mol, Belgium. URL: http://publications.sckcen.be/dspace/bitstream/10038/827/1/er_68.pdf.
- Labouse, V., Sauthier, C., and You, S. (2013). Hollow cylinder simulation experiments of galleries in Boom Clay formation. *Rock Mechanics and Rock Engineering*.
- Laloui, L. (1993). *Modélisation du comportement thermo-hydro-mécanique des milieux poreux anélastiques*. PhD thesis.

- Li, X., Bernier, F., Vietor, T., and Lebon, P. (2007). Deliverable 2: State of the art THMC. Technical report, Thermal Impact on the Damaged Zone Around a Radioactive Waste Disposal in Clay Host Rocks (TIMODAZ).
- Lima, A. (2011). *Thermo-hydro-mechanical behaviour of two deep Belgian clay formations: Boom and Ypresian Clays*. PhD thesis, Universitat Politècnica de Catalunya (UPC), Barcelona, Spain.
- Mertens, J., Bastiaens, W., and Dehandschutter, B. (2004). Characterisation of induced discontinuities in the Boom Clay around the underground excavations (URF, Mol, Belgium). *Applied Clay Science*, 26(1–4):413–428. URL: www.euridice.be/downloads/mertens%20et%20al.pdf.
- Piriyakul, K. and Haegeman, W. (2007). Void ratio function for elastic shear moduli for Boom Clay. *Géotechnique*, 57(2):245–248.
- Plaxis (2010). PLAXIS 2D 2010 - Reference manual. Brinkgreve, R.B.J. and Swolfs, W.M. and Engin, E. (eds.). PLAXIS bv, Delft, The Netherlands.
- Plaxis (2011a). PLAXIS 2D 2011 - Material models manual. Brinkgreve, R.B.J. and Swolfs, W.M. and Engin, E. (eds.). PLAXIS bv, Delft, The Netherlands.
- Plaxis (2011b). PLAXIS 2D 2011 - Reference manual. Brinkgreve, R.B.J. and Swolfs, W.M. and Engin, E. (eds.). PLAXIS bv, Delft, The Netherlands.
- Plaxis (2011c). PLAXIS 2D 2011 - Tutorial manual. Brinkgreve, R.B.J. and Swolfs, W.M. and Engin, E. (eds.). PLAXIS bv, Delft, The Netherlands.
- Plaxis (2013). PLAXIS 3D 2013 - Material models manual. Brinkgreve, R.B.J. and Swolfs, W.M. and Engin, E. (eds.). PLAXIS bv, Delft, The Netherlands.
- Plaxis (2014a). PLAXIS 2D Anniversary Edition - Material models manual. Brinkgreve, R.B.J. and Swolfs, W.M. and Engin, E. (eds.). PLAXIS bv, Delft, The Netherlands.
- Plaxis (2014b). PLAXIS 2D Anniversary Edition - Reference manual. Brinkgreve, R.B.J. and Swolfs, W.M. and Engin, E. (eds.). PLAXIS bv, Delft, The Netherlands.
- Rijkers, R. H. B., Huisman, D. I., de Lang, G., Weijers, J. P., and Witmans-Parker, W. (1998). Inventarisatie geomechanische, geochemische en geohydrologische eigenschappen van Tertiaire kleipakketten CAR Fase II - Eindrapport. Technical report, Nederlands Instituut voor Toegepaste Geowetenschappen (TNO). URL: <http://www.covra.nl/cms-file/get/iFileDialog/2475>.
- Romero, E. (1999). *Characterisation and Thermo-Hydro-Mechanical behaviour of unsaturated boom clay: An experimental study*. PhD thesis, Universitat Politècnica de Catalunya (UPC), Barcelona, Spain.
- Roscoe, K. and Burland, J. (1968). On the generalized stress-strain behaviour of wet clay. In *Engineering Plasticity (ed J. Heyman F.A. Leckie)*, pages 535–609. Cambridge University Press.

- Rowe, P. W. (1962). The stress-dilatancy relation for static equilibrium of an assembly of particles in contact. *Proceedings of the Royal Society of London. Series A. Mathematical and Physical Sciences*, 269(1339):500–527.
- Schanz, T. (1998). *Zur Modellierung des mechanischen Verhaltens von Reibungsmaterialien*. Inst. für Geotechnik, Stuttgart, Germany.
- Schanz, T. and Vermeer, P. (1996). Angles of friction and dilatancy of sand. *Geotechnique*, 46(1):145–152.
- Schanz, T., Vermeer, P., and Bonnier, P. (1999). The hardening soil model: formulation and verification. In *Beyond 2000 in computational geotechnics: 10 years of PLAXIS International; proceedings of the International Symposium beyond 2000 in Computational Geotechnics, Amsterdam, The Netherlands, 18-20 March 1999*. Rotterdam: Taylor & Francis.
- Skempton, A. W. (1964). The long-term stability of clay slopes. *Geotechnique*, 14(2):77–101.
- Sultan, N. (1997). *Etude du comportement thermo-mécanique de l'argile de Boom: expériences et modélisation*. PhD thesis, École Nationale des Ponts et Chaussées, Paris, France.
- Sultan, N., Cui, Y.-J., and Delage, P. (2010). Yielding and plastic behaviour of Boom Clay. *Géotechnique*, 60(9):657–666.
- Tsang, C.-F., Bernier, F., and Davies, C. (2005). Geohydromechanical processes in the Excavation Damaged Zone in crystalline rock, rock salt, and indurated and plastic clays - in the context of radioactive waste disposal. *International Journal of Rock Mechanics and Mining Sciences*, 42(1):109–125.
- Verhoef, E., Neeft, E., Grupa, J., and Poley, A. (2011). Outline of a disposal concept in clay, OPERA-PG-COV008. Technical report, Centrale Organisatie Voor Radioactief Afval (COVRA). URL: <http://www.covra.nl/cms-file/get/iFileId/2417>.
- Vermeer, P. and Neher, H. (1999). A soft soil model that accounts for creep. In *Proceedings of the International Symposium beyond 2000 in Computational Geotechnics*, pages 249–261.
- Volckaert, G., Bernier, F., Sillen, X., Van Geet, M., Mayor, J.-C., Göbel, I., Blümling, P., Frieg, B., and Su, K. (2004). Similarities and Differences in the Behaviour of Plastic and Indurated Clays. In *6th European Commission Conference on the Management and Disposal of Radioactive Waste (Euradwaste '04), Community Policy and Research & Training Activities*, Luxembourg. URL: ftp://ftp.cordis.europa.eu/pub/fp6-euratom/docs/euradwaste04pro_6-7-volckaert_en.pdf.
- Wildenborg, A., Orlic, B., de Lange, G., de Leeuw, C. S., van Weert, F., Veling, E. J. M., de Cock, S., Thimus, J. F., Lehnens-de Rooij, C., and den Haan, E. J. (2000). Transport of RAdionuclides disposed of in Clay of Tertiary ORigin (TRACTOR) - Final report. Technical report, Netherlands Institute of Applied Geoscience TNO - National Geological Survey, Utrecht, the Netherlands. URL: <http://www.covra.nl/cms-file/get/iFileId/2478>.
- Yu, H.-D., Chen, W.-Z., Jia, S.-P., Cao, J.-J., and Li, X.-L. (2012). Experimental study on the hydro-mechanical behavior of Boom clay. *International Journal of Rock Mechanics and Mining Sciences*, 53:159–165.

- Yu, L., Rogiers, B., Gedeon, M., Marivoet, J., De Craen, M., and Mallants, D. (2013). A critical review of laboratory and in-situ hydraulic conductivity measurements for the Boom Clay in Belgium. *Applied Clay Science*, 75–76:1–12.
- Zeelmaekers, E., Honty, M., Derkowsky, A., De Craen, M., Vandenbergh, N., and Geet, M. V. (2010). A new and improved methodology for qualitative and quantitative mineralogical analysis of Boom Clay. In *Fourth international meeting on Clays in Natural & Engineered Barriers for Radioactive Waste Confinement*, pages 73–74, Nantes, France. URL: http://www.nantes2010.com/doc/abstracts/data/pdf/073_074_0_03A_3.pdf.

